FZD-517

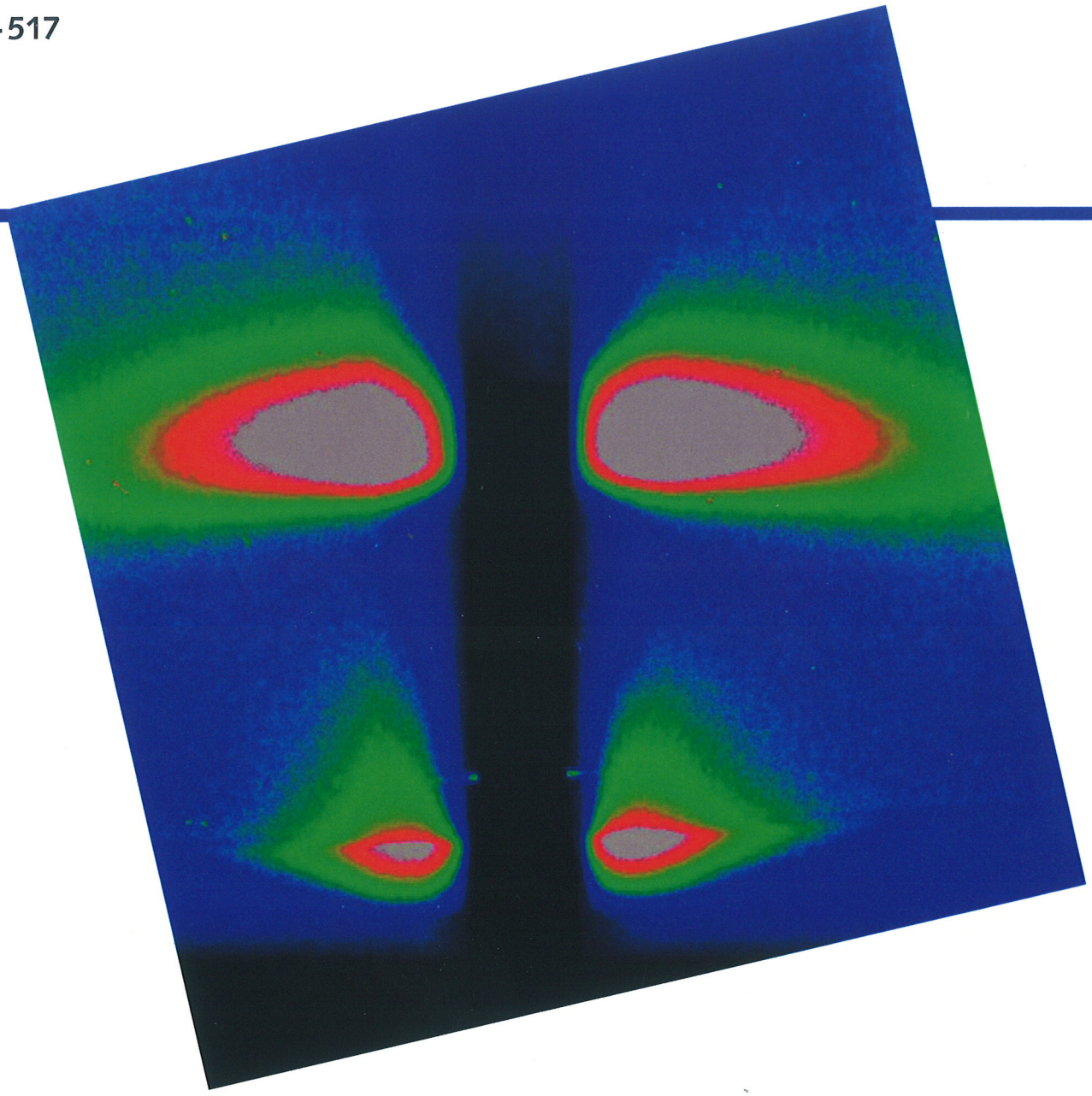

Wissenschaftlich-Technische Berichte
FZD-517 2009 · ISSN 1437-322X

BI-ANNUAL REPORT 2007/08

ROSSENDORF BEAMLINE AT ESRF (ROBL-CRG)

Forschungszentrum
Dresden Rossendorf

Wissenschaftlich-Technische Berichte
FZD-517
2009

Bi-Annual Report 2007/2008

The Rossendorf-Beamline at ESRF (ROBL-CRG)

Editors:
A.C. Scheinost and C. Baehtz

Forschungszentrum Dresden Rossendorf

Preface

The **Ro**ssendorf **B**eam**l**ine (**ROBL**) - located at BM20 of the European Synchrotron Radiation Facility (ESRF) in Grenoble, France - is in operation since 1998. This 6th report covers the period from January 2007 to December 2008. In these two years, 50 peer-reviewed papers have been published based on experiments done at the beamline. The average citation index, which increased constantly over the years, has now reached 3.5 (RCH) and 3.0 (MRH), indicating that papers are predominately published in journals with high impact factors. Six exemplary highlight reports on the following pages should demonstrate the scientific strength and diversity of the experiments performed on the two end-stations of the beamline, dedicated to Radiochemistry (RCH) and Materials Research (MRH).

Demand for beamtime remains very high as in the previous years, with an average oversubscription rate of 1.8 for ESRF experiments. The attractiveness of our beamline is based upon the high specialization of its two end-stations. RCH is one of only two stations in Europe dedicated to x-ray absorption spectroscopy of actinides and other radionuclides. The INE beamline at ANKA provides superior experimental flexibility and extends to lower energies, including important elements like P and S. In contrast, ROBL-RCH provides a much higher photon flux, hence lower detection limits crucial for environmental samples, and a higher energy range extending to elements like Sb and I. Therefore, both beamlines are highly complementary, covering different aspects of radiochemistry research. Once the MARS beamline at SOLEIL is ready to run radionuclides (>2010), it will cover a third niche (Materials Science of actinides, including irradiated fuel) not accessible for the two other beamlines.

The Materials Research Hutch MRH has realized an increasing number of in-situ investigations in the last years. On the one hand thin film systems were characterized during magnetron sputtering. On the other hand diffraction experiments under controlled atmosphere were performed. A high variety of experimental parameters was covered by varying pressure, temperature and atmospheric compositions including highly reactive gases. Furthermore structural investigations were combined with electrical conductivity measurements. These kind of in-situ experiments are the key to monitor and understand reaction mechanism or the influence of process parameters, which are again the basis to tailor materials properties on demand. The core competences of MRH are these experimental possibilities, which make it unique among other diffraction beamlines.

In fall 2007, ROBL was reviewed by an international panel on behalf of the ESRF. The very positive panel report recommended a renewal of the contract between ESRF and FZD for the next five years, and a major upgrade of critical optical components of the beamline to keep ROBL competitive for the next decade. The FZD will provide 2 Mio € from 2009 to 2011 for this upgrade, which will be performed in parallel to the major upgrade of the ESRF to minimize the downtime. According to the current plans of the ESRF, our users have to expect that ROBL will have only limited or no operation for several months from August 2011 on.

Since July 2004 the beamline is a member of the pooled facilities of ACTINET – European Network of Excellence. In the reported period, RCH has provided 27 % of its inhouse beamtime to perform 11 ACTINET experiments. The success of ACTINET within FP-6 has now led to a renewal of ACTINET within FP-7, running until end of 2011.

The beamline staff would like to thank all partners, research groups and organizations who supported the beamline during the last 24 months. Special thanks to the FZD

management, the CRG office of the ESRF with Axel Kaprolat as liaison officer, and to the ESRF safety group members, Paul Berkvens, Patrick Colomp and Yann Pira.

Furthermore, we would like to thank our external proposal review members, Prof. Andre Maes (KU Leuven), Prof. Laurent Charlet (UJF Grenoble), and Prof. Dirk Meyer (TU Dresden), who evaluated the inhouse proposals in a thorough and timely manner, thereby ensuring that beamtime was distributed according to scientific merit.

Andreas Scheinost and Carsten Baehtz

Contents

1. Scientific Highlights

Experimental insight into the radiation resistance of zirconia-based americium ceramics

Renaud C. Belin[1], Philippe M. Martin[1], Philippe J. Valenza[1], Andreas C. Scheinost[2]

[1] CEA, DEN, DEC, CEN Cadarache, 13108 Saint-Paul-Lez-Durance, France

[2] Institute of Radiochemistry, Forschungszentrum Dresden-Rossendorf, 01314 Dresden, Germany

Introduction

Ceramics intended for use as nuclear fuels, transmutation targets or actinide immobilization matrices have to withstand severe conditions including internal radiation. Resistance to amorphization and limited swelling are therefore key requirements. Oxygen deficient compounds with structures related to fluorite often meet these criteria. Pyrochlore oxides with the formula $A_2B_2O_7$ (A and B are metallic cations) are especially appealing because they are able to host high amounts of actinides. The ratio of the two cation radii, r_A/r_B, may vary between 1.46 and 1.78, thereby defining the stability field for pyrochlore. At the lower limit, cation disorder increases and the tendency of pyrochlore to transform into a defect-fluorite structure is higher [1]. Experiments have shown that this transition can be induced by irradiating selected $A_2^{3+}Zr_2^{4+}O_7$ pyrochlores, the resulting phase being highly radiation-resistant [2]. Up to now, most studies have been performed on surrogate rare-earth compounds using ion-beam irradiation in order to simulate α self-irradiation. This external irradiation induces only localized disturbed regions, whereas α-emitting actinides within the structure irradiate the compound homogeneously. Due to the radiotoxicity of α-emitting actinides and the associated handling problems, however, such studies, which would represent realistic conditions much better, are rare [3,4,5,6].

We investigated the order-disorder phase transition of pyrochlore to defect-fluorite by closely following structural changes of $^{241}Am_2Zr_2O_7$ under α self-irradiation. The presence of 62 wt% of ^{241}Am ($t_{1/2}$=432 y) in the structure provided a high dose rate which enabled us to follow within only four years an α self-irradiation-induced aging process corresponding to much longer time periods in the case of immobilization ceramics [7]. X-ray diffraction (XRD) and X-ray absorption spectroscopy (XAS) analyses were combined to selectively probe the long-range and the short-range order and the local environment of both cations [8,9].

Materials and methods

Synthesis conditions for $Am_2Zr_2O_7$ are described in [belin2008]. During the aging process, the compound was stored in a hermetic container under N_2 atmosphere to prevent oxidation.

XRD measurements were performed at room temperature with a Siemens D5000 X-ray diffractometer (Cu Kα1 radiation, λ=1.5406 Å). Diffraction patterns were obtained by scanning from 25° to 148° 2Θ using 0.02° step-intervals. XAS measurements were performed at 15K at the Rossendorf Beamline (BM20) located at the European Synchrotron Radiation Facility (ESRF, Grenoble, France). Americium L_{II} (22952 eV) and zirconium K (17998 eV) edge spectra were collected for each sample in fluorescence mode using a 13 elements Ge detector. The ATHENA software [10] was used for extracting EXAFS oscillations from the raw absorption spectra. Experimental EXAFS spectra were Fourier transformed using a Hanning window over the full k space range available for each edge: 2.1-13.3 $Å^{-1}$ for americium and 2.5-10.3 $Å^{-1}$ for zirconium. Curve fitting was performed in k^3 for R-values in the range 1.3-4.1 Å for both edges. Phases and amplitudes for the interatomic scattering paths were calculated with the *ab initio* code FEFF8.20 [11]. At the Zr edge, a multi-scattering path corresponding to the doubling of the

Zr-O single-scattering path (Zr-O-Zr-O) was fitted, correlating R and σ^2 to double the values used for the Zr-O single-scattering shell.

Results and discussion

As expected from the ionic radius ratio criterion (r_{Am}/r_{Zr}=1.51), the compound gradually transformed to the defect-fluorite structure in about 370 days corresponding to 0.21 displacements per atom (dpa) (Fig. 1A). In contrast to the commonly observed increase in volume under α self-irradiation, e.g. for $^{241}AmO_2$ [12], we found a decrease in the cell parameter by 0.02 Å, corresponding to a volume contraction of 0.6% (Fig. 1B). To our knowledge, such a volume reduction has never been observed before in irradiated pyrochlore. After the phase transition was completed, the volume remained constant. Within the whole experimental period of 1,360 days, no amorphization was observed. The cumulated dose during this period was 9.4×10^{18} α-decay events·per gram; corresponding to 0.80 dpa. This is equivalent to the dose accumulated by multiphase ceramics with 20wt% ^{239}Pu during 1,000 years of storage [7]. The defect-fluorite structure is therefore remarkably resistant to such radiation doses.

What drives the resistance to radiation and the unusual negative lattice expansion observed in $Am_2Zr_2O_7$? We believe that the answer lies in a thorough understanding of how lattice point defects are formed and recombined during the order-disorder transition.

Atomistic simulations based on energy minimization techniques best describe the disorder transition by the formation of cation antisites and oxygen Frenkel pairs [13,14]. The $A_2Zr_2O_7$ Fd-3m cubic structure is a fluorite-type superstructure with doubled cell parameter, which can be regarded as two distinct cationic and anionic sublattices: A occupies the 16*d* (1/2, 1/2, 1/2) site, Zr the 16*c* (0, 0, 0) site, and O the 8*b* (3/8, 3/8, 3/8) and 48*f* (x, 1/8, 1/8) sites. Only the "x" value of the O(48*f*) is unconstrained. The O site 8*a* (1/8, 1/8, 1/8) is vacant. In the defect-fluorite Fm-3m structure, both A and Zr occupy the 4a (0,0,0) site, while O is in 8*c* (1/4, 1/4, 1/4). In $A_2Zr_2O_7$ pyrochlore, a cation antisite involves the substitution of an A cation at the 16*d* Zr site and of a Zr cation at the 16*c* A site. An oxygen Frenkel consists of a 48*f* vacancy and the occupation of an 8*a* site. The exact sequence of recombinations during the order-disorder transition is still a matter of debate: anionic disorder followed by cationic recombination [15], cationic disorder driving the transition [16],17] or the concomitant occurrence of both cationic and anionic defects [18]. Although difficult to perform, studying partial disorder is therefore essential to understand the underlying processes. To address this issue, we have characterized short-lived intermediate states with XRD and XAS in addition to the initial and the defect-fluorite structure states.

X-ray profiles collected from the initial to the fluorite states were refined with the Rietveld method [19] using JANA 2000 [20]. To obtain low isotropic displacement parameters for both Am and Zr, we had to introduce concomitant cation antisite and anion Frenkel pair defects to account for the progressive disorder occurring in both sublattices. A cation antisite is defined by: $Am_{Am} + Zr_{Zr} \leftrightarrow Am_{Zr} + Zr_{Am}$ and an oxygen Frenkel by: $O_{O(48f)} \leftrightarrow V_{O(48f)} + O_{i(8a)}$. Accordingly, the 16*d* site was refined with Am_{Am} and Zr_{Am} type atoms, and the 16*c* site with Am_{Zr} and Zr_{Zr} type atoms. In addition, oxygen originally at 48*f* was proportionally distributed to the 8*a* vacancy site ($O_{i(8a)}$). The O(8*b*) site was kept fully occupied (Table 1). While the initial state showed no cation exchange, the intermediate states revealed an increasing cationic disorder. Already after 0.02 dpa, 7% of the cations had swapped positions. This percentage increased to about 40% for 0.14 dpa and to 50% above 0.21 dpa, where the defect-fluorite state was reached. The increasing disorder during the transition is further revealed by the increase in the average O(48*f*) positional and displacement parameters. Once the defect-fluorite state was reached, disorder remained constant and the overall long-range order was maintained.

TABLE 1
Details of the Rietveld structure refinements including site occupation fractions (SOF) and isotropic displacement parameters $U_{iso}(Å^2)$. The following constraints were applied: identical SOF for Am_{Am} and Zr_{Zr}, as well as for Zr_{Am}, Am_{Zr} and $O_{i(8a)}$ and all U(O) identical. The defect-fluorite patterns were refined in the Fm-3m space group with only two sites. Thus, Fd-3m SOF and $x(O_{O(48f)})$ values are meaningless in the corresponding columns.

dpa	**0**	**0.02**	**0.06**	**0.12**	**0.14**	**0.21**	**0.38**	**0.80**
Days after synthesis	0	40	100	200	250	370	650	1360
Space Group	Fd-3m	Fd-3m	Fd-3m	Fd-3m	Fd-3m	Fm-3m	Fm-3m	Fm-3m
a(Å)	10.6678(1)	10.6686(1)	10.6605(2)	10.6505(2)	10.6489(4)	5.3233(1)	5.3243(1)	5.3233(1)
R_p	3.38	5.83	3.53	3.12	4.03	5.11	4.60	4.74
R_{wp}	4.31	7.37	4.52	3.93	5.08	6.47	5.74	5.99
R_{Bragg}	3.18	2.34	2.42	2.22	3.27	1.94	2.05	3.24
GoF	1.28	1.11	1.30	1.17	1.12	1.17	1.38	1.08
SOF (Am_{Am}/Zr_{Zr})	0.986(1)	0.927(3)	0.804(3)	0.642(6)	0.62(1)	n.a.	n.a.	n.a.
SOF ($Zr_{Am}/Am_{Zr}/O_{i(8a)}$)	0.014(1)	0.073(3)	0.196(3)	0.357(6)	0.38(1)	n.a.	n.a.	n.a.
SOF ($O_{O(48f)}$)	0.9976(2)	0.9879(5)	0.9674(6)	0.941(1)	0.937(2)	n.a.	n.a.	n.a.
$x(O_{O(48f)})$	0.3372(7)	0.343(1)	0.367(1)	0.373(3)	0.368(5)	n.a.	n.a.	n.a.
$U_{iso}(Am_{Am}/Zr_{Am})$	0.0129(4)	0.016(1)	0.019(1)	0.021(1)	0.021(2)	0.026(1)	0.026(1)	0.018(2)
$U_{iso}(Zr_{Zr}/Am_{Zr})$	0.0121(6)	0.016(1)	0.021(1)	0.028(2)	0.026(3)	0.026(1)	0.026(1)	0.018(2)
$U_{iso}(O)$	0.044(2)	0.045(4)	0.057(2)	0.083(3)	0.088(5)	0.079(3)	0.074(3)	0.072(7)

Cation disordering provides an opportunity to elucidate the cause of the volume contraction observed during the transition. We eliminated Am oxidation as a potential cause: the Am-L_{II} XANES (X-ray Absorption Near Edge Structure) spectrum showed no detectable amount of Am^{4+} up to 0.80 dpa. Instead, the progressive lattice contraction may be due to the smaller ionic radius of Am^{3+} at the sixfold coordinated Zr site, occurring via Am-Zr antisite disorder, as compared to the larger radius in the initial eightfold coordination. This result is in line with molecular dynamics simulations by Rushton *et al.* [21] predicting negative volume changes for zirconate pyrochlores during the order-disorder transition, if r_A/r_B is between 1.48 and 1.57. Therefore, the cause for the volume contraction is most likely inherent to the ability of the structure to accommodate disorder and to form cation antisites.

The local structure around both cations was then studied with Am L_{II} and Zr K-edges EXAFS (Extented X-ray Absorption Fine Structure) spectroscopy on four representative samples: one at 0.02 dpa, *i.e.* still in an intermediate pyrochlore state, and three more at 0.21, 0.36 and 0.55 dpa in defect-fluorite states. Fourier transforms are shown in Fig. 1, fit results in Table 2.

In line with the XRD results, we observe for the 0.02 dpa state identical Am-O(8*b*) and shorter Am-O(48*f*) distances in comparison to the initial structure, confirming the randomization of oxygen atoms through Frenkel pairs. This is further supported by the high Debye-Waller factors (σ^2), which reflect only static disorder since the samples were measured at 15 K. In contrast to americium, the local coordination around zirconium does not show any randomization of the oxygen sublattice (6 equidistant O(48*f*) atoms at 2.13 Å and low σ^2). The ability of EXAFS to measure the expansion of selected bonds [22] offers complementary information on the disordering processes: while the Am-Am distance is in agreement with that of XRD, Am-Zr and Zr-Zr distances are shorter. However, Am-Zr (Am L_{II}-edge) and Zr-Am (Zr K-edge) distances are identical, providing evidence for the cation antisite formation in this intermediate structural state.

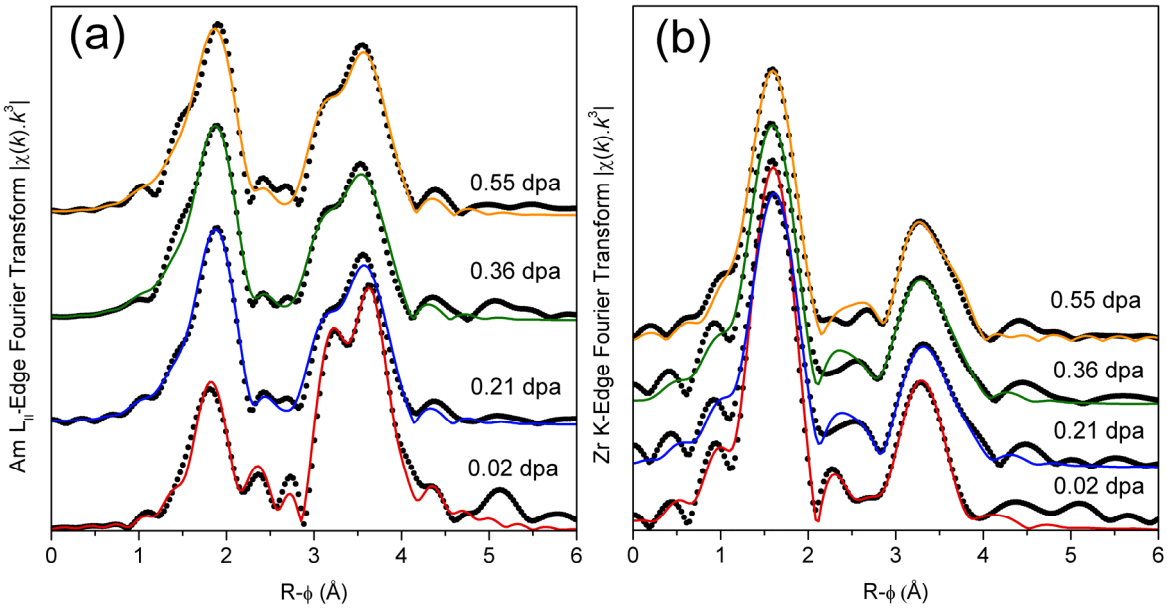

Fig. 1.
Am L_{II}-edge **(a)** and Zr K-edge **(b)** Fourier transform EXAFS spectra for the 0.02, 0.21, 0.36 and 0.55 dpa states. Experimental data are displayed by symbols and fits by lines. **(a)** At 0.02 dpa, the two peaks at ~1.9 Å and ~2.2 Å correspond to the two Am-O distances (O(8*b*) and O(48*f*)) in the pyrochlore structure. A more intense peak at the shorter distance coupled with the fading peak at ~2.2 Å is indicative of the conversion to the fluorite structure (dpa ≥0.21), where Am is surrounded only by equidistant oxygen atoms. **(b)** The intense peak at ~1.6 Å corresponds to Zr-O distances and remains nearly identical for all the spectra. The Zr-Am and Zr-Zr interactions give rise to the peak at ~3.3 Å, which broadens between 0.02 and 0.21 dpa because shells separate in distance.

EXAFS spectra for the 0.21, 0.36 and 0.55 dpa fluorite states are nearly identical, demonstrating the stability of the defect-fluorite structure. Both Am and Zr cations are surrounded by only 7 equidistant oxygen atoms, in comparison to the eightfold coordination of the perfect fluorite structure. Along with the larger σ^2 in comparison to the 0.02 dpa pyrochlore, this gives ample evidence for the randomization of the oxygen sublattice and for a more disordered environment after the phase transition.

The Am-O distance of 2.36 Å is higher than that derived from the defect-fluorite XRD structural model; however, it is in agreement with the distance observed in 30wt% Am-doped, yttria-stabilized zirconia [23]. Since both Am and Zr cations occupy the same crystallographic position in the fluorite structure lattice (insert Fig. 1B), we would have expected the same oxygen distance for both the Am and Zr coordination spheres. Surprisingly, the Zr-O distance of 2.15 Å is much shorter than the Am-O distance. Li *et al.* observed a similar Zr-O distance for sevenfold-coordinated polyhedra in cubic stabilized zirconia [24]. The Zr-O distance remains always close to the distances of the initial states, i.e. is almost unaffected by irradiation. Another evolution in the defect-fluorite structure is the disorder observed for the cation-cation coordination shells reflected by the very high σ^2 values, in particular for zirconium. From the detailed analysis of distances, important conclusions become apparent. While the Am-Am distances are in agreement with XRD, the Am-Zr and Zr-Zr distances are shorter, implying that the Am and Zr local environments are non-equivalent. For all irradiation levels, Am-Zr and Zr-Am distances are identical, in line with the cation antisite formation. As proposed by earlier studies [16,25], such a disorder in the Zr cation shell reveals a loss of second neighbour periodicity due to rotations of the Zr polyhedra along shared edges and corners. This polyhedral flexibility thereby contributes to accommodate the increasing disorder within the structure.

TABLE 2
Am L_{II} and Zr K-edges EXAFS fit results for 0.02, 0.21, 0.36 and 0.55 dpa states (R=interatomic distance in Å, C.N.=coordination number, σ^2=Debye-Waller factor in $Å^2$). For comparison, interatomic distances obtained from the XRD Rietveld refinement are reported at initial, 0.02 and 0.21 dpa states.

		XRD	**EXAFS**		
		R (Å)	R (Å)	C.N.	σ^2 ($Å^2$)
Am-O(8*b*)	initial	2.3097(2)			
Fd-3m	0.02 dpa	2.3098(2)	2.31(2)	2.8(5)	0.006(1)
Am-O(48*f*)	initial	2.563(5)			
Fd-3m	0.02 dpa	2.52(1)	2.53(2)	4.8(5)	0.015(1)
Am-O(8*c*)	0.21 dpa	2.3050(4)	2.35(2)	6.6(5)	0.009(1)
Fm-3m	0.36 dpa		2.36(1)	7.0(5)	0.011(1)
	0.55 dpa		2.36(1)	7.0(5)	0.011(1)
Am-Am	initial	3.7716(4)			
	0.02 dpa	3.7719(4)	3.76(1)	6.0(5)	0.004(1)
	0.21 dpa	3.7641(7)	3.75(1)	5.2(5)	0.007(1)
	0.36 dpa		3.75(1)	6.0(5)	0.009(1)
	0.55 dpa		3.75(1)	6.0(5)	0.010(1)
Am-Zr	initial	3.7716(4)			
	0.02 dpa	3.7719(4)	3.74(1)	6.0(5)	0.008(1)
	0.21 dpa	3.7641(7)	3.65(1)	6.3(5)	0.012(1)
	0.36 dpa		3.64(1)	6.0(5)	0.011(1)
	0.55 dpa		3.65(1)	6.0(5)	0.011(1)
Am-O(48*f*)	initial	4.318(2)			
	0.02 dpa	4.332(4)	4.26(4)	17(2)	0.01(1)
Zr-O(48*f*)	initial	2.103(3)			
Fd-3m	0.02 dpa	2.131(7)	2.13(1)	6.3(5)	0.005(1)
Zr-O(8*c*)	0.21 dpa	2.3050(4)	2.15(1)	6.6(5)	0.008(1)
Fm-3m	0.36 dpa		2.14(1)	6.7(5)	0.008(1)
	0.55 dpa		2.15(1)	7.5(5)	0.008(1)
Zr-Am	initial	3.7716(4)			
	0.02 dpa	3.7719(4)	3.75(2)	6(1)	0.004(1)
	0.21 dpa	3.7641(7)	3.64(2)	6(1)	0.010(1)
	0.36 dpa		3.64(2)	6(1)	0.011(1)
	0.55 dpa		3.64(2)	6(1)	0.010(1)
Zr-Zr	initial	3.7716(4)			
	0.02 dpa	3.7719(4)	3.75(2)	6(1)	0.008(1)
	0.21 dpa	3.7641(7)	3.51(2)	6(1)	0.017(1)
	0.36 dpa		3.51(2)	6(1)	0.015(1)
	0.55 dpa		3.52(2)	6(1)	0.015(1)

Conclusion

Our work provides experimental insight into the disordering processes occurring in $Am_2Zr_2O_7$ when subjected to α self-irradiation. The compound is extremely radiation-tolerant and free from swelling due to the concurrent disorder in both the anionic and cationic networks and to the flexibility of the Zr polyhedra. There is strong interest in nuclear materials with such properties. They are attractive candidates as durable actinide immobilization hosts and as stable transmutation targets [26,27].

Acknowledgements

We would like to thank E. Gavilan and A. Pieragnoli for their support at the Rossendorf Beamline at ESRF during EXAFS and C. Belin for assistance in X-ray data analysis. We acknowledge the Rossendorf Beamline and the European Synchrotron Radiation Facility for provision of synchrotron radiation facilities.

References

[1] R. Ewing, W. Weber, J. Lian, *J. Appl. Phys.* **95** (2004) 5949-5971.

[2] S. Wang, B. Begg, L. Wang, R. Ewing, W. Weber, K. Kutty, *J. Mater. Res.* **14** (1999) 4470-4473.

[3] G. Lumpkin, R. Ewing, *Phys. Chem. Miner.* **16** (1988) 2-20.

[4] W. Weber, J. Wald, H. Matzke, *J. Nucl. Mater.* **138** (1986) 196-209.

[5] I. Farnan, H. Cho, W.J. Weber, *Nature* **445** (2007) 190-193.

[6] R. Sykora, P. Raison, R. Haire, *J. Solid State Chem.* **178** (2005) 578-583.

[7] W. Weber, R. Ewing, C. Catlow, T. de la Rubia, L. Hobbs, C. Kinoshita, H. Matzke, A. Motta, M. Nastasi, E. Salje, E. Vance, S. Zinkle, *J. Mater. Res.* **13** (1998) 1434-1484.

[8] S. Conradson, D. Manara, F. Wastin, D. Clark, G. Lander, L. Morales, J. Rebizant, V. Rondinella, *Inorg. Chem.* **43** (2004) 6922-6935.

[9] P. Martin, S. Grandjean, C. Valot, G. Carlot, M. Ripert, P. Blanc, C. Hennig, *J. Alloy. Compd.* **444-445** (2007) 410-414.

[10] B. Ravel, M. Newville, *J. Synchrotron. Radiat.* **12** (2005) 537-541.

[11] J. Rehr, R.C. Albers, *Rev. Mod. Phys.* **72** (2000) 621.

[12] T. Chikalla, L. EYRING, *J. Inorg. Nucl. Chem.* **30** (1968) 133-145.

[13] K. Sickafus, L. Minervini, R. Grimes, J. Valdez, M. Ishimaru, F. Li, K. McClellan, T. Hartmann, *Science* **289** (2000) 748-751.

[14] L. Minervini, R. Grimes, K.E. Sickafus, *J. Am. Ceram. Soc.* **83** (2000) 1873-1878.

[15] J. Lian, W. Weber, W. Jiang, L. Wang, L. Boatner, R. Ewing, Nucl. Instrum. Meth. B 250 (2006) 128-136.

[16] N. Hess, B. Begg, S. Conradson, D. McCready, P. Gassman, W. Weber, *J. Phys. Chem. B* **106** (2002) 4663-4677.

[17] A. Chartier, C. Meis, J. Crocombette, W. Weber, L. Corrales, *Phys. Rev. Lett.* **94** (2005) 025505.

[18] K. Sickafus, R. Grimes, J. Valdez, A. Cleave, M. Tang, M. Ishimaru, S. Corish, C. Stanek, B. Uberuaga, *Nat. Mater.* **6** (2007) 217-223.

[19] H. Rietveld, *J. Appl. Crystallogr.* **2** (1969) 65-71.

[20] V. Petricek, M. Dusek, L. Palatinus, Jana 2000. The Crystallographic Computing System., Institute of Physics, Praha, Czech Republic, 2000.

[21] M. Rushton, C. Stanek, A. Cleave, B. Uberuaga, K. Sickafus, R. Grimes, *Nucl. Instrum. Meth. B* **255** (2007) 151-157.

[22] R. Howell, S. Conradson, A. Garcia-Adeva, *J. Phys. Chem. B* **111** (2007) 159-167.

[23] M. Walter, C. Nastren, J. Somers, R. Jardin, M.A. Denecke, B. Brendebach, *J. Solid State Chem.* **180** (2007) 3130-3135.

[24] P. Li, I. Chen, J. Penner-Hahn, *J. Am. Ceram. Soc.* **77** (1994) 118-128.

[25] R. Ewing, B. Chakoumakos, G. Lumpkin, T. Murakami, R. Greegor, F. Lytle, *Nucl. Instrum. Meth. B* **32** (1988) 487-497.

[26] P. M. Martin, R. C. Belin, P. J. Valenza, A. C. Scheinost, *J. Nucl. Mater.* **385**, 126–130 (2009)

[27] R. C. Belin, P. M. Martin, P. J. Valenza, A. C. Scheinost, *Inorg. Chem.* in press (2009)

Evidence for the [2*p*4*f*] double-electron excitations in X-ray absorption spectra of actinides

Christoph Hennig[1], Claire Le Naour[2], Christophe Den Auwer[3]

[1] Institute of Radiochemistry, Forschungszentrum Dresden-Rossendorf, 01314 Dresden, Germany

[2] CNRS/Univ. Paris-Sud, Institut de Physique Nucléaire, 91406 Orsay Cedex, France

[3] CEA Marcoule, DEN/DRCP/SCPS, 30207 Bagnols sur Cèze Cedex, France

Introduction

EXAFS spectroscopy became more and more popular in actinide solution chemistry and environmental research because it probes exclusively the environment of the excited atom. Data analysis of EXAFS is getting nowadays more sophisticated and the key to the interpretation of a coordination sphere often depends only on very tiny spectral features. Therefore it becomes important to understand competitive electronic effects superimposed to the one-electron photoexcitation process in the EXAFS spectra.

The inner-shell photoexcitation of an electron is often accompanied by the excitation of secondary electrons with lower binding energies. These electrons can be excited into unoccupied states (shake-up) or ejected into the continuum (shake-off). Such processes are revealed as satellite lines in X-ray fluorescence and photoelectron spectra. X-ray absorption spectra yield directly the energy level of the multielectron excitations in noble gases whose atomic absorption is modulated by discrete resonances and slope modifications. Multielectron resonances have been observed above the *K* edge of Ne [1], Xe [2], Ar [3] and Kr [4] but also above their *L* edges [5]. In noble gases, the absorption signal is not affected by photoelectron backscattering effects from neighboring atoms that cause the extended X-ray absorption fine structure (EXAFS). Although the single-electron EXAFS oscillation is able to cover double-electron excitations, they have been also revealed in the spectra of liquids and solids. As example, solid compounds of the *3*rd period show *KL* multielectron transitions, e.g α-Si [6] and salts of P, S, and Cl [7]. Ca^{2+} hydrate, as example of the *4*th period, shows KM_1 and $KM_{2,3}$ resonances [8]. For *5*th period, multielectron transitions has been observed at the KN_1, $KM_{4,5}$, and $KM_{2,3}$ edges of gaseous Br_2 and HBr [9]. In the *6*th period, e.g. for the lanthanides, the resonances are associated with $LN_{4,5}$ edges [10,11]. Up to now it has not been investigated whether the actinides, as members of the *7*th period, show also multielectron excitations. The low vapor pressure and radioprotection aspects prevent investigations in the gas phase. In the last decade, several EXAFS data of actinides in aqueous solution has been published with the aim to reveal their near-order structure. A part of these spectra has been reinvestigated with regard to multielectron features [12,13].

Results and discussion

Double-electron excitations are usually associated with slope changes and anomalous structures in the atomic background of the X-ray absorption cross section. Noble gases and monoatomic metal vapor [14,15] are appropriated to investigate these effects, whereas condensed systems suffer from the backscattering of the photoelectron wave by the coordinated neighbor atoms. Hydrates, who are the dominating species in aqueous solution at low *pH* values, are only associated with water molecules by electrostatic interactions. The thermal movement of the associated ligands results partly in destructive interference effects in the single-electron scattering amplitude. Such systems are well suited for the study of multielectron resonances.

The actinide elements show numerous oxidation states in particular for the elements Np to Pu, where they range from III to VII. The electronic structure involves besides *6d* states partly filled *5f* shells. The *5f* states are less strictly located than the *4f* states of the

lanthanides, and can therefore participate in the chemical bond. This electronic configuration affects the physical and chemical properties and posses a large variation in the coordination geometry. U, Np, Pu and Am can occur as transdioxo cations, AnO_2^{n+} (n = 1 and 2). These transdioxo bonds are strongly covalent having the character of a triple bond [16].

Although the species in aqueous solution are expected to be appropriate for investigating multielectron effects, a closer inspection revealed limitations in presence of actinyl ions. As an example, the k^3 weighted L_3 edge EXAFS spectra of Np in different oxidation states are shown in Figure 1 together with their corresponding Fourier transforms. The modulus of the Fourier transform represents the pseudoradial distribution of the next neighbor atoms. The Fourier transform is not corrected for the scattering phase shift Δ, so that the peaks are shifted with respect to the true distance R.

Actinide aquo ions in oxidation state IV, V, VI and VII show a wide variation in coordination. As example EXAFS spectra of neptunium species in aqueous solution are shown in Fig. 1.

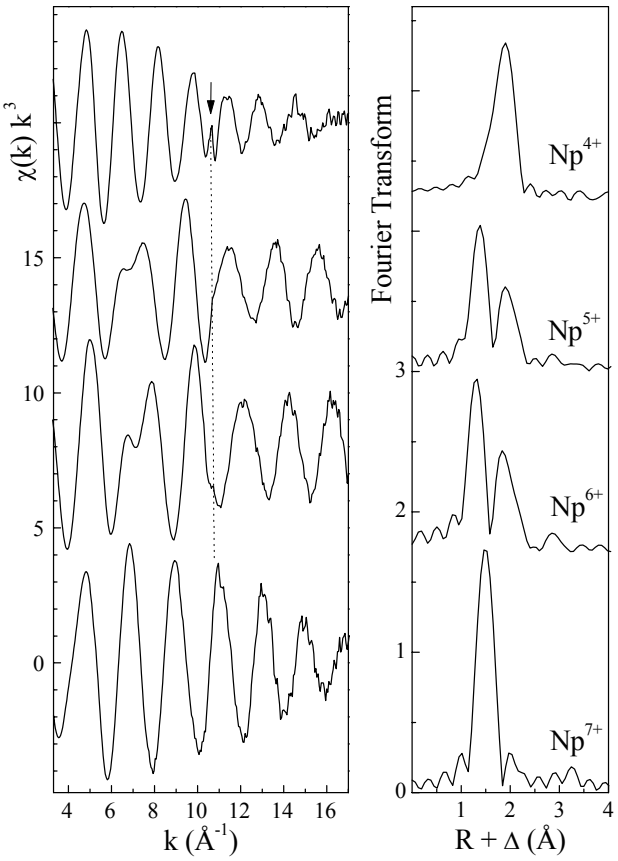

Fig. 1. Np L_3-edge k^3 weighted EXAFS data (left) of Np^{4+}, Np^{5+}, Np^{6+}, and Np^{7+} and their corresponding Fourier transforms (right). The FT is shown in the k range 3.3-13 $Å^{-1}$..

The Np^{4+} hydrate, present here, is coordinated by 9 water molecules with a Np-O distance of 2.41 Å [12]. Its single oxygen coordination shell is related with a sinusoidal oscillation in $\chi(k)$. The coordination polyhedron of Np^{5+} and Np^{6+} shows two axial arranged trans-oxygen atoms (O_{ax}), completed by 4 and 5 equatorial oxygen atoms (O_{eq}), respectively [17,18]. With increasing central atom charge, the bond lengths are shortened around 0.07 Å. A beat node feature occurs in the $\chi(k)$ due to the superposition of axial and equatorial scattering contributions. Structural parameters of aqueous Np^{7+} hydroxide has been published by Bolvin et al. [19]. It has been shown that the coordination polyhedron

comprises four covalent oxygen atoms with a Np-O distance of 1.89 Å. These actinyl oxygen atoms dominate the scattering signal. The coordination polyhedron of $NpO_4(OH)_2^{3-}$ comprises two OH^- ions with a Np-O distance of 2.32 Å. It is obvious that the scattering amplitude at higher *k* range is much more pronounced in presence of actinyl oxygen atoms, than in their absence. The reason is, that the EXAFS amplitude, which is related to the next-neighbor distance with $1/R^2$, is stronger affected by the close located actinyl ions than by the water molecules. In each spectrum anomalous features are observed, indicated in the Figure 1 by an arrow and a dotted line. The most significant feature occurs for Np^{4+}. Weak anomalous structures can be also indicated on the right side of the EXAFS oscillation for Np^{5+}, on the left side for Np^{6+} and on top of the oscillation maximum for Np^{7+}; but there appearance is less pronounced in relation to the anomalous feature visible in the spectrum of Np^{4+}. Similar effects were observed also for other actinyl ions. Therefore, at least under the applied conditions, actinide species with strong covalent coordinated oxygen atoms are less appropriated for the study of multielectron effects than species with a one single hydrate coordination sphere.

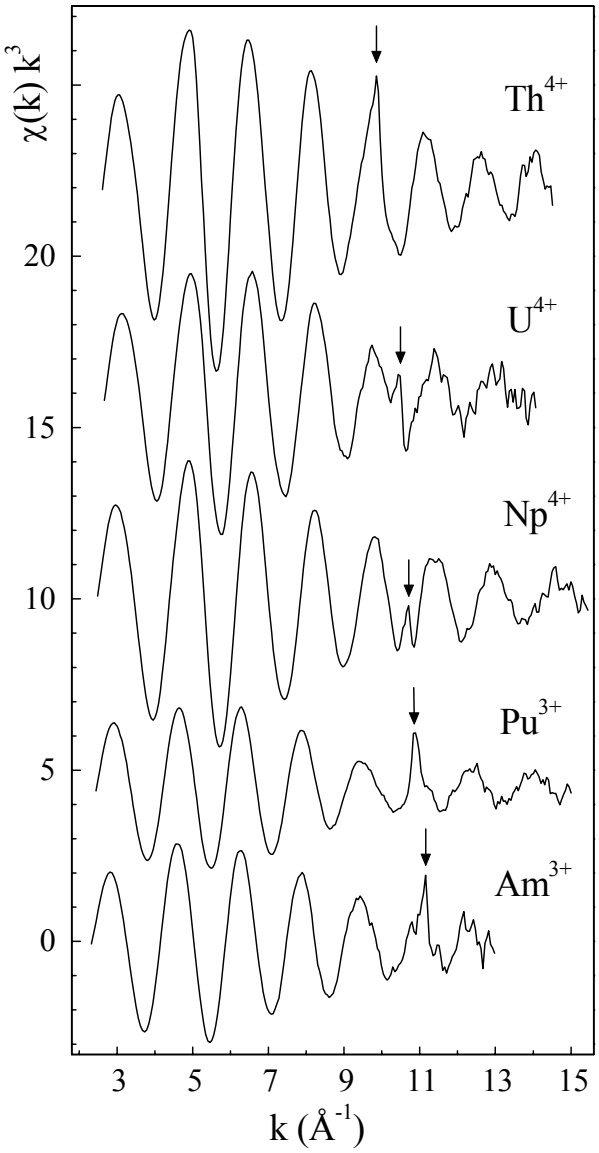

Fig. 2. Experimental k^3 weighted extended X-ray absorption fine structure at the L_3 edge of Th^{4+}, U^{4+}, Np^{4+}, Pu^{3+} and Am^{3+} hydrate. Arrows indicate the maximum of the double-electron excitation.

In order to investigate the multielectron excitation as in the L_3-edge k^3 EXAFS spectra of different actinide hydrates in aqueous solution the actinides Th [12], Pa [13], U [12], Np [12], Pu [12] and Am [12] have been investigated at the Rossendorf Beamline. As example, the double electron excitation features of Th^{4+}, U^{4+}, Np^{4+}, Pu^{3+}, and Am^{3+} are shown in Figure 2.

In the k range 9.8–11.2 $Å^{-1}$ small anomalous features appear superimposed to the main oscillations. These features are indicated individually by arrows in Figure 2. Their position appears shifted to higher k values with increasing atomic number Z. All features show a relative sharp maximum. Sharp, resonance-like absorption features appear only if the core electron excitation is accompanied by a shake-up of the second electron to a bound state.

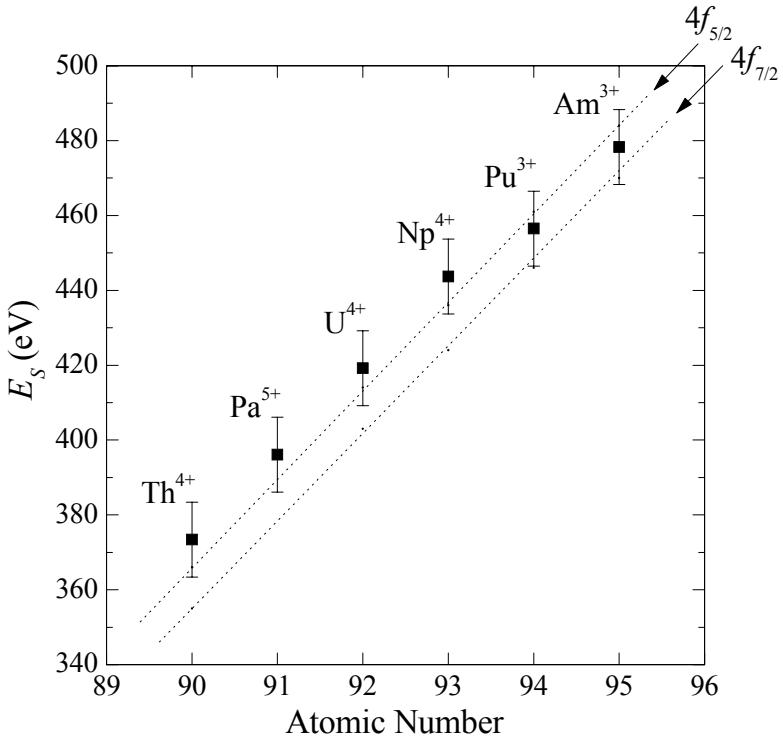

Fig. 3. Experimental energy E_S in comparison with the theoretical Z+1 $4f_{5/2}$ and $4f_{7/2}$ energy of the actinides with oxidation state 0. The error bars represent absolute errors, while the relative errors are in the dimension of the data points.

In order to assign the experimental features to a specific electron excitation channel, the difference between the energy of the anomalous maximum E_f and the energy of the absorption edge threshold, E_0, was estimated. Among the different definitions of E_0, the first maximum of the derivative of the raising edge, E_{1st}, has been used [12]. The energy position of the anomalous maximum E_f is taken directly from the raw data, without fitting and subtracting the $\chi(E)$ background signal. The energy of the shake-up transition E_S, was estimated by the difference of the maximum of the double-electron excitation E_f and E_{1st}. Due to the edge-like structure of the shake-up effect, E_S needs a correction for the energy difference between the white line maximum E_{WL} and E_{1st}. as discussed in Ref. [12]. The resulting E_s is given as function of the atomic number in Figure 3. In order to assign the shake-up process to the experimental value E_S, a comparison with the electron energies in presence of the $2p_{3/2}$ core-hole is required. The relaxation of an atom due to core-hole creation is usually described in the frame of the $Z+1$ approximation. Tabulated bonding energies of shells close to the ionization limit are rather scarce for actinides. The energies for this study were taken from Porter and Freedman [20]. Evidence was found between E_S

and the $Z+1$ $4f_{5/2}$ and $4f_{7/2}$ energy level. The comparison allows us to assign the spectral feature to an excitation of a core $2p_{3/2}$ electron accompanied by the autoionization of a *4f* electron. This process creates a [$2p_{3/2}4f_{5/2}/4f_{7/2}$] double hole configuration, or, in the edge terminology, a $L_3N_{6,7}$ edge. The shake-up of one of the 14 *4f* electrons to the lowest unoccupied MO results in a feature strong enough to be detectable.

Consequences for EXAFS data analysis

The double-excitation affects the EXAFS signal and can influence the data analysis. An excitation of a second electron reduces the transition probability in the main scattering path and opens a new one. This may affect especially the integral scattering amplitude for $E \geq E_f$. Therefore, the coordination numbers N_{ij}, extracted from the amplitude function, is expected to be influenced. In contrast, there is no correlation of the double-electron excitation to origin of the wave vector $E_{k=0}$. Therefore, the influence on R, which is extracted from the phase function, is not expected to be significant. A second effect may occur in the data extraction process. The atomic background signal $\mu_0(E)$ is usually approximated by a spline function that equilibrates the EXAFS oscillations. This estimation might be affected either if the EXAFS oscillation is very weak in comparison to the double-electron feature or if the multielectron resonance is in coincidence with a maximum of the EXAFS oscillation. For example, the L_3 edge EXAFS spectrum of Th^{4+} hydrate represents such a superposition of the $L_3N_{6,7}$ double-electron excitation with an EXAFS oscillation maximum. It is well known, that deviations between $\mu_0(E)$ and the spline function lead to artificial peaks at $R \leq 1.2$ Å. There exist at least two concepts to avoid this problem. One possibility is, to subtract the double-electron excitation as a step function. Applications are given for the L_3 spectra of lanthanides [21]. A second solution suppresses the artificial peaks at $R \leq 1.2$ Å. Such a procedure is available in most of the recent EXAFS programs.

References

[1] J. M. Esteva, B. Gauthé, P. Dhez, and C. R. Karnatak, *J. Phys B* **16** (1983) L263.

[2] M. Deutsch and P. Kizler, *Phys. Rev. A* **45** (1992) 2112.

[3] R. D. Deslattes, R. E. LaVilla, P. L. Cowan, and A. Henins, *Phys. Rev. A* **27** (1983) 923.

[4] E. Bernieri and E. Burattini, *Phys. Rev. A* **35** (1987) 3322.

[5] K. Zhang, E. A. Stern, J. J. Rehr, and F. Ellis, *Phys. Rev. B* **44** (1991) 2030.

[6] A. Filipponi, E. Bernieri, and S. Mobilio, *Phys. Rev. B* **38** (1988) 3298.

[7] A. Filipponi, T. A. Tyson, K. O. Hodgson, and S. Mobilio, *Phys. Rev. A* **48** (1993) 1328.

[8] P. D'Angelo, P.-E. Petit, and N. V. Pavel, *J. Phys. Chem. B* **108** (2004) 11857.

[9] P. D'Angelo, A. Di Cicco, A. Filipponi, and N. V. Pavel, *Phys. Rev. A* **47** (1993) 2055.

[10] J. Chaboy, A. Marcelli, and T. A. Tyson, *Phys. Rev. B* **49** (1994) 11652.

[11] J. A. Solera, J. García, and M. G. Proietti, *Phys. Rev. B* **51** (1995) 2678.

[12] C. Hennig, *Phys. Rev. B.* **75** (2007) 035120.

[13] C.Hennig, C. Le Naour, C. Den Auwer, *Phys. Rev. B* **77** (2008) 235102.

[14] J. Padežnik Gomilšek, A. Kodre, I. Arčon, and M. Hribar, *Phys. Rev. A* **68** (2003) 042505.

[15] A. Filipponi, L. Ottaviano, and T. A. Tyson, *Phys. Rev. A* **48** (1993) 2098.

[16] R. G. Denning, *Structure and Bonding* Springer-Verlag, Heidelberg, 1992, Vol. **79**, p.217.

[17] T. Reich, G. Bernhard, G. Geipel, H. Funke, C. Hennig, A. Rossberg, W. Matz, N. Schell, and H. Nitsche, *Radiochim. Acta* **88** (2000) 633.

[18] A. Ikeda-Ohno, A., Hennig, C., Rossberg, A., Funke, H., Scheinost, A.C., Bernhard, G., Yaita T. *Inorg. Chem.* **47** (2008) 8294.

[19] H. Bolvin, U. Wahlgren, H. Moll, T. Reich, G. Geipel, T. Fanghänel, and I. Grenthe, *J. Phys. Chem. A* **105** (2001) 11441.

[20] F.T. Porter, M.S. Friedman, *J. Phys. Chem. Ref. Data* **7** (1978) 1267.
[21] P. D'Angelo, A. Di Cicco, A. Filipponi, and N. V. Pavel, *Phys. Rev. A* **47** (1993) 2055.

Selenite retention by abiotic redox processes

A.C. Scheinost[1], R. Kirsch[1,2], D. Banerjee[1], H. Zaenker[1], L. Charlet[2], R.L.d.A. Loyo[3], S.I. Nikitenko[3,4]

[1] Institute of Radiochemistry, Forschungszentrum Dresden-Rossendorf, 01314 Dresden, Germany

[2] LGIT, Université Joseph-Fourier, 38041 Grenoble, France

[3] Chimie Nucléaire Analytique et Bioenvironnementale, Université de Bordeaux I,II, CNRS, 33175 Gradignan, France

[4] Laboratoire de Sonochimie, ICSM Centre de Marcoule, CEA, 30207 Bagnols sur Cèze

Introduction

The radionuclide ^{79}Se is one of the elements of concern for the safe storage of high-level nuclear waste. First, it has a long half-life ($t_{1/2}$=1.1 Mio a), and second, the oxyanions selenate ($Se^{VI}O_4^{2-}$) and selenite ($Se^{IV}O_3^{2-}$) are considered as highly mobile, since they are only weakly absorbed by clay barriers and Fe-oxide-poor geological formations at considered disposal sites in Europe and elsewhere. In contrast to these mobile tetravalent and hexavalent species, however, Se also occurs in oxidation states 0 and –II, where it forms the very insoluble solids elemental selenium (gray, red, and other allotropes) and – in the presence of ubiquitous ferrous iron - selenides like FeSe and ferroselite ($FeSe_2$). Microorganisms are able to use both selenate and selenite as terminal electron acceptors of anaerobic respiration, thereby forming Se(0) precipitates as well as a range of volatile organoselenium compounds [1]. While these biotic processes play a substantial role in metabolically active surface and near-surface environments [2,3], it appears questionably that they dominate the Se cycle under the harsh near-field conditions in the deep underground. Therefore, abiotic redox reactions may be more relevant. It has been shown that Se^{IV} and Se^{VI} are reduced by Fe^{II}-containing solids, including green rust [4,5], magnetite, mackinawite and siderite [6], pyrite [7], and troilite [8], as well as by Fe^0 [9]. The Fe^{2+} hexaqua ion, which is ubiquitous in water-logged soils and aquifers, does not seem to reduce significant amounts of selenite. When it is adsorbed by clay minerals via complexation with surface hydroxyl groups, however, it reduces Se in a slow reaction, which continues for several weeks [10].

In most experiments with either biotic or abiotic Se redox reactions, elemental Se was observed, while Fe selenide phases like ferroselite, dzharkenite and Se-substituted pyrite prevail in soils, sediments and ore deposits, pointing to their greater thermodynamic stability [11]. The intention of our study was therefore, to elucidate this obvious contradiction. In order to gain insight into possible controls, we investigated selenite reduction by a variety of Fe^{II}-bearing minerals which differ by elemental composition including Fe^{II} content, surface structure, solubility, surface area, point of zero charge and other physical and chemical variables [12]. In addition, selenite reduction by nanoparticulate zerovalent iron was investigated [9]. The redox intermediates and end products were characterized by Se K-edge XANES and EXAFS spectroscopies, supplemented by XPS [6,12].

Controls on selenite reduction

Table 1 shows the Se oxidation states after reaction with selected surfaces. The clay mineral montmorillonite with structural Fe(II) or with sorbed Fe^{2+} does not show any selenite reduction at pH values above 7.5, where selenite does not adsorb. Only when selenite is adsorbed by montmorillonite edge sites (pH <7), reduction takes place. Note that the measured redox potential of about 0 V (see Table 2) is not sufficient to reduce selenite within 24 hours, although thermodynamics predict selenite reduction under these conditions [12,13]. Therefore, the heterogeneous surface reaction accelerates the redox kinetics.

Table 1. Quantitative selenium oxidation state distribution after 1 day reaction time (or as indicated) by Iterative Transformation Factor Analysis of Se K-edge XANES spectra. References used with fixed fractions are shown in bold letters.

No	Sample	Se(IV)	Se(0)	Se(-II)	sum	Error/%
1	Montm Fe(II)struct pH7.9	1.00	0.00	0.00	1.00	0.7
2	Montm Fe(II)ads pH8.1	0.95	0.00	0.04	0.99	0.9
3	Montm Fe(II)ads pH6.8	0.59	0.43	0.00	1.02	1.3
4	Sid pH8.3	0.41	0.60	0.00	1.01	1.4
5	Magn pH5.3	0.11	0.12	0.78	1.01	1.5
6	GR 1d	0.09	0.19	0.72	1.00	1.7
7	GR 30d	0.08	0.19	0.74	1.01	1.7
8	Mack pH9.7	0.07	0.18	0.75	1.00	1.6
9	Mack pH7.6	0.04	0.07	0.89	1.00	1.1
10	Fe(0)	0.01	0.03	0.98	1.02	1.3
	sorbed SeIV	**(1.00)**	**(0.00)**	**(0.00)**	1.00	0.1
	gray Se0	**(0.00)**	**(1.00)**	**(0.00)**	1.00	0.3
	FeSe	**(0.00)**	**(0.00)**	**(1.00)**	1.00	0.2

Among the Fe(II) solid phases, the Fe(II) carbonate siderite reduces only about 60 % of selenite, while magnetite, green rust, and mackinawite, as well as Fe(0) cause an almost complete reduction within 24 hours (Table 1). These differences in redox kinetics can be explained by the stoichiometry of the reactions. Selenite reduction to Se^0 or Se^{-II} requires transfer of 4 or 6 electrons, while the reactions $Fe^{II} \rightarrow Fe^{III}$ and $S^{-I} \rightarrow S^0$ provide only one and $S^{-II} \rightarrow S^0$ only two electrons. Therefore, electron transfer chains from several Fe and/or S centers in conducting or semi-conducting solids towards the reactive surface are more likely to provide the required electrons than a homogeneous reaction with the unlikely coincidence of several Fe/S ions with one selenite ion.

Table 2. Selected solution chemistry data after selenite reaction.

Label	Eh_{end}	$\{Se\}_{end}$	Se_{uptake}	$\{Fe^{2+}\}_{ini}$	$\{Fe^{2+}\}_{end}$
	[mV]	[mM]	%	[mM]	[mM]
Montm Fe(II)struct pH7.9	60	0.996	0.4	<0.003	0.003
Montm Fe(II)ads pH8.1	-40	0.99	1.0	0.08	0.003
Montm Fe(II)ads pH6.8	-152	0.475	5.0	4.4	2.5
Sid pH8.3	-130	0.006	99.4	0.06	0.039
Magn pH5.3	210	<6.3E-05	100.0	31	30
GR 1d	-140	<6.3E-05	100.0	85	77
GR 30d	nd	nd	100.0	nd	nd
Mack pH9.7	-220	<6.3E-05	100.0	0.31	<0.003
Mack pH7.6	-110	<6.3E-05	100.0	3.9	2.8

The fast reactions of Fe(0), mackinawite, GR and magnetite are hence in line with the small band gap or conduction band of these solids (about 1 eV band gap for magnetite and pyrite), which facilitates electron transfer from the structure to the solid-water interface [7]. The slow reduction by siderite and montmorillonite, in contrast, reflects the large band

gap of these minerals. Similarly, the aqueous redox reaction would require the coincidence of at least four Fe cations with one selenite anion to transfer the required electrons in one step, a rather unlikely event.

Controls on Se^0 vs. $FeSe_x$ formation

The XANES analysis indicates reduction of selenite to Se(0) by montmorillonite and siderite, and reduction to Se(-II) by magnetite, GR, mackinawite and Fe(0) (Table 1). To further elucidate the short-range structure of the reduced Se species, we used EXAFS spectroscopy. While the identification of oxidized selenite (and selenate) is straight forward based on the Se-O backscattering peak, elemental Se and ferrous selenites have a Fourier transform peak at almost the same distance, arising from either Se-Se or Se-Fe backscattering, respectively (Fig. 1). The proper discrimination of Fe and Se backscattering atoms required use of the wavelet technique, which provides analysis of the EXAFS signal both in R-space (distance information) and k-space (atomic number information) [14,15]. The wavelet plots demonstrate the excellent discrimination of Fe and Se backscattering paths using reference phases (Fig. 1, right, top), and show that the Se redox phases formed in the presence of magnetite, GR and mackinawite have prevalently Fe first neighbors, in line with ferrous selenides (Fig. 1, right, bottom).

Shell fits based on the wavelet results revealed a variety of solid Se(0) (gray and red Se) and $FeSe_x$ phases, all with a very limited structural range typical for amorphous and nanoparticulate phases [6,16]. Interestingly, the fast selenite reductions (complete or almost complete within 24 h) always caused precipitation of $FeSe_x$ phases, while the slow reductions (incomplete within 24 hours) always led to elemental Se (Table 1, Fig. 2).

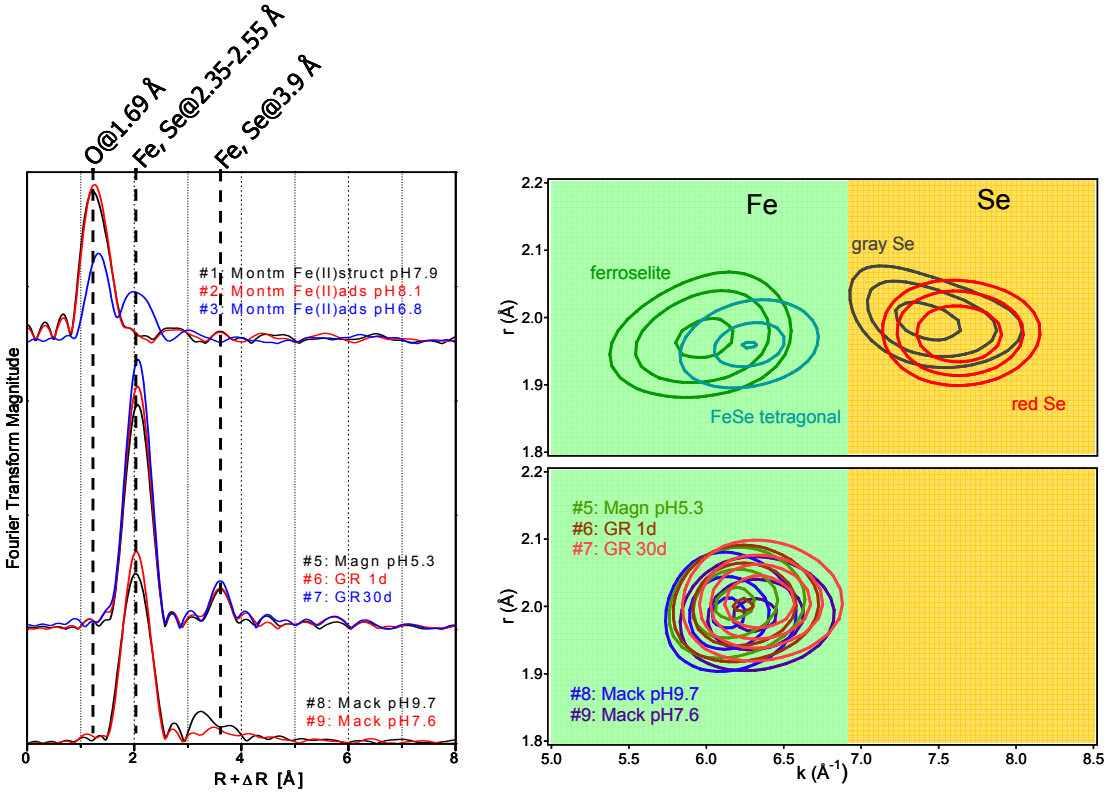

Fig. 1. Fourier transform Se K-edge EXAFS spectra (left) and corresponding wavelet transforms (right) of selected reaction samples.

Thermodynamic modeling was performed with the GWB package, using the most recent reaction equations and equilibrium constants for Se [17] implemented into the thermo V8.R6+ data base provided by Lawrence Livermore National Laboratories (LLNL). The aqueous solutions of the mackinawite, magnetite and GR samples are almost in equilibrium or oversaturated with respect to trigonal Se. The saturation indices for monoclinic Se are slightly below that of trigonal Se, but remain above saturation for Mack pH7.6 and Magn pH5.3. The solutions always remain undersaturated with respect to ferroselite and FeSe (ferroselite in Mack pH7.6 being closest to saturation with an index of -0.8). Therefore, elemental Se is predicted to be the most likely solid phase for these four samples, while precipitation of Fe selenides is unlikely. For the samples, where Se concentrations remain above the lower detection limit, however, the model predicts a high supersaturation for ferroselite followed by the two Se allotropes, and even for FeSe. For all samples, the model predicted that HSe^- is the prevalent aqueous Se species. In conclusion, one might expect that at the start of the experiment, ferroselite forms and then converts into elemental Se. Therefore, the thermodynamic predictions are in evident contrast to the XANES and EXAFS results shown above.

We believe the contradictory results may be explained by different rate limiting reactions. In the case of the less reactive surfaces, Se reduction is slow. While total aqueous Se concentrations as measured by ICP-MS is high, the concentration of the reduced aqueous species predicted to be in equilibrium under the given conditions (HSe^-), has to be low. It is this low HSe^- concentration, which favors formation of elemental Se. In contrast, the prevalence of Fe selenides in the case of highly reactive surfaces, suggests a rapid reduction and hence an initially high concentration of reduced Se, which induces the precipitation of Fe selenide phases. Even when the solution concentrations decrease below the solubility of Fe selenides, most likely by formation of a smaller amount of Se, the selenide phases remain. Even after one month, Fe selenide prevailed in the GR system, with no detectable transformation from the phase formed within one day. The persistence of these - now metastable – phases indicate slow kinetics of the subsequent transformation into the more stable elemental Se phases. The transformation of Fe selenide to elemental Se can be envisioned only as a dissolution/re-precipitation process (as opposed to a solid state transformation), since Fe has to be removed from the structure. Hence the transformation kinetics is limited by the low solubility of Fe selenides.

In conclusion, the locally and temporally constrained equilibrium conditions are strongly dependent on complex interactions between (1) varying Se reduction kinetics and hence local concentration of reduced aqueous Se species, (2) the differences in solubility of elemental Se and Fe selenides, and (3) slow kinetics of Se phase transformations. With such complex interactions, it is not surprising that the nature of observed reaction products is readily changed by slight variations in experimental conditions.

Se redox couples

For the Fe(II) clays, siderite, magnetite and green rust samples, there is no doubt that the electrons required for selenite reduction are ultimately provided by Fe^{II} oxidation, even if there may be intermediate redox couples as has been observed for Fe^{2+} sorbed montmorillonite [6,10]. For mackinawite, however, electrons may also be provided by S^{-II} oxidation. For instance, reduction of arsenite by troilite (FeS) and pyrite (FeS_2) was accompanied by oxidation of both surface S^{-II} and Fe^{II} [18]. To investigate the Fe and S speciation of mackinawite before and after reaction with selenite, we employed cryo-XPS.

The fitted S 2p spectrum of pure mackinawite reveals three main doublets, arising from the spin-orbit splitting of $2p_{3/2}$ and $2p_{1/2}$ peak (separated by 1.18 eV) of three different types of S species at the surface. The main contribution, at 162.3 ± 0.1 eV is assigned to bulk monosulfide and the minor contribution at 161.5 ± 0.1 eV is surface monosulfide, according to previous XPS studies on mackinawite and other iron sulfide minerals. The minor contribution at higher energy, around 163.5 ± 0.1 eV, is attributed to surface

polysulfide species, which has been reported on mackinawite as well as other iron sulfide mineral surfaces. There is a tiny contribution around 160.0 eV which is rather uncommon, and could be attributed to monosulfides at surface defects. After reaction with Se^{IV}, the S 2p spectrum appears significantly different, with a decrease of bulk S^{-II} and an increase of surface S^{-II} species, suggesting an increase of surface defects. Furthermore, elemental sulfur is evident by a peak around 164.5 eV. The low energy peak around 160.0 eV, which was observed at the surface of pure mackinawite is absent in the reacted sample, suggesting that the monosulfides at surface defects have been oxidized. In conclusion, the XPS data show that both Fe and S atoms at the mackinawite-water interface have been oxidized due to selenite reduction, leading to structural defects at the mackinawite surface.

Based on the XAS and XPS results, we can postulate an equation for the reaction of selenite with mackinawite. Selenite was reduced to a FeSe at the surface of mackinawite. A corresponding oxidation of both sulfide and Fe^{II} was observed. The Fe(II) concentration in solution remained at about 3 mM before and after reaction with selenite, suggesting that selenite sorption and reduction did not enhance mackinawite dissolution significantly, in spite of the increase of surface defects. After the selenite reaction we observed a relative increase of Fe^{III} from 45 to 68 % of total Fe, hence an increase of 23 %. In contrast, S^0 increased only from 0 to 6 %. Therefore, the ratio of S to Fe^{II} oxidation is approximately ¼. The following equation would be consistent with the observed reaction products and stoichiometry:

$$4 \equiv Fe^{II} + 1 \equiv S^{-II} + HSeO_3^- + Fe^{2+} + 2\,H^+ \rightarrow 4 \equiv Fe^{III} + \equiv S^0 + FeSe(s) + 3\,OH^-$$

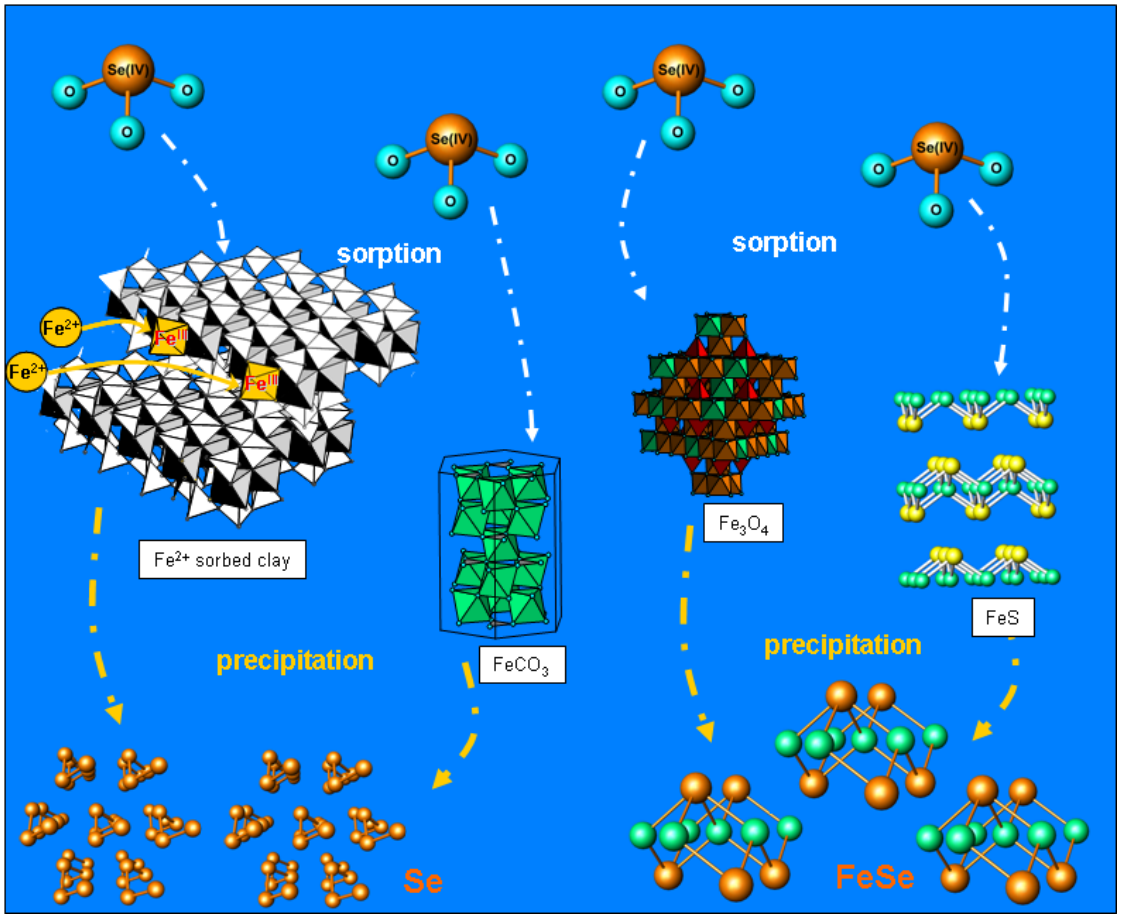

Fig. 2. Illustration of the redox processes of selenite with Fe^{II}-bearing mineral surfaces. Slow reduction of selenite with Fe^{2+} sorbed clay and siderite ($FeCO_3$) leads to precipitation of Se(0), and fast reduction with magnetite (Fe_3O_4) and mackinawite (FeS) leads to precipitation of FeSe solids.

where $\equiv Fe^{II}$ and $\equiv S^{-II}$ represent mackinawite surface atoms before the reaction, and $\equiv Fe^{III}$ and $\equiv S^{0}$ represent surface atoms after the reaction. It should be noted that this equation is based on only one XPS sample and has to be further validated.

Consequences for the safety of nuclear waste repositories

Our experiments suggest that selenite reduction should be a common process at the surface of (corroding) steel claddings and clay liners in the near-field of nuclear waste repositories, as well as in deep-underground rocks and sediments and aquifers, where Fe(II) minerals are commonly present. After complete reduction and precipitation, Se concentrations dropped below the ICP-MS detection limit, 6.3×10^{-8} M, suggesting an efficient scavenging of Se from groundwater. Even when reduction was not completed within the relatively short time scale of our experiments, we anticipate a complete reduction for longer time periods representative for underground migration processes (years to millennia). Although the observed Se phases have most likely a nanoparticulate nature, we did not observe a tendency to form potentially mobile Se colloids [12]. However, this has to be investigated in more detail. Furthermore, in some cases, where we would have expected selenite reduction, the reduction did not happen. The reasons seem to be only partly understood, and further investigations are needed. Finally, there is only little work published demonstrating that not only selenite, but also selenate is reduced by Fe(II) systems [4].

Acknowledgements

This work was supported by ACTINET: European Network of Excellence.

References

[1] R. S. Oremland; J. T. Hollibaugh; A. S. Maest; T. S. Presser; L. G. Miller and C. W. Culbertson, *Appl. Environ. Microbiol.* **55** (1989) 2333-2343.

[2] W. T. Frankenberger and M. Arshad, *Biofactors* **14** (2001) 241-254.

[3] Y. Q. Zhang and J. N. Moore, *Journal of Environmental Quality* **26** (1997) 910-916.

[4] S. C. B. Myneni; T. K. Tokunaga and G. E. Brown, *Science* **278** (1997) 1106-1109.

[5] A. M. Scheidegger; D. Grolimund; D. Cui; J. Devoy; K. Spahiu; P. Wersin; I. Bonhoure and M. Janousch, *J Phys. IV* **104** (2003) 417-420.

[6] A. C. Scheinost and L. Charlet, *Environ. Sci. Technol.* **42** (2008) 1984–1989.

[7] C. Bruggeman; A. Maes; J. Vancluysen and P. Vandemussele, *Environmental Pollution* **137** (2005) 209-221.

[8] E. Breynaert; C. Bruggeman and A. Maes, *Environ. Sci. Technol.* **42** (2008) 3595-3601.

[9] R. L. d. A. Loyo; S. I. Nikitenko; A. C. Scheinost and M. Simonoff, *Environ. Sci. Technol.* **42** (2008) 2451-2456.

[10] L. Charlet; A. C. Scheinost; C. Tournassat; J. M. Greneche; A. Géhin; A. Fernández-Martínez; S. Coudert; D. Tisserand and J. Brendle, *Geochim. Cosmochim. Acta* **71** (2007) 5731-5749.

[11] A. L. Ryser; D. G. Strawn; M. A. Marcus; J. L. Johnson-Maynard; M. E. Gunter and G. Möller, *Geochem. Trans.* **6** (2005) 1-11.

[12] A. C. Scheinost; R. Kirsch; D. Banerjee; A. Fernandez-Martinez; H. Zaenker; H. Funke and L. Charlet, *J. Contam. Hydrol.* **102** (2008) 228-245.

[13] A. Olin; G. Nolang; E. Osadchii; L. O. Ohman and E. Rosen Chemical Thermodynamics of Selenium; 1st ed.; North Holland Elsevier Science Publishers B. V.: Amsterdam, Netherlands, 2005.

[14] H. Funke; A. C. Scheinost and M. Chukalina, *Physical Review B* **71** (2005) 094110.

[15] H. Funke; M. Chukalina and A. C. Scheinost, *Journal of Synchrotron Radiation* **14** (2007) 426-432.

[16] L. Charlet; A. C. Scheinost; C. Tournassat; J. M. Greneche; A. Gehin; A. Fernandez-Martinez; S. Coudert; D. Tisserand and J. Brendle, *Geochim. Cosmochim. Acta* **71** (2007) 5731-5749.

[17] A. Olin; B. Nolang; L.-O. Ohman; E. Osadchii and E. Rosen Chemical Thermodynamics 7: Chemical Thermodynamics of Selenium; Elsevier: Amsterdam, 2005.

[18] B. C. Bostick and S. Fendorf, *Geochim. Cosmochim. Acta* **67** (2003) 909-921.

In-situ X-ray diffraction studies during co-sputtering deposition of Ni-Ti shape memory alloy films

R.M.S. Martins[1,2], N. Schell[3], K.K. Mahesh[2], R.J.C. Silva[2], F.M. Braz Fernandes[2]

[1] Institute of Ion Beam Physics and Materials Research, Forschungszentrum Dresden-Rossendorf, 01314 Dresden, Germany

[2] CENIMAT/I3N, Campus da FCT/UNL, 2829-516 Monte de Caparica, Portugal

[3] GKSS Research Center Geesthacht, Max-Planck-Str. 1, 21502 Geesthacht, Germany

Introduction

Ni-Ti Shape Memory Alloys (SMA) are smart materials undergoing first order martensitic transformations driven by temperature and/or stress. Crystallized binary Ni-Ti SMAs transform martensitically from cubic B2 (CsCl type) austenite phase into monoclinic B19' martensite either directly or via rhombohedral R–phase [1]. Ni-Ti SMA films have been recognized as promising high performance materials in the field of micro-electromechanical systems (MEMS). The capability to transmit particularly high forces along with a large stroke makes Ni-Ti SMAs a material with the greatest specific work output of several actuation mechanisms. However, despite several methods proposed for resolving some of the processing difficulties, the deposition of Ni-Ti films with definite stoichiometry and high purity remains a challenge. Moreover, important issues like the formation of film texture and its control are still unresolved. The study of the crystallographic texture of the Ni-Ti films assumes a major importance, since it has a strong influence on the extent of the strain recovery.

Our group has performed studies concerning the deposition of Ni-Ti films on different types of substrates by co-sputtering at the Rossendorf Beamline ROBL at ESRF, Grenoble. The first experiments reported in the published literature concerning *in-situ* X-ray diffraction (XRD) investigations of the microstructural development during Ni-Ti film growth have been presented in Ref. [2]. It has been shown that an amorphous SiO_2 buffer layer induces the development of the (100) orientation of the B2 phase during deposition on heated substrates ($\approx$ 470ºC) [3]. However, after $\approx$ 70 min deposition ($\approx$ 540 nm film thickness) a constant intensity of the B2(200) diffraction peak (Bragg-Brentano geometry) has been observed. This gradual change of the preferential crystallographic direction along which the columnar crystals grow, after an initial stacking of the B2 phase onto (h00) planes, has been attributed to the combined effects of low surface mobility and shadowing. In the present report, the effect of increasing the deposition temperature from 470°C to 520°C is revealed again without applying substrate bias voltage V_b. A TiN buffer layer allows controlling the crystallographic orientations of Ni-Ti films and acts as an efficient diffusion barrier avoiding silicide formation at the substrate. Ni-Ti films mainly containing grains with (110) or (211) planes of the B2 phase parallel to the film surface could be produced using TiN buffer layers [4]. Here, the effect of a negative V_b applied to the substrate [TiN/SiO_2/Si(100)] during the Ni-Ti growth on its preferred orientation is presented.

Materials and methods

The *in-situ* studies of Ni-Ti film growth have been performed at the Materials Research Hutch of the Rossendorf Beamline (ROBL-MRH), using a sputtering deposition chamber inserted into the six-circle diffractometer. It is equipped with two-unbalanced miniature magnetrons each positioned at a distance of 100 mm from the substrate and tilted 30° away from the substrate normal. Ni-Ti (49 at% Ni – 51 at% Ti) and 99.99 % pure Ti disks of 25.4 mm diameter were used as targets.

Polycrystalline films were grown onto thermally oxidized Si(100) substrates (15×15 mm^2, d_{Ox} = 140 nm). For the deposition of the TiN films (thickness of $\approx$ 15 nm, i.e.,

3 min deposition time) a substrate temperature of 470°C has been selected and the working pressure (flux ratio Ar/N_2 = 4/1) was set to 0.35 Pa. The topmost layer of the TiN film does not show a dominating orientation. Primarily, <100> and <111> oriented grains of TiN nucleate and grow (<hkl> grains are here defined as grains with a plane from the {hkl} family parallel to the film surface). A V_b of −30 V has been applied to the substrate during the TiN film growth while the Ti target was running at a constant power of 80 W. For the deposition of the near equiatomic Ni-Ti films, the Ni-Ti and Ti magnetrons were driven for ≈120 min at a power of 40 W and 20 W, respectively (working pressure Ar set to 0.42 Pa), resulting in final thicknesses of approximately 760 ± 50 nm. Different experiments have been performed as shown in Table 1.

Substrate	Buffer layer	Substrate bias (V)		Deposition temperature (°C)
		TiN deposition	Ni-Ti deposition	
SiO_2/Si(100)	-	-	0	470
SiO_2/Si(100)	-	-	0	520
SiO_2/Si(100)	TiN (15 nm)	-30	0	470
SiO_2/Si(100)	TiN (15 nm)	-30	-45	470

Tab. 1 – Deposition parameters for the various samples investigated.

The radiation was monochromatized to λ = 0.0675 nm (18.367 keV) and large angle XRD in Bragg-Brentano geometry was employed, thus probing the diffraction vector situated in a plane perpendicular to the plane of deposition. A sequence of scans has been performed during Ni-Ti film processing in order to monitor the B2(110), B2(200) and B2(211) XRD peaks; these scans are intended to reveal the type of preferential orientation and to determine off-plane lattice parameter variations.

Results and discussion

Figure 1 shows the results obtained for the Ni-Ti films deposited directly on thermally oxidized substrates without applying V_b. In both cases, i.e. films grown at 470°C and 520°C, there was a preferential stacking of B2 phase on (h00) planes parallel to the substrate surface (due to the oxide layer [3]). However, for the deposition at 470°C, after approximately 70 min of film growth (≈ 540 nm film thickness), a stabilization of the intensity of the B2(200) diffraction peak was observed (Fig. 1a). This has been attributed to a gradual tilting (relative to the substrate normal) of the growing direction of the columnar crystals (see Fig. 1b). A dashed line was inserted indicating the thickness related with the deposition time corresponding to the stabilization of the intensity of the B2(200) peak [detected during the *in-situ* XRD studies (Figs 1a and c)]. As it can be observed, in particular, when examining the columns indicated by the arrows, a gradual change of the growing direction of the columnar crystals occurred. The grains near the top surface, grown later, are tilted towards the direction of the incident flux (preferentially towards the magnetron with the Ni-Ti target running at 40 W). This gradual change of the preferential crystallographic direction along which the columnar crystals grow, after an initial stacking of the B2 phase onto (h00) planes, is attributed to the combined effects of low surface mobility and shadowing (regions with a relatively greater initial height or growth rate can obstruct the flow of incident flux to other areas – due to tilting of the magnetrons). It is suggested that as the film thickness increases and the grains grow, the depositing particles cannot migrate around them thereby increasing the effect of shadowing. Shadowing becomes more relevant as the film thickness increases. The competition between shadowing and atomic migration is, thus, supposed to determine the crystallographic orientation during growth when the deposition direction is inclined to the substrate normal. An increase of the deposition temperature from 470°C to 520°C leads to a continuous increase of the B2(200) peak intensity during deposition due to higher ad-atom surface mobility (Fig. 1c).

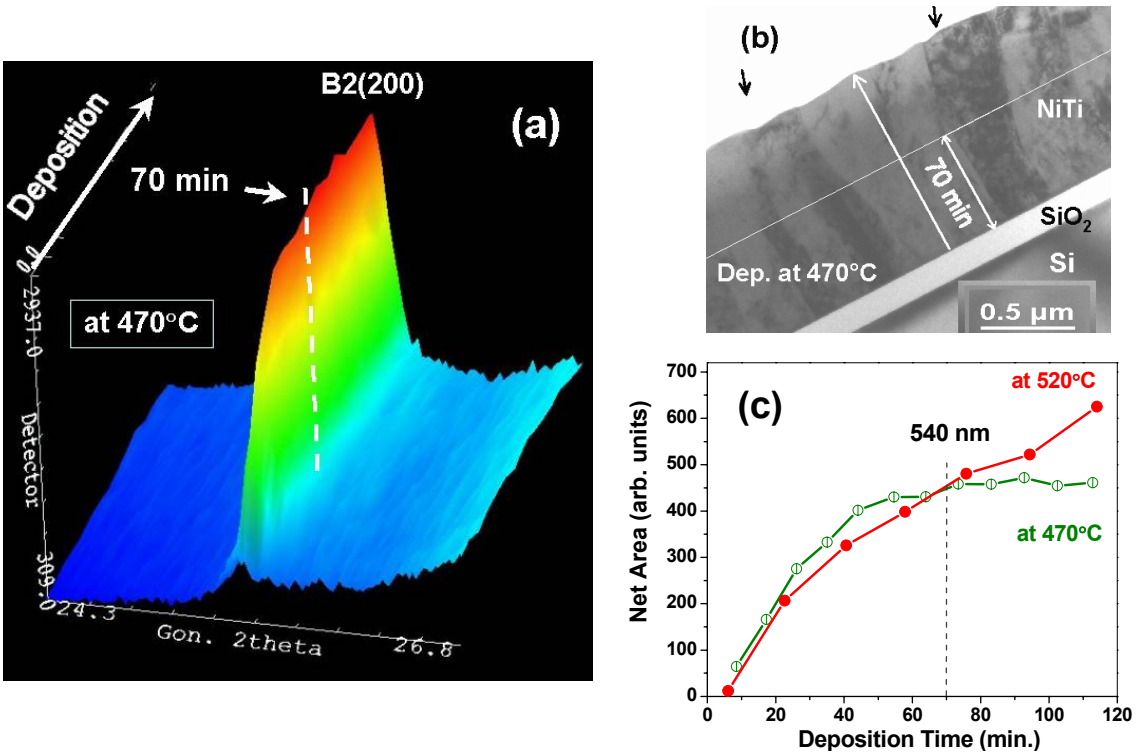

Fig. 1.
Results obtained for Ni-Ti deposition on thermally oxidized Si(100) substrates: (a) XRD data of the growing film at 470°C; (b) bright field TEM micrograph of the film deposited at 470°C; (c) net areas of the B2(200) peak recorded as a function of deposition time at 470°C and at 520°C.

Figure 2 shows results obtained from the *in-situ* XRD measurements for the Ni-Ti depositions on top of the TiN buffer layers, without and with V_b. For the Ni-Ti film deposited without V_b, the 110 diffraction peak of the B2 phase dominated at the beginning of the deposition, while the B2(211) diffraction peak assumed higher values at a later stage of the deposition. It is suggested that the thin TiN buffer layer (≈15 nm) exhibits a rough or granular surface with different crystal facets playing an important role on the growth direction of the columnar crystals of Ni-Ti, together with the fact that the targets are tilted 30° away from the substrate normal. During the initial Ni-Ti deposition period, there is a (110) stacking and a columnar growth such that <110> lies close to the substrate normal because (110) is the more densely packed crystallographic plane for the B2 structure [5]. However, due to the surface morphology of the TiN layer and the geometrical shadowing effects, as growth proceeds the growth direction is more influenced by the direction of incident particles. This favoured the diffraction peak (in Bragg–Brentano geometry) of (211) of the B2 phase. Therefore, it is suggested that this crystallographic preferential orientation development is associated with the combined effects of low surface mobility and shadowing as shown in the previous system above. In the case of the Ni-Ti film deposited with V_b the <110> oriented grains dominated since the beginning (Fig. 2a). The increase of the energy of the ions bombarding the film surface during growth results in an enhanced mobility of the ad-atoms in the near-surface region. This leads to the same effect as the higher substrate surface temperature.

The analysis of the variation of the lattice distance a_0 values for the Ni-Ti B2 phase of the film deposited without V_b shows a continuous decrease of this parameter (Fig. 2b). This decrease suggests that the film experiences compressive stress, which significantly relaxes with increasing film thickness. The *in-situ* analysis of the variation of the a_0 values for the Ni-Ti B2 phase of the film deposited with a V_b of –45 V has shown a reasonable stability along the processing steps. Furthermore, there is an overall decrease of this value

(≈ 0.303 nm) compared to the deposition without V_b (0.304 nm at the end of the annealing step). This indicates that an increase of energy of the incident ions resulted in enhanced

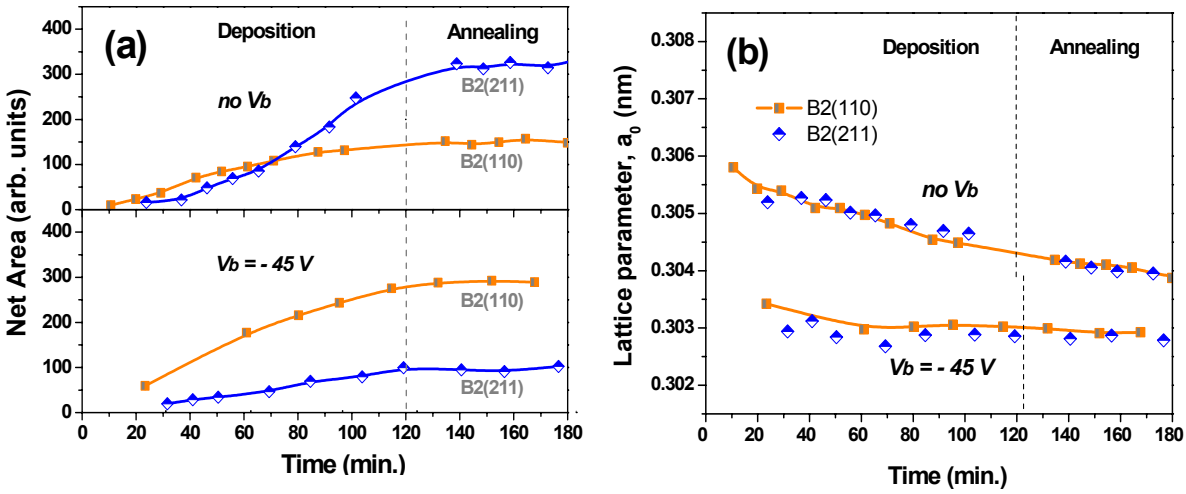

Fig. 2.
In-situ XRD results for Ni-Ti films deposited without and with V_b on TiN: (a) the variation of the net areas of the B2(110) and B2(211) diffraction peaks; (b) the variation of the a_0 values (as calculated from the lattice constant, *d*, according to the B2(110) and B2(211) peak positions), *versus* time.

mobility of the ad-atoms allowing them to diffuse on the substrate surface and, as a result, the ad-atoms are no longer kinetically constrained. Most likely this contributes significantly to the lower biaxial compressive stress state when using V_b (–45 V) during the Ni-Ti deposition on the TiN buffer layer of thickness ≈15 nm. Thermodynamics drives the system towards the minimum possible sum of surface and strain energies under the restrictions imposed by kinetics. The increase in the energy of the ad-atoms allows them to diffuse on the substrate surface.

Conclusions

The first experiments reported in the published literature regarding *in-situ* XRD investigations of the microstructural development during Ni-Ti SMA film growth have been performed at ROBL. Their texture evolution is affected by the substrate type and the ion bombardment (using V_b). The competition between shadowing and atomic migration during deposition plays an important role on the crystallographic orientation of Ni-Ti films when the depositing particles incidence is oblique to the substrate normal.

Acknowledgements

The authors would like to thank the FCT/MCTES for a Ph.D. scholarship (POCI 2010/FSE for R.M.S.M.), U. Strauch for his technical assistance during the measurements at ROBL and to the Division for Structural Studies (FWIS-FZD) for providing excellent working conditions. Financial support from the ESRF for the experiments at ROBL is gratefully acknowledged by the authors.

References

[1] K. Otsuka, X. Ren, *Prog. Mater. Sci.* **50** (2005) 511.

[2] R.M.S. Martins, N. Schell, R.J.C. Silva, F.M.B. Fernandes, *Nucl. Instr. Meth. B* **238** (2005) 319.

[3] R.M.S. Martins, N. Schell, M. Beckers, K.K. Mahesh, R.J.C. Silva, F.M.B. Fernandes, *Appl. Phys. A* **84** (2006) 285.

[4] R.M.S. Martins, N. Schell, R.J.C. Silva, L. Pereira, K.K. Mahesh, F.M.B. Fernandes, *Sens. Actuators B* **126** (2007) 332.

[5] J.-M. Zhang, F. Ma, K.-W. Xu, *Surf. Interf. Anal.* **35** (2003) 662.

Clarify the origin of the ferromagnetism in transition metal implanted ZnO or Si: the importance of synchrotron radiation XRD

S. Zhou, K. Potzger, J. von Borany, J. Grenzer, M. Helm, J. Fassbender

Institute of Ion Beam Physics and Materials Research, Forschungszentrum Dresden-Rossendorf, 01314 Dresden, Germany

Introduction

Transition metal (TM) doped ZnO has been extensively investigated due to its potential application as a diluted magnetic semiconductor with Curie temperature above room temperature (RT) and are well known in literature [1-3]. However, the magnetic properties using the same dopant vary considerably. For example, the saturation moment and Curie temperature for Mn-doped ZnO ranges from 0.075 μ_B/Mn, 400 K, to 0.17 μ_B/Mn, 30–45 K, respectively [3]. In contrast to these publications, other groups reported the observation of antiferromagnetism, spin-glass behavior, and paramagnetism in TM-doped ZnO [4]. A possible reason leading to such a controversial view on the materials is the poor characterization [2]. Publications claiming the intrinsic ferromagnetism in TM doped ZnO are often based solely on magnetization measurements using high sensitivity superconducting quantum interference device magnetometry (SQUID) and structure characterizations using laboratory-equipped x-ray diffraction. The latter has been demonstrated to be not sensitive enough to detect nanoscale precipitates [5]. In this highlight, we review our recent effort to clarify the origin of the ferromagnetism in TM implanted semiconductors by a combination of structural and magnetic characterization.

Materials and methods

Commercial ZnO(0001) single crystals were implanted with transition metal ions. All samples were investigated using XRD and superconducting quantum interference device (SQUID) magnetometry. Synchrotron-radiation XRD (SR-XRD) was performed at the Rossendorf Beamline (BM20) at the ESRF with an x-ray wavelength of 0.154 nm. Laboratory-equipped XRD (Lab-XRD) was performed using a Siemens D5005 with an x-ray wavelength of 0.154056 nm.

Results and discussion

(1) The importance of SR-XRD

In contrast to conventional XRD, the much higher x-ray intensity in SR-XRD allows one to detect small quantities of very tiny nanoparticles. Figure 1 shows a symmetric 2θ/θ scan for the Fe implanted ZnO, with the implantation energy of 180 keV and the fluence of 4×10^{16} cm^{-2}. Sharp, high intensity peaks from bulk ZnO are visible at (0002) 2θ ~ 34.4° and (0004) 2θ ~ 72.6°. At 2θ ~ 44.5°, a rather broad and low intensity peak originating from bcc-Fe(110) with a theoretical Bragg angle of 2θ = 44.66° occurs. The nanoparticle size is estimated to be around 8 nm using the Scherrer formula. Note that by Lab-XRD one cannot observe the peak of Fe(110). Using SR-XRD we also studied the formation of metallic Fe depending on the implantation temperature and fluence as well as post-annealing [6, 7].

Another example is given by Mn implanted Si(001) [8] where rapid thermal annealing (RTA) at 1073 K for 5 min in N_2 flow was applied. Lab-XRD reveals for the as-implanted and RTA samples that there are no crystalline precipitates. Moreover, even at SR-XRD in a symmetric 2θ/θ scan, one fails to detect any Mn-silicides (Fig. 2a). Therefore, the near-surface sensitive grazing incidence geometry was used for this measurement, where the incident x-ray beam is aligned at a small angle of 0.4° to the sample surface. The diffraction peaks at around 42° and 46.3° cannot be attributed to the Si substrate, but to

$MnSi_{1.7}$. Correspondingly ferromagnetism is only observed in the sample after RTA, in which $MnSi_{1.7}$ nanoparticles present (Fig. 2b).

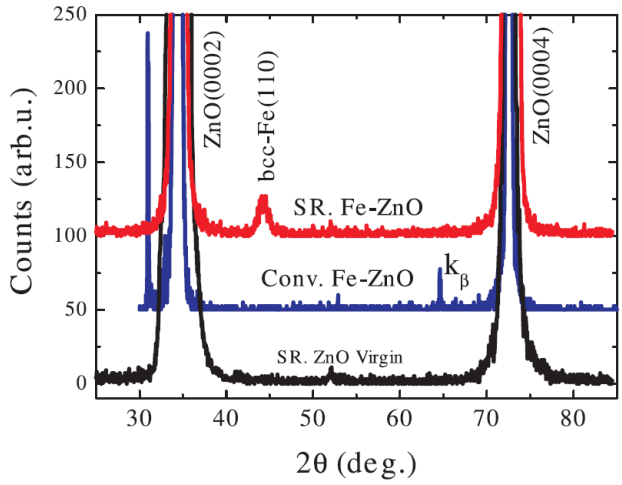

Fig. 1. Conventional (Conv.) and SR-XRD pattern (2θ-θ scan) for the Fe implanted ZnO. A virgin sample is shown for comparison. From ref. [5].

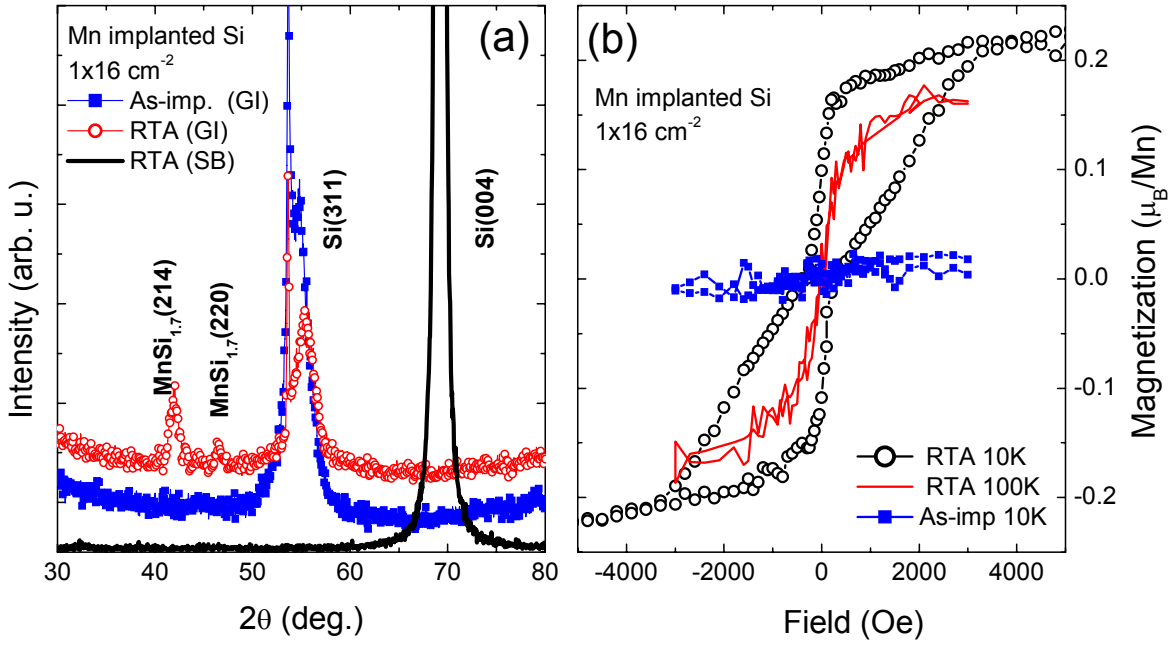

Fig. 2. (a) SR-XRD patterns of Mn implanted Si. GI: grazing incidence, and SB: symmetric 2θ/θ scan.(b) Magnetization of the As-implanted and RTA samples. From Ref. 8.

(2) Metallic Co nanocrystals: hcp or fcc?

Co nanocrystals were observed in Co implanted ZnO [9]. However, the Bragg angles (θ) for hcp-Co(0002) (θ=22.38º) and fcc-Co(111) (θ=22.12º) are rather close to each other. It is difficult to distinguish orientated hcp- or fcc-Co by a simple 2θ/ θ scan. The Φ-scan on one of the diffraction planes not parallel with the sample surface (i.e. tilted by an angle χ from sample surface) helps to identify hcp or fcc-Co NCs and also reveals the crystallographical orientation relationship. With the knowledge of hcp-Co(0001)//ZnO(0001) or fcc-Co(111)//ZnO(0001), we chose hcp-Co(10$\underline{1}$1) (θ=23.78º and χ ~ 61.9º) and fcc-Co(002) (θ=25.76º and χ ~ 54.8º) reflections. By using this approach as shown in Fig. 3, we find only hcp-Co in the as-implanted and the annealed (923 K) samples, while both fcc and hcp-Co are present in the 823 K annealed sample. The

crystallographical orientation relationship between Co NCs and ZnO is hcp-Co(0001)[11$\underline{2}$0]//ZnO(0001)[11$\underline{2}$0]//fcc-Co(111)[110]. Due to the phase transformation of metallic Co nanocrystals upon annealing, their magnetic properties were varied accordingly [9].

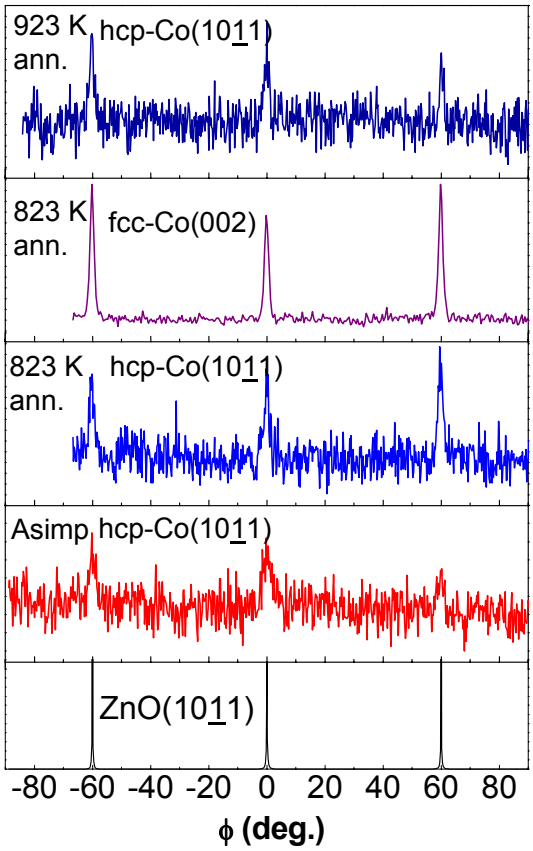

Fig. 3 XRD Φ-scans for hcp-Co(10$\underline{1}$1) (θ=23.78° and χ~61.9°) , fcc-Co(002) (θ=25.76° and χ~54.8°) and ZnO(10$\underline{1}$1) (θ=18.13° and χ~61.6°) reveal the in-plane orient relationship for Co NCs respect to ZnO. From Ref. 9.

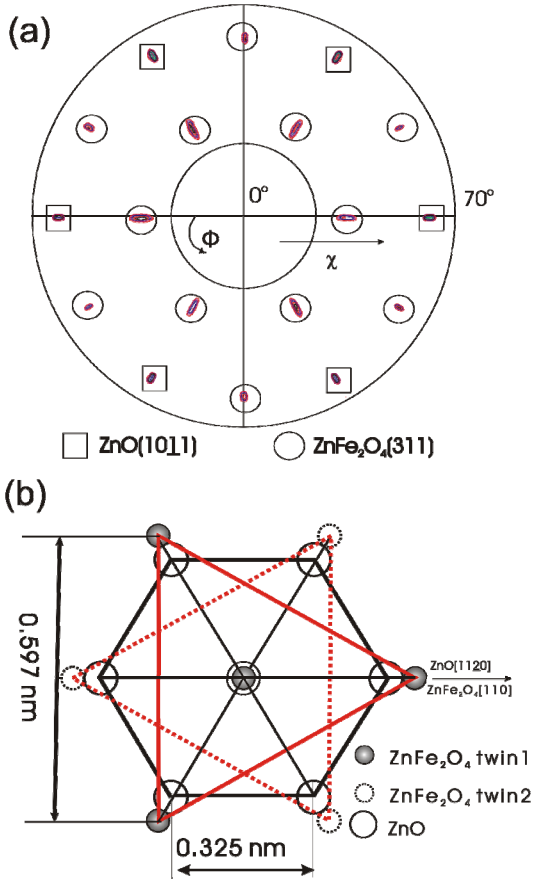

Fig. 4 (a) Pole figure of $ZnFe_2O_4$(311) reveals the crystallographical orientation of $ZnFe_2O_4$ and its twin crystallites. (b) A schematics for the crystallographical orientation of $ZnFe_2O_4$ onto ZnO is also shown. From Ref. 6.

(3) Nanocrystalline spinel $ZnFe_2O_4$

Another sources of ferromagnetic signals are inverted spinels involving both Zn and O elements. Bulk $ZnFe_2O_4$ crystals are antiferromagnetic, but at nanoscale it can become ferromagnetic. The explanation for such behavior is an additional occupation of tetrahedral A sites by Fe and octahedral B sites by Zn. The intrasite interaction of the magnetic moment of the cations on the B sites is much weaker than the AB inter-site one. The Fe^{3+} ions between A and B sites couple antiferromagnetically, which leaves some net spins from the non A-B paired Fe^{3+} ions. The formation of nanocrystalline $ZnFe_2O_4$ has been evidenced by SR-XRD [5]. After 3.5 hours annealing at 1073 K, crystalline and oriented $ZnFe_2O_4$ particles are clearly identified by the appearance of three peaks (111), (222) and (333). The crystallographical orientation of $ZnFe_2O_4$ was revealed by the XRD pole figure. The pole figure for $ZnFe_2O_4$(311) given in Fig. 4a shows poles of $ZnFe_2O_4$(311) at χ ~ 29.5° and 58.5°, respectively, with a sixfold symmetry. Since ZnO(10$\underline{1}$1) (2θ=36.25°) has a close Bragg angle with $ZnFe_2O_4$(311) (2θ=35.27°), the poles of ZnO(10$\underline{1}$1) also show up at χ ~ 61.6° with much more intensities. The result is consistent with the theoretical

$ZnFe_2O_4$(311) pole figure viewed along [111] with rotation twins. The in-plane orientation relationship is $ZnFe_2O_4$[110]//ZnO[11$\underline{2}$0]. Due to the fcc structure of $ZnFe_2O_4$ (a=0.844 nm), it is not difficult to understand its crystallographical orientation onto hcp-ZnO (a=0.325 nm) with twin-crystallites of $ZnFe_2O_4$ of an in-plane rotation by 60º (Fig. 4b). The lattice mismatch between $ZnFe_2O_4$ and ZnO is ~6%. Additionally we show the possibility of nanocrystalline spinel ferrites AFe_2O_4 (A=Zn, Co, Ni) embedded inside ZnO by co-implantation pulsing post-annealing at 800 ^oC [10], which opens an avenue of magnet/semiconductor hybrids.

Conclusion

In conclusion, we have shown the formation of magnetic precipitates in transition metal doped semiconductors, and addressed the difficulty to detect these nanocrystals. The nanocrystals can be crystallographically oriented or randomly distributed inside the substrate matrix. Obviously, in a 2θ-θ scan, the most often used method in phase identification by XRD, crystalline precipitates are easy to be detected when orientated since all precipitates contribute to the diffraction intensity. If randomly distributed, the techniques presented here (e.g. grazing incidence) must be applied to identify the precipitates since the conventional technique is not sufficiently sensitive [11, 12]. Despite the flooding reports of transition metal doped Si, Ge and oxides matrixes, one cannot claim an intrinsic ferromagnetism in such materials before a detailed structural characterization was performed.

Acknowledgements

The authors thank the technical support from Dr. Carsten Baehtz, Dr. Frank Eichhorn and Dr. Nobert Schell.

References

[1] T. Dietl, H. Ohno, F. Matsukura, J. Cibert, and D. Ferrand, *Science* 287, 1019 (2000).

[2] T. Fukumura, Y. Yamada, H. Toyosaki, T. Hasegawa, H. Koinuma, and M. Kawasaki, *Appl. Surf. Sci.* **223**, 62 (2004).

[3] C. Liu, F. Yun, and H. Morkoc, *J. Mater. Sci.: Mater. Electron.* **16**, 555 (2005).

[4] S. Zhou, K. Potzger, H. Reuther, K. Kuepper, W. Skorupa, M. Helm, and J. Fassbender, *J. Appl. Phys.* **101**, 09H109 (2007).

[5] K. Potzger, S. Q. Zhou, H. Reuther, A. Mücklich, F. Eichhorn, N. Schell, W. Skorupa, M. Helm, J. Fassbender, T. Herrmannsdorfer et al., *Appl. Phys. Lett.* **88**, 052508 (2006).

[6] S. Zhou K. Potzger, H. Reuther, G. Talut, F. Eichhorn, J. von Borany, W. Skorupa, M. Helm, and J. Fassbender, *J. Phys. D: Appl. Phys.* **40**, 964 (2007).

[7] S. Zhou, K. Potzger, G. Talut, H. Reuther, J. von Borany, R. Grötzschel, W. Skorupa, M. Helm, J. Fassbender, N. Volbers, and M. Lorenz, *J. Appl. Phys.* **103**, 023902 (2008).

[8] S. Zhou, K. Potzger, G. Zhang, A. Mücklich, F. Eichhorn, N. Schell, R. Grotzschel, B. Schmidt, W. Skorupa, M. Helm et al., *Phys. Rev. B* **75**, 085203 (2007).

[9] S. Zhou, K. Potzger, J. von Borany, R. Grötschel, W. Skorupa, M. Helm, and J. Fassbender, *Phys. Rev. B* **77**, 035209 (2008).

[10] S. Zhou, K. Potzger, Qingyu Xu, K. Kuepper, G. Talut, D. Marko, A. Muecklich, M. Helm, J. Fassbender, E. Arenholz and H. Schmidt, *Phys. Rev. B*, submitted (2009).

[11] S. Zhou, K. Potzger, G. Talut, J. von Borany, W. Skorupa, M. Helm, and J. Fassbender, *J. Appl. Phys.* **103**, 07D530 (2008).

[12] S. Zhou, G. Talut, K. Potzger, A. Shalimov, J. Grenzer, W. Skorupa, M. Helm, J. Fassbender, E. Čižmár, S. A. Zvyagin, and J. Wosnitza, *J. Appl. Phys.* **103**, 083907 (2008).

High temperature XRD and electrical measurements on PCRAM materials

S. Teichert[1], L. Wilde[2], J. Krügener[3], C. Baehtz[4], J. von Borany[4]

[1] Qimonda Dresden GmbH & Co. OHG, 01079 Dresden, Germany

[2] Fraunhofer CNT, 01079 Dresden, Germany

[3] Leibniz-Universität Hannover, 30167 Hannover, Germany

[4] Institute of Ion Beam Physics and Materials Research, Forschungszentrum Dresden-Rossendorf, 01314 Dresden, Germany

Introduction

One of the new concepts for non volatile memory applications is based on a structural change of a certain active material (phase change RAM or PCRAM) which is accompanied with a dramatic change of the electrical resistivity [1, 2]. Thus, an information bit can be stored, defining 1 as amorphous state (high resistivity) and 0 as crystalline state (low resistivity). The change from amorphous to a crystalline state is reached by a longer pulse of a comparatively low current. To reset the material to the amorphous state, a short pulse of a higher current is needed, causing a partial re-melting and fast quenching of the material. The material group of chalcogenides is among the potential candidates with the desired structural properties and thermal behaviors. In order to integrate these materials into a product, they must fulfill a number of criteria, such as low melting temperature (reset current), fast crystallization speed (write speed) and a sufficiently high crystallization temperature (retention). A promising compound is $Ge_2Sb_2Te_5$ (GST), which can crystallize in cubic or hexagonal structure. Typically, additional structural dopants such as Si, O and N can be used to tune to the material properties to the desired working point.

Materials and methods

In the experiment we studied a series of SiO_2 - doped GST films by means of high temperature X-ray diffraction (XRD) at 12 keV with simultaneous measurement of the electrical resistance. The films were deposited by a sputtering process on Si substrate covered by a 100 nm SiO_2 layer. Finally the GST film was capped in situ with a 10 nm SiO_2 layer in order to avoid the oxidation of the chalcogenide. The dopant concentration was varied by tuning the RF sputtering power on the SiO_2 target between 0 – 350 W. The thickness of the doped GST films was about 100 nm. The measurements were carried out in a high temperature chamber with a Beryllium dome, having a feedthrough for four electrical contacts. The vacuum within the temperature chamber was better than 5×10^{-6} mbar. The temperature was ramped from room temperature up to 450°C with a heating rate of 4.3 K/min. During the heating, continuously 2:1 symmetric scans in the 2Θ range between 16° – 20.5° were taken, with scan duration of about 1.5 min. A scintillation counter as detector was used. For the electrical 4-point measurements a constant current was applied via two contacts and the resulting voltage was taken every second. After 10 measurements, which were averaged for resistance calculation, the polarity of the current was changed to compensate the thermoelectric voltage. The electrical measurements were started a couple of minutes ahead of the XRD scans. This time was taken by stopwatch for the synchronization of the structural and electrical measurements.

Results and discussion

All GST films of the SiO_2 series were amorphous after deposition. Measurements with Rutherford Backscattering Spectrometry and Time of Flight Secondary Mass Ion Mass Spectrometry revealed that the silicon content in the sample increases with about 1 at% Si per 100 W RF sputtering power.

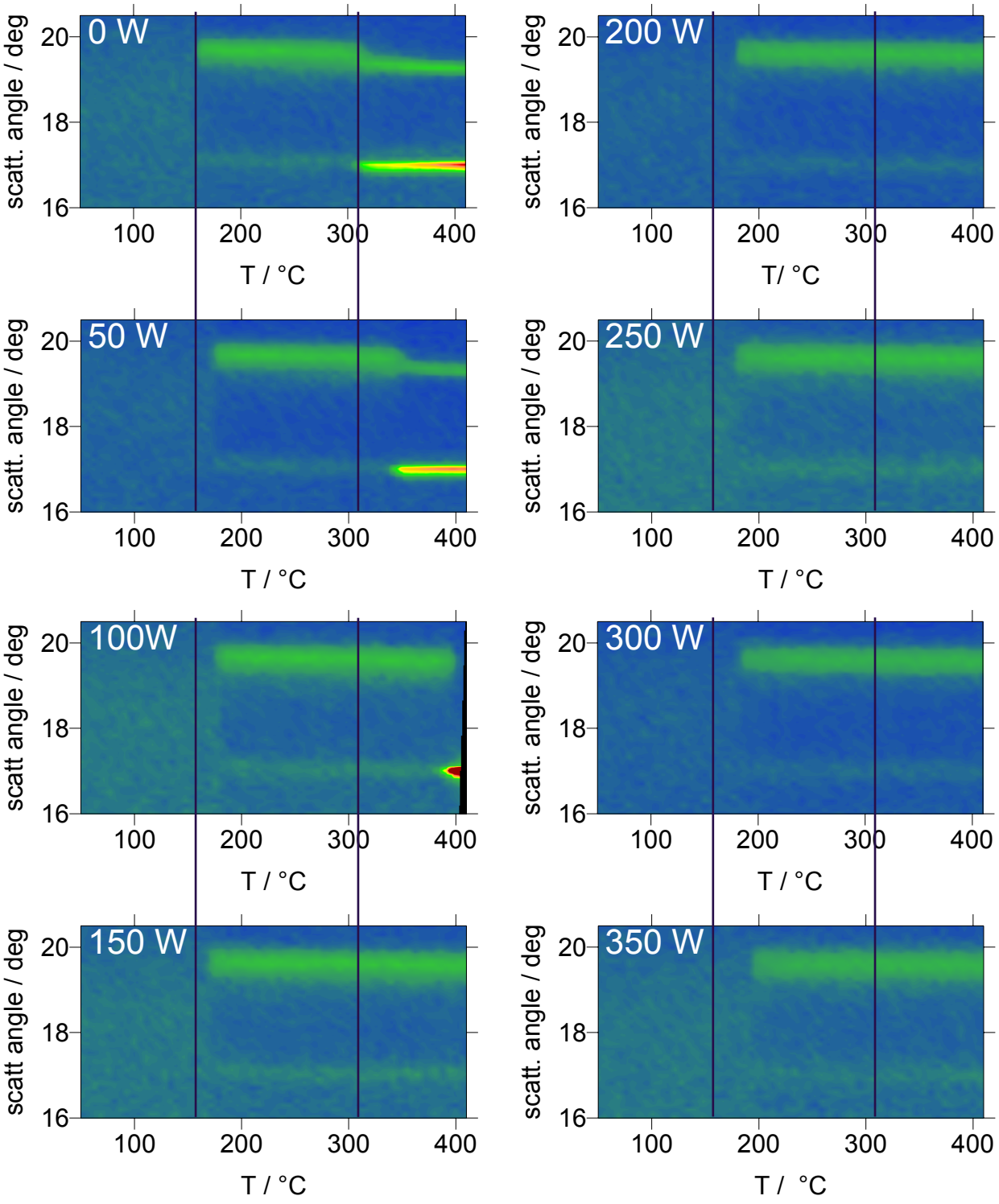

Fig. 1 a-h:
Color-coded maps of temperature dependent XRD measurements of Si doped GST layers with varying SiO_2 concentration (RF sputtering power 0 W – 350 W).

As shown in Fig. 1 a-h the first phase change from amorphous to crystalline cubic phase is observed in the temperature range between 160°C and 200°C, depending on the Si concentration. A second phase transition from cubic to hexagonal phase was obtained in the range between 300°C and 390°C, but only for samples with low Si concentration (up to 100 W RF power; see Fig. 1 a-c).

The simultaneous electrical measurements showed a significant decline about two orders of magnitude in resistance correlating with the first phase transition. A smaller decline in resistance was observed during the transition cubic to hexagonal (see Fig. 2). On subsequent cooling afterwards, the resistance remains in the same order of magnitude.

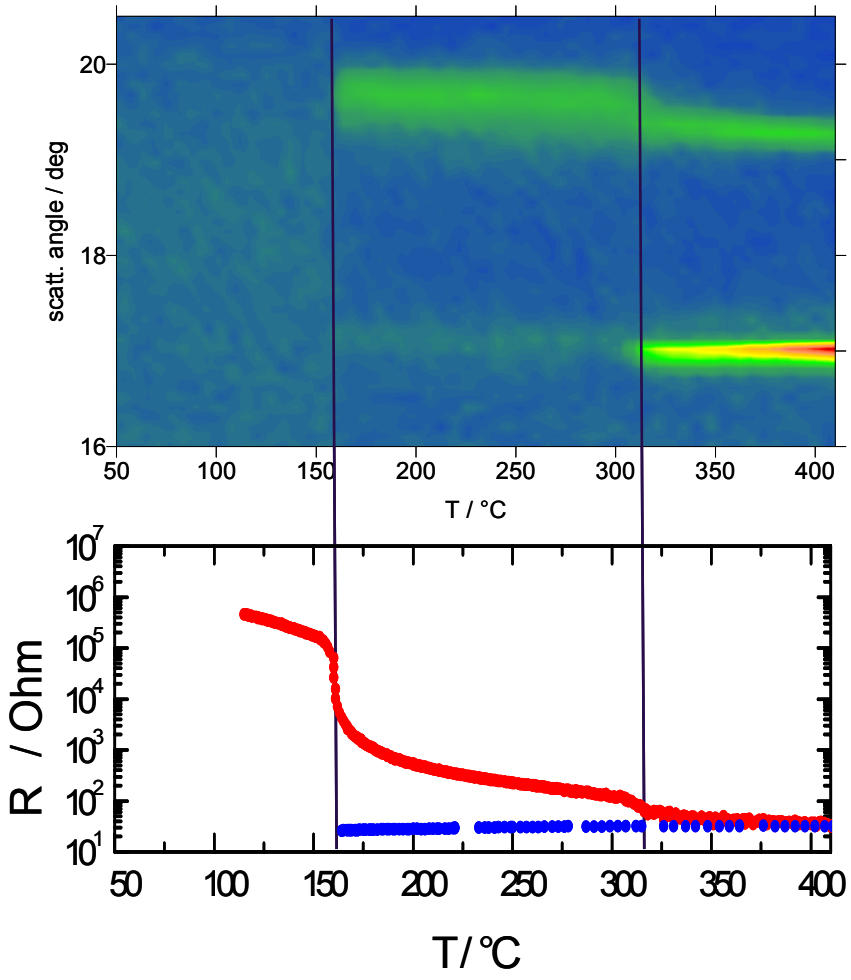

Fig. 2:
Simultaneous measurement of structural and electrical properties; resistance drops significantly upon phase change, here shown for sample with 0 W SiO_2 sputtering power. Blue dots in R vs. T curve indicate cooling phase. For this sample a metallic behaviour is observed (R decreases with decreasing temperature).

The samples, which underwent a phase transition to the hexagonal phase, showed metallic conduction behavior during cooling down, whereas the samples that remained in the cubic phase, showed semiconducting conduction behavior (Fig. 3).

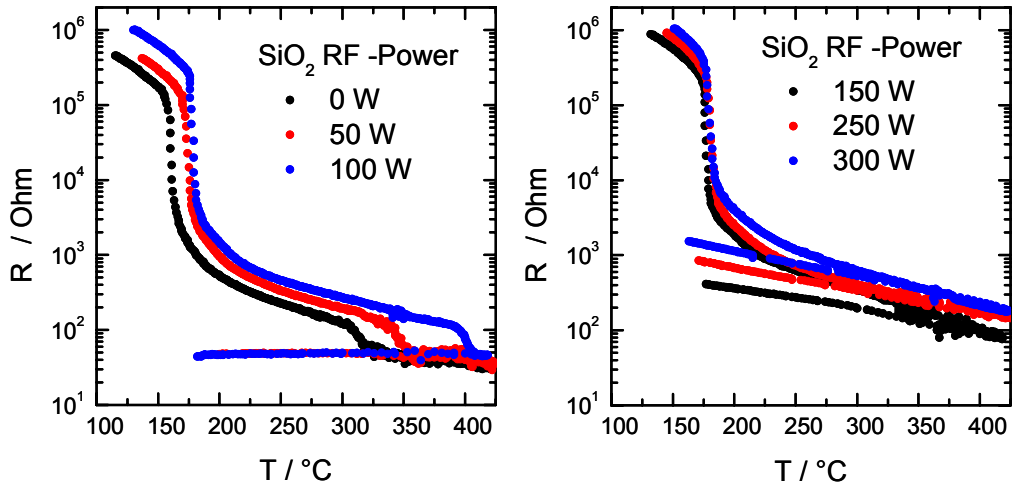

Fig. 3:
Comparison of resistance measurements for all samples: semiconducting conduction behavior after second phase transformation, metallic behavior after first phase transformation.

Conclusion

This study demonstrates that the Si content influences the phase transformation temperature in doped GST materials, especially for the change from cubic to hexagonal phase. Both crystalline phases have different conduction properties. Si doping allows tailoring the characteristics of the GST film over a wide range.

Acknowledgements

This work was financially supported by the Federal Ministry of Education and Research of the Federal Republic of Germany (Project No 01M3171A). The authors are responsible for the content of the paper.

References

[1] M. Ichinose, T. Ishida, Y. Takagai, M. Ito, S. Ohara, I. Satoh, Y. Okazaki, R. Imanaka, Jpn. *J. Appl. Phys.* **32** (1993) 5320.

[2] M. Wuttig, N. Yamada, *Nature Mat.* **6** (2007) 824.

2. Technical Documentation and Statistics

2.1. Technical status and developments

Overview and optical characteristics

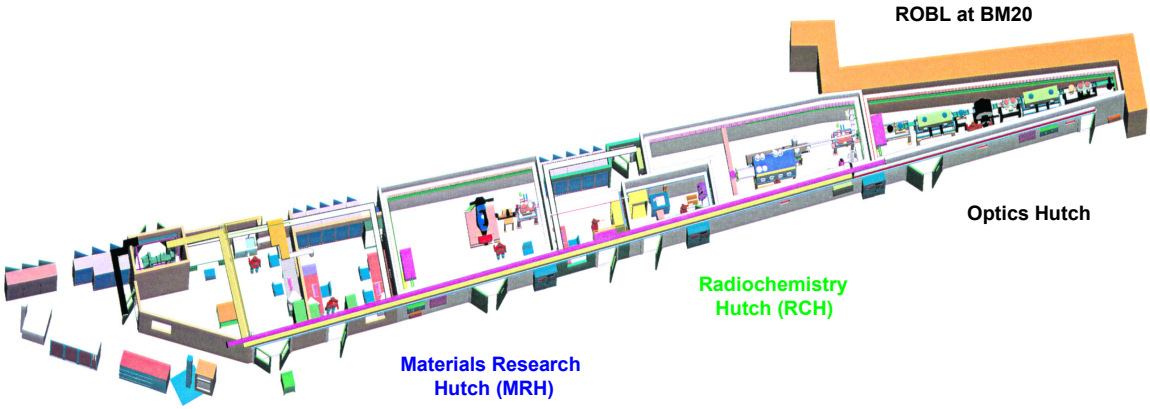

The optics with two mirrors and a double-crystal monochromator in fixed-exit mode provide both a high flux at high angular resolution (for diffraction) and a high flux over a wide energy range with high energy resolution (for EXAFS spectroscopy).

energy range	**5 – 35 keV**
with Si-mirrors	5 – 12 keV
energy resolution Si(111)	1.5 – 2.5x10^{-4}
energy resolution Si(311)	0.5 – 1.0x10^{-4}
integrated flux (calc.)	**6·10^{11} phot. / s** @ 20 keV/200 mA
standard beam size	20 × 3 mm^2 (w×h)
focussed beam size	≤ 0.5 x 0.5 mm^2

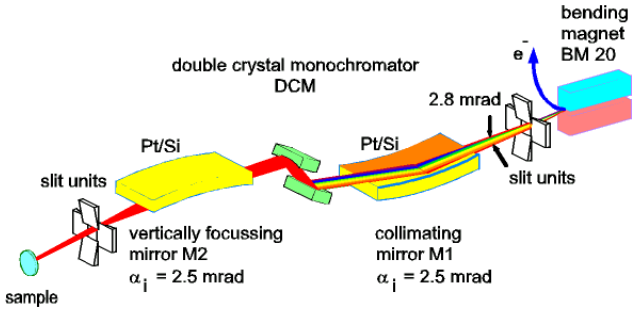

1a	2a	3b	4b	5b	6b	7b	8			1b	2b	3a	4a	5a	6a	7a	0
H																	He
Li	Be											B	C	N	O	F	Ne
Na	Mg											Al	Si	P	S	Cl	Ar
K	Ca	Sc	Ti	V	Cr	Mn	Fe	Co	Ni	Cu	Zn	Ga	Ge	As	Se	Br	Kr
Rb	Sr	Y	Zr	Nb	Mo	Tc	Ru	Rh	Pd	Ag	Cd	In	Sn	Sb	Te	I	Xe
Cs	Ba	La	Hf	Ta	W	Re	Os	Ir	Pt	Au	Hg	Tl	Pb	Bi	Po	At	Rn
Fr	Ra	Ac	Rf	Ha													

Lan	Ce	Pr	Nd	Pm	Sm	Eu	Gd	Tb	Dy	Ho	Er	Tm	Yb	Lu
Act	Th	Pa	U	Np	Pu	Am	Cm	Bk	Cf	Es	Fm	Md	No	Lr

The energy range allows to investigate the elements in yellow by K-edge EXAFS, and those in blue by L-edge EXAFS. Radionuclides presently permitted at the beamline are shown in red.

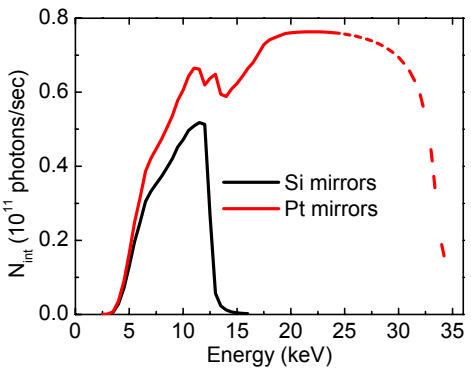

Energy range with different crystals and mirror materials

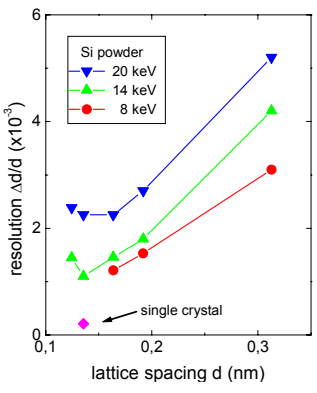

Experimental resolution determined with Si(111) and Si powder

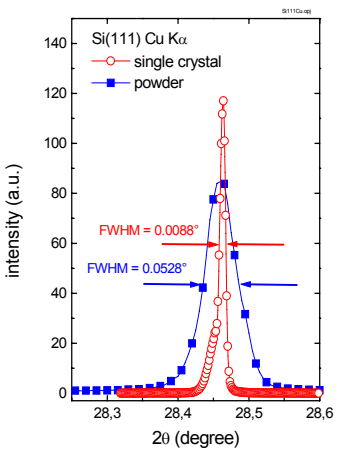

FWHM comparison

Technical characteristics of the Radiochemistry station

The Radiochemistry experimental station is a highly specialized *unique* **radiochemical laboratory** designed for **radioecological research** using x-ray absorption spectroscopy (XAS) in transmission and fluorescence mode. Solid and liquid samples with a total activity of **185 MBq** (5 mCi) and a surface dose rate of **15 µSv/h** can be investigated. A **multi-barrier safety concept** with separate ventilation, constant radiation monitoring and redundancy of all essential components was developed to satisfy legal requirements.

Tc-99	**Po-208**	**Po-209**	**Ra-226**	**Th-nat**	**Pa-231**
30,000	0.008	0.3	5	10^6	106
U-nat	**Np-237**	**Pu-238**	**Pu-239**	**Pu-240**	**Pu-241**
10^6	7000	0.3	80	22	0.049
Pu-242	**Am-241**	**Am-243**	**Cm-244**	**Cm-246**	**Cm-248**
124	1.4	25	0.062	17	1,156

List of permitted **radionuclides** and their maximum amount in mg (shown in blue). Additional radionuclides may be used if accepted by the ESRF safety group.

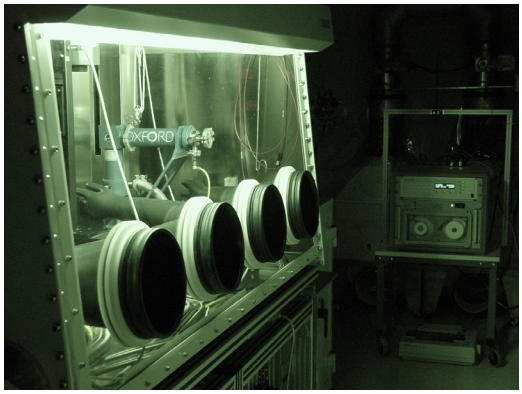

During the measurement, the **spectroscopic glove box** envelops the samples, which are mounted either on a remote-control 8-fold multistage holder or in a cryostat. The fluorescence and transmission detectors remain outside of the glove box.

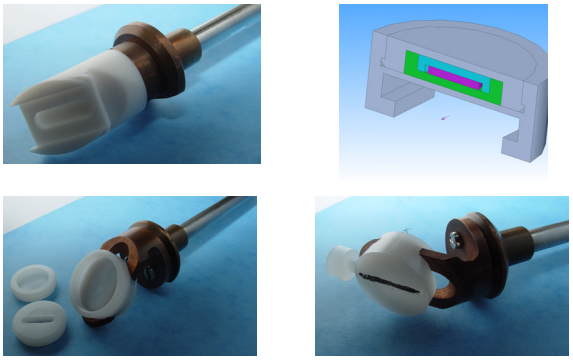

Sample holders fulfilling the necessary safety requirements exist in a wide variety to match different sample. Technical drawings and detailed information on filling procedures may be downloaded from our home page.

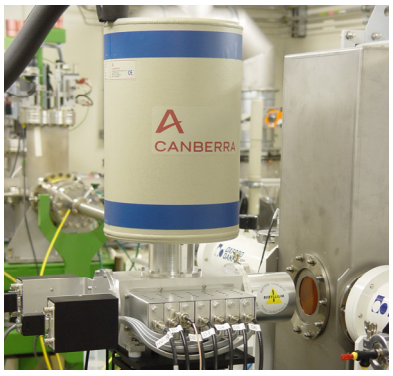

13 element LEGe detector with a high-rate digital multi-channel analysis spectrometer (XIA) and dedicated analysis program integrated into the XAS data collection software XATROS.

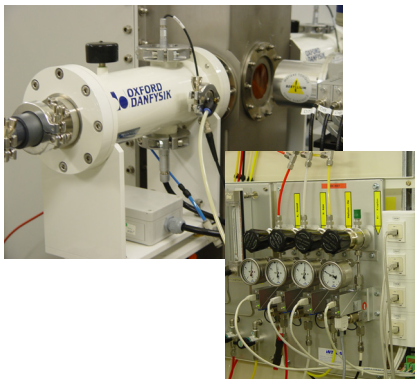

3-kV ionization chambers with remote-controlled gas mass-flow controllers.

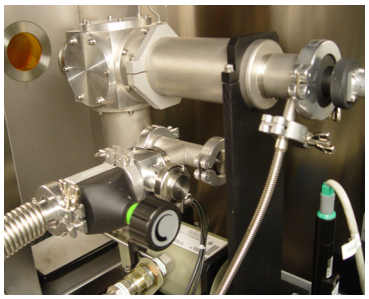

Closed-cycle He cryostat with large fluorescence window adapted to the 13-element detector and very low vibration levels cools samples down to 15 K.

Technical characteristics of the Materials Research station

The materials research hutch MRH with a the high load six-circle diffractometer is designed for the various scattering and diffraction experiments for identification and precise determination of crystal structures, stress and strain analysis, crystal size and orientation evaluation, as well as thin film characterization by thickness, roughness and periodicity. The core competence of MRH are in the field of in-situ investigations, where the system under investigation is characterized during synthesis or processing while also physical properties like electrical conductivity can be measured. For this purposed MRH is equipped with different sample environments and detector system, which can also be completed by the use of the ESRF-detector pool.

Detectors

- Scintillation detectors (BEDE EDRa) with motorized slits, analyzing crystal or Soller collimator are available.
- energy-dispersive PIN-Diode (AmpTec, energy resolution 200 eV, area 7 mm^2)
- one-dimensional linear position sensitive detector (PSD-50m-ASA, M. Braun)
- CCD detector (axs-SMART) pixel size 150 µm

Sample environment

- High temperature chamber of Bühler design up to 2.000 °C
- In-house developed heating chamber with a semispherical Be-dome for different diffraction geometry up to 1200°C and under controlled atmospheres up to 10 mbar, optional in-situ conductivity measurement by 4 point probe setup
- *in-situ* magnetron sputter deposition chamber with two magnetrons and an ion gun port allows temperature up to 700°C. The arrangement of the Be-windows allows in-plane and out-off-plane diffraction experiments as well as GISAXS

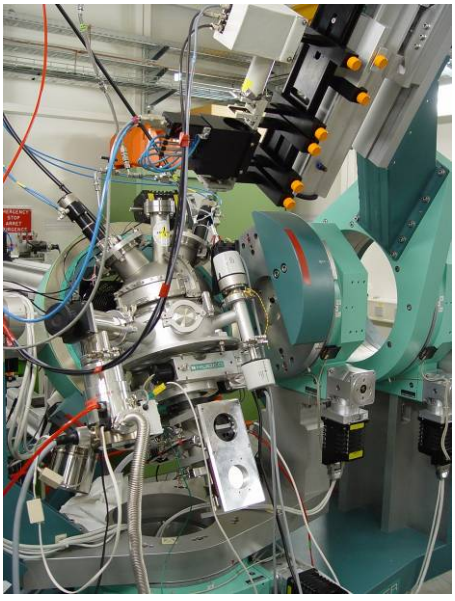

Sputter deposition chamber

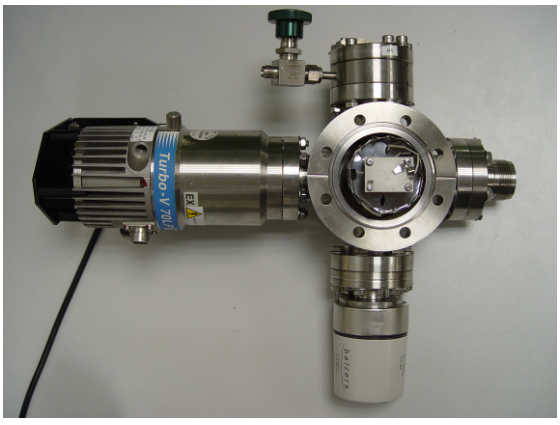

Be-dome furnace

Technical developments at ROBL

W. Oehme[1], A. Büchner[1], J. Claußner[1], S. Dienel[1], J. Hauser[1], D. Pröhl[1], C. Baehtz[2,3], D. Banerjee[2,4], N. Jeutter[2,3], M. Hesse[2], H. Witsch[5], H. Funke[2,4], C. Hennig[2,4], A. Ikeda-Ohno[4], A. Roßberg[2,4], A.C. Scheinost[2,4], K. Takao[4], S. Takao[4]

[1] Department of Research Technology, FZD, 01314 Dresden, Germany
[2] The Rossendorf Beamline (ROBL/BM20) at ESRF, 38043 Grenoble, France
[3] Institute of Ion Beam Physics and Materials Research, FZD, 01314 Dresden, Germany
[4] Institute of Radiochemistry, FZD, 01314 Dresden, Germany
[5] BLISS, European Synchrotron Radiation Facility, 38043 Grenoble, France

Introduction

This report summarizes the most important technical developments realized in 2007 and 2008 in the field of experiment automation at ROBL. This work was performed by members of the technical infrastructure of the FZD in cooperation with the scientists working at the beamline in Grenoble and with the BLISS group of the ESRF. The work comprises special tasks in the fields of mechanical construction, electronic instrumentation and engineering, as well as software development.

Beamline upgrade

For 2012, a substantial upgrade of the optical components of the beamline is planned. Therefore calculations have been carried out to analyze the existing system and prove the feasibility of different possible future beamline setups.

Raytracing of the current system and of several new variants were simulated with SHADOW [1]. The new design should use new optical devices to make use of the technological progress in the last decade, achieving a higher photon flux, a wider energy range, and a microfocused spot at a new endstation designed for combined spectroscopy and scattering experiments. Results are compiled in the Upgrade Design Report.

Materials research station

New gas line system

For the extension of the research field in the Materials Research Hutch the gas-line system has been renewed. Now there is the possibility for more *in–situ* research with different gas environments, useable with different chambers.

The old gas-line has been built only for the in-situ sputtering experiments. Therefore the main used gas was argon sometimes nitrogen, depending on the studied systems. To overcome limitations in the variety of gases the new gas line has been adapted on the new upcoming needs in research. In order to study *in-situ* growth out of gases (e.g. carbon nanotubes), nanoparticles behavior under different gas atmospheres and catalyst formation out of nano-particles under different defined atmospheres, we can now offer the possibility to use four different gases at the same experimental setup.

The gases argon, nitrogen and oxygen are installed permanently in the hutch, but they can be replaced by other gases (e.g. H_2), if necessary. These lines are equipped with mass flow controllers working in the range of 1-30sccm, 1-10sccm and 1-10sccm, respectively. A fourth line is always free for the users needs for a special gas. It is equipped with a N_2 or Ar mass flow controller, which can be replaced by a mass flow dedicated to the used gas. The new setup can be connected to the *in-situ* magnetron-sputter chamber, the standard Be-dome oven and to the oven for conductivity measurements.

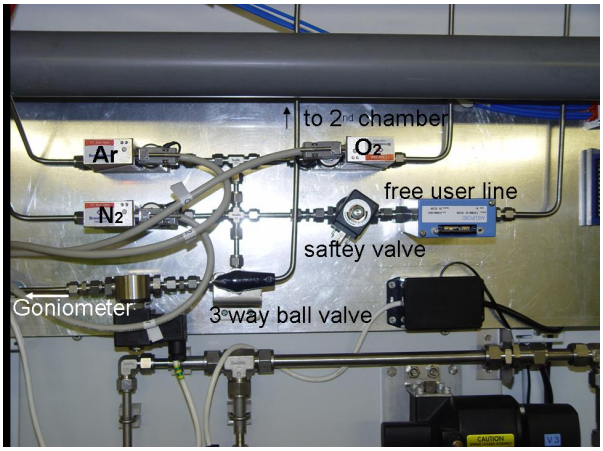

New gas flow control system in MRH

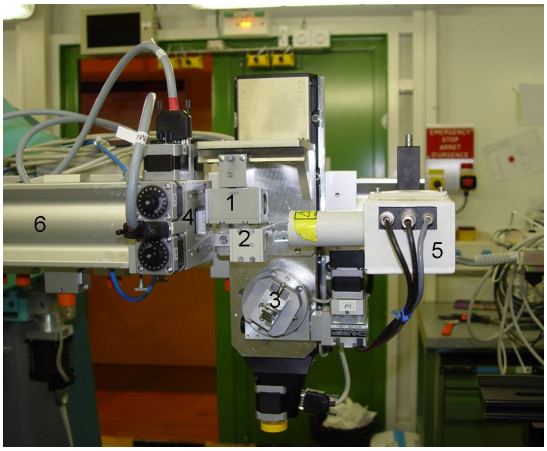

New detector optics system in MRH. 1) horizontal and 2) vertical soller slit, 3) Ge channel cut crystal, 4) motorized slit system, 5) scintillation counter and 6) evacuated flight tube.

The magnetron sputter chamber can now also be used without being mounted on the diffractometer for ex-situ sample synthesis or process parameter calibration by the use of a second gas line. Between the goniometer and the ex-situ gas lines can be chosen by a 3 way ball valve, installed directly after the mass flows.

Additionally is the new gas line also integrated in the interlock system, which supervises all safety relevant process parameters. In the case of emergency, the line will be closed automatically. This of course, enhances safety for experimenters and equipment.

New detector bench and improvements of the detector optics

The variety of the different experiments performed at MRH accounts for the big variety of detectors, e.g. PSD, scintillators, Bruker CCD, Photonics camera, MAR CCD or image plate etc. Therefore the station was extended by a new optical bench [2] which consists of a XZ-table driven by two 5-phases stepper motors from Oriental [3]. This table was constructed to move loads of up to 50 kg and is located around 1.20 m behind the goniometer, but can be moved further downstream upon demand. This way, heavy detectors as mentioned above, can be easily adjusted and simultaneously used with the detector system mounted on the instrument.

The old setup of detector optic used to have fixed slits. For this reason every change of the slit-size or detector optics like Soller slit or analyzing crystal has to be done manually. The new setup consist of two motorized JJ-XRAY slits systems [4] which is also equipped with stepper motors from Oriental. This slit is controlled by a unit developed at the FZD [5]. Additionally a linear stage LS-110 from micos [6] moves Soller slits (vertical and horizontal) or a Ge-analyzer crystal into the beam path on purpose. This stage is controlled by a new stepper motor driver “icePap” developed by the ESRF. This will be the favorite controller for further extensions and is therefore been tested at ROBL-MRH. The advantages of this new detector system are clear; it is fully motorized, so within an experiment, the detector optics can be changed without interruption of the experiment. It ranges from high instrumental resolution by a Ge-channel cut crystal over medium resolution (slit system for XRR and normal diffraction) to the low resolution but high flux

setup (Soller slit to identify nano-crystalline materials). This change can also be controlled by a macro describing the planed measurements.

This is a great step in automation of the measurements, because now the experimentalists have the opportunity to run sophisticated long macros for capacious measurements without being present all the time.

Automatic filter control depending on the incoming count rate

The automatic filter control was improved by a new algorithm. This way the detector is better protected from high counting rates, and we save measurement time.

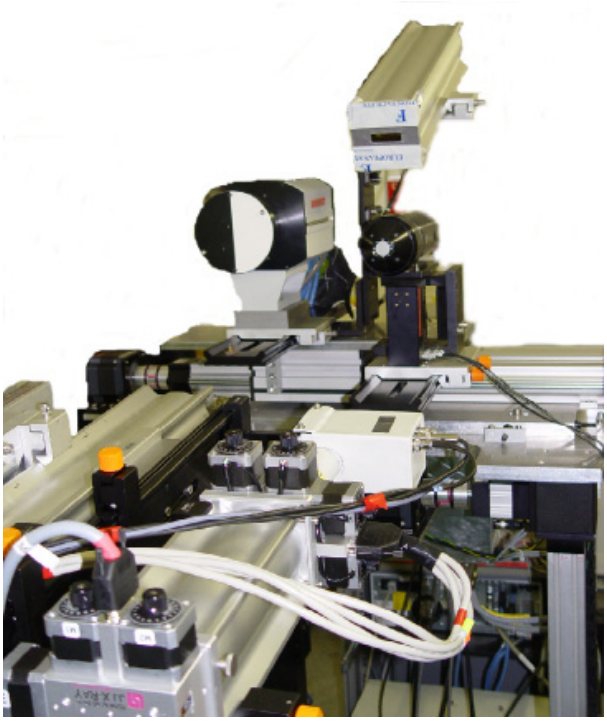

New detector bench in MRH

Axes Driver JJ-XRAY (front and rear side)

Bruker-CCD

The Smart-Detector by Bruker is now integrated into the standard measurement equipment (spec [7]) by using a software solution of the ESRF. This detector is now mounted on the new detector bench mentioned above.

A new software psdViewJ

We ported and improved the software psdView from C++ to a Java version which can run on most computer platforms. The new version takes now into account filter factors and is able to transform the measured data into the Q-space. This software makes it easier to analyze the large amount of data measured by applying the position sensitive detector (PSD).

Radiochemistry station

Electrochemical cell

A new electrochemical cell was constructed [8], which can be used to measure in-situ reactions of actinides by X-ray absorption spectroscopy. There is also a remote-control available (electric, electronics, and software). The equipment is completed by a slit-system (JJ-XRAY, 2 phases stepper motors connected to a Pegasus controller from MICOS [6]) to adjust the beam to the X-ray window of the cell.

Automated temperature scans with the cryostat

We are using a cryostat from CryoVac [9] mainly because cryogenic temperatures often improve the EXAFS signal and prevent photon-induced redox effects. Now, a new feature has been implemented to perform temperature scans at different pre-selected temperatures automatically. This way, the temperature dependence of the Debye-Waller factor and phase transitions can be studied more easily. To get stable temperatures at the chosen set-point we have to adjust some parameters of the device TIC304-MA which controls the cryostat depending on the temperature set-point. This dependency is implemented inside the device server software [10] and the set-point can be chosen as one of our objects handled automatically before an EXAFS run takes place.

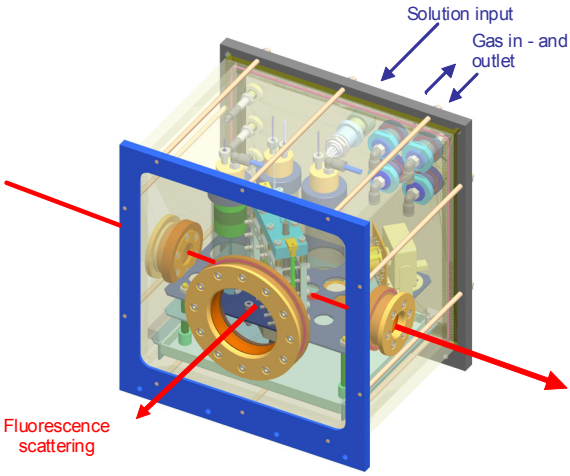

Spectro-electrochemical cell inside the safety confinement

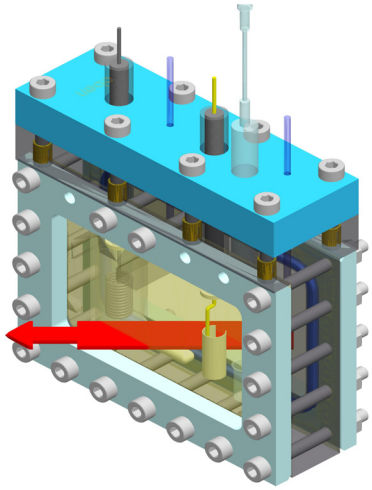

Electrochemical cell

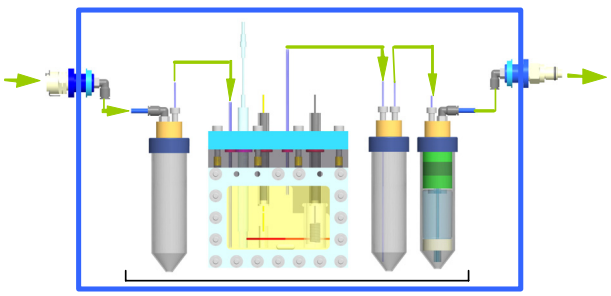

Gas flow and aerosol purging system

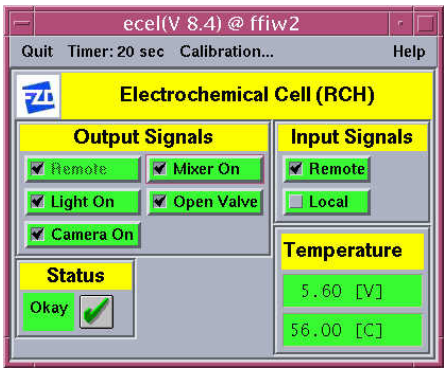

Software control system

New amplifiers for the ionization chambers

The OXFORD ionization chambers are now equipped with new low noise current amplifiers DLPCA-200 [11]. There was an inverter/buffer-amplifier device added [12] which makes it easier to adjust the amplifiers to the other electronic equipment. We also implemented a remote gain control with an automatic gain setting.

Inverter/buffer unit (front and rear side)

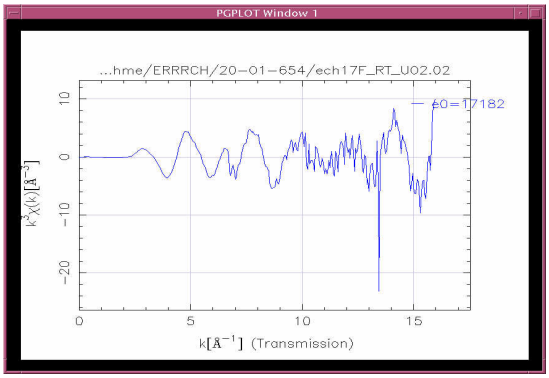

EXFAS-signal (online presentation)

Improvements of the spectroscopy software "XATROS"

Several improvements were integrated in our measurement program "XATROS" [13].

- the new amplifiers DLPCA-200 were integrated
- automatic support of "temperature scans" with the cryostat
- the XRF spectra collected by the Ge-13-element detector can now be calibrated within XATROS
- There is a new mode which allows an automatic beam optimization (piezo-driven pitch rocking curve of 2nd DCM crystal) at the start of each XAFS energy scan by employing the D-Mostab device [14]. This is especially important in case of orbit instabilities during an injection cycle or after beam re-injections.
- The transmission and fluorescence EXAFS-signals are now converted in real time into k^3-weighted $\chi(k)$ spectra. Parts of the software package "IFEFFIT" developed at the University of Chicago [15] were integrated into XATROS for this purpose. This allows an immediate visual evaluation of the signal-to-noise ratios and other quality criteria, which are crucial for determining the useful k-range and the required number of scans. This helps to save always scarce measurement time.
- The slit-system used for the electrochemical cell has been integrated.

Porting specific software to Linux/Redhat

Since the ESRF discontinues the support of Sun computers running the SOLARIS operating system, we started to port our software from SOLARIS to LINUX computers compatible to ESRF beamlines.

References:

[1] C. Welnak, G.J. Chen, F. Cerrina, SHADOW: a synchrotron radiation and X-ray optics simulation tool, *Nuclear Instruments and Methods in Physics Research A* **347** (1994) 344-347

[2] J. Hauser: Hubtisch, *Internal Documentation FZD*, Zeichnungsnr.: 5.053(1)

[3] 5-Phase Stepping Motor Unit, RK Series ,Operating Manual, Oriental Motor Co., Ltd. 2007

[4] JJ-XRAY:http://www.jjxray.dk

[5] S.Dienel, D. Pröhl: Steppermotordriver für Slitsystem von JJ-XRAY, 12.515-53.00, Internal documentation FZD

[6] MICOS: “Linear Stage LS-110”, http:///www.micos.ws/LS_110.html

[7] Certified Scientific Software: spec™ X-Ray Diffraction Software, http://www.certif.com

[8] J. Claussner: „Elektrochemische Zelle“, Zeichnungsnr.: 11.101(1)

[9] CryoVac Gesellschaft für Tieftemperaturphysik mbH & Co KG, Heuserweg 14, 53842 Troisdorf

[10] W. Oehme: Description of the CRYOVAC Device Server, internal ROBL, 6.7.2007

[11] DLPCA-200, datasheet, FEMTO Messtechnik GmbH, Paul-Lincke Ufer 34, D-1099 Berlin, Germany

[12] D. Pröhl: Inverter / Buffer- Amplifier for Ionchambers, 12.515 - 50, internal FZD

[13] W. Oehme, T. Reich, Chr. Hennig, A. Scheinost: “Program XATROS - User’s Guide”, Internal ROBL documentation, 8.8.2007

[14] K. H. Meß: D_Mostab Manual, Device Description, ROBL internal product description

[15] IFEFFIT: University of Chicago, http://cars9.uchicgao.edu/ifeffit

2.2. Beamline personnel

Head of the beamline / responsible for RCH: Andreas Scheinost (-2462)
Responsible for MRH: Carsten Bähtz (-2367)

	Name (phone)	Position/Education/Research Interests
	Marion Glückert (-1967)	Office administration
	Marco Hesse (-2372)	Beamline Technician
Radiochemistry	Dipanjan Banerjee (-2463)	Postdoc *since 11/2007* Ph.D. in Geology (1999), Univ. of Western Ontario, Canada ACTINET, Sorption and redox processes at solid-solution interface, focusing on transition metal sulfides and oxides
	Harald Funke (-2339)	Beamline Scientist Ph.D. in Physics (1974), University of Moscow (Russia) development of wavelet analysis for EXAFS
	Christoph Hennig (-2005)	Beamline Scientist Ph.D. in Crystallography (1995), Universität Leipzig aqueous chemistry and electrochemistry of actinides
	Regina Kirsch (-2849)	Ph.D. student diploma in Chemistry (2007), Universität Leipzig redox reactions under anoxic conditions and EXAFS of surface complexes of Sb and Pu on iron minerals
	Andre Rossberg (-2847)	Beamline Scientist Ph.D. in Chemistry (2002), TU Dresden new methods for EXAFS analysis sorption chemistry of actinides
	Andreas Scheinost (-2462)	Head of Beamline Ph.D. in Agricultural Engineering (1994), TU München radionuclide speciation in soils, sediments and aquifers, interfacial redox processes
Materials Research	Carsten Baehtz (-2367)	Beamline Scientist, responsible for MRH Ph.D. in Chemistry (2000), TU Darmstadt in-situ XRD techniques, carbon nanotube growth mechanisms
	Nicole Jeutter (-2872)	Postdoc Ph.D. in surface crystallography (2006), LMU München X-ray diffraction and small-angle scattering of semiconductors

Postal address Rossendorf Beamline
(ROBL-CRG, BM20)
ESRF / sector 21
BP 220
F-38043 Grenoble cedex France

Phone: +33 (476) 88 xxxx
Fax: +33 (476) 88 2505
E-mail: surname@esrf.fr

FZD personnel involved in the scientific and technical programme

Department of Research Technology

Frank Herbrand	Winfried Oehme	Jürgen Claussner
Siegfried Dienel	Dieter Proehl	

Institute of Ion Beam Physics and Materials Research

Johannes von Borany	Joerg Grenzer	Natalia Shevchenko
Sybille Kirch	Andrea Scholz	Rene Weidauer

Institute of Radiochemistry

Gerd Bernhard	Satoru Tsushima	Christian Lucks
Stephan Weiss	Alix Guenther	Heidemarie Heim
Cordula Nebelung	Anette Rumpel	Astrid Barkleit

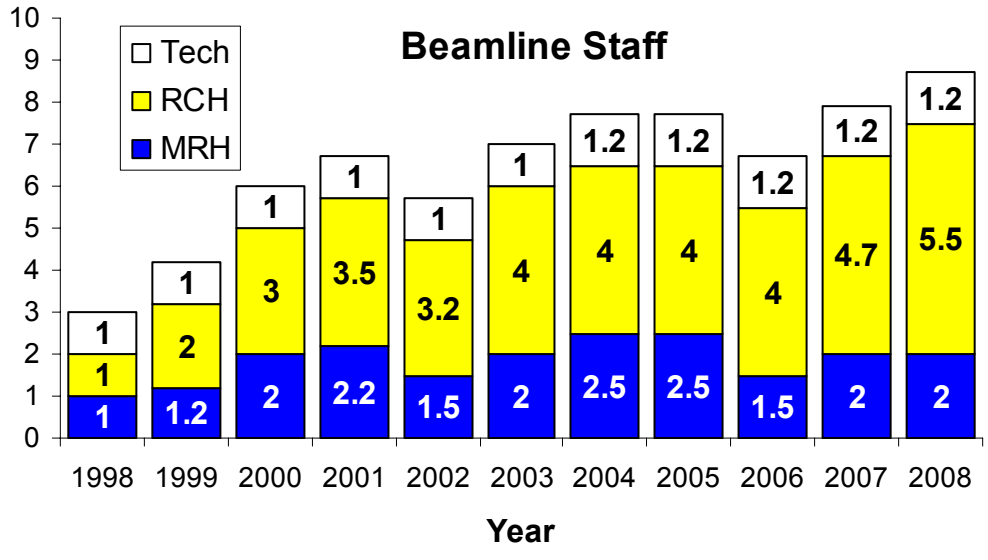

Fig. 2.2.1.
Evolution of beamline personnel since 1998.

2.3. Beamtime allocation and user groups

In the past two years, 212 experiments have been performed involving 231 users traveling to the ESRF (Table 2.3.1). A total of 1298 shifts have been delivered for experiments, i.e. 98 % of the available beam, and only 2 % for commissioning and other technical shifts. Distribution of time between RCH and MRH was 52/48, while RCH performs almost twice as many experiments. ESRF experiments were using 28 % of the total shifts. 27 % of the inhouse shifts of RCH have been provided for Radiochemistry experiments in the framework of ACTINET - EU Network of Excellence (see below).

Table 2.3.1. Use of beamtime at the Rossendorf Beamline.

	Year	FZD shifts	ESRF shifts	Actinet shifts	Technical shifts	Experiments FZD / ESRF / Actinet	Users FZD / ESRF / Act
RCH	**2007**	183	100	45	21	24 / 11 / 5 = 40	15 / 39 / 10 = 64
RCH	**2008**	178	84	86	0	21 / 8 / 9 = 38	28 / 21 / 26 = 75
MRH	**2007**	231	92	-	0	16 / 7 / - =23	25 / 20 / - =45
MRH	**2008**	203	87	-	21	15 / 5 / - = 20	32 / 15 / - = 47
sum		**795**	**363**	**131**	**42**	**76/31/14 = 121**	**100/95/36 = 231**

Figure 2.3.1 shows the beamline overbooking by giving the ratio between requested and allocated beamtime of ESRF experiments. In the last two years, the overbooking factor was always close to 1.8, which is the long term average. This high overbooking factor demonstrates the continuous attractiveness of ROBL for outside users.

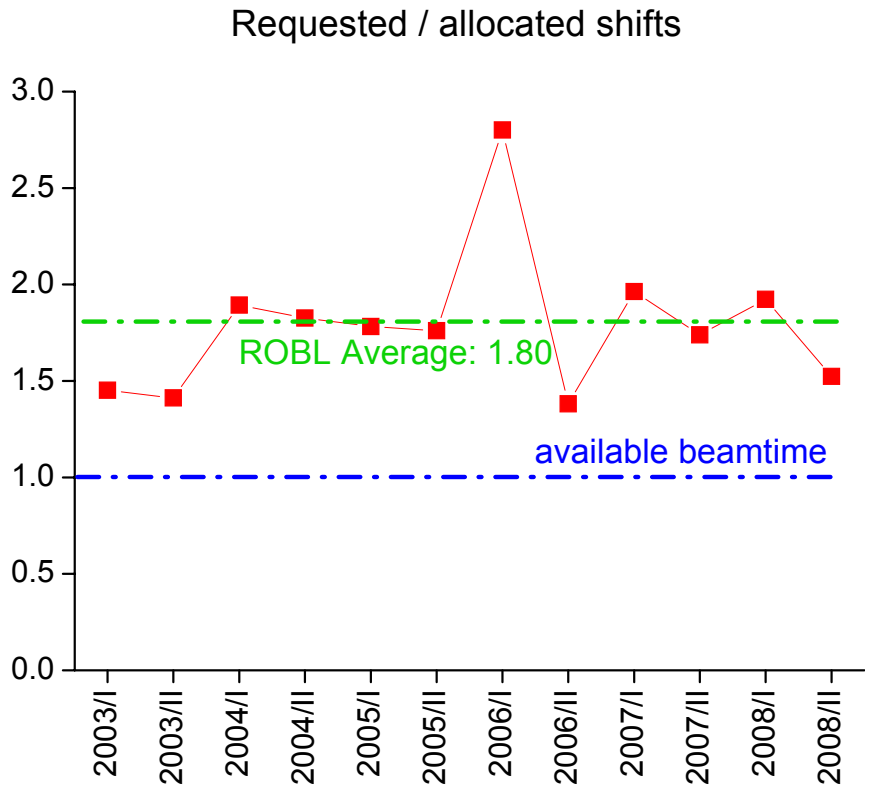

Fig. 2.3.1.
Beamtime request for ESRF experiments.

User Groups

Figure 2.3.2 shows the origin of user groups, excluding all FZD groups. The heaviest demand for beamtime in MRH is from Germany, and for RCH from France. Nevertheless, users from ten other European countries have performed experiments at ROBL. For the first time, users were coming from overseas, the USA and Japan. The University of Tokyo and the Japan Atomic Energy Agency (JAEA) have established a collaborative agreement with the FZD, to ease the access of Japanese scientists to the radiochemical facilities at FZD and ROBL.

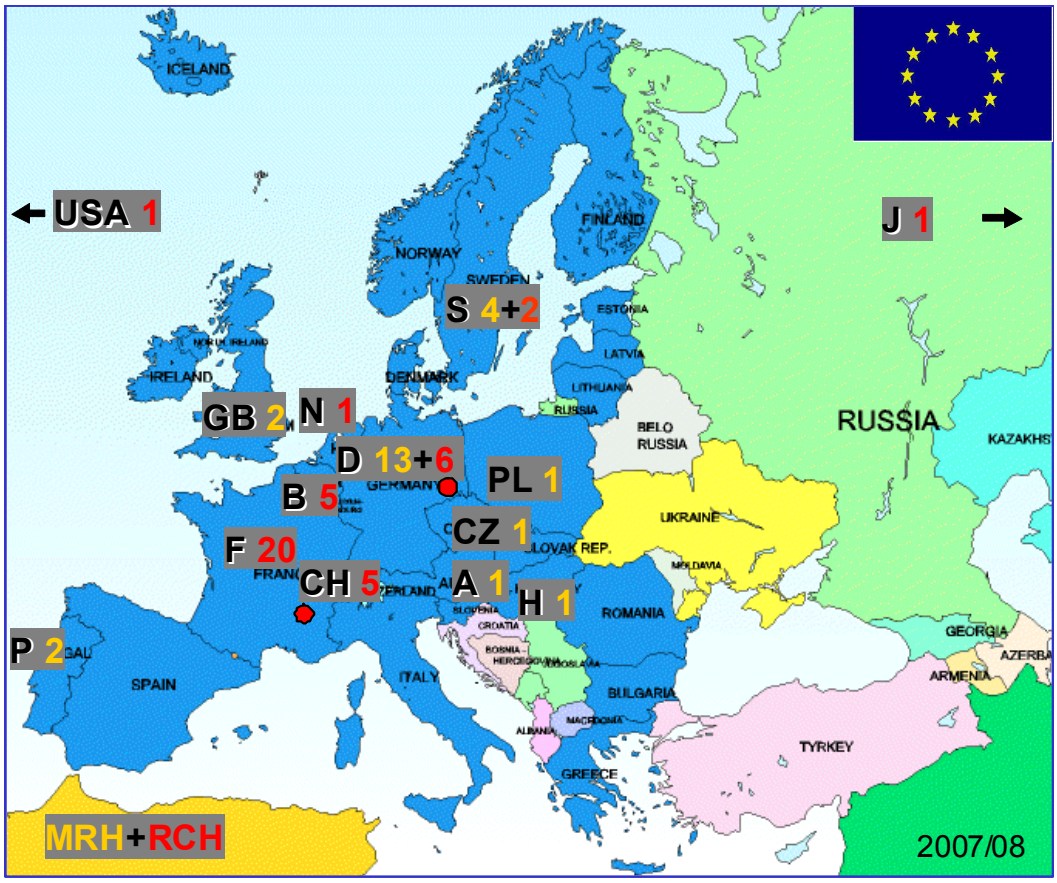

Fig. 2.3.2.
Inhouse and ESRF experiments per country. RCH experiments are shown in red, MRH experiments in yellow. German experiments excluding inhouse.

Germany

- Advanced Micro Devices (AMD) Saxony, Dresden
- Center for Advanced European Studies and Research, Bonn
- Institut für Kernchemie, Universität Mainz
- Department of Geology, TU Freiberg
- Institut für Optik und Quantenelektronik, Friedrich-Schiller-Universität Jena
- Institute of Inorganic Chemistry, Univ. Leipzig
- Department of Physics, Univ. Siegen
- Fachgruppe Festkörperanalytik, Martin-Luther-Universität Halle-Wittenberg
- Institute for Bio-and Nanosystems, Forschungszentrum Jülich
- Institut für Röntgenphysik, Universität Göttingen
- Max-Planck Institut für Eisenforschung GmbH (MPIE), Düsseldorf

	– Qimonda, Dresden
Austria	– Institute of Semiconductor Physics, J. Kepler University, Linz
Belgium	– Departement Chemie, Katholieke Universiteit Leuven – Studiecentrum voor Kernenergie (SCK), Mol
Czech Republic	– Department of Condensed Matter Physics, Masaryk University, Brno
France	– CEA at Marcoule and Cadarache – Centre National de la Recherche Scientifique (CNRS) at Grenoble, Dijon and Gradignan – Institut de Physique Nucléaire, Université Paris XI, Orsay – Institut Laue-Langevin, Grenoble – Institut de Recherches Subatomiques (IRES), CNRS-IN2P3, Strasbourg – LGIT, Université Joseph Fourier (UJF), Grenoble
Great Britain	– Centre for Advanced Photonics & Electronics, University of Cambridge
Hungary	– MFA-KFKI, Research Institute for Technical Physics and Materials Science, Hungarian Academy of Sciences, Budapest
Netherlands	– Department of Earth Sciences, Utrecht University
Poland	– Institute of Electronic Materials Technology (ITME), Warsaw
Japan	– Department of Nuclear Engineering & Management, The University of Tokyo
Portugal	– CENIMAT F.C.T./Universidade Nova de Lisboa, Monte da Caparica
Sweden	– Royal Institute of Technology , KTH Stockholm – Thin Film Physics Division, Department of Physics, Chemistry and Biology, Linköping University, Linköping
Switzerland	– Department of Environmental Sciences, ETH Zurich – Laboratory for Waste Management, Paul-Scherrer-Institut, Villigen
USA	– Department of Plant, Soil and Entomological Sciences, University of Idaho, Moscow, Idaho

ACTINET European Network for Actinide Sciences

Since March 2004 the beamline is a member of ACTINET – European Network for Actinide Science, one of the Networks of Excellence within the 6th Framework Programme for Research and Technological Development. ACTINET gathers more than twenty-five European research institutions into a consortium dedicated to actinide sciences. The objective of ACTINET is to take steps in order to bring both research infrastructures and human expertise in Europe to an adequate performance level, thereby contributing to the development of the European Research Area in the fields of physics and chemistry of actinides. The three lines of action are:

- Stimulating the emergence of a European infrastructure policy by pooling the major actinide laboratory facilities
- Promoting excellence by supporting ambitious shared research programmes, taking advantage of the pooled facilities
- Increasing the attractiveness of actinide sciences among European students and young researchers, and allowing the next generation of actinide scientists and engineers to gain hands-on experience as part of their training.

The Rossendorf beamline contributes its radiochemistry end station to the ACTINET Pooled Facilities, providing beamtime for Joint Research Projects granted by ACTINET. In return, ROBL receives annual funds for user support. In 2007/2008, 11 experiments have been performed for ACTINET (see list of experiments 2.5.1.). ROBL has thus provided 27 % of its available inhouse beamtime in agreement with ACTINET. With this, RCH belongs to one of the most heavily used facilities of ACTINET, providing a fundamental contribution to actinide research. The success of ACTINET within FP-6 has now led to a renewal of ACTINET within FP-7, running until end of 2011.

2.4. Publications

This section lists all publications which are based on experiments at the Rossendorf Beamline, whether they have been performed using in-house or ESRF allocated shifts. In contrast to previous Biannual Reports, only peer-reviewed journal articles are listed. As a further selection criterion, only journals listed in the Journal Citation Report (ISI Web of Knowledge) were accepted.

Figure 2.4.1 gives an overview on the publication activities since the commissioning of the beamline. After a continuous increase from 1999 to 2002, publication activity decreased in 2003 and 2004, followed by a sharp rise in 2005. Since then, the total number varies between 25 and 38 publications per year. As shown in Fig. 2.4.2, both endstations produce a slowly increasing number of publications in journals with the highest citation indices in their respective scientific fields (Inorganic Chemistry, Environmental Science & Technology, Geochimica et Cosmochimica Acta for RCH, Applied Physics Letters for MRH). In 2008, two papers in Analytical Chemistry and Physical Review Letters raised the bar even further. In conclusion, the number of publications as well as their quality has achieved a very high level, and the task for the years to come will be to maintain this level.

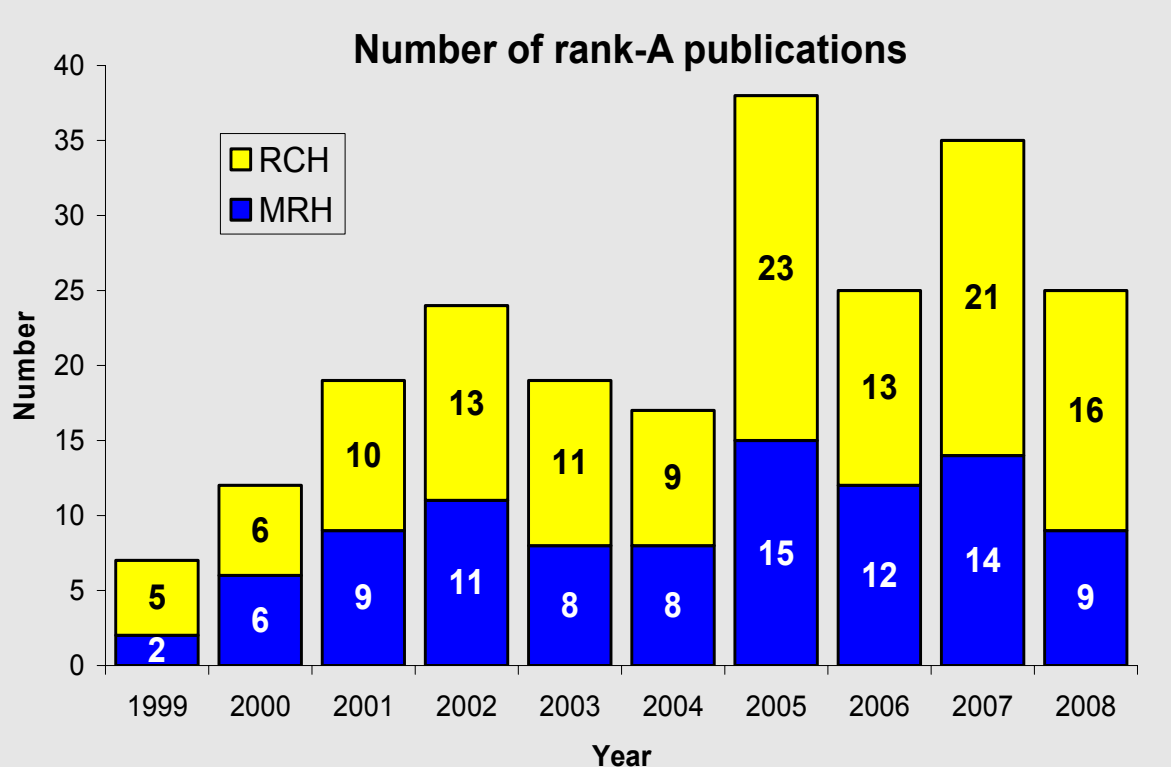

Fig. 2.4.1.
Number of publications per year, based on data collected in RCH and MRH by internal and external user groups. Note that only peer-reviewed articles in citation-indexed journals are listed.

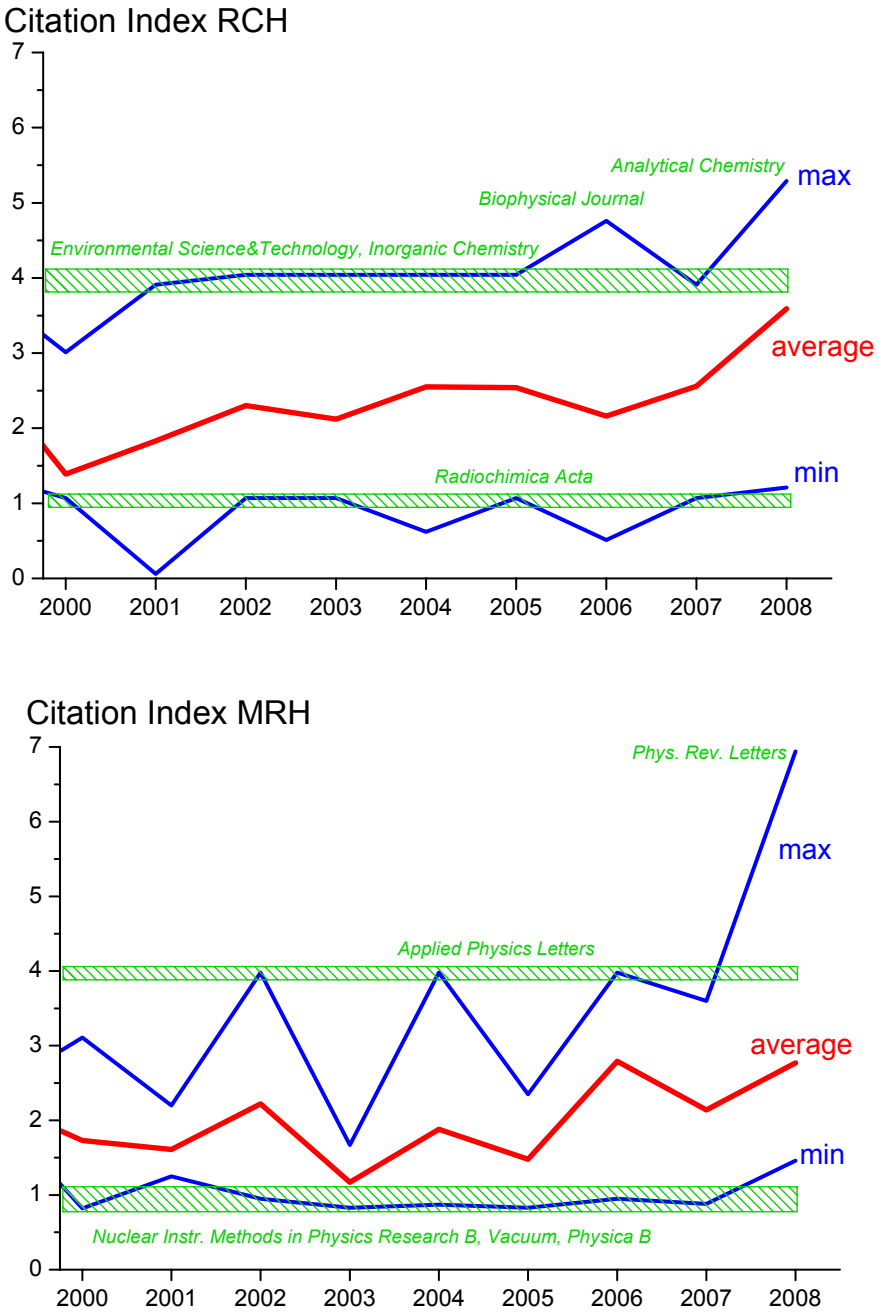

Fig. 2.4.2.
Citation indices of the articles listed in Fig. 2.4.1 and section 2.4.1. Top: RCH, bottom: MRH.

2.4.1. Publications in Radiochemistry

2007

Billard, I., Gaillard, C., and Hennig, C.
Dissolution of UO_2, UO_3 and of some lanthanide oxides in Bumim Tf_2N: effect of acid and water and formation of $UO_2(NO_3)_3$
Dalton Transactions (2007) 4214-4221

Charlet, L., Scheinost, A.C., Tournassat, C., Greneche, J.M., Géhin, A., Fernández-Martínez, A., Coudert, S., Tisserand, D., and Brendle, J.
Electron transfer at the mineral/water interface: Selenium reduction by ferrous iron sorbed on clay
Geochim. Cosmochim. Ac. **71** (2007) 5731-5749

Creamer, N.J., Mikheenko, I.P., Yong, P., Deplanche, K., Sanyahumbi, D., Wood, J., Pollman, K., Merroun, M.L., Selenska-Pobell, S., and Macaskie, L.E.
Novel supported Pd hydrogenation bionanocatalyst for hybrid homogeneous/heterogeneous catalysis
Catalysis Today **128** (2007) 80-87

El Aamrani, S., Gimenez, J., Rovira, M., Seco, F., Grive, M., Bruno, J., Duro, L., and de Pablo, J.
A spectroscopic study of uranium(VI) interaction with magnetite
Applied Surface Science **253** (2007) 8794-8797

Fillaux, C., Berthet, J.C., Conradson, S.D., Guilbaud, P., Guillaumont, D., Hennig, C., Moisy, P., Roques, J., Simoni, E., Shuh, D.K., Tyliszczak, T., Castro-Rodriguez, I., and Den Auwer, C.
Combining theoretical chemistry and XANES multi-edge experiments to probe actinide valence states
Comptes Rendus Chimie **10** (2007) 859-871

Funke, H., Chukalina, M., and Scheinost, A.C.
A new FEFF-based wavelet for EXAFS data analysis
J. Synchrotron. Radiat. **14** (2007) 426-432

Gaillard, C., Chaumont, A., Billard, I., Hennig, C., Ouadi, A., and Wipff, G.
Uranyl coordination in ionic liquids: The competition between ionic liquid anions, uranyl counterions and Cl^- anions investigated by EXAFS, UV-vis spectroscopies and molcular dynamics simulations
Inorg. Chem. **46** (2007) 4815

Ghabbour, E.A., Scheinost, A.C., and Davies, G.
XAFS studies of cobalt(II) binding by solid peat and soil-derived humic acids and plant-derived humic acid-like substances
Chemosphere **67** (2007) 285-291

Hennig, C.
Evidence for double-electron excitations in the L_3-edge x-ray absorption spectra of actinides
Physical Review B **75** (2007) 035120-1 - 035120-7

Hennig, C., Schmeide, K., Brendler, V., Moll, H., Tsushima, S., and Scheinost, A.C.
EXAFS investigation of U(VI), U(IV), and Th(IV) sulfato complexes in aqueous solution
Inorg. Chem. **46** (2007) 5882 - 5892

Ikeda, A., Hennig, C., Tsushima, S., Takao, K., Ikeda, Y., Scheinost, A.C., and Bernhard, G.
Comparative study of uranyl(VI) and -(V) carbonato complexes in an aqueous solution
Inorg. Chem. **46** (2007) 4212-4219

Jroundi, F., Merroun, M.L., Arias, J.M., Rossberg, A., Selenska-Pobell, S., and González-Muñoz, M.T.
Spectroscopic and microscopic characterization of uranium biomineralization in Myxococcus xanthus
Geomicrobiology Journal **24** (2007) 441-449

Martin, P., Grandjean, S., Valot, C., Carlot, G., Ripert, M., Blanc, P., and Hennig, C.
XAS study of $(U_{1-y}Pu_y)O^{-2}$ solid solutions
J. Alloy. Compd. **444** (2007) 410-414

Merroun, M., Rossberg, A., Hennig, C., Scheinost, A.C., and Selenska-Pobell, S.
Spectroscopic characterization of gold nanoparticles formed by cells and S-layer protein of Bacillus sphaericus JG-A12
Materials Science & Engineering C-Biomimetic and Supramolecular Systems **27** (2007) 188-192

Nedelkova, M., Merroun, M.L., Rossberg, A., Hennig, C., and Selenska-Pobell, S.
Microbacterium isolates from the vicinity of a radioactive waste depository and their interactions with uranium
Fems Microbiology Ecology **59** (2007) 694-705

Nikitenko, S.I., Hennig, C., Grigoriev, M.S., Le Naour, C., Cannes, C., Trubert, D., Bossé, E., Berthon, C., and Moisy, P.
Structural and spectroscopic studies of the complex $[BuMeIm]_2[UCl_6]$ in the solid state and in hydrophobic room temperature ionic liquid $[BuMeIm][Tf_2N]$
Polyhedron **26** (2007) 3136-3142

Opel, K., Weiss, S., Hubener, S., Zanker, H., and Bernhard, G.
Study of the solubility of amorphous and crystalline uranium dioxide by combined spectroscopic methods
Radiochim. Acta **95** (2007) 143-149

Servaes, K., Hennig, C., Billard, I., Gaillard, C., Binnemans, K., Görler-Walrand, C., and Van Deun, R.
Speciation of uranyl complexes in acetonitrile and in the ionic liquid 1-butyl-3-methylimidazolium bis(trifluoromethylsulfonyl)imide
European Journal of Inorganic Chemistry (2007) 5120-5126

Soldatov, A.V., Lamoen, D., Konstantinovic, M.J., Berghe, S.V.d., Scheinost, A.C., and Verwerft, M.
Local structure and oxidation state of uranium in some ternary oxides: X-ray absorption analysis
J. Solid State Chem. **180** (2007) 54-61

Tsushima, S.
Hydration and water-exchange mechanism of the UO_2^{2+} ion revisited: The validity of the "n + 1" model
J. Phys. Chem. A **111** (2007) 3613-3617

Tsushima, S., Rossberg, A., Ikeda, A., Müller, K., and Scheinost, A.C.
Stoichiometry and structure of uranyl (VI) hydroxo dimer and trimer complexes in aqueous solution
Inorg. Chem. **46,** (2007) 10819-10826

2008

Abrasonis, G., Scheinost, A.C., Zhou, S., Torres, R., Gago, R., Jimenez, I., Kuepper, K., Potzger, K., Krause, M., Kolitsch, A., Moller, W., Bartkowski, S., Neumann, M., and Gareev, R.R.
X-ray spectroscopic and magnetic investigation of C : Ni nanocomposite films grown by ion beam cosputtering
Journal of Physical Chemistry C **112** (2008) 12628-12637

Bosse, E., Den Auwer, C., Berthon, C., Guilbaud, P., Grigoriev, M.S., Nikitenko, S., Le Naour, C., Cannes, C., and Moisy, P.
Solvation of UCl_6^{2-} anionic complex by MeBu3N+, BuMe2IM+, and BuMeIm(+) cations
Inorg. Chem. **47** (2008) 5746-5755

Hennig, C., Ikeda, A., Schmeide, K., Brendler, V., Moll, H., Tsushima, S., Scheinost, A.C., Skanthakumar, S., Wilson, R., Soderholm, L., Servaes, K., Gorrler-Walrand, C., and Van Deun, R.
The relationship of monodentate and bidentate coordinated uranium(VI) sulfate in aqueous solution
Radiochim. Acta **96** (2008) 607-611

Hennig, C., Kraus, W., Emmerling, F., Ikeda, A., and Scheinost, A.C.
Coordination of a uranium(IV) sulfate monomer in an aqueous solution and in the solid state
Inorg. Chem. **47** (2008) 1634-1638

Hennig, C., Le Naour, C., and Den Auwer, C.
Double photoexcitation involving 2p and 4f electrons in L3-edge x-ray absorption spectra of protactinium
Physical Review B **77** (2008) 235102 1-6

Hennig, C., Servaes, K., Nockemann, P., Van Hecke, K., Van Meervelt, L., Wouters, J., Fluyt, L., Gorller-Walrand, C., and Van Deun, R.
Species distribution and coordination of uranyl chloro complexes in acetonitrile
Inorg Chem **47** (2008) 2987-2993

Ikeda, A., Hennig, C., Rossberg, A., Tsushima, S., Scheinost, A.C., and Bernhard, G.
Structural determination of individual chemical species in a mixed system by iterative transformation factor analysis-based x-ray absorption spectroscopy combined with UV-visible absorption and quantum chemical calculation
Analytical Chemistry **80** (2008) 1102-1110

Ikeda-Ohno, A., Hennig, C., Rossberg, A., Funke, H., Scheinost, A.C., Bernhard, G., and Yaita, T.
Electrochemical and complexation behavior of neptunium in aqueous perchlorate and nitrate solutions
Inorg. Chem. **47** (2008) 8294-8305

Kirsch, R., Scheinost, A.C., Rossberg, A., Banerjee, D., and Charlet, L.
Reduction of antimony by nano-particulate magnetite and mackinawite
Mineralogical Magazine **72** (2008) 185-189

Krepelova, A., Reich, T., Sachs, S., Drebert, J., and Bernhard, G.
Structural characterization of U(VI) surface complexes on kaolinite in the presence of humic acid using EXAFS spectroscopy
J Colloid Interf Sci **319** (2008) 40-47

Loyo, R.L.d.A., Nikitenko, S.I., Scheinost, A.C., and Simonoff, M.
Immobilization of selenite on Fe_3O_4 and Fe/FeC_3 ultrasmall particles
Environ. Sci. Technol. **42** (2008) 2451-2456

Montes-Hernandez, G., Fernández-Martínez, A., Charlet, L., Renard, F., Scheinost, A.C., and Bueno, M.
Synthesis of a Se^0/calcite composite using hydrothermal carbonation of $Ca(OH)_2$ coupled to a complex selenocystine fragmentation
Crystal Growth & Design **8** (2008) 2497-2504

Scheinost, A.C. and Charlet, L.
Selenite reduction by mackinawite, magnetite and siderite: XAS characterization of nanosized redox products
Environ. Sci. Technol. **42** (2008) 1984–1989

Scheinost, A.C., Kirsch, R., Banerjee, D., Fernandez-Martinez, A., Zaenker, H., Funke, H., and Charlet, L.
X-ray absorption and photoelectron spectroscopy investigation of selenite reduction by FeII-bearing minerals
Journal of Contaminant Hydrology **102** (2008) 228-245

Tsushima, S.
Hydrolysis and dimerization of Th^{4+} ion
Journal of Physical Chemistry B **112** (2008) 7080-7085

Vigier, N., Den Auwer, C., Fillaux, C., Maslennikov, A., Noel, H., Roques, J., Shuh, D.K., Simoni, E., Tyliszczak, T., and Moisy, P.
New data on the structure of uranium monocarbide
Chemistry of Materials **20** (2008) 3199-3204

2009

Livi, K.J.T., Senesi, G., Scheinost, A.C., and Sparks, D.L.
A microscopic examination of nanosized mixed Ni-Al hydroxide surface precipitates on pyrophyllite
Environ. Sci. Technol. **43** (2009) 1299–1304

Martin, P.M., Belin, R.C., Valenza, P.J., and Scheinost, A.C.
EXAFS study of the structural phase transition in the americium zirconate pyrochlore
J. Nucl. Mater. **385** (2009) 126–130

Rossberg, A., Ulrich, K.-U., Weiss, S., Tsushima, S., Hiemstra, T., and Scheinost, A.C.
Identification of uranyl surface complexes on ferrihydrite: Advanced EXAFS data analysis and CD-MUSIC modeling
Environ. Sci. Technol. **43** (2009) 1400–1406

Seco, F., Hennig, C., Pablo, J.d., Rovira, M., Rojo, I., Mart, V., Gimnez, J., Duro, L., Griv, M., and Bruno, J.
Sorption of Th(IV) onto iron corrosion products: EXAFS study
Environ. Sci. Technol. **43** (2009) 2825–2830

2.4.2. Publications in Materials Research

2007

Almtoft, K.P., Ejsing, A.M., Bøttiger, J. Chevallier, J., Schell, N., and Martins, R.M.S.
The dependence of the nanostructure of magnetron sputtered Cu-Ag alloy films on composition and temperature
*Journal of Materials Research **22** (2007) 1018*

Beckers, M., Schell, N., Martins, R.M.S., Mücklich, A., Möller, W., and Hultman, L.
Nucleation and growth of Ti_2AlN thin films deposited by reactive magnetron sputtering onto MgO (111)
*Journal of Applied Physics **102** (2007) 074916*

Cantelli, V., Borany, J. von, Mücklich, A., and Grenzer, J.
Influence of energetic ions and neutral atoms on the $L1_0$ ordering of FePt films
*Nuclear Instruments and Methods in Physics Research B **257** (2007) 406*

J. Cieslak, S.M. Dubiela, F. Eichhorn, M. Menzel and H. Reuther
Investigation of single-crystals of chromium implanted with ^{119}Sn-ions of various energies
*Journal of Alloys and Compounds **442** (2007) 235*

J. Cieslak, Th. Hahn, H. Metzner, J. Eberhardt, W. Witthuhn, J. Kräußlich, and F. Wunderlich
Epitaxial $CuIn_{1-x}Ga_xS_2$ on Si(111) ($0 \le x \le 1$): Lattice match and metastability
*Physical Review B **75** (2007) 245306.*

Höglund, C., Beckers, M., Schell, N., Borany, J. von, Birch, J., and Hultman, L.
Topotaxial growth of Ti_2AlN by solid state reaction in AlN / Ti(0001)multilayer thin films
*Applied Physics Letters **90** (2007) 174106.*

Kögler, R., Mücklich, A., Eichhorn, F., Schell, N., and Skorupa, W.
Praseodymium compound formation in silicon by ion beam synthesis
*Vacuum **81** (2007) 1318*

Kräußlich, J., Dubs, C., Lorenz, A., and Tinnemann, A.
In-plane lattice parameter determination of Zn:$LiNbO_3$ thin films epitaxially grown on x-cut $LiNbO_3$ substrates using x-ray diffraction methods
*Physica status solidi A **204** (2007) 2585*

Martins, R.M.S. , Schell, N., Silva, R.J.C. , Pereira, L. , Mahesh, K.K. and Braz Fernandes, F.M.
In-situ study of Ni–Ti thin film growth on a TiN intermediate layer by x-ray diffraction
*Sensors and Actuators B **126** (2007) 332 - 337*

Meduna, M., Novák, J., Bauer, G., Holý, V., Falub, C.V., Tsujino, S., and Grützmacher, D.
In situ investigations of Si and Ge interdiffusion in Ge-rich Si/SiGe multilayers using x-ray scattering
*Semiconductor Science and Technology **22** (2007) 4467*

Talut, G., Reuther, H., Zhou, S., Potzger, K., Eichhorn, F., and Stromberg, F.
Ferromagnetism in GaN induced by Fe ion implantation
*Journal of Applied Physics **102** (2007) 083909*.

Zhou, S., Potzger, K., Reuther, H., Kuepper, K., Skorupa, W., Helm, M., and Fassbender, J.
Absence of ferromagnetism in V-implanted ZnO single crystals
*Journal of Applied Physics **101** (2007) 09H109*

Zhou, S., Potzger, K., Reuther, H., Talut, G., Eichhorn, F., von Borany, J., Skorupa, W., Helm, M., and Fassbender, J.
Crystallographically oriented magnetic $ZnFe_2O4$ nanoparticles synthesized by Fe implantation into ZnO
*Journal of Physics D: Applied Physics **40** (2007) 964*

Zhou, S., Potzger, K., Mücklich, A., Eichhorn, F., Schell, N., Grötzschel, R., Schmidt, B., Skorupa, W., Helm, M., Fassbender, J., and Geiger, D.
Structural and magnetic properties of Mn-implanted Si
*Physical Review B **75** (2007) 085203*

2008

Martins, R.M.S., Schell, N., Mücklich, A., Reuther, H., Beckers, M., Silva, R.J.C., Pereira, L., and Braz Fernandes, F.M.
Study of graded Ni-Ti shape memory alloy film growth on Si(100) substrate
*Applied Physics A **91** (2008) 291 - 299*

Martins, R.M.S., Schell, N., Beckers, M., Silva, R.J.C., Mahesh, K.K., and Braz Fernandes, F.M.
Role of the substrate on the growth of Ni–Ti sputtered thin films
*Materials Science and Engineering A **481-482** (2008) 626-629*

Salditt, T., Krüger, S.P., Fuhse, C., and Bähtz, C.
High-transmission planar X-ray waveguides
*Physical Review Letters **100** (2008) 184801*

Zhou, S. Potzger, K., von Borany, J., Grötzschel, R., Skorupa, W., Helm, M., and Fassbender, J.
Crystallographically oriented Co and Ni nanocrystals inside ZnO formed by ion implantation and postannealing
*Physical Review B **77** (2008) 035209*

Zhou, S., Potzger, K., Talut, G., Reuther, H., von Borany, J., Grötzschel, R., Skorupa, W., Helm, M., Fassbender, J., Volbers, N., Lorenz, M., and Herrmannsdörfer, T.
Fe-implanted ZnO: Magnetic precipitates versus dilution
*Journal of Applied Physics **103** (2008) 023902*

Zhou,S., Potzger, K., Talut, G., von Borany, J., Skorupa, W., Helm, M., and Fassbender, J.
Using x-ray diffraction to identify precipitates in transition metal doped semiconductors
*Journal of Applied Physics **103** (2008) 07D530*

Zhou, S., Potzger, K., Talut, G., Reuther, H., von Borany, J., Grötzschel, R., Skorupa, W., Helm, M., and Fassbender, J.
Fe-implanted ZnO: Magnetic precipitates versus dilution
*Journal of Applied Physics **103** (2008) 023902*

Zhou,S., Talut, G., Potzger, K., Shalimov, A., Grenzer, J., Skorupa, W., Helm, M., Fassbender, J., Čižmár, E., Zvyagin, S.A., and J. Wosnitza, J.
Crystallographically oriented Fe nanocrystals formed in Fe-implanted TiO_2
*Journal of Applied Physics **103** (2008) 083907*

Zschech, E., Geisler, H., Rinderknecht, J., Schneider, G., Spolenak, R., Schmeisser, D.
Nano-Scale analysis using synchrotron-radiation: Applications in the semiconductor industry
*Current Nanoscience **4** (2008) 256-266*

2.5. Experiments

The following tables list all experiments which have been performed at the beamline, separated by end-station (RCH, MRH) and by type of experiment (in-house, ESRF, Actinet). Experiments with more than 18 shifts indicate that these experiments have been performed during several experimental runs and are part of long-term research programs.

2.5.1. List of RCH Experiments

RCH in-house experiments 2007

Number	Title	Proposer	Institution	Experimenter	Shifts
20-01-618	Spectroelectrochemical cell for in-situ XAS measurements of uranium solution species	Ch. Hennig, J. Tutschku, G. Geipel, A. Rossberg, G. Bernhard	FZD	Ch. Hennig, A. Rossberg A. Scheinost, H. Funke, A. Ikeda, M. Hesse	17
20-01-622	Chemical speciation of metals in shooting-range soils	A. Scheinost, Ch. Hennig, D. Vantelon, I. Xifra	FZD, ETHZ	A.Rossberg, Ch. Hennig, H. Funke	3
20-01-624	Speciation of Zn in rhizosphere soil	A. Scheinost, Ch. Hennig, A. Rossberg, H. Funke, A. Voegelin, S, Pfister	FZD, ETHZ	A. Scheinost, H. Funke, C. Hennig, A. Rossberg	11
20-01-625	Interaction between microorganisms and metals using EXAFS	M. Merroun, S. Selenska-Pobell, J. Raff, Ch. Hennig	FZD	M. Merroun, Ch. Hennig, A. Rossberg, A. Scheinost	3
20-01-638	X-ray absorption spectroscopy on gold nanoparticles formed by bacteria and their surface layer proteins	M. Merroun, S. Selenska-Pobell, A. Scheinost, Ch. Hennig	FZD	A. Rossberg, U. Jankowski, M. Merroun, A. Scheinost, Ch. Hennig, H. Funke , K. Deplanche	9
20-01-639	Investigation of U(V II)//U(V) carbonato complexes in aqueous solution by spectro-electrochemistry	Ch. Hennig, I. Grenthe, G. Palladino	FZD, KTH	CH. Hennig, A.. Ikeda, H. Funke, A. Rossberg, A. Scheinost	12
20-01-652	Reduction of Eu and Se by Fe(II) at the clay edge surface	A. Scheinost, L. Charlet, A. Gehin, C. Hennig	FZD LGIT Grenoble	A. Scheinost, C. Hennig, L. Charlet, A. Rossberg, R. Kirsch, H. Funke	12

RCH in-house experiments 2007 [cont.]

Number	Title	Proposer	Institution	Experimenter	Shifts
20-01-653	Uranyl sorption to clay minerals and analogues	A. Scheinost, Ch. Hennig, A. Rossberg, N. Baumann, Th. Arnold, V. Brendler	FZD	A. Scheinost, Ch. Hennig, H. Funke, A. Rossberg	9
20-01-656	EXAFS investigations of uranium species formed by monocellular and polycellular algae	A. Guenther, A. Rossberg, A. Scheinost	FZD	A. Rossberg, H. Funke, A. Guenther	9
20-01-657	EXAFS-investigations on U(IV) pseudocolloids	S. Weiss	FZD	C. Hennig, H. Funke, A. Scheinost, A. Rossberg	7
20-01-661	Interaction of uranium with bioligands produced by soil bacteria and with related model compounds using X-ray absorption spectroscopy	H. Moll, A. Rossberg	FZD	A. Rossberg, A. Scheinost, H. Funke, C. Hennig, M. Glorius	12
20-01-662	Investigation of chemical bonding structure and coordination of fullerene-like carbon-metal nanocomposite thin films by means of XANES and EXAFS	G. Abrasonis	FZD	G. Abrasonis, A. Scheinost, A. Rossberg	6
20-01-663	Coprecipitation of actinides with biogenic minerals: X-ray absorption spectroscopy characterization	M. Merroun	FZD	M. Merroun, A. Scheinost, H. Funke, C. Hennig, A. Rossberg, U. Jankowski	21
20-01-664	Structure of neptunium species in solution	C. Hennig, A. Ikeda	FZD	A. Ikeda, C. Hennig, A. Scheinost, H. Funke, A. Rossberg	19
20-01-665	Speciation of aqueous uranyl(VI) polymeric species using EXAFS spectroscopy	S. Tsushima, A. Rossberg, A. Scheinost	FZD	S. Tsushima, A. Rossberg, A. Scheinost, C. Hennig, H. Funke	3
20-01-666	Speciation of 4-fold uranyl(VI) hydrate by EXAFS spectroscopy	S. Tsushima, A. Rossberg, C. Hennig, A. Scheinost	FZD	S. Tsushima, A. Rossberg, A. Scheinost, C. Hennig, H. Funke	3
20-01-668	Abiotic antimony reduction by Fe(II) systems	A. Scheinost, R. Kirsch, L. Charlet	FZD, LGIT Grenoble	A. Scheinost, L. Charlet, R. Kirsch, H. Funke, A. Rossberg, C. Hennig, M. Hesse	18
20-01-670	Characterization of Mn speciation on clay minerals	D. Strawn	FZD, Univ. Idaho	D. Strawn, A. Scheinost	9

RCH ESRF experiments 2007

Number	Title	Proposer	Institution	Experimenter	Shifts
CH-2297	EXAFS spectro-electrochemical study of U(III), U(IV), U(V) and U(VI) chloro complexes in ionic liquids	C. Cannes, C. Le Naour, C. Hennig, P. Moisy	IPN Orsay	C. Le Naour, M. Sornein, V. Di Giandomenic	9
CH-2300	Se(IV) / Fe(II) on imogolites: sorption and redox processes	A. Fernandez-Martinez, G. Cuello, G. Roman-Ross, L. Charlet, F. Bardelli	ILL	A. Fernandez-Martinez, F. Bardelli, L. Charlet, G. Cuello, G. Roman-Ross, D. Tisserand,	11
CH-2303	Tc(IV) eigencolloid formation and characterization	A. Maes, E. Breynaert, C. Brugeman	KU Leuven	A. Maes, E. Breynaert	12
CH-2421	Neptunium and plutonium complexation by pentapeptide	C. Den Auwer, A. Jeanson, S. Coantic, C. Vidaud, P. Solari	CEA Marcoule	C. Den Auwer, A. Jeanson, V. Di Giandomenico S. Dahou, C. Le Naour, P. Solari, D. Guillaneux, C. Duffieux, C. Hubert	15
CH-2423	Free and silica-gel-bound tetraazamacrocycles as complexing agents of actinide cations: investigation of the solid-state coordination scheme	M. Meyer, A. Scheinost	CNRS Dijon	A. Scheinost, S. Faure, M. Meyer, H. Funke, C. Hennig, A.Rossberg	14
CH-2424	EXAFS study of the uranyl speciation in a new task specific ionic liquid	R. Van Deun, P. Nockemann	Uni Leuven	R. van Deun, D. Huys, P. Nockemann	9
EC-144	EXAFS study of neptunium(V) uptake by kaolinite	T. Reich, S. Amayri	Uni Mainz	T. Reich, S. Amayri, J. Drebert, M. Breckheim.	9
HS-3178	EXAFS/XANES investigation of plutonium and americium pyrochlores considered as targets for transmutation	R. Belin, J. Cambedou, P. Martin, P. Valenza, H. Palancher	CEA Cadar.	R .Belin, P. Valenza, A. Pieragnoli, P. Martin	9
MA-233	XAS study of uranium and plutonium local environment in (U,Pu)O2 solid solution: influence of the Pu/(U+Pu) ratio and of the synthesis method	P.Martin, H. Palancher, C. Robisson-Thomas, B. Arab-Chapelet, S. Grandjean, C. Valot	CEA Cadar.	P. Martin, C. Robisson-Thomas, N. Vigier, G. Leturcq, S. Costenoble, H. Mokhtari	12

RCH Actinet experiments 2007

Number	Title	Proposer	Institution	Experimenter	Shifts
20-01-639	Investigation of U(VI)/U(V) carbonato complexes in aqueous solution by spectro-electrochemistry	C. Hennig, I. Grenthe, G. Palladino, A. Scheinost	ROBL, KTH	C. Hennig, A. Rossberg, H. Funke, A. Scheinost, A. Ikeda	12
20-01-654	Solvation and complexation of uranium(VI) in room temperature ionic liquids (RTILs): Influence of the dissolved salt and of the RTIL composition	C. Gaillard, I. Billard	IRES	A. Ouadi, C. Gaillard	9
20-01-658	Studies of the Chemical Forms of Actinides and Fission Products Adsorbed on Nanocrystalline Magnetite	S. Nikitenko, A. Scheinost	CNRS Gradign.	S. Nikitenko	6
20-01-667	EXAFS study of Np(V) sorption onto montmorillonite	T. Reich, S. Dierking, B. Baeyens, R. Daehn, A. Scheinost	Uni Mainz	B. Baeyens, R. Daehn, S. Dierking, A. Scheinost, S. Amayri, J. Drebert, M. Myers	12

RCH in-house experiments 2008

Number	Title	Proposer	Institution	Experimenter	Shifts
20-01-639	Investigation of U(V II)//U(V) carbonato complexes in aqueous solution by spectro-electrochemistry	Ch. Hennig, I. Grenthe, G. Palladino	FZD, KTH	C. Hennig, K. Takao	9
20-01-652	Reduction of Eu and Se by Fe(II) at the clay edge surface	A. Scheinost, L. Charlet, A. Gehin, C. Hennig	FZD, LGIT Grenoble	A. Scheinost, C. Hennig, A. Rossberg, R. Kirsch, H. Funke	6
20-01-653	Uranyl sorption to clay minerals and analogues	A. Scheinost, Ch. Hennig, A. Rossberg, N. Baumann, Th. Arnold, V. Brendler	FZD	A. Scheinost, A. Rossberg	3
20-01-656	EXAFS investigations of uranium species formed by monocellular and polycellular algae	A. Guenther, A. Rossberg, A. Scheinost	FZD	A. Rossberg, M. Vogel	6

RCH in-house experiments 2008 [cont.]

Number	Title	Proposer	Institution	Experimenter	Shifts
20-01-661	Interaction of uranium with bioligands produced by soil bacteria and with related model compounds using X-ray absorption spectroscopy	H. Moll, A. Rossberg	FZD	H. Moll, A. Rossberg, C. Hennig, A. Scheinost, H. Funke, D. Banerjee	8
20-01-663	Coprecipitation of actinides with biogenic minerals: X-ray absorption spectroscopy characterization	M. Merroun	FZD	K. Deplanche, M. Merroun, H. Funke, A. Rossberg, C. Hennig, A. Scheinost, J.J. Ojeda	14
20-01-664	Structure of neptunium species in solution	C. Hennig, A. Ikeda	ROBL, FZD	C. Hennig, A. Scheinost, H. Funke, A. Rossberg, A. Ikeda, K. Takao, S. Takao, D. Banerjee	24
20-01-668	Abiotic antimony reduction by Fe(II) systems	A. Scheinost, R. Kirsch, L. Charlet	FZD, LGIT Grenoble	A. Scheinost, R. Kirsch, L. Charlet, H. Funke, A. Rossberg, C. Hennig	12
20-01-671	Studies on the coordination environments of UO_2^{2+} on gibbsite surface in the presence of natural ligands	T- Saito	Univ. of Tokyo	S. Takumi, S. Nagasaki, T. Hattori, K. Ishida	12
20-01-672	Comparative investigation of the uranium complexation by proteins by means of FT-IR and EXAFS spectroscopy	J.Raff, B. Li, H. Foerstend., C. Hennig, A. Rossberg, A. Scheinost	FZD	A. Rossberg, A. Scheinost, J. Raff, B. Li, H. Foerstend.	21
20-01-675	Investigation of the aqueous phase in the ternary sorption system uranium(VI), goethite, organic model compounds	A. Rossberg, A. Scheinost	ROBL	A. Rossberg, A. Scheinost, A. Ikeda, C. Hennig, H. Funke, D. Banerjee, C. Lucks	30
20-01-677	Selenium solid phase speciation in Boom Clay conditions	A. Maes	KU Leuven	A. Maes, S. Hertsens. A. Scheinost, E. Breynaert	12
20-01-678	EXAFS/XANES investigation of plutonium and americium pyrochlores considered as targets for transmutation	P. Martin, R. Belin, A. Scheinost, P. Valenza, H. Palancher	CEA Cadar., ROBL	R. Belin, P.Martin, E. Gavilan	9

RCH in-house experiments 2008 [cont.]

Number	Title	Proposer	Institution	Experimenter	Shifts
20-01-680	Identification of thioarsenate XAS spectra in liquid and solid samples	E. Suess, G. Bernhard, B. Merkel, B. Planer-Friedrich, W. Gezahegne	TU Freiberg	B. Planer-Friedrich. E. Suess, A. Scheinost, W. Gezahegne	9
20-01-681	Development of a 2nd generation spectro-electochemical cell for in situ electrolysis	C. Hennig, K. Takao, A. Scheinost	ROBL, FZD	C. Hennig, A. Scheinost	3

RCH ESRF experiments 2008

Number	Title	Proposer	Institution	Experimenter	Shifts
CH-2539	Uptake of neptunium and plutonium by topologically constraint peptides	C. Den Auwer, A. Jeanson, S. Coantic, P. Moisy	CEA Marcoule	C. Den Auwer, S. Dahou, C. Le Naour, A. Jeanson, M. Mendes, S. Petit	15
CH-2544	Hydration, hydrolysis and sorption of Sm^{3+} and Eu^{3+} in the interlayer space of the clay mineral	O. Sobolev, L. Charlet, G. Cuello, A. Scheinost	LGIT, ILL, ROBL	O. Sobolev	9
CH-2540	Reduction of uranium(VI) by adsorbed Fe(II) on clays and by structural Fe(II) in O_2, CO_2 free atmosphere	S. Chakrabor., F. Favre Boivin, L. Charlet, A. Scheinost	LGIT, ROBL	S. Chakrabor., D. Banerjee, A. Scheinost	9
EC-205	Uranium solid-phase speciation in presence of pyrite (FeS_2) at slightly alkaline conditions	C. Bruggeman N. Maes	SCK-CEN	C. Bruggeman S. Qerts, F. Raeymake.	12
EC-279	Adsorption of U(VI) onto FeS and its subsequent reduction	T. Behrends	Uni Utrecht	T. Behrends, V. Alexandrat., A. Scheinost, C. Hennig, D. Banerjee, P. Kleingeld	15
EC-363	EXAFS study of neptunium(V) sorption onto gibbsite	T. Reich, S. Amayri, T. Wu	Uni Mainz	T. Reich, S. Amayri, T. Wu, J. Drebert, D. Froehlich	9
CH-2739	Structure of uranyl-arsenate complexes sorbed on bentonite	E. Suess	TU Freiberg	W. Gezaheg., A. Scheinost, H. Funke	6
CH-2649	Investigation of the uranyl coordination chemistry in novel thiocyanate ionic liquid mixtures by U L_{III} EXAFS spectroscopy	R. Van Deun	KU Leuven	R. Van Deun, C. Hennig, D. Banerjee, A. Rossberg	9

RCH Actinet experiments 2008

Number	Title	Proposer	Institution	Experimenter	Shifts
20-01-644	Interaction of actinide cations with metalloproteins	C. Den Auwer, P. Moisy, C. Vidaud	CEA Marcoule	C. Filaux, A. Jeanson, C. Den Auwer, E. Galbis Fuster	3
20-01-658	Studies of the chemical forms of actinides and fission products adsorbed on nanocrystalline magnetite	S. Nikitenko, A. Scheinost	CNRS, ROBL	T. Chave, A. Scheinost, S. Nikitenko	9
20-01-659	Actinide selective recognition by bio mimetic molecules	C. Den Auwer, A. Jeanson, S. Coantic, V. di Giandomenico	CEA Marcoule	T. Dumas, G. Dupouy, X. Crozes V. di Giandomenico	12
20-01-667	EXAFS study of Np(V) sorption onto montmorillonite	T. Reich, S. Dierking, B. Baeyens, R. Daehn, A. Scheinost	Uni Mainz, PSI, ROBL	T. Reich, S. Amayri, J. Drebert, B. Baeyens, R. Daehn	15
20-01-673	Investigations of Am(III) and U(VI) sorption on clay minerals in presence of carbonate	M. Marques Fernandes, B. Baeyens, R. Daehn	PSI	B. Baeyens, M. Marques Fernandes, R. Daehn. N. Mace, A. Kitamura	18
20-01-674	EXAFS investigations of U(VI) uptake by cementitious materials	N. Mace, R. Daehn, E. Wieland, J. Tits, D. Kunz	PSI	N. Mace, R. Daehn, J. Tits, D. Kunz	18
20-01-676	Reduction of uranium(VI) by adsorbed Fe(II) on clays and by structural Fe(II) in smectites in O_2 and CO_2 free atmosphere	S. Chakrabor., A. Scheinost	LGIT Grenoble ROBL	S. Chakrabor. D. Banerjee, A. Scheinost	11

2.5.2. List of MRH Experiments

MRH in-house experiments 2007

Number	Title	Proposer	Institution	Experimenter	Shifts
20-02-645	XRD and GISAXS investigations on ion beam induced Si surface ripples	J. Grenzer	FZD	J. Grenzer A. Keller C. Baehtz	21
20-02-642	Thermal expansion coefficient of lateral nanostructures in semiconductor multilayers	U. Pietsch, B. Brüser, V. Gottschalch	Uni Leipzig, Uni Siegen	S. Grigorian, B. Brüser, J. Grenzer	15
20-02-643	Materials Characterization for DRAM-Trench-Technology	J. von Borany, S. Teichert, F. Eichhorn	FZD, Qimonda	S. Teichert, L. Wilde, J. von Borany, J. Krueger	15
20-02-647	Wafer-bonded x-ray waveguides	T. Salditt	Uni Göttingen	T. Salditt, S. Krueger	18
20-02-648	SR-μ-XRD stress measurements of ultra low-k dual damascene inlaid copper interconnect structures at temperatures between RT and 500°C	J. Rinderkn., H. Prinz	AMD	H. Prinz, J. Rinderkn., I. Zienert	36
20-02-649	In-situ x-ray diffraction during sputter deposition of V-Al-N MAX-phase thin films	M. Beckers	Uni Linköping	M. Beckers	15
20-02-650	Single phase formation of TM implanted reduced ZnO	S. Zhou	FZD	S. Zhou, J. Grenzer	6
20-02-651	Real-time evolution of ZnO:Al thin film structure and electrical properties during annealing	N. Shevchen., A. Rogozin, M. Vinnichen.	FZD	N. Shevchen., A. Rogozin	18
20-02-652	Investigation of the amorphisation and recrystallisation of sputter induced nanoscale surface ripples on Si(100) by surface sensitive X-ray scattering	J. Grenzer, A. Keller, S. Facsko	FZD	J. Grenzer, A. Keller, A. Hanisch, C. Baehtz, A. Biermanns	30
20-02-653	Micro focusing with capillary optics and/or KB Mirror systems at ROBL	C. Baehtz	ROBL	C. Baehtz, A. Scheinost	21
20-02-654	Single phase formation of TM implanted reduced ZnO and structural investigation of Fe implanted MgO and YSZ crystals	S. Zhou	FZD	S. Zhou, A. Shalimov	15
20-02-657	Thermal behaviour of Fe and Ni thin film onto Si	C. Baehtz, G. Abrasonis	ROBL, FZD	C. Baehtz, N. Jeutter	6
20-01-669	EXAFS and XANES investigations on transition metal implanted wide band gap materials	J. Grenzer, K. Potzger, G. Brauer	FZD	J. Grenzer, G. Talut, R. Grynszpan	15

MRH ESRF experiments 2007

Number	Title	Proposer	Institution	Experimenter	Shifts
HS-3291	Structure stability of short-period GaAs/AlGaAs and AlInAs/InGaAs superlattices	J. Gaca, K. Mazur, M. Wojcik	ITME Poland	J. Gaca, K. Mazur, M. Wojcik	9
HS-3443	In-situ x-ray scattering during formation of MAX phase $(V,Cr)_2AlN$ thin films by reactive co-sputtering and solid-state reaction	M. Beckers	IFM-Linköping	M. Beckers, J. Lauridsen, F. Eriksson	18
MA-232	Ion irradiation of Ni-Ti thin films	F.M. Braz Fernandes, N. Schell, R. Martins, K. Mahesh	CENIMAT, Campus FCT/UNL, Monte da Caparica, GKSS	C. Baehtz, T. Slobodskyy, J. von Borany, F. Braz Fernandes, R. Cordeiro Silva, N. Schell, R. Martins	18
SI-1518	Lattice parameter determination of structured Zn:$LiNbO_3$ thin films	J. Kraeusslich, O. Wehrhan, C. Dubs, K. Goetz	Uni Jena	J. Kraeusslich, I. Uschmann, U. Zastrau,	18
SI-1616	In-situ high-temperature reflectivity study of Fe/Pt multilayers	N. Zotov	CAESAR	N. Zotov, J. von Borany, J. Feydt	11
SI-1617	Interdiffusion studies in $Si_{(1-x)}Ge_x$ alloys with high Ge content by x-ray diffraction	M. Meduna, P. Mikulik, G. Bauer, E. Wintersb. D. Gruetzm.	Uni-Masaryk, Uni-Linz, FZ-Jülich	O. Caha, M. Meduna, M. Keplinger	18

MRH in-house experiments 2008

Number	Title	Proposer	Institution	Experimenter	Shifts
20-02-656	Investigation of carbon encapsulated transition metal nanoparticles by the means of GISAXS	G. Abrasonis, G. Kovacs	FZD, MFA KFKI Hungary	G. Kovacs, M. Berndt, A. Martinavic., G. Abrasonis	9
20-02-658	In-situ growth of Si NC´s out of a SiO_x/SiO_2 multilayer structure	N. Jeutter, C. Baehtz	ROBL	J. von Borany, M. Zschintz.	36
20-02-660	SR-µ-XRD stress measurements of ultra low-k vs. low-k dual damascene inlaid copper interconnect structures with different line widths at temperatures between RT and 500°C	J. Rinderkn., H. Prinz, I. Zienert	AMD	J. Rinderkn. H. Prinz, I. Zienert	18
20-02-661	In-situ study of oscillations during epitaxial and non-epitaxial thin film growth studied by specular and diffuse x-ray scattering	M. Beckers, C. Baehtz	Linköping Univ, ROBL	F. Eriksson, M. Beckers	18
20-02-662	Investigation of Fe and Pt implanted MgO and YSZ crystals	A. Shalimov	FZD	A. Shalimov, G. Talut	9
20-02-663	Spinodal decomposition and formation and structural properties of transition metal clusters	J. Grenzer	FZD	J. Grenzer, D. Buerger, G. Talut	8
20-02-664	Characterization of x-ray waveguides optimized for high transmission	T. Salditt	Uni Göttingen	H. Neubauer, T. Salditt, M. Tolkiehn, S. Krueger	9
20-02-665	In-situ structural investigations of the L10 ordering in FePt layers during magnetron sputtering	V. Cantelli	FZD	J. von Borany, V. Cantelli	9
20-02-666	In-situ XRD/XRR of thin film catalysts during carbon nanotube growth	C.T. Wirth, C. Bähtz	Univ. Cambrid., FZD	C.T. Wirth, C. Bähtz	9
20-02-670	Optical properties of planar and lithographic x--ray waveguides	T. Salditt	Uni Göttingen	T. Salditt, S. Krueger, H. Neubauer	12
20-02-669	In situ studies of recrystallization and phase transformation in ZnO:Al thin films during annealing	N. Shevchen.	FZD	N.Shevchen., A. Rogozin	12
20-02-671	In-situ XRD/XRR of thin film catalysts during carbon nanotube growth	C. Baehtz, S. Hofmann	ROBL, Uni Cambrid.	C. Baehtz, T. Wirth, C.Esconjaur.	21
20-02-672	Structural analysis of Mn implanted Ge by X-ray diffraction	S. Zhou	FZD	S. Zhou, A. Shalimov, A. Kanjilal,	12
20-02-674	GeO_x-SiO_2 superlattice structures on oxide Surfaces	N. Jeutter, M. Zschintz.	ROBL FZD	N. Jeutter, J. von Borany, M. Zschintz.	15

MRH ESRF experiments 2008

Number	Title	Proposer	Institution	Experimenter	Shifts
MA-419	In situ study of nanostructured NiTi shape memory alloys during annealing after severe plastic deformation	F. Braz-Fernandes, K. Mahesh	Cenimat	R. Martins, J. von Borany, K. Mahesh, R. Silva Cordeiro, F. Braz Fernandes	15
SI-1711	In-situ evolution of phase composition and internal growth stresses in nanostructured oxide layers grown on iron aluminides	H. Pinto, A. Pyzalla, P. Paiva Brito	MPI Düsseldorf	P. Paiva Brito, H. Pinto, D. Cardinali, C. Barbatti	21
MA-644	XRD study of nano glass--ceramic powders	C. Eisenschm.	Uni Halle	M. Hanke, C.Eisenschm. B. Henke	12
HS-3586	Structural investigation of metallic nanoclusters in wide band gap semiconductors	D. Novikov, B. Walz	Hasylab	D. Novikov, B. Walz, J. Grenzer, Georg Talut	18
HS-3741	Influence of nitrogen vacancies on phase separation patterns in ternary nitrides	M. Beckers	IFM	C. Hoglund, M. Beckers	21

3. Experimental Reports

3.1. Experimental Reports Radiochemistry

ROBL-CRG	**Experiment title:** Spectroelectrochemical cell for in situ XAS measurements of uranium solution species	**Experiment number:** 20-01-618
Beamline: BM 20	**Date of experiment:** from: 31. 01. 07 to: 03. 02. 07; 16. 05. 07 to 17. 05. 07; 02. 11. 07 to 03. 11. 07	**Date of report:** 24.3.2009
Shifts:17	**Local contact(s):** Christoph Hennig	*Received at ROBL:*
Names and affiliations of applicants (* indicates experimentalists): Christoph Hennig*, Atsushi Ikeda-Ohno*, K. Takao*, G. Geipel, J. Tutschu, G. Bernhard, A.C. Scheinost*		

Actual, the speciation and complex formation of U(IV) in sulfuric media is not well understood. The current NEA thermodynamic database reports only two sulfate species, USO_4^{2+} and $U(SO_4)_2(aq)$. This was the motivation to use a spectro-electrochemical cell to perform *in situ* EXAFS measurements under anoxic conditions while and maintaining uranium in reduced oxidation state. Figure 1, left side, shows the FT of EXAFS spectra of 50 mM U(IV) in sulfate media with increasing $[SO_4]^{2-}$ at pH 1.

The pure U(IV) hydrate is coordinated by nine water molecules with a U-O distance of 2.40 Å. The Fourier transformed spectrum of U(IV) sulfate comprises two additional peaks at 3.08 Å and 3.67 Å, indicative of bidentate and monodentate sulfate groups, respectively. Figure 1, right side, shows the coordination number N_{Sbid} and N_{Smon} as a function of the sulfate concentration. The coordination number N_{Sbid} increases, whereas N_{Smon} decreases with increasing $[SO_4^{2-}]$. Hence, with increasing sulfate concentration the bidentate coordination becomes more dominant. In consequence, U(IV) in acidic solutions with high sulfate concentration can be coordinated by 4 and 5 SO_4^{2-} molecules. EXAFS can provide the coordination number and the type of sulfate coordination, but not the spatial arrangement of the ligands.

Therefore, in further experiments, where the pH value has been restricted to 1.5, single crystals have been grown from this solution with the aim to preserve the solution species in the crystal structure [1]. The obtained compound $Na_{1.5}(NH_4)_{4.5}[U(SO_4)_5{\cdot}H_2O]{\cdot}H_2O$ crystallizes in the triclinic space group $P\bar{1}$ with two $[U(SO_4)_5{\cdot}H_2O]^{6-}$ units in the unit cell. In this structure U(IV) is coordinated by 2 monodentate and 3 bidentate sulfate ions and one water molecule. This coordination may represent the coordination geometry of the solution species. The high coordination numbers of 4 and 5 sulfate groups which have been observed can count for a high solubility and stability of U(IV) sulfate in aqueous solution which may enforce the migration of uranium in an low pH environment.

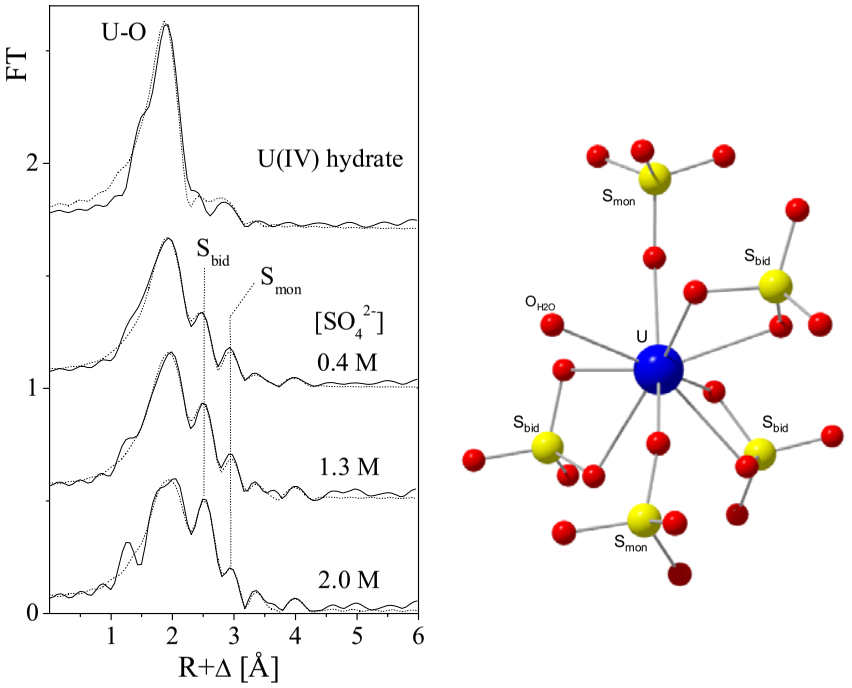

Fig. 1: Left side: Fourier transform of U L_3-edge k^3-weighted EXAFS data of U(IV) hydrate and sulfato species. Right side: Coordination of the $[U(SO_4)_5H_2O]^{6-}$ unit.

[1] Hennig, C., Kraus, W., Emmerling, F., Ikeda, A., Scheinost, A.C. Coordination of a uranium(IV) monomer in aqueous solution and in solid state *Inorg. Chem.* **47** (2008) 1634-1638.

ROBL-CRG	**Experiment title:** Investigation of U(VI)/U(V) carbonato complexes in aqueous solution by spectro-electrochemistry	**Experiment number**: 20-01-639
Beamline: BM 20	**Date of experiment**: from: 13. 04. 07 to: 17.04. 07; 03. 12. 08 06. 12. 08	**Date of report**: 24.3.2009
Shifts: 21	**Local contact(s)**: Christoph Hennig	*Received at ROBL:*
Names and affiliations of applicants (* indicates experimentalists): Atsushi Ikeda-Ohno*, Christoph Hennig*, K. Takao*, I. Grenthe, G. Palladino, A.C. Scheinost*		

The carbonato complex of uranium in aqueous solution is due to its good solubility one of the most important species for the migration study on nuclear waste repositories. Although uranium can change its oxidation state from U(III) to U(VI) in aqueous solution, only U(VI) and U(IV) are dominant species under subsurface conditions. U(V) is in absence of strong ligands metastable, but it may play an importand role if the solution undergoes a change in the redox condition. However, reliable information about the structure of uranyl(VI)- and uranyl(V) carbonato complexes is still missing. Hence, we have investigated the structure of these uranyl carbonato complexes in aqueous solution by EXAFS spectroscopy.

The uranyl(V) carbonate species is extremely sensitive to O_2 and reoxidezes promptly. Therefore, the uranyl(V) carbonate sample was placed in a glass cuvette under dry N_2 atmosphere in a glove box (O_2 concentration in the glove box was less than 1 ppm). The cuvette was then sealed up by hot melting. The sealed uranyl(V) sample was confirmed to be stable at least for two weeks by successive UV-visible absorption measurements, indicating that the measured XAFS spectrum for the uranyl(V) sample comprises the information only for the uranyl(V) carbonate species. Fig. 1 shows the Fourier transforms (FTs) of the U L_{III}-edge EXAFS spectra for uranyl(VI)- and uranyl(V) carbonate species. It is obvious that both uranyl(VI)- and uranyl(V) ions form a bidentate-coordinated tricarbonato complex, $[UO_2(CO_3)_3]^{n-}$ (n = 4 for uranyl(VI) and 5 for uranyl(V)), in the present basic Na_2CO_3 solution. As a result of the reduction of U(VI) to U(V), U-O_{ax} and U-O_{eq} distances become 0.10 and 0.06 Å longer, respectively. Because the ligand arrangement is unchanged, the changes of the bond length is affected only by the charge difference of uranium. Additionally, we succeeded in obtaining the detailed structural information about the outer coordination sphere. Surprisingly, the U-O_{dist} distances show a relative small difference. These structural parameters are in good agreement with the results by DFT quantum calculation, assuring the validity of our EXAFS results.

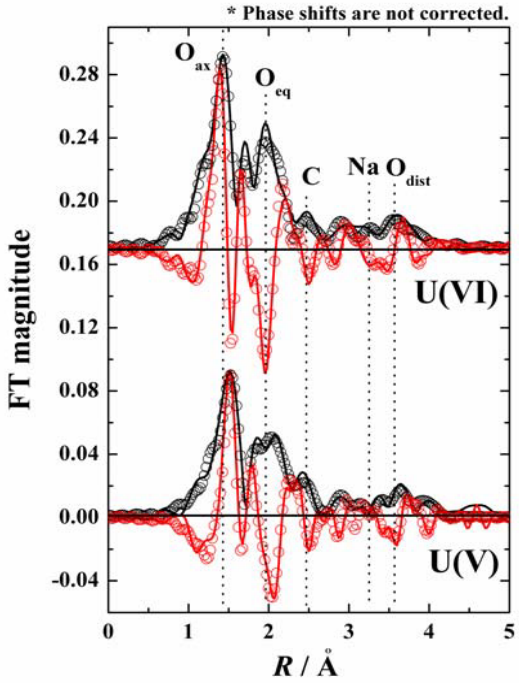

Fig. 1: Fourier transforms of U L_{III}-edge EXAFS for uranyl(VI)- and uranyl(V) carbonate species in 1.4 M Na_2CO_3 solution: -; experimental data, o; theoretical curve fit, black-colored data; FT magnitude, red-colored data; imaginary part

Ikeda, A., Hennig, C., Tsushima, S., Takao, K., Ikeda, Y., Scheinost, A.C., Bernhard, G. Comparative study of uranyl(VI) and -(V) carbonato complexes in an aqueous solution *Inorg. Chem.* **46** (2007) 4212-4219.

ROBL-CRG	**Experiment title:** Interaction of actinide cations with metalloproteins	**Experiment number:** 20-01-644
Beamline: BM 20	**Date of experiment:** from: 30/06/2008 to: 01/07/08	**Date of report:** 27/11/2008
Shifts: 3	**Local contact(s):** C. Hennig	*Received at ROBL:*

Names and affiliations of applicants (* indicates experimentalists):

C. Den Auwer* CEA Marcoule, DEN/DRCP/SCPS, Bagnols sur Cèze, Fr
D. Guillaumont*
A. Jeanson*
Ph. Moisy
C. Vidaud CEA Marcoule, DSV/SBTN, Bagnols sur Cèze, Fr

Report:

Transferrins are monomeric glycoproteins of about 80 kDa with a single polypeptide chain of 670-700 amino acids, used for the solubilization, sequestration, and transport of ferric iron. However, they can accommodate a wide variety of other metal ions, including most of the first row transition elements, several of the second and third rows, group 13 metal ions, lanthanides and actinides [1]. It should be noted that transferrins have a strong preference for cations with a high positive charge. The polypeptide chain is first of all folded into two globular lobes, representing the N-terminal and C-terminal halves of the molecule. The two lobes are joined by a short connecting polypeptide. Each lobe contains a single iron binding site, and each has essentially the same folding. It is composed of two separately folded domains, which confers the protein a great flexibility. When Fe(III) is complexed in a site of transferrin, the lobe is closed, as its two domains draw nearer. Target organs' cells of transferrin possess membrane receptors which selectively bind the diferric form of transferrin (holotransferrin), where both lobes are closed, to the detriment of its free form (apotransferrin), fully open.

A few Extended X-ray Absorption Fine Structure (EXAFS) studies of transferrins have already been carried out, mainly by Garrat *et al*. [2]. These studies, undertaken with ovotransferrin and serum transferrin lead to a coordination number of six low-Z ligands with bond distances of 1.9-2.1 Å, consistent with X ray crystallography studies. Harris *et al.* [3] have studied thorium(IV) complexation with transferrin, with nitrilotriacetic acid (NTA) as a synergistic anion, using a difference ultraviolet spectroscopy method. They showed that at physiological pH, transferrin binds two thorium ions at non-equivalent sites. Complexation of plutonium(IV) with transferrin has also been confirmed [4]. Although UV difference spectra are equivocal, it seems likely that two Pu(IV) are bound. However, *in vitro* studies have shown that Pu(IV) apparently does not induce the closure of the transferrin lobes, and that $Pu(IV)_2$-Tf was not recognised by membrane receptors of transferrin of liver cells [5].

Although the EXAFS spectrum of holotransferrin has been reported in the literature as stated above, no complete description of the environment has been provided in aqueous phase yet. Study at the molecular level of the complexation of actinide(IV) by apotransferrin is also lacking. This is the purpose of this project (see also experimental report 06-Sep-05) to investigate the complexation of $An(IV)NTA_2$ molecules by apotransferrin (NTA = nitrilotriacetic acid), where NTA is a protecting ligand against hydrolysis.

Our results on the structure in solution of the iron binding site in holotransferrin are reported in reference [6]. Best EXAFS model for data fitting was deduced from a screening of the Protein Data Bank over all the crystallographic structures of transferrin proteins. They reflect a distorded octahedral polyhedron has suggested by average of the crystal structures reported in the PDB.

We have also investigated the influence of the actinide cation (from Th to Pu) on the actinide(IV)/transferrin complex [7]. Various theoretical models were used and combined to the EXAFS data to obtain a possible schematic view of the actinide binding site.

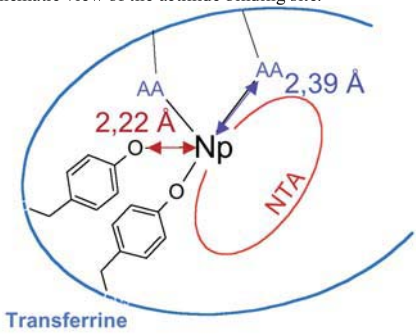

Fig. 1 : schematic possible structure of the neptunium/transferrein complex, one lobe. Distances were obtained from EXAFS fits.

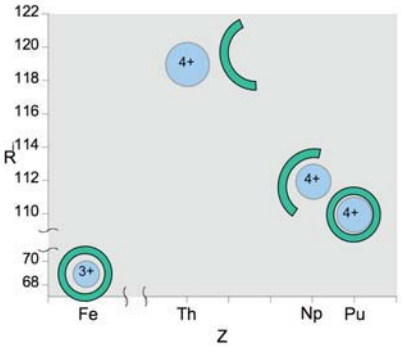

Fig. 2 : conformation of the transferrin lobe from EXAFS data and neutron scattering. Z = cation atomic number; Ri = cation ionic size; circle = close lobe, arc = open lobe.

Figure 1 shows one possible schematic view of the actinide environment in one of the two lobes (both lobes are considered here identical). Similar metric parameters where obtained with EXAFS for Np and Pu. Np(IV) and Pu(IV) form stable complexes with an increase in complexation percentage from pH = 6.5 to 7.5, the maximum being at physiological pH. Surprisingly, in our experimental condition, Th(IV) is never complexed by apotransferrin and stays in the $Th(IV)NTA_2$ form in solution. Complementary neutron small angle scattering measurements have also been carried out and suggest a change in the protein tertiary structure from Np to Pu (see Figure 2). This very promising result should how be confirmed by further neutron measurements. All these results will be described in detail in an incoming paper.

[1] E. N. Baker, *Advances in inorganic chemistry* (1994), **41**, 389.
[2] R. C. Garratt, R. W. Evans, S. S. Hasnain, P. F. Lindley, *Biochem. J.* (1986), **233**, 479.
[3] W. R. Harris, C. J. Carrano, V. L. Pecoraro, K. N. Raymond, *J. Am. Chem. Soc*. (1981), **103**, 2231.
[4] H. Lee, P. J. Sadler, H. Sun, *Eur. J. Biochem.* (1996), **242**, 387.
[5] D. M. Taylor, A. Seidel, F. Planas-Bohne, U. Schuppler, M. Neu-Müller, R. Wirth, *Inorg. Chim. Acta* (1987), **140**, 361.
[6] A. Jeanson, C. Den Auwer, P. Moisy, C. Vidaud, *OECD-NEA Proceedings on Speciation, Techniques and Facilities for Radioactive Materials at Synchrotron Light Sources* n°6288 (2007), 235-247.
[7] PhD thesis, A. Jeanson, *Interaction des actinides avec les acides aminés : du peptide à la protéine* Paris XI University, October 2008.

ROBL-CRG	**Experiment title:** complexation of uranium(VI) in room temperature ionic liquids	**Experiment number**: 20-01-654
Beamline: BM 20	**Date of experiment**: from: 27/06/2007 to: 30/06/08	**Date of report**: 04/2008
Shifts: 6	**Local contact(s)**: Dr. Christoph Hennig	*Received at ROBL:*
Names and affiliations of applicants (* indicates experimentalists): C. Gaillard*, I. Billard, A. Ouadi* Institut Pluridisciplinaire Hubert Curien, Chimie Nucléaire, Strasbourg, France.		

Report:

The aim of this experiment is to characterize the stoechiometry and structure of uranyl-nitrato complexes in a room temperature ionic liquid, C_4mimTf_2N (1-methyl-3-butylimidazolium$^+$, Tf_2N^- = $(CF_3SO_2)_2N^-$), as a function of the nitrate/uranyl ratio (from 0 to 4) and as a function of the nature of the uranyl salt. Nitrate ligands were chosen because they are of interest in the frame of the nuclear cycle reprocessing and a previous study has shown unexpected uranyl-nitrates interaction in RTIL [1]. EXAFS was coupled to UV-visible spectroscopy, the samples being measured by both techniques. Two uranyl salts used were uranyl triflate ($UO_2(CF_3SO_3)_2$) and $UO_2(Tf_2N)_2$, in order to check a possible influence of the uranyl counteranion on complexation [2]. Nitrates were introduced as tetrabutylammonium-NO_3. Figure 1 displays the EXAFS for $UO_2(Tf_2N)_2$ solutions, as a function of the nitrate concentration. Addition of nitrates entails notable changes on spectra, as a sign of the uranyl complexation to nitrates. Fit results (table1) show that in every case the complexation is total, leading to the formation of respectively $UO_2(NO_3)^+$, $UO_2(NO_3)_2$ and $UO_2(NO_3)_3^-$ species. The same results are obtained for solutions in which uranyl was introduced as the triflate salt. These experiments show that in ionic liquids, and contrary to what happens in water, nitrates are strong ligands to uranyl, which is confirmed by the fact that the same results are obtained using uranyl triflate and uranyl-Tf_2N salts. The same behaviour was observed in organic solvents (acetonitrile), the structure of the formed species being identical [3].

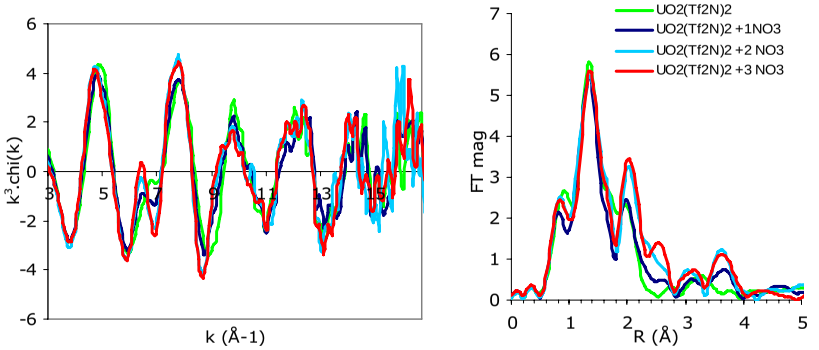

Figure 1: EXAFS spectra and their corresponding Fourier transforms of $UO_2(Tf_2N)_2$ solutions in C_4mimTf_2N for different $[NO_3^-]/[UO_2^{2+}]$ ratio: 0, 1, 2, 3.

$[NO_3^-]/[UO_2^{2+}]$	shell	N	R (Å)	σ^2 (Å²)	Rfactor
1	O_{axial}	2	1.75	0.002	0.02
	$O_{equatorial}$	4.7	2.45	0.008	
	N	0.9	2.92	0.003	
	O_{distal}	0.9	4.16	0.003	
2	O_{axial}	2	1.76	0.002	0.02
	$O_{equatorial}$	5.9	2.47	0.008	
	N	2.3	2.92	0.003	
	O_{distal}	2.3	4.16	0.006	
3	O_{axial}	2	1.76	0.002	0.01
	$O_{equatorial}$	5.9	2.47	0.007	
	N	2.8	2.92	0.003	
	O_{distal}	2.8	4.15	0.006	

Table 1: Fit results for $UO_2(Tf_2N)_2$ solutions in C_4mimTf_2N, as a function of the nitrates concentration.

[1] I. Billard, C. Gaillard, C. Hennig, Dalton Trans., 2007, 4214.
[2] C. Gaillard, A. Chaumont, I. Billard, C. Hennig, A. Ouadi, G. Wipff, Inor. Chem., 2007, 46, 4815.
[3] A. Ikeda, C. Hennig, A. Rossberg, S. Tsushima, A. Scheinost, G. Bernhard, Anal. Chem., 2008, 80, 1102.

ROBL-CRG	**Experiment title:** EXAFS investigations of uranium species formed by monocellular and polycellular algae	**Experiment number:** 20 - 01 - 656
Beamline: BM 20	**Date of experiment:** from: 23/01/07 to: 26/01/07; from: 06/12/08 to: 08/12/08	**Date of report:** 23/03/09
Shifts: 15	**Local contact(s):** André Roßberg	*Received at ROBL:*

Names and affiliations of applicants (* indicates experimentalists):
A. Günther[1], M. Vogel*[1] A. Roßberg*[2], A. Scheinost*[2], C. Hennig*[2], H. Funke*[2]
[1]Forschungszentrum Dresden-Rossendorf e.V., Institute for Radiochemistry, P.O. Box 510119, 01314 Dresden, Germany
[2]ESRF-ROBL/CRG, Avenue des Matryrs, B.P. 220, 38043 Grenoble Cedex, France

Report:

Experimental

The aim of this study is to determine the structural parameters of the formed uranyl complex species in inactive and active monocellular *Chlorella vulgaris* cells in the pH range from 3 to 7. The stored algal biomass was re-suspended in 0.9% $NaClO_4$ solution and contacted 72 h with $UO_2(ClO_4)_2$ (inactive cells). For the experiments with active algal cells the biomass was contacted 96 h with uranium containing mineral medium. After separation of the washed algal biomass by centrifugation the fresh samples were put into polyethylene sample holder surrounded with Kapton tape. The U L_{III}-edge spectra were measured in fluorescence mode at room temperature and at 30K using a closed-cycle He-cryostat. The EXAFS spectra were analyzed using the suite of program EXAFSPAK /1/. The theoretical scattering phases and amplitudes were calculated by using x-ray structural data of meta-autunite with the scattering code FEFF8 /2/.

Results

Figure 1 shows the raw U L_{III}-edge k^3-weighted EXAFS spectra and their corresponding Fourier transforms (FT) of uranium containing inactive algal cells (samples A-C) measured at room temperature and at 30 K after shock freezing of the samples as examples. The spectra of algal cells contaminated at pH 3, 5 and 6 and measured at RT (A1, B1, C1) are well reproduced by taking only backscattering of O atoms into account. In the case of U(VI)-algae species formed at pH 3 we obtained for the axial oxygen a radial U-O_{ax} distance of 1.77 Å and for the equatorial oxygen a radial U-O_{eq} distance of 2.38 Å. At pH 5 and 6 the U-O_{eq} signal is splitted in two different U-O_{eq} distances (U-$O_{eq(1)}$= 2.27 or 2.28 Å and U-$O_{eq(2)}$= 2.45 Å). But no significant uranyl-phosphate interactions were found in these samples.

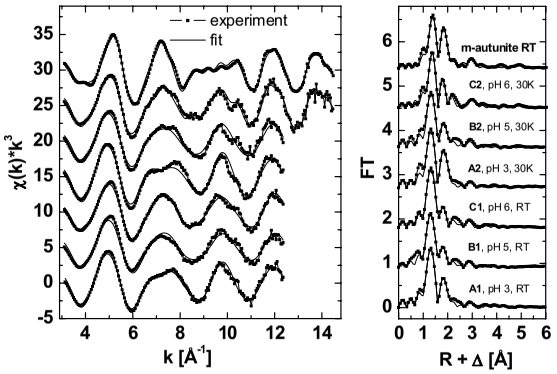

Fig. 1. Raw U L_{III}-edge k^3-weighted EXAFS spectra (left) and corresponding Fourier transform (right) of different algal samples [Algae] = 0.75g $_{dry\ mass}$ / L [U(VI)] = $1 \cdot 10^{-4}$ M

After shock freezing of the algal samples (A2, B2, C2) four phosphate groups coordinate in a bidentate fashion with four O_{eq} at 2.31 Å, four P at 3.59 Å and four U atoms at a U-U distance of 5.21 Å according to the XRD of m-autunite were obtained at pH 6. The long U-O_{eq1} distance of 2.45 Å - 2.50 Å in the complex species in all samples is similar to those observed for bidentate coordinated carboxylic groups. Factor analysis of the EXAFS spectra shows that two principal chemical environments coexist. This is also supported by the fact that in both cases (RT, 30K) the spectra of the sample at pH 5 can be reproduced by a linear combination of the spectra of the samples at pH 3 and pH 6. Therefore, we conclude that at pH 3 U(VI) is coordinated mostly by carboxylic groups, at pH 5 by carboxylic and phosphate groups, while at pH 6 U(VI) mostly interacts with phosphate groups. Currently, the corresponding analyses of the spectra of uranyl complex species formed with active *Chlorella* cells are performed.

References

/1/ George, G. N., Pickering, I. J.: EXAFSPAK A Suite of Computer Programs for Analysis of X-Ray Absorption Spectra. Stanford Synchrotron Radiation Laboratory, Stanford, CA. USA. (1995)

/2/ Ankudinov et al.: Real-space multiple scattering calculation and interpretation of x-ray absorption near-edge structure, Phys. Rev. B 58 (1998), 7565-7576

ROBL-CRG	**Experiment title:** **Immobilisation of selenite onto Fe_3O_4 , Fe/Fe_3C nanoparticles and mesoporous silica**	**Experiment number**: 20-01-658
Beamline: BM 20	**Date of experiment**: from: 10/04/07 to: 02/10/07	**Date of report**: 28/03/08
Shifts: **12**	**Local contact(s)**: A. Scheinost	*Received at ROBL:*
Names and affiliations of applicants (* indicates experimentalists): Dr. Sergei Nikitenko CNAB, UMR 5084, CNRS – Université de Bordeaux I, Le Haut Vigneau, 19 rue de Solarium, B.P. 120, 33175 Gradignan, France Dr. Andreas Scheinost Rossendorf Beamline BM20-CRG, ESRF, B.P. 220, 38043		

Report:

Abstract. During this experiment, we performed XAS speciation of selenite sorbed onto Fe_3O_4 and Fe/Fe_3C nanoparticles (NPs). Fe_3O_4 NPs (d=4-6 nm) have been prepared by co-precipitation of Fe(II) and Fe(III) in basic solutions under ultrasound. Air-stable Fe/Fe_3C NPs (d=25-100 nm) have been prepared by $Fe(CO)_5$ sonicating in diphenylmethane solutions and subsequently annealing the as-prepared product at 700°C in pure argon. Also the preliminary data were obtained on the preparation of zero-valent selenium NPs inserted within the mesoporous silica using power ultrasound. The results on selenite immobilization has been published in ***Environ. Sci. Technol.***

Arroyabe Loyo R.L., Nikitenko S.I., Scheinost, A.C., Simonoff, M. Immobilisation of Selenite on Fe_3O_4 and Fe/Fe_3C Ultrasmall Particles, *Environ. Sci. Technol.*, **2008**, *42*, p.2451.

Immobilization of selenite onto Fe_3O_4 and Fe/Fe_3C NPs:

Figure 1 shows the XANES spectra at selenium *K*-edge for Se(IV) adsorbed onto Fe_3O_4 NPs at different pH values. The strong similarity of the edges in these spectra with that of aqueous selenite indicates that the oxidation state of Se(IV) did not change due to the sorption in the pH range of 4.8–8.0. The selenium k^3-weighted EXAFS signal of the sorption sample at pH 7.9 shows a single sine-like oscillation, corresponding to a backscattering shell at a distance of 1.4 Å before correcting for the phase shift. This shell could be fitted by three O atoms at a distance of 1.70 Å, in line with the structure of Se(IV) compounds. After reduction to Se(0) or Se(−II), one would observe a significant shift of the coordination shell to longer distances, since Se and Fe coordination shells in a variety of solids vary between 2.3 to 2.6 Å. Since no significant backscattering contribution in this range could be found, this is clear evidence that no reduction of Se(IV) took place. The same conclusion applies for the EXAFS spectra at pH 5.6 and 4.8.

In contrast to Fe_3O_4, sorption of Se(IV) onto Fe/Fe_3C NPs causes significant changing in the selenium oxidation state (Figure 2). The XANES absorption edge (12654.8 eV) is 5.5 eV lower than that of aqueous selenite, 1.3 eV lower than that of trigonal Se(0), and similar to that of FeSe (12655.2 eV). At the same time, the white line is reduced in intensity in comparison to Se(IV), suggesting an increased population of the valence 4p levels. Both features are in line with a complete reduction to Se(−II). Thus it can be concluded that the removal of selenite ions with Fe/Fe_3C NPs at anaerobic conditions occurs via Se(IV) reduction to Se(−II). The EXAFS spectrum and the corresponding Fourier transform of the Fe/Fe_3C NPs sample are more similar to those of FeSe than to those of Se(0) and $FeSe_2$. A multishell fit of the spectrum achieved the following structural data: 3.3 Fe @ 2.42 Å, 1.8 Se @ 3.46 Å, and 3.6 Se @ 3.98 Å, which are different from those of tetragonal FeSe: 4 Fe @ 2.37 Å, 8 Se @ 3.77 Å, and 4 Se @ 3.91 Å. The relatively small coordination numbers suggest formation of ultrasmall FeSe particles with a structure somewhat different from that of bulk crystalline FeSe.

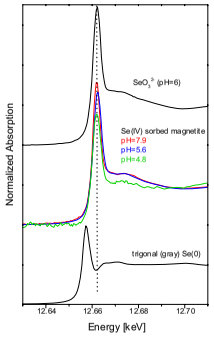

Fig. 1. Se K-edge XANES spectra of Se sorbed at Fe_3O_4 NPs.

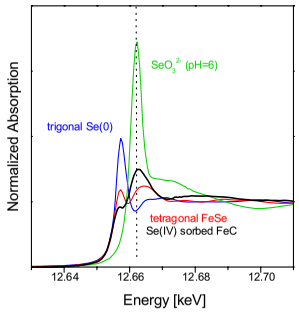

Fig. 2. Se K-edge XANES spectra of Se sorbed at Fe/Fe_3C NPs.

Preliminary XAS study revealed formation of a red form of Se(0) NPs after Se(IV) reduction with hydrazine at pH=3.0 in the presence of mesoporous silica SBA-15 under the effect of power ultrasound (I= 30 W/cm^2, f= 20 kHz, T= 36°C, Ar). MET images show that Se(0) NPs are embedded within the mesopores of SBA-15.

ROBL-CRG	**Experiment title:** **Study of the alumina-uranium interaction under ultrasonic cavitation**	**Experiment number**: **20-01-658**
Beamline: BM 20	**Date of experiment**: from: 12/05/2008 to: 16/05/2008	**Date of report**: 13/11/2008
Shifts: 8	**Local contact(s)**: Andreas Scheinost	*Received at ROBL:*
Names and affiliations of applicants (* indicates experimentalists): Tony Chave ICSM, Marcoule Sergey Nikitenko CNAB, CNRS, Gradignan Andreas Scheinost ROBL ESRF		

Report:

I. Context and objectives

A preliminary study carried out on MSU-X type mesoporous alumina has shown the drastic effect of ultrasound on its behavior in aqueous solution at ambient temperature. Thus, it was shown that sonication causes aluminum oxyhydroxyde (boehmite) formation instead of the aluminum hydroxide which is the main phase under stirring conditions [1-2]. The resulting boehmite forms a 2x20 nm fibrils with a significant specific surface area. The dehydration of $Al(OH)_3$ into AlOOH without ultrasound is observed under hydrothermal conditions at temperature about 150-200°C [3-5]. The current project is focused on interaction of uranyl ions with mesoporous alumina as a model matrix for the radionuclide confinement.

II. Materials and methods

Ultrasonic treatment was performed with a 20 KHz generator (Vibra Cell 600) coupled with a 1 cm^2 titanium horn under argon atmosphere in glass reactor thermostated at 37±1°C. The acoustic power absorbed by the media was around 0.6 $W.mL^{-1}$ with an intensity of 30 $W.cm^{-2}$. In each experiment, 300 mg of MSU-X type mesoporous alumina was mixed with a 50 ml total aqueous volume prepared with ultrapure water (18.2 MΩ.cm). Uranyl chloride solution was added to the system under acoustic cavitation and weakly acidic conditions in order to reach a given uranium mass percentage between 5 and 30%. After a 30 min treatment, solution pH was adjusted to 11, thanks to ammonia addition, and the system was left under power ultrasound for further 30 to 60 min. This procedure was followed in order to optimize the formation of high aspect ratio boehmite and thus to maximize the interaction of alumina and uranium. Finally, powder samples were centrifugated, washed until neutral pH, dried at 70°C and calcinated at 800°C prior to U L_{III} XAFS and TEM analysis.

III. Results and discussion

First of all, it can be seen in Figure 1 that the fibrilar shape of the boehmite, observed in our previous study, remains even after its transformation into δ/θ alumina at 800°C. In the same way, experiment with 5% uranium and 60 min ultrasonic treatment in basic conditions leads to the formation of 5 nm uranium nanoparticles dispersed within the alumina matrix as it can be seen in Figure 2. XAFS analysis reveals the presence in this sample the uranyl species as shown in Figure 4 (U5% 800°C). Both XANES and EXAFS spectra are quite similar to those obtained for uranyl ions adsorbed onto gamma alumina at pH 6.

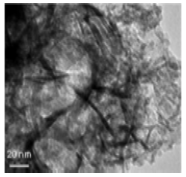

Figure 1: TEM picture of calcinated sample after 30 min pH 4 + 30 min pH 11 ultrasonic treatment with 5% uranium.

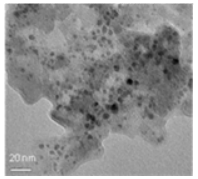

Figure 2: TEM picture of calcinated sample after 30 min pH 4 + 60 min pH 11 ultrasonic treatment with 5% uranium.

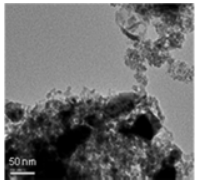

Figure 3: TEM picture of calcinated sample after 30 min pH 4 + 60 min pH 11 ultrasonic treatment with 30% uranium.

On the other hand, increasing the uranium concentration to 30% induces a drastic evolution of the sample after calcination with the occurrence of 50 nm crystals (Fig. 3) which could remind U_3O_8. In contrast to the previous sample, EXAFS spectrum points out in this case a strong U-U interaction at 4 Å (raw value) comparable with that of U_3O_8 reference sample. However, the XANES part of this analysis looks quite different and could not confirm for certain the presence of this formerly expected phase in our system.

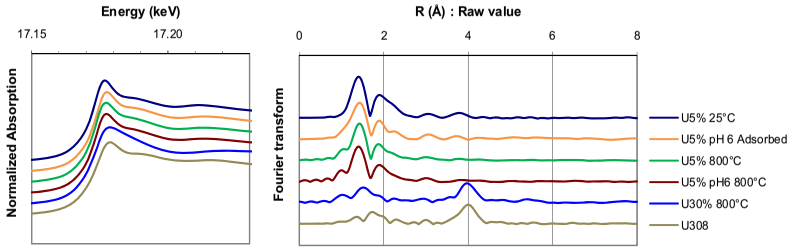

Figure 4: U L_{III} XANES and EXAFS spectra of samples obtained after various treatments. 'U5% 25°C' and 'U5% pH 6 adsorbed' samples were not calcinated and 'U5% pH 6 Adsorbed' was carried out under mechanical stirring.'U5% pH6 800°C' was obtained with the described procedure however the final pH was adjusted to 6 instead of 11 whereas 'U3O8' refers to a reference sample prepared at 800°C.

IV. Conclusions and perspectives:

To conclude these preliminary results, it can be focus on that, depending on the uranium concentration in the system, uranium nanoparticles could be formed and finely dispersed within the alumina matrix. However, further experiments are needed in order to understand the interaction of the uranyl group with the alumina matrix (5% U) and to characterize the large crystals formed with higher uranium concentration (30% U). In order to answer these questions, solid state ^{27}Al NMR and UV/Visible spectroscopy analysis are planned for the low uranium concentration system whereas X-Ray diffraction should enable the identification of the phases formed in the other case.

V. References:

[1] Carrier, X.; Marceau, E.; Lambert, J.-F.; Che, M. *J. Coll. Interface Sci.* **2007**, *308*, 429-437.
[2] Roelofs, F.; Vogelsberger, W. *J. Coll. Interface Sci.* **2006**, *303*, 450-459.
[3] Chen, X. Y.; Lee, S. W. *Chem. Phys. Lett.* **2007**, *438*, 279–284.
[4] Park, J.H.; Lee, M.K.; Rhee, C.K.; Kim, W.W., *Mater. Sci. Eng. A* **2004**, *375–377*, 1263–1268.
[5] Music S.; Dragcevic D.; Popovic S.; Vdovic N. *Mater. Sci. Eng. B* **1998**, *52*, 145-153.
[6] Suslick, K.S.; Cline, R.E.; Hammerton, Jr. D.A. *J. Am. Chem. Soc.* **1986**, 108, 5641.

ROBL-CRG	**Experiment title:** Actinide selective recognition by biomimetic molecules	**Experiment number:** 20-01-659
Beamline: BM 20	**Date of experiment:** from: 18/09/08 to: 22/09/08	**Date of report:** 20/11/2008
Shifts: 12	**Local contact(s): C. Hennig**	*Received at ROBL:*

Names and affiliations of applicants (* indicates experimentalists):

C. Den Auwer*, S. Coantic, V. Di Giandomenico*, A. Jeanson*

CEA Marcoule DEN/DRCP/SCPS, 3207 Bagnols sur Cèze, France
Université Montpellier 1, IBMM, Montpellier, France

Report:

Most data available on the interaction of actinides with biological systems are based on macroscopic measurements, with very few structural information at the molecular level. However, in case of accidental release of radionuclides, internal contamination with actinides (Th, U, Np, Pu, Am) under either acute or chronic conditions has the potential to induce both radiological and chemical toxicity. For instance Pu(IV) retention in the human body is 50% in bone and 30% on liver.[1] Although there is a tremendous volume of data available on the interaction of plutonium with living organisms as plants, nearly all the studies are limited to macroscopic or physiological measurements with no specific information at the molecular level. Molecular approaches have been very seldom due to the combined intricacy of metallo biochemistry and actinide chemistry.[2] However, such "molecular speciation" related to actinide in biomolecules is of considerable interest to understand the potential transport of radionuclide inside living organisms. It also has an important input in providing guidance on the structure, affinity and design of potential specific chelating agents synthesized and used for the elimination of incorporated radionuclides. One of the strategies to understand the interaction of actinide elements with biomolecules is to consider metallobiomolecules as elaborated coordination complexes with well-designed metal active sites. Comparison with biorelevent "analogues", as Fe(III) has revealed a very promising tool in order to rationalize the selective propensity of organic ligands to chelate actinide cations. More generally, a spread belief is that the coordination properties of some actinides at oxidation state +IV (Th, Np, Pu) in biological systems compare with that of iron, particularly Fe(III). For instance, the chemical similarity between Pu(IV) and Fe(III) has been observed in the siderophore-mediated uptake of Pu by *Microbacterium flavescens*[3] or in the transferrin system.[4] But, in fact, very few studies directly addressed that issue with biomimetic compounds.

Our approach was to consider simple organic ligands that bear some of the functional groups of a protein binding site without the intricacy of tertiary structure properties. A simple linear penta-peptide, acetyl-aspartyl-aspartyl-prolyl-aspartyl-aspartyl-amide (Ac-Asp-Asp-Pro-Asp-Asp-NH_2, named PP1 further in the text), was then chosen as a model.[5]

EXAFS spectra of M-PP1 (M = Fe, Th, Np, Pu) have been recorded at various metal to ligand ratios and various pH (see experimental reports 2001659_BM20_0207 and CH2539_BM20_0208). The pseudo radial distribution function corresponding to the EXAFS spectra of all An-PP1 (An = Th, Np, Pu) show similar features: the first shell is split into two main contributions, and a M-M contribution clearly appears at distance > 3.5 Å. Thus, one can assume that the metal-peptide complexes are at least binuclear. The first low-Z contribution of the first shell, being at a very short distance, could be attributed to μ_2-oxo or μ_2-hydroxo bridges between the actinide cations. The Fourier transform of the EXAFS spectrum of Fe-PP1 also possesses a Fe – Fe contribution around 3 Å. Consequently, all the EXAFS spectra were adjusted in a similar way, assuming that the complexes form linear chains of $[M(\mu_2\text{-}O(H))_2(PP1)_x]$ moieties (M = Fe, Th, Np, Pu). It can be noticed that, whatever the sample, the first oxygen contribution is at a shorter distance than classical M – O(aquo) distances. Indeed, the M – O distance is 0.09 Å shorter for Fe-PP1 than for Fe aquo,[6] and respectively 0.15 Å and 0.17 Å shorter in the case of Np-PP1 and Pu-PP1, compared to the corresponding aquo species.[7] This supports the assumption that μ-oxo or μ-hydroxo bridges occur. Notably, the M – M distance in M-PP1 complexes are significantly shorter than the one in the hydrolysis products (coll) : $\Delta(d^{Coll}_{Th-Th} - d^{ThPP1}_{Th-Th})$ = 0.08 - 0.10 Å $\Delta(d^{Np(OH)_5}_{Np-Np} - d^{NpPP1}_{Np-Np})$= 0.1 Å and $\Delta(d^{Coll}_{Pu-Pu} - d^{PuPP1}_{Pu-Pu})$= 0.06 - 0.08 Å. The nuclearity of the M-PP1 complexes was also estimated. Fe-PP1 nuclearity is around 2, which confirms the fact, pointed out with mass spectroscopy, that the iron complex is binuclear. Similar nuclearities were obtained for Np-PP1, Pu-PP1 and Th-PP1 with values higher than 2, suggesting that the complexes form oligomeric chains. However the exact value of nuclearity is difficult to estimate and no significant differences were observed between Th, Np and Pu. The EXAFS data also show a second shell of oxygen atoms, which can be attributed to the peptide interaction with the cation. According to the NMR study, this interaction occurs through the carboxylato functions and vicinity of the amido functions of the peptide bounds in a way that is not fully understood yet. Note that the carboxylato oxygen atoms of the peptide, as hard bases, usually interact with hard acids like iron(III) or actinide(IV).

The combination of the EXAFS best fit parameters and other spectroscopic data strongly suggests that the interaction of PP1 with Fe(III), Th(IV), Np(IV) and Pu(IV) cations relies on a original type of peptidic complexes. The formation of such molecular species prevents the actinide and iron cations from the hydrolysis that usually occurs under comparable conditions.

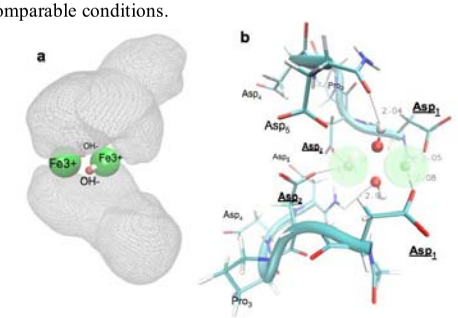

Fig. 1 : a) 3D volumetric densities maps of the peptide around the Fe^{3+}/OH^- ionic system which demonstrated, for a same threshold value, the possibility to place two copies of the β-turn folded peptide without any steric clash. b) Model in which Asp1 and Asp2 are complexing the Fe^{3+} cations.

Finally, for Fe^{3+}, a 3D statistical molecular dynamics calculation was performed which aim was to determine the most favorable orientations of the peptide around the ionic system. For each independent trajectory, the method consisted to fit all the obtained snapshots on the Fe^{3+} ions and then to statistically analyze all the resulting positions of the peptide through atomic densities maps in 3D. Visualization of these maps in 3D using increasing threshold values lead to statistically equivalent positions of the peptide around the ionic system. For each independent trajectory, these analyses revealed the possibility to place two copies of PP1 around both Fe^{3+} ions without any steric clash (Figure 1a), and in agreement with the experimental observations. Such a model is represented in Figure 2b in which each Fe^{3+} interacts with two Asp residues.

[1] E. Ansoborlo, O. Prat, P. Moisy, C. Den Auwer, P. Guilbaud, M. Carriere, B. Gouget, J. Duffield, D. Doizi, T. Vercouter, C. Moulin, V. Moulin, *Biochimie*, 2006, **88**, 1605.
[2] A. E. Gorden, J. Xu, K. N. Raymond, P. Durbin, *Chem. Rev.*, 2003, **103**, 4207.
[3] M. P. Neu, in *Advances in Plutonium Chemistry* 1967-2000, ed. D. C. Hoffman, Am. Nucl. Soc., 2002, 169.
[4] H. Li, P. J. Sadler, H. Sun, *Eur. J. Biochem.*, 1996, **242**, 387.
[5] A. Jeanson, C. Berthon, S. Coantic, C. Den Auwer, N. Floquet, H. Funke, D. Guillaneux, C. Hennig, J. Martinez, P. Moisy, S. Petit, O. Proux, E. Quémeneur, P. Lorenzo Solari, G. Subra, *New J. Chem.* Accepted.
[6] P. D'Angelo, M. Benfatto, *J. Phys. Chem. A*, 2004, **108**, 4505.
[7] M. R. Antonio, L. Soderholm, C. W. Williams, *Radiochim. Acta*, 2001, **89**, 17.

ROBL-CRG	**Experiment title:** Interaction of uranium with bioligands produced by soil bacteria and with related model compounds using X-ray absorption spectroscopy	**Experiment number:** 20-01-661
Beamline: BM 20	**Date of experiment:** from: 20.04. to: 24.04.2007 05.10. to: 09.10.2007	**Date of report:** 11.04.2008
Shifts: 24	**Local contact(s):** A. Rossberg	*Received at ROBL:*
Names and affiliations of applicants (* indicates experimentalists): H. Moll, M. Glorius*, A. Rossberg*, A. Scheinost*, Ch. Hennig*, H. Funke*, G. Bernhard		

Report: Synchrotron-based EXAFS spectroscopy is a powerful technique to obtain structural information on radionuclide bioligand species in solution. As an example pyoverdin-type siderophores are a unique class of bioligands, with a high potential to dissolve, bind, and thus transport uranium in the environment. Pyoverdins are secreted from fluorescent *Pseudomonas* species which are ubiquitous soil bacteria. The aim of this study is to explore structural parameter of soluble U(VI) species with pyoverdins and related model compounds. This includes also relevant model systems for the cell envelope of bacteria. The present report is focussed on the first topic: soluble U(VI) bioligand species and their structural characteristics.

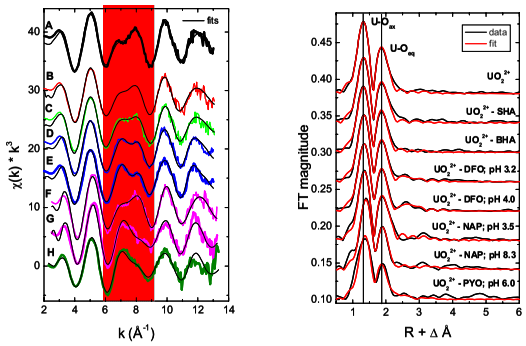

Fig. 1: U L_{III}-edge k^3-weighted EXAFS spectra (left) and the corresponding Fourier transforms (right) and the theoretical fits (red line).

Experimental. U L_{III}-edge EXAFS measurements were carried out with test solutions containing $5x10^{-4}$ or 0.001 M UO_2^{2+} and pyoverdins (PYO) or related model compounds at an ionic strength of 0.1 M $NaClO_4$. The pH was varied between 2 and 8 depending on the bioligand. The samples were measured at room temperature either in fluorescence or in transmission mode. The model compounds simulate the hydroxamate function [salicylhydroxamic acid (SHA), benzohydroxamic acid (BHA) and desferrioxamine B (DFO)] and the chromophore [2,3-dihydroxynaphthalene (NAP)] of the pyoverdin molecule.

Results. A selection of the measured EXAFS oscillations and corresponding Fourier transforms are presented in Fig. 1. The extracted structural parameters are summarized in Table 1.

Table 1: Summary of the determined structural parameters.

Sample	Shell	N	R (Å)	σ^2 (Å^2)	ΔE_0 (eV)
A	U-O_{axial}	2f	1.76_6	0.0016	10.5
	U-$O_{equatorial}$	5.0	2.41_6	0.0068	
B (SHA)	U-O_{axial}	2f	1.77_5	0.0026	13.4
	U-$O_{equatorial}$	4.7	2.41_5	0.0063	
C (BHA)	U-O_{axial}	2f	1.77_3	0.0027	12.3
	U-$O_{equatorial}$	4.8	2.40_2	0.0064	
D (DFO)	U-O_{axial}	2f	1.78_1	0.0023	10.3
pH 3.2	U-$O_{equatorial}$	4.9	2.40_0	0.0070	
	U-C/N	2f	3.22	0.0040	
E (DFO)	U-O_{axial}	2f	**1.78_5**	0.0024	9.7
pH 4.0	U-$O_{equatorial}$	4.8	**2.38_7**	0.0069	
	U-C/N	2f	3.22	0.0015	
F (NAP)	U-O_{axial}	2f	1.76_8	0.0017	18.6
pH 3.5	U-$O_{equatorial}$	5.6	2.40_5	0.0078	
G (NAP)	U-O_{axial}	2f	**1.79_7**	0.0018	18.3
pH 8.3	U-$O_{equatorial}$	6.3	**2.36_9**	0.0095	
H (PYO)	U-O_{axial}	2f	**1.78_8**	0.0023	12.8
pH 6.0	U-$O_{equatorial}$	6f	**2.35_3**	0.0107	
	U-C/N	2f	2.89	0.0047	
U(VI)-PCA[1]	U-O_{axial}	2f	**1.81**	0.0013	-14
pH 10.0	U-$O_{equatorial}$	5.8	**2.37_4**	0.0071	

f: fixed during the fit.

The differences in the EXAFS oscillations of the bioligand containing samples B to H compared to the free uranyl ion (sample A) within a k-range between 6 and 9 Å^{-1} clearly indicates the complexation of U(VI). These U(VI)-species are characterized by both a lengthening of the U-O_{ax} and a shortening of the U-O_{eq} distance with increasing pH. The structural parameters of the U(VI)-pyoverdin sample shows strong similarities with those of 1:1 complexes of U(VI) with protocatechuic acid and catechol [1]. Hence there is a strong affinity of U(VI) to the catechol functionality of the pyoverdin molecule. However, the coordination of U(VI) to hydroxamate groups (samples B to E) results also in a shortening of the U-O_{eq} distance.

Acknowledgements. This work is supported by the BMWi (no. 02E9985).

Reference

/1/ Roßberg, A. et al. (2000) Radiochim. Acta 88, 593-597.

ROBL-CRG	**Experiment title:** Investigation of chemical bonding structure and coordination of fullerene-like carbon-metal nanocomposite thin films by means of XANES and EXAFS	**Experiment number:** **20-01-662**
Beamline: BM 20	**Date of experiment:** from: 01/03/2007 to: 03/03/2007	**Date of report:** 03/04/2008
Shifts: 6	**Local contact(s):** A. Scheinost	*Received at ROBL:*

Names and affiliations of applicants (* indicates experimentalists):
Gintautas ABRASONIS*
Institute of Ion Beam Physics and Materials Research, Forschungszentrum Dresden-Rossendorf, PF-510119, 01314 Dresden, Germany.

Report:

Carbon-nickel (~30 at.%) nanocomposite thin films grown in the temperature range of RT-500°C have been investigated by the means of XANES and EXAFS at the ROBL beamline. The samples had been previously characterized by the means of transmission electron microscopy and x-ray diffraction. The latter shows that nickel is in the form of nanoparticles whose shape, size and phase depends on the growth conditions: Ni nanoparticles are nanorods with the diameter 3-10 nm in the temperature range of 500-300°C while lower temperatures prevent the columnar growth and particles exhibit granular shape. At 500-400°C, Ni is essentially in fcc metallic phase. When the temperature decreases, new hexagonal phase starts to form which becomes dominat at 300°C. For lower growth temperatures, no crystalline structure could be determined due to possible particle size effects or inherent amorphous structure.

The purpose of the EXAFS investigations was to get some information on the nearest neighbour coordination, local degree of atomic disorder and to identify possible size effects. The results are summarized in Fig. 1 which presents the amplitude of the Fourrier transform of the EXAFS oscillations of the C:Ni nanocomposites grown at different temperatures. These amplitude variations represent the distribution of the nearest neighbours in the coordination shells. One can see at 500-400°C a highly ordered Ni phase forms with the well defined first Ni-Ni and, more importantly, higher coordination shells. This structure corresponds to fcc Ni. At 300°C, one can identify additional nearest coordination shell which is attributed to Ni-C bonds. This allows identifying that the hexagonal phase observed by x-ray diffraction should be attributed to nickel carbide. At this temperature, still higher coordination shells could be identified which shows certain degree of crystallinity. Further decrease in temperature results in significant drop of the intensity of the coordination shells higher than the first Ni-C and Ni-Ni. This indicates about significant degree of disorder present within the nickel nanoparticles. No significant variation in the Ni-C intensity allows to demonstrate that indeed this effect cannot be attributed to the size effects but to the internal structure of Ni nanoparticles. These tendecies have been confirmed in the XANES spectra of the corresponding films.

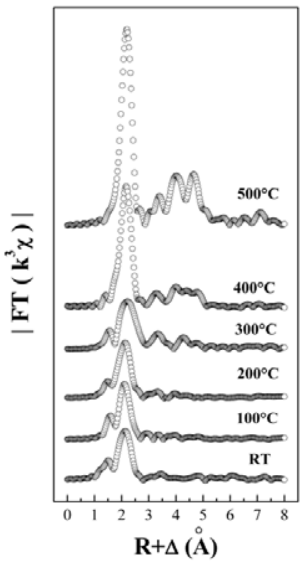

Fig. 1. The amplitude of the Fourrier transform of EXAFS oscillations of the C:Ni nanocomposites grown at RT-500°C.

In summary, EXAFS and XANES investigations have allowed to get deeper insights in the atomic structure of the Ni nanoparticles of C:Ni nanocomposite films. Thes results have been correlated with the magnetic properties. A manuscript has been submitted and now is in the review process.

ROBL-CRG	**Experiment title:** Structure of Neptunium Species in Solution	**Experiment number:** 20-01-664
Beamline: BM 20	**Date of experiment:** from: to:	**Date of report:** 6.2.2009
Shifts:	**Local contact(s):** Christoph Hennig	*Received at ROBL:*
Names and affiliations of applicants (* indicates experimentalists): Atsushi Ikeda-Ohno*, Christoph Hennig*, A.C. Scheinost*		

The solution samples investigated in this proposal were prepared by dissolving $NpO_2(ClO_4)_2{\cdot}nH_2O$ into aqueous solutions, to give a Np concentration of 0.04 M. The oxidation state of Np in the samples was electrochemically adjusted. Np L_{III}-edge (17.625 keV) EXAFS measurements were carried out in transmission mode using a Si(111) double-crystal monochromator, and two Pt-coated mirrors for rejection of higher harmonics.

Figure 1 shows the k^3-weighted Np L_{III}-edge EXAFS spectra for Np(IV), -(V), and -(VI) in 1.0 M $HClO_4$ (left), and their corresponding Fourier transforms (right). Perchlorate is known to be a noncomplexing ligand to actinide ions in aqueous solution, and hardly coordinates to the primary coordination sphere of actinide ions. Accordingly, the chemical species formed in aqueous $HClO_4$ solution are considered to be pure hydrate species. The EXAFS spectrum of Np(IV) is composed of a single oscillation pattern, giving a peak at 1.9 Å in the Fourier transform. The structural parameters determined by shell fitting are a Np-O distance ($R_{Np\text{-}O}$) of 2.40 Å with a coordination number (CN) of 10.4, corresponding to water molecules of the primary coordination sphere. The EXAFS spectra for the two higher oxidation states, V and VI, exhibit more intricate oscillation patterns and the corresponding Fourier transforms show several significant backscattering peaks. The most prominent peak at around 1.4 Å arises from the single scattering of the double-bond axial oxygen atoms (O_{ax}), indicative of the neptunyl unit (NpO_2^{n+}). The following two peaks at around 1.9 Å arise from oxygen atoms of the water molecules in the neptunyl equatorial plane ($O_{eq}(H_2O)$, while the small but sufficiently distinguishable peak at 2.9 Å is due to the multiple scattering of O_{ax}, respectively. The shell fitting results reveal that the neptunyl(V) ion is coordinated in its equatorial plane by 5.2 water molecules with O atoms at a distance of 2.49 Å, whereas the neptunyl(VI) ion is coordinated by 5.3 water molecules with a shorter interatomic distance of 2.42 Å. Our EXAFS data show therefore a structural rearrangement of Np hydrate species with oxidation state as illustrated in Figure 2: both Np(V) and (VI) ions exist predominately as pentaaquo neptunyl complexes, $[NpO_2(H_2O)_5]^{n+}$ with n = 1 for Np(V) and 2 for Np(VI), whereas the Np(IV) ion forms a spherically coordinated decaaquo complex, $[Np(H_2O)_{10}]^{4+}$. It is this drastic change in complex structure between Np(IV) and Np(V), which makes the transition between these two redox states almost irreversible (DE ~0.9 V), while the transition between Np(V) and Np(VI) requires no structural change, hence is quasi-reversible (DE = ~0.2 V). These results support our initial hypothesis that there is a strong relationship between the electrochemical behaviour of Np and its complex structure.

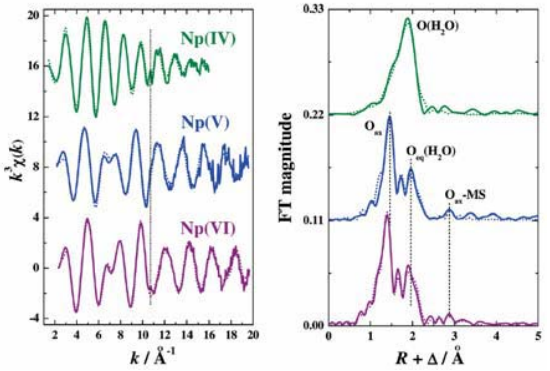

Fig. 1: k^3-weighted Np-L_{III} edge EXAFS spectra. Solid lines represent experimental data and dotted lines represent theoretical fit. The line colours reflect the actual colour of sample solutions.

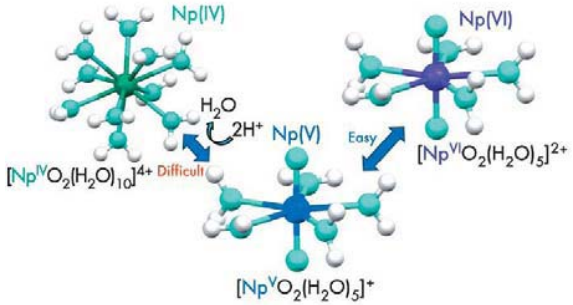

Fig. 2: Structural rearrangement of Np hydrate species through the redox reaction.

Ikeda-Ohno, A., Hennig, C., Rossberg, A., Funke, H., Scheinost, A.C., Bernhard, G., Yaita T. Electrochemical and complexation behavior of neptunium in aqueous perchlorate and nitrate solutions, *Inorg. Chem.* **47** (2008) 8294-8305.

ROBL-CRG	**Experiment title:** Speciation of aqueous uranyl(VI) polymeric species using EXAFS spectroscopy	**Experiment number:** 20_01_665
Beamline: BM 20	**Date of experiment:** from: 30.06.2007 to: 01.07.2007	**Date of report:** 31.3.2008
Shifts: 3	**Local contact(s):** Dr. Andreas C. Scheinost	*Received at ROBL:*
Names and affiliations of applicants (* indicates experimentalists): S.Tsushima* , A.Rossberg * , A.C.Scheinost * Forschungszentrum Dresden-Rossendorf, Germany		

Report:

In this work, we used EXAFS spectroscopy to solve the structures of uranyl(VI) hydroxo dimer and trimer complexes in aqueous solution. One of the main challenges for EXAFS is to prepare solutions in which the target polymeric species are dominant, while in the uranium concentration range suitable for EXAFS measurements, there is always a mixing of several species. Therefore, uranium(VI) concentration and pH was optimized as far as possible based on thermodynamic calculations to reduce the number of coexisting species, while vibrational spectroscopy (FTIR) and UV-vis absorption spectroscopy was used to support the discrimination of coexisting species, in case they could not be avoided experimentally.

Experimental

The EXAFS measurements were recorded at the Rossendorf Beamline at BM20. The Uranium L_{III}-edge spectrum of samples were recorded either in fluorescence mode or in transmission mode at room temperature. The energy scale was calibrated using the maximum of the first derivative of the K-edge spectrum of yttrium (17038 eV), which was simultaneously measured with each spectrum. The threshold energy, E_0, of the uranium L_{III}-edge was defined as 17185 eV. The EXAFS spectra were analyzed according to standard procedures using EXAFSPAK including statistical weighting of the 13 fluorescence channels and dead-time correction. Theoretical scattering phases and amplitude functions were calculated with the *ab initio* calculation program FEFF8 by using the structure of the most stable form of the trimer complex obtained by DFT calculations.

RESULTS

The k^3-weighted EXAFS spectra of the uranyl (VI) dimer and trimer samples and corresponding Fourier transforms are shown in Figure 1. According to the FTIR and UV-vis measurements, the samples contain mixtures of UO_2^{2+}, $(UO_2)_2(OH)_2^{2+}$ and $(UO_2)_3(OH)_5^{+}$. The formation of polynuclear complexes is confirmed by EXAFS for both samples which show U-U backscattering. By shell fitting we obtained a U-U radial distance of 3.82-3.83 Å, which is in line with the trimer complex $(UO_2)_3(OH)_5^{+}$. For dimer sample, a weak FT peak at 3.71 Å could be fitted by 0.5 U atoms at a radial distance of 3.88 Å. The U-U distances found here show good agreement with crystal structure data and the DFT calculations. The averaged U-U distances are 3.875Å (DFT) versus 3.88 Å (EXAFS) for $(UO_2)_2(OH)_2^{2+}$, and 3.834 Å (DFT) versus 3.81 - 3.82 Å (EXAFS) for $(UO_2)_3(\mu_3\text{-}O)(OH)_3^{+}$. A shorter U-U distance of 3.81 – 3.82 Å in the trimeric complex suggests the presence of the central oxo bridging instead of the OH bridging. The U-U coordination numbers is less than 1 and hence too small for the dimer and the trimer. This is related to the fact that the sample was a mixture of monomeric and polymeric species. In addition, the CN obtained from EXAFS always have an error of 10 ~ 20%. Clearly, the coordination numbers obtained from EXAFS do not help to identify the polymer structures, while the U-U distances give reliable results.

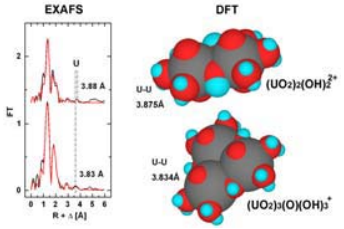

Figure 1: Both the EXAFS spectroscopy and DFT calculations show that the trimer complex $(UO_2)_3(O)(OH)_3^{+}$ has the U-U distance which is significantly shorter than that of the dimer complex $(UO_2)_2(OH)_2^{2+}$, thereby the presence of oxo bridging in the trimer complex has been confirmed.

To summarize, the EXAFS spectra of two uranyl(VI) samples show two distinct U-U distances of 3.88 Å and 3.81~3.82 Å which correspond to $(UO_2)_2(OH)_2^{2+}$ and $(UO_2)_3(\mu_3\text{-}O)(OH)_3^{+}$, respectively. These distances agree well with the results of the DFT calculations. Our combined DFT and EXFAS results confirm that $(UO_2)_3(OH)_5^{+}$ in aqueous solution exists as $(UO_2)_3(\mu_3\text{-}O)(OH)_3^{+}$ with an oxo central bridging.

Reference

[1] S.Tsushima, A.Rossberg, A.Ikeda, K.Müller, A.C.Scheinost, *Inorg. Chem.* 2007, 46, 10819-10826.

ROBL-CRG	**Experiment title:** EXAFS study of Np(V) sorption onto montmorillonite	**Experiment number:** 20-01-667
Beamline: BM 20	**Dates of experiment:** 08.-11.03.2008, 08.-10.11.2008	**Date of report:** 20.03.2009
Shifts: 15	**Local contact(s):** D. Banerjee, A. Roßberg	*Received at ROBL:*

Names and affiliations of applicants (* indicates experimentalists):
S. Amayri[1*], B. Baeyens[2*], M.H. Bradbury[2], R. Dähn[2*], S. Dierking[1*], J. Drebert[1*], D. Föhlich[1*], A.C. Scheinost[3*], T. Reich[1*]
[1]Institue of Nuclear Chemistry, Johannes Gutenberg-Universität Mainz, 55099 Mainz, Germany
[2]Laboratory for Waste Management, Paul Scherrer Institut, 5232 Villigen PSI, Switzerland
[3]Institute of Radiochemistry and Rossendorf Beamline at ESRF, Forschungszentrum Dresden-Rossendorf, 01314 Dresden, Germany

Report:

The sorption of Np(V) on Na-montmorillonite (STx-1) has been studied in the absence of inorganic carbon and under air-equilibrated conditions. Batch experiments were performed with 0.1 and 0.01 M $NaClO_4$ as background electrolyte, 8×10^{-12} and 9×10^{-6} M Np(V), and $3 \le pH \le 10$. At $pH > 8$ the presence of inorganic carbon has a strong influence on the sorption behaviour of Np(V) due to the formation of aqueous Np(V) complexes with carbonate.

Neptunium L_{III}-edge extended X-ray absorption fine structure (EXAFS) measurements on Np(V)/montmorillonite samples with Np(V) loadings in the range of 0.3-3.5 µmol/g have been performed to determine the local structure of Np at the solid-liquid interface. Wet paste samples were prepared at pH 9.0 and 9.5 in the absence and presence of inorganic carbon. The EXAFS spectra of samples prepared under ambient air conditions ($p_{CO2} = 10^{-3.5}$ atm) revealed the formation of Np(V)-carbonate complexes at the montmorillonite surface (see Table 1).

Table 1: Structural parameters of Np(V) sorbed onto montmorillonite

CO_2	pH	Shell	N*	R(Å)	σ^2(Å^2)
no	9.0	O_{ax}	2	1.85	0.003
		O_{eq}	5	2.54	0.014
no	9.5	O_{ax}	2	1.84	0.003
		O_{eq}	5	2.50	0.016
yes	9.0	O_{ax}	2	1.84	0.002
		O_{eq}	5	2.56	0.012
		C	2	2.99	0.004*
		O_{dis}	2	4.24	0.004
yes	9.5	O_{ax}	2	1.84	0.002
		O_{eq}	5	2.55	0.010
		C	2	2.99	0.004*
		O_{dis}	2	4.30	0.008

*parameters fixed during the fit

The results of the batch experiments obtained under CO_2-free conditions could be modelled using the two site protolysis non-electrostatic surface complexation and cation exchange (2SPNE SC/CE) model described in [1]. For modelling the sorption behaviour of Np(V) on montmorillonite in the air-equilibrated system, the aqueous complexation of Np(V) with carbonate [2] was included and the following additional surface complexation reaction was required: $\equiv SOH + NpO_2^+ + CO_3^{2-} \Leftrightarrow \equiv SONpO_2CO_3^{2-} + H^+$. This study, combining batch experiments, spectroscopic measurements, and surface complexation modelling contributes towards a better understanding of the sorption of neptunium in the near field (bentonite) and far field (argillaceous rocks) of nuclear waste repositories.

[1] M.H. Bradbury, B. Baeyens, Modelling the sorption of Mn(II), Co(II), Ni(II), Zn(II), Cd(II), Eu(III), Am(III), Sn(IV), Th(IV), Np(V) and U(VI) on montmorillonite: Linear free energy relationships and estimates of surface binding constants for some selected heavy metals and actinides, Geochim. Cosmochim. Acta 69, 875-892, 2005. [2] Chemical Thermodynamics of Neptunium and Plutonium, (Eds. J. Fuger et al.) Elsevier, Amsterdam 2001.

ROBL-CRG	**Experiment title:** Abiotic antimony reduction by Fe(II) systems	**Experiment number:** 20-01-668
Beamline: BM 20	**Date of experiment:** from: Sept 14 to: Sept 18 2007; from: Nov 26 to: Nov 29 2007; from: April 18 to: April 22 2008	**Date of report:** Nov 17 2008
Shifts: 29	**Local contact(s):** A.C. Scheinost, H. Funke	*Received at ROBL:*

Names and affiliations of applicants (* indicates experimentalists):
A. C. Scheinost*[1], R. Kirsch*[1,2],
[1]Institute of Radiochemistry, FZD, Dresden, Germany
[2]Laboratoire de Géophysique interne et Tectonophysique, Université Joseph Fourier, Grenoble, France

Report:

Iron(II)minerals occur naturally in anoxic soils or form as corrosion products of reactive barriers and waste containers. They may react with metal contaminants via sorption and electron-transfer reactions. Redox reactions with selenium, arsenic, chromium, plutonium or neptunium have been shown [1,2,3,4,5]. The mobility of these contaminants is either reduced (if the resulting species is less soluble than the original one), enhanced (if the resulting species is more mobile) or left unaffected. Furthermore, surface sorption/precipitation reactions play a considerable role in determining environmental contaminant mobility. Through the present experiments it could be shown that aqueous Sb^{III} and Sb^{V} species form inner-sphere sorption complexes on the surface of magnetite ($Fe^{II}Fe^{III}_2O_4$), mackinawite ($Fe^{II}S$) and siderite ($Fe^{II}CO_3$), and that Sb^{V} is reduced to Sb^{III} by magnetite and mackinawite, the former reaction taking place on a much longer timescale than the latter.

Experimental:

Magnetite[6], mackinawite[7] and siderite[8] were synthesized in a glove box under anoxic conditions (< 2 ppmv O_2). They were reacted in 25 mM $CaCl_2$ with Sb(III) (Sb_2O_3 in 2M HCl) or Sb(V) ($KSbOH_6$ in 2M HCl or H_2O) ([Sb]=0.1mM; 40 or 3 g/L Fe_3O_4; 25 or 1.9 g/L FeS, 10g/L $FeCO_3$) in the pH range 4 to 9 and for time periods from 1h to 67d. The wet pastes resulting from centrifugation were put into XAS sample holders and stored in liquid nitrogen until measurement in a closed-cycle helium cryostat at 15K. XANES and EXAFS spectra at the Sb-K-edge 30.491 keV were collected in fluorescence mode using a 13-element Ge detector; an Sb foil was used for energy calibration.

Results:

Reaction of siderite with Sb(V) for up to 7 days at near-neutral pH resulted in no reduction of Sb(V) as observed by XANES (not shown). Sb(V) is adsorbed via inner-sphere surface complexation with Sb-Fe distances of 3.18 Å and 3.55 Å, characteristic of edge and corner-sharing arrangements between $Sb(O,OH)_6$ and $Fe(O,OH)_6$ octahedra (Fig. 1).

Reaction of mackinawite with Sb(V) caused a fast (~1 h) and complete reduction to Sb(III) and formation of a surface complex with a $Sb(S)_3$-structure, characterized by a (Sb-S) distance of 2.48 Å (Fig. 2).
Reaction of magnetite with Sb(V) also produced Sb(III), the extent of reduction being dependent on reaction pH and time. Under our experimental conditions antimony reduction was complete for pH>6.5 and reaction times >7 days (further depending on the solid/liquid ratio and loading with antimony). The reduction process is orders of magnitude slower than adsorption of Sb(V) to the surface, which is complete within 30 minutes. The resulting surface complex of Sb(III) is characterized by corner sharing of an $Sb(III)O_3$-pyramide with up to 6 $Fe(O,OH)_6$-octahedra, a position else occupied by $Fe(III)0_4$ tetrahedra in the magnetite-structure (Fig. 3). The identified structure of the Sb(III) surface complex is similar to the one found for As(III) on {111} faces of magnetite [9].

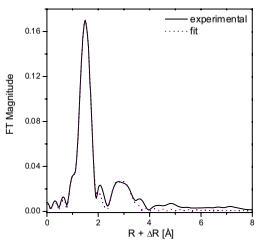

Fig. 1: Experimental FT and fit of Sb(V) sorbed on siderite

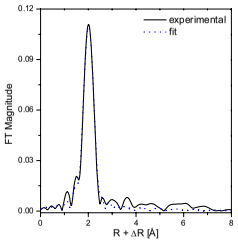

Fig. 2: Experimental FT and fit of Sb(III) on mackinawite

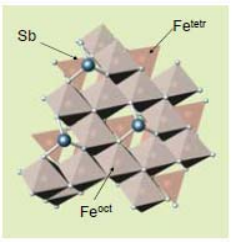

Fig. 3: Model of Sb(III)-complex on {111}-faces of magnetite

Conclusion:

The structure of the surface complexes of Sb(III) and Sb(V) on the surface of magnetite, mackinawite and siderite could be elucidated by shell fitting [10]. However, a number of questions remain open concerning the reduction mechanisms of Sb by magnetite and mackinawite. While Sb(V) is reduced by FeS over a wide pH range, it remains to be elucidated whether this reduction is due to oxidation of Fe^{II} or S^{2-} or a combination of both. It also remains open whether the lower reactivity of magnetite at low pH is solely due to (surface) oxidation of the mineral to maghemite or whether other mechanisms come into play.

References:

[1] Scheinost and Charlet, Environ. Sci. Technol. 42 (2008) 1984.
[2] Gallegos *et al.*, Environ. Sci. Technol. 41 (2007) 7781.
[3] Mullet *et al.*, Colloids Surf. A 244 (2004) 77.
[4] Powell *et al.*, Environ. Sci. Technol. 38 (2004) 6016.
[5] Nakataka *et al.*, Radiochim. Acta 92 (2004) 145.
[6] Jolivet *et al.*, Clays Clay Miner. 40 (1992) 531.
[7] Rickard, Stockholm Cont. Geol. 20 (1969) 67.
[8] Charlet *et al.*, Geochim. Cosmochim. Acta 54(1990) 2329.
[9] Wang *et al.*, Geochim. Cosmochim. Act. 72 (2008) 2573.
[10] Kirsch et al., Mineral. Mag. 72 (2008) 185.

ROBL-CRG	**Experiment title:** **Characterization of Mn Speciation on Clay Minerals**	**Experiment number**: Run-Nr. 670
Beamline: BM 20	**Date of experiment**: from: Nov. 3 2007 to: Nov. 5 2007	**Date of report**: Nov. 6, 2008
Shifts:	**Local contact(s)**: A.C. Scheinost	*Received at ROBL:*
Names and affiliations of applicants (* indicates experimentalists): Daniel G. Strawn University of Idaho PO Box 442339 Moscow, Idaho 83844-2339 208 893 0958		

Report:

In these experiments we adsorbed Mn(II) to montmorillonite under different ionic strength and pH conditions (Figure 1). Results from these experiments suggest that Mn(II) adsorbed in the interlayer, presumably as a fully hydrated hexaqua complex, has much slower oxidation rates than Mn(II) adsorbed on the edge sites via surface complexation.

This experiment was a first attempt at collecting XAFS data on a new expeirmental system. Results from the experiment were used to prepare a proposal to submit to a joint USA-NSF and Germany-DFG International Collaboration funding program.

XAFS data were collected on six samples and two standards. The XAFS for the low Mn concetrated samples had a significant amount of noise and showed evidence of a multi-electron excitation, there-by making advanced data analysis challenging. One sample was air dried, which allowed for denser packing of the clay, and subsequently better S/N. Preliminary evalaution suggest that air drying did not have any affect on the Mn oxidation state, thus this may be a suitable method for preparing low loading samples for XAFS analysis. We are seeking funding to continue these expeiments, and the data collected in this run was critical to providing initial data to support our hypothesis: Oxidation kinetics, speciation, and reactivity of Mn on mineral surfaces are a function of the type of interaction between the Mn cation and the surface (i.e., electrostatic or covalent bonds). XAFS is the ideal tool to investigate the chemistry occurring in these systems.

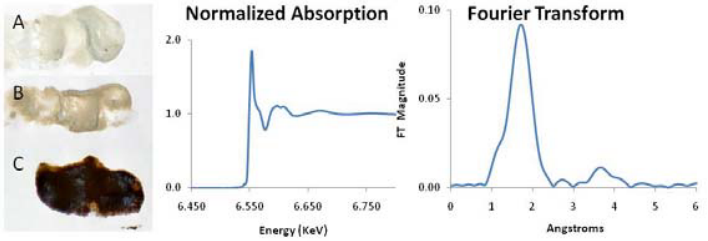

Figure 1. Mn-clay mineral equilibration experiments. Photographs A, B, C show color differences in montmorillonite-Mn pastes smeared on paper. Photo A is a paste of clay incubated with Mn(II) for 15 days, ionic strength 0.0005 pH=4.1, and adsorbed Mn=329 mmol kg^{-1}. Photo B is a paste of clay incubated with Mn(II) for 1 day, ionic strength 0.1 pH=6.0, and adsorbed Mn=42.6 mmol kg^{-1}. Photo C is a paste of clay incubated with Mn(II) for 15 days, ionic strength 0.1 pH=6.4, and adsorbed Mn=52.2 mmol kg^{-1}. The photos show that the color of the clay mineral is a function of the loading levels, equilibration conditions, and time. The color is visual evidence of speciation differences. Spectra show Mn K-edge normalized XANES and Fourier transform of EXAFS for clay mineral in sample A equilibrated for 6 days. From the normalized absorption spectrum (i.e., XANES) the oxidation state can be determined. The Fourier transform of the EXAFS spectrum shows relative positions of the backscattering peaks in the molecular environment of the adsorbed Mn. These preliminary experiments suggest that there are unique molecular speciation and oxidation states of Mn on clay minerals, and XAFS spectroscopy data can be collected to allow for discovery of these species.

ROBL-CRG	**Experiment title:** Studies on the coordination environments of UO_2^{2+} on gibbsite surface in the presence of natural ligands	**Experiment number**: 20-01-671
Beamline: BM 20	**Date of experiment**: from: 23.02.2008 to: 27.02.2008	**Date of report**: 10.11.2009
Shifts:	**Local contact(s)**: A. Scheinost	*Received at ROBL:*

Names and affiliations of applicants (* indicates experimentalists):

T. Saito*, T. Hattori*, K. Ishida* and S. Nagasaki

Department of Nuclear Engineering and Management, School of Engineering, The University of Tokyo
7-3-1 Hongo, Bunkyo-ku, Tokyo 113-8656, JAPAN

Report:

Structures of sorption complexes that hazardous radionuclides or heavy metals form on mineral surfaces are key information to develop thermodynamic models for reliable prediction of their adsorption amounts in soils, ground waters and deep geological environments. Such information is never obtained from macroscopic adsorption experiments only and must be determined independently via *in-situ* spectroscopy and/or theoretical calculations. In this study we investigated the structures of uranyl (UO_2^{2+}) sorption complexes on gibbsite (α-$Al(OH)_3$) with silicic acid (H_4SiO_4) by extended X-ray absorption fine structure (EXAFS) spectroscopy. The obtained structural parameters were used to constain density functional theory (DFT) calculations and to optimize plausible sorption geometries of UO_2^{2+} on gibbsite.

The EXAFS measurements of U-L_{III} edge were carried out in fluorescence mode at 15 K. All sorption samples were prepared in N_2-filled glove box. The concentrations of UO_2^{2+}, H_4SiO_4, gibbsite and $NaClO_4$ were 10 μM, 0.5 mM, 2 g/L and 0.1 M, respectively, and the pH was adjusted to 5.5 or 9.6. For comparison the sorption samples without H_4SiO_4 were also prepared in a similar way. Gibbsite with adsorbed UO_2^{2+} was separated by centrifugation and the resulting wet pastes were loaded into EXAFS sample holders. The concentrations of UO_2^{2+} in the supernatants were measured by an ICP-MS to determine the surface loading of UO_2^{2+} on gibbsite. In all samples more than 90 % of UO_2^{2+} adsorbed on gibbsite both with and without H_4SiO_4. Adsorption structures of uranyl onto gibbsite were optimized by DFT calculations with B3LYP functional. A neutral Al hexamer cluster, $Al_6(OH)_{18}(H_2O)_6$, was used as a model of gibbsite surface. Model clusters with adsorbed UO_2^{2+} and H_4SiO_4, if present, were fully optimized without any symmetry and structural constraints. Solvation was taken into account by explicitly placing water molecules on the equatorial plane of UO_2^{2+} in geometry optimization and further performing conductor-like polarizable continuum model calculation with the optimized structures.

In the absence of H_4SiO_4 EXAFS spectroscopy revealed the same interatomic distances of the UO_2^{2+} coordination environment, $R_{U\text{-}Oax} \approx 1.80$ Å, $R_{U\text{-}Oeq} \approx 2.40$ Å, and towards the gibbsite surface, $R_{U\text{-}O} \approx 2.87$ Å, $R_{U\text{-}Al} \approx 3.38$ Å. In addition, two U-U distances were observed, 3.92 Å at pH 9.7 and 4.30 Å at pH 5.6, both with coordination numbers (CN) of ~1. The shorter U-U distance is close to that of the aqueous uranyl hydroxo dimer, $UO_2(OH)_2$, reported as 3.875 Å in the literature [1]. The longer U-U distance (4.30 Å) at acidic pH, however, is not in line with known aqueous uranyl polymer complexes. The DFT calculations of monomeric uranyl sorption complexes show an energetic preference of the corner-sharing versus the edge-sharing configuration on the edge face of gibbsite. The energy difference is so small, however, that possibly both surface species may coexist. In contrast to the edge sites, sorption to the basal face was energetically not favorable. Based on the EXAFS findings we further refined dimeric surface complexes with DFT. Two structural models were obtained: in the acidic region, the observed long U-U distance can be explained with a distortion of the uranyl dimers to form both a corner-sharing and an edge-sharing linkage to neighboring Al octahedral, leading to $R_{U\text{-}U} = 4.150$ Å (Figure 1 (a)). In the alkaline region, a corner-sharing uranyl dimer complex is most favorable (Figure 1 (b)). The U-O path at ~2.87 Å in the EXAFS spectra arises from the oxygen atom linking two Al cations in corner-sharing arrangement.

In the presence of H_4SiO_4 distinct broadening or even splitting of the U-O_{eq} shell was observed. It is also apparent that the backscattering from Si is now recognizable in additon to that from Al around 3.3 Å: $R_{U\text{-}Si} = 3.09$ and 3.82 with CN ≈ 1 for acidic pH; $R_{U\text{-}Si} = 3.07$ with CN ≈ 1 for alkaline pH. These findings suggest the formation of ≡Al-O-U-O-SiO_4H_n ternary sorption complexes (the type-B ternary complex [2]). At acidic pH the contribution of neighboring U in the FT modulus was rather small (< 2 %), suggesting that complexation with H_4SiO_4 on gibbsite surface prevented UO_2^{2+} clustering. The structures of the ternary sorption complexes were optimized in DFT calculations on the basis of the obtained EXAFS parmeters and the corresponding sorption geometries in the binary system. The obtained structures consistent with the EXAFS results are shown in Figure 1 (c) and (d). It was turned out that silicic acid coordinated to sorbed UO_2^{2+} via monodenate complexation at at acidic pH (Figure 1 (c)), while via bidentate complexation at alkaline pH (Figure 1. (d)).

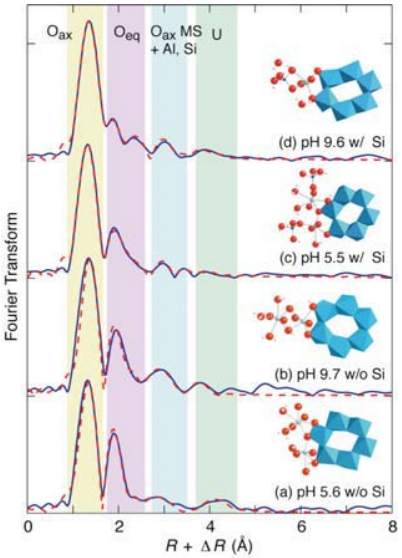

Figure 1. Fourier transform modulus of U-L_{III} edge EXAFS spectra (blue) and theoretical fittings (red) of uranyl adsorbed on gibbsite surface with and without silicic acid. The concentration of UO_2^{2+}, H_4SiO_4 (if present), $NaClO_4$ and gibbsite were 10 μM, 500μM, 0.1 M and 2 g/L, respectively. The pH values of the sampels and the sorption geometires by DFT calculations were inserted in the figure.

Literature cited

1. Tsushima, S.; Rossberg, A.; Ikeda, A.; Muller, K.; Scheinost, A. C., *Inorg. Chem.* **2007,** 46, 10819-10826.
2. Alcacio, T. E.; Hesterberg, D.; Chou, J. W.; Martin, J. D.; Beauchemin, S.; Sayers, D. E., *Geochim. Cosmochim. Acta* **2001,** 65, 1355-1366.

ROBL-CRG	**Experiment title:** Comparative investigation of the uranium complexation by proteins by means of FT-IR and EXAFS spectroscopy	**Experiment number**: 20-01-672
Beamline: BM 20	**Date of experiment**: from: 28.01.2008 to: 31.01.2008	**Date of report**: 02.04.08
Shifts: 9	**Local contact(s)**: Dr. André Rossberg	*Received at ROBL:*
Names and affiliations of applicants (* indicates experimentalists): Main applicant: Dr. Johannes Raff* Applicant: Bo Li* Applicant: Dr. André Rossberg* Applicant: Dr. Harald Foerstendorf Applicant: Dr. Andreas Scheinost		

Report:

The aim of the experiment was to determine the functional groups of the S-layer protein interacting with U(VI). In particular, distinguish between carboxylic and phosphate groups in case of U(VI) protein complexation was expected from the results. Thus, polyglutamate and phosvitin were set up as an organic carboxylic and an organic phosphate model compound with the protein backbone to complex with U(VI). An S-layer with a slightly higher phosphate content was also chosen in the experiment.

The infrared spectra of U(VI) polyglutamate complexes show a characteristic frequency for the $\nu_{as}(UO_2^{2+})$ mode representing a U(VI) complexation to carboxylic groups. The EXAFS spectra confirm these findings by observation of a bidentate binding of the U(VI) to carboxylic groups. Furthermore, in the complex with a U(VI):carboxyl ratio of 1.47:1 two coordinated O-atoms with a shorter U-O distance were detected. The assignment of these O-atoms to distinct functional groups or to the protein backbone has to be verified.

In the phosvitin samples, the U(VI) preferentially binds to phosphate groups, which is demonstrated by the $\nu_{as}(UO_2^{2+})$ peak at 918 cm^{-1} on the IR spectra. With increasing U(VI):phosphate ratio, the binding to carboxylic groups and/or to hydroxyl groups becomes more relevant. This has been demonstrated by a shift of the $\nu_{as}(UO_2^{2+})$ mode to 925 cm^{-1} which is very close to the characteristic frequency of 923 cm^{-1} found for the $\nu_{as}(UO_2^{2+})$ mode after complexation to carboxylic groups of proteins. However, this effect was not observed in the EXAFS spectra. The EXAFS spectra of the phosvitin samples are in good agreement with the spectra of other organic phosphate-U(VI) complexes such as U(VI)–AMP and U(VI)–fructose(1,6)diphosphate complex. In this complexes U(VI) is not only complexed by a phosphate group, but presumably also by a hydroxyl group. Therefore, a formation of a U(VI) complex, which is similar to the so-called "Feldman complex", can be suggested.

In case of the S-layer samples, both IR and EXAFS show that U(VI) mainly binds to carboxylic groups. Particularly, the EXAFS spectra of the S-layer samples are similar to the polyglutamate sample with a U(VI):carboxyl ratio of 1.47:1, where two shorter interatomic U-O distances were found. Furthermore, there are differences between EXAFS spectra of the U(VI)–S-layer complex from this experiment and spectra of the U(VI) complex with an S-layer containing less phosphate groups. Whether the spectral deviations can be assigned to specific U(VI)–phosphate interactions in the S-layer with much lower phosphate content has to be evaluated in future experiments.

Finallly, we would like to express our great appreciation to Dr. Rossberg for the diligant EXAFS data analysis, and of course, to all the ROBL group members for all the support.

ROBL-CRG	**Experiment title:** Influence of carbonate on actinides sorption on clay minerals	**Experiment number:** 20-01-673
Beamline: BM 20	**Date of experiment:** from: 08/04 **to:** 14/04/08	**Date of report:** 26/11/08
Shifts: 18	**Local contact(s):** Dr. Andreas Scheinost	*Received at ROBL:*

Names and affiliations of applicants (* indicates experimentalists):
Maria Marques Fernandes*, Bart Baeyens*, Rainer Daehn*, M. H. Bradbury
Laboratory for Waste Management (LES), Paul Scherrer Institut, 5232 Villigen, Switzerland,

Report:

Clay minerals play an important role in the retention/retardation of radio-contaminants in the near- and far-fields of a radioactive waste repository. In natural environments, the predominant aqueous phase reactions of trivalent actinides and U(VI) are hydrolysis and complexation with dissolved inorganic ligands e.g. carbonates. The formation of strong carbonate complexes in solution can potentially lead to a decrease in metal ion sorption and thus increase the migration rates of actinides
The aim of this work is to improve the mechanistic understanding at the molecular level of the uptake of Am(III) and U(VI) onto clay minerals by investigating the influence of carbonate complexation. This information will prove whether or not ternary complexes form and thereby extend the currently available thermodynamic models for radionuclide sorption (Eu(III)/ Am(III)/ Cm(III)) and U(VI) onto clay minerals by inclusion of carbonates.

Preliminary results

EXAFS spectra were analyzed and fitted using WINXAS and IFEFFIT software package. Backscattering phases and amplitudes were obtained from FEFF8.0 calculations. The Am(III) and U(VI) loaded clays samples were measured at the L_{III} edges of Am(III) (18510 eV) and of U(VI) (17166 eV) resp. in fluorescence mode.

Sorption of Am(III) on *montmorillonite*

EXAFS measurements were performed on Am(III) loaded wet montmorillonite pastes and self supporting montmorillonite films respectively. Samples were prepared in the absence (pH=8) and presence of inorganic carbon (20 mM $NaHCO_3$ at pH 7.4 and 8.3) at a range of Am(III) loadings down to 200 ppm. Fig. 1 shows the Fourier transform and EXAFS spectra of Am loaded Na-montmorillonite (~350 ppm) at pH 8 in the absence of carbonate. The EXAFS parameters obtained by fitting the spectra of the carbonate free sample are consistent with bond lengths from Am-O and Am-Si/Al backscattering pairs. A first shell with 7.9 ± 1.6 O at a distance of 2.48 ± 0.01 Å and a second shell with 1.6 ± 0.5 Si at 3.18 ± 0.01 Å. The identification of Am-Al/Si distances is a clear indication that Am(III) forms inner sphere complexes at the SWy-1 surface.
The EXAFS spectra obtained for the samples prepared in the presence and absence of carbonate clearly show different features (Fig. 2). All the measured carbonate samples show additional peaks in the FT (R~3.8 Å) which might be an indication of the formation of ternary Am-carbonate surface complexes, but could also be due to the precipitation of the solubility liming phase $NaAm(CO_3)_2$. Evaluation of structural parameters (coordination number, bond length) is on-going. To verify whether this features are due to the formation of ternary Am(III)/carbonate complexes or the precipitation of Am(III) solid carbonates at the clay surface measurements on pure reference compounds as well on sorption samples are necessary.

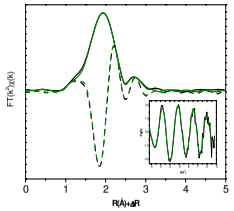

Fig. 1: Fourier transform and k^3-weighted EXAFS spectra of Am loaded Na-montmorillonite. Black line: experimental data, green line: modelled data, broken lines: imaginary part.

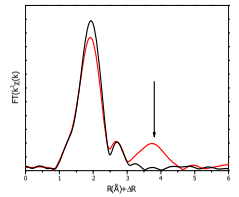

Fig.2. Fourier transform spectra of Am loaded Na-SWy. Black line: in the absence of carbonate, red line: in the presence of carbonate

Sorption of U(VI) on clay minerals

Macroscopic sorption experiments have shown that the presence of inorganic carbonate leads to a strong decrease of the sorption of U(VI) on montmorillonite (Na-SWy-1). P-EXAFS measurements were performed on U(VI) loaded self supporting Na-SWy-1 films. The investigated samples were prepared at pH~8 in the absence and presence of inorganic carbon (1mM $NaHCO_3$). Table.1 summarizes the experimental conditions used for the U(VI) sorption on Na-SWy-1.

Table.1: Summary of experimental conditions

Sample	Conditions 0.1 M $NaClO_4$	pH	Initial U (M)	log Rd ($L.kg^{-1}$)	U loading (ppm)
A	carbonate free	7.9	$1.5 \cdot 10^{-5}$	3.97	1680
B	in 1 mM $NaHCO_3$	7.9	$2.0 \cdot 10^{-5}$	2.7	1190

Fig.3 shows the experimental EXAFS spectra as well as the experimental and fitted Fourier transform spectra of the U(VI) loaded Na-montmorillonite at pH 8 in the absence (A) and presence of carbonate (B) measured at 35°. The EXAFS parameters obtained by fitting the spectra of both samples are summarized in Table 2. Structural data for both systems show unambiguously that U(VI) forms inner-sphere complexes at the clay surface (splitting of the O_{eq} shell, Si shell and Fe shell). However, no considerable difference is observed for these two samples in the absence and presence of carbonate (no C shell ~ 2.90 Å, no O_{dist} shell). This might be an indication that under the given experimental conditions no measurable U(VI)-carbonate ternary complexe forms at the clay surface or that the U-C backscattering amplitude is too weak compared to the U-Si backscattering pairs.

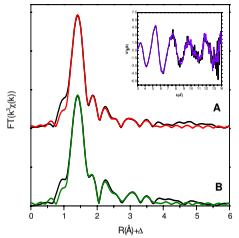

Fig.3. Fourier transform spectra of U(VI) loaded self supporting montmorillonite films. A) in the absence of carbonate, B) in the presence of carbonate. Black line: experimental data, red and green line: modelled data

Table 2: Structural information derived from the EXAFS analysis of U(VI) loaded self supporting montmorillonite films prepared in the absence and in the presence of carbonate at pH~8.

Sample	Shell	N	R (Å)	σ^2(Å^2)	E_0
A	U-O_{ax}	2*	1.80	0.002	8.4
	U-O_{eq1}	3.6	2.29	0.008	
	U-O_{eq2}	3.1	2.48	0.008	
	U-Si/Al	0.5	3.09	0.003*	
	U-Fe	0.3	3.41	0.003*	
	U-Si/Al	2.3	3.84	0.013	
B	U-O_{ax}	2*	1.80	0.002	9.6
	U-O_{eq1}	3.5	2.29	0.007	
	U-O_{eq2}	2.9	2.50	0.007	
	U-Si/Al	0.8	3.10	0.003*	
	U-Fe	0.5	3.43	0.003*	
	U-Si/Al	1.6	3.86	0.011	

*Fixed values, fitting range: k:3.6-12.6 $Å^{-1}$. MS path of the uranyl moiety was linked to U-Oax scattering as described in[1]

1. Hudson, E.A., Allen, P.G., Terminello, L.J., Denecke, M.A. and Reich, T., Polarized x-ray-absorption spectroscopy of the uranyl ion: Comparison of experiment and theory. Physical Review B, 1996. 54(1): p. 156.

ROBL-CRG	**Experiment title:** EXAFS investigations of U(VI) uptake by cementitious materials	**Experiment number**: 20-01-674
Beamline: BM 20	**Date of experiment**: from: 14/04/2008 at 8:00 to: 18/04/2008 at 8:00	**Date of report**: 14.11.08
Shifts: 9	**Local contact(s)**: Dr. Dipanjan BANERJEE (banerjee@esrf.fr)	*Received at ROBL:*
Names and affiliations of applicants (* indicates experimentalists): **N. Macé (*), R. Daehn (*),J. Tits (*),D. Kunz (*) and E. Wieland** Laboratory for Waste Management Paul Scherrer Institut, Villigen-PSI, Switzerland		

Uranium L_{III}-edge (17166 eV) extended X-ray absorption fine structure (EXAFS) spectra were recorded at room temperature (RT). We used XAS spectroscopy to determine the local chemical environment of U(VI) in cementitious materials: calcium silicate hydrates (C-S-H phases) and crushed and fully hydrated hardened cement pastes (HCP). In addition, Soddyite, Uranophane and $CaUO_4.H_2O$ (phase X) have been measured as U(VI) references compounds. EXAFS data were reduced with the Iffefit software package. Theoretical scattering paths were calculated with FEFF8.0, including multiple scattering paths.

Figure 1a shows EXAFS spectra for the most important U(VI) reference compounds ($CaUO_4.xH_2O$ or phase X, uranophane and soddyite), employed as dry powder, together with those of U(VI) sorption samples (HCP/U(VI) and C-S-H/U(VI)), which were used as wet pastes. **Figure 1b** shows their corresponding Radial Structural functions (RSFs) calculated from Fourier transforming k^3-weighted EXAFS functions between 2 and 11 Å. The sorption samples were prepared by adding U(VI) solution to crushed-fully-hydrated HCP in ACW or C-S-H suspension, respectively, and subsequently equilibrating the suspensions for 30 days. After separation from the supernatant solution by centrifugation, the wet pastes were mounted in a Plexiglas sample-holder and sealed with kapton® tape.

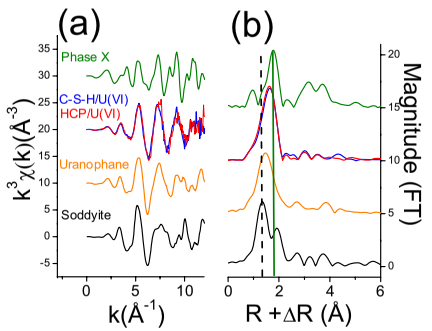

Figure 1: k^3-weighted experimental EXAFS data for selected U(VI) reference compounds and U(VI) sorption samples (a) and their corresponding RSFs (b), k range was taken between 2 and 11 $Å^{-1}$ for all FTs.

At low loadings, the EXAFS data showed that the chemical environments of U(VI) taken-up by C-S-H and HCP are similar. Thus, one may conclude that C-S-H phases are most likely responsible for the U(VI) immobilization in HCP. Furthermore, at low loadings, the chemical environments of the U(VI) taken-up by C-S-H and HCP species are different from a soddyite-like or phase-X-like coordination environment but resemble that of U(VI) in uranophane.

Future Outlook:

The next step of this study is to determine the long term behavior of U(VI) in cementitious systems. The next XAS measurements will be dedicaced to U(VI) immobilized samples in C-S-H (with variable C/S ratio) and HCP with at least 300 days of contact time. The measurements will be done at RT.

Conferences contributions:

07/2008 : Actinide XAS 2008, 5th workshop on speciation, techniques and facilities for radioactive materials at synchrotron light sources (Saint-Aubin, France). **N. MACE, M. HARFOUCHE, R. DÄHN, J. TITS, A. SCHEINOST AND E. WIELAND**. *EXAFS Investigation of U(VI) Speciation In Cementitious Materials*. **Poster**

ROBL-CRG	**Experiment title:** Investigation of the aqueous phase in the ternary sorption system uranium(VI), Goethite, organic model compounds.	**Experiment number:** 20-01-675
Beamline: BM 20	**Date of experiment:** from: 01.03. 23.07. 10.11. to: 04.03.08 27.07.08 14.11.08	**Date of report:** 20.03.08
Shifts: 30	**Local contact(s):** A. Rossberg	*Received at ROBL:*
Names and affiliations of applicants (* indicates experimentalists): A. Rossberg*, C. Lucks*		

EXPERIMENTAL. Sample solutions were prepared by dissolving UO_3 in perchloric acid and adding the needed amount of solid DL-tartaric acid. After the pH was adjusted to pH 7 the UV-visible pH titration experiment was performed by adding negligible small volumes of highly concentrated acids. The UV-vis data was collected on a Cary 50 spectrophotometer in the spectral range from 700 to 350 nm. At seven selected pH points solutions were prepared for measuring both EXAFS and UV-vis. The uranium L_{III}-edge EXAFS measurements were performed in transmission.

RESULTS. The UV-visible pH titration data was treated using the program pHab [1]. For the computation complex stability constants from literature [2,3,4] were used as initial values. It has been approved that between pH 3 and 5 the dimeric uranyl tartrate$(UO_2)_2(H_{-1}Tar)_2^{2-}$ is the dominant species and that at higher pH values a further oligomerization to the trimer $(UO_2)_3(H_{-1}Tar)_3(OH)_2^{5-}$ occurs. Furthermore there was found no evidence for the occurrence of a tridentate monomer which was also postulated in literature [2-4]. EXAFS analyses were done using iterative target transform factor analyses. Three factors were found to be sufficient for fitting the data. According to the speciation these factors must be the hydrated uranyl ion, the dimer and the trimer. This suggestion is supported by the fact that the relative concentrations of those factors fit very well to the speciation that was computed using the UV-vis data.
Factor 2 and 3 show a strong U-U interaction at 3.93 Å and 3.81 Å respectively (Tab. 1). These distances are in fair agreement with U-U distances of dimers or trimers of the

Table 1: EXAFS structural parameters for the three factors.

	Atom	N	R	σ^2
Factor 1	Oax	2*	1.766(1)	0.00112(6)
	Oeq	5*	2.404(3)	0.0075(3)
Factor 2	Oax	2*	1.787(9)	0.00129(6)
	Oeq	5*	2.356(2)	0.0061(2)
	C	2.1(8)	3.28(1)	0.006(3)
	U	1*	3.927(6)	0.0054(4)
	U-U distance of $(UO_2)_2(OH)_2^{++}$: 3.87 [5]			
Factor 3	Oax	2*	1.803(1)	0.00142(7)
	Oeq	5*	2.360(4)	0.0113(4)
	C	1.5(5)	3.29(2)	0.006*
	U	2*	3.806(2)	0.0048(2)
	U-U distance of $(UO_2)_3(O)(OH)_3^+$: 3.83 [5]			

* fixed ()- standard deviation

hydrolysis species in aqueous phase from DFT calculations [5]. The determined U-C distances give evidence for the formation of five or six membered rings. According to the sum formulas of both complexes the tartrate ion connects tridentately to uranium using one hydroxyl and two carboxyl groups. These pieces of information lead to the postulation of the following structures (Fig. 1).

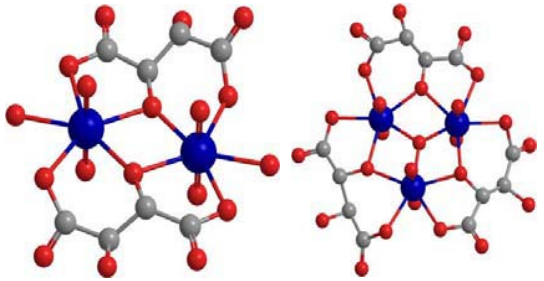

Figure 1: Proposed structures for the uranium tartrate dimer (left) and uranium tartrate trimer (right).

REFERENCES

[1] Gans, P. et al. (1999) *Annali di Chimica*, **89**, 45-49.
[2] Feldman, I. et al. (1960) *Annali di Chimica*, **64**, 1224-1230.
[3] Rajan, K.S. et al. (1964) *J. Inorg. Nucl. Chem.* **26**, 1927-1944.
[4] Sircar, J.K. et al. (1982) *J. Chem. Eng. Data*, **27**, 231-233.
[5] Tsushima, S. (2007) *Inorg. Chem.* **35**, 784-787.

ROBL-CRG	**Experiment title:** Selenium solid phase speciation in Boom Clay conditions	**Experiment number:** 20-01-677
Beamline: BM 20	**Date of experiment:** from: 04-07-08 to: 08-07-20	**Date of report:** 23-12-2008
Shifts: 9	**Local contact(s):** Andreas SCHEINOST	*Received at ROBL:*

Names and affiliations of applicants (* indicates experimentalists):

* Dr. Eric Breynaert (KULeuven)
* Dirk Dom (KULeuven)
* Sam Hertsens (KULeuven)
  Prof. André Maes (KULeuven)
* Dr. Andreas SCHEINOST (FZD)

Report:

According to the latest performance assessment calculations for the current geological storage scenario for high level radioactive waste in the Belgian Boom Clay formation, Se will contribute the highest dose to man. Since the mobility and consequently also the dose contribution is highly related to the speciation of selenium, the knowledge on its behaviour in the far field of the Boom Clay formation is very important for the safety case of the future Belgian high level waste disposal program.

Previous XAS-based results on the interaction of selenite with FeS_2 and FeS at circum-neutral pH have shown that selenite is reduced to respectively Se^0 and $FeSe_x$ (Breynaert et al., 2008; Scheinost and Charlet, 2008; Scheinost et al., 2008). Since pyrite (FeS_2) is one of the main minerals governing the redox conditions of the Boom Clay solid phases, it is expected that selenite will be reduced to Se^0 in the Boom Clay system, thereby effectively limiting the solution concentration to the solubility of Se^0, provided that there is no interaction with the mobile Boom Clay organic matter.

During the present experiment, cryostat (15K) XAS measurements were performed on different fractions of Boom Clay batch systems, separated after equilibration with three concentrations of selenite (10^{-5}, 10^{-4},10^{-3} M) for one month with the complete Boom Clay batch systems in a glovebox. After the equilibration period each batch system was separated into 4 solid phase fractions (sand, clay/silica, pyrite, immobile organic matter) and one supernatant by respectively: 1/ gravitational precipitation (2x10 minutes), 2/ centrifugation at 270 g (2x 10 minutes), 3/ centrifugation at 4350g (10 minutes) and 4/ centrifugation at 27200g (60 minutes). XAS measurements were done on solid phase fractions 2 to 4 and on the supernatant.

Based on the XANES/EXAFS analysis, all solid phase fractions contained Se^0, confirming the reduction of selenite to metallic selenium in the Boom Clay system. Except for the samples equilibrated with 10^{-5} M of selenite, different levels of unreduced selenite were also observed in addition to Se^0. This was confirmed by the results obtained for the supernatant phases of systems equilibrated with 10^{-4} and 10^{-3}M of Se, where the dominant speciation was found to be selenite. For the system equilibrated with 10^{-5} M of Se, the equilibrium solution concentration dropped down to $5x10^{-6}$M of Se. Despite of the low equilibrium concentration, XANES measurements were possible and unexpectedly indicated the presence of a selenide phase (FeSe or and organic selenide), although Se^0 was observed on the respective solid phase fractions (Figure 1). This indicates that the theoretically expected reduction of Se(IV) to Se(-II) is indeed possible in Boom Clay batch systems, although Se(-II) has not been experimentally observed before in the Boom Clay system.

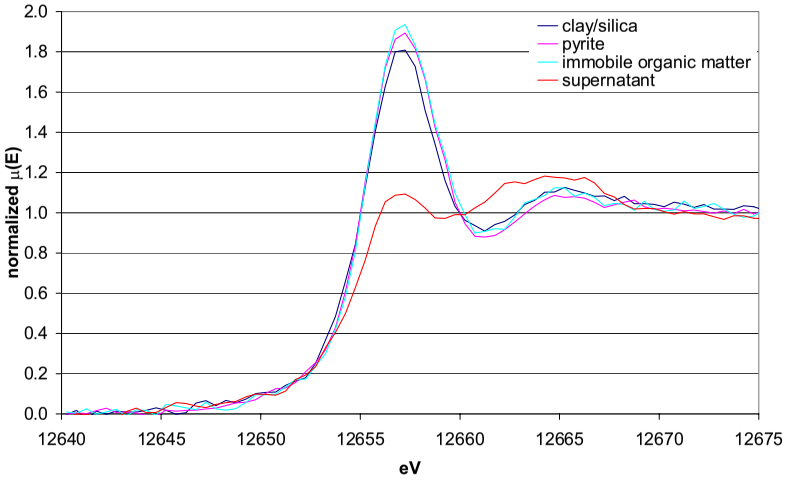

Figure 1: XANES spectra (15K) of different fractions of a Boom Clay batch system equilibrated with $5x10^{-6}$M Se(IV) for 1 month.

Conclusions

XAS based solid phase speciation has demonstrated that selenite [Se(IV)] is reduced to Se^0 on the Boom Clay systems solid phase. After 1 month equilibration of 10^{-5} M of selenite in Boom Clay batch systems, a selenide phase (FeSe or and organic selenide) was observed in the supernatant solution, although Se^0 was observed on the different solid phases.

Breynaert E., Bruggeman C., and Maes A. (2008) XANES−EXAFS analysis of Se solid-phase reaction products formed upon contacting Se(IV) with FeS_2 and FeS. *Environ. Sci. Technol.* **42**(10), 3595-3601.

Scheinost A. C. and Charlet L. (2008) Selenite reduction by mackinawite, magnetite and siderite: XAS characterization of nanosized redox products. *Environ. Sci. Technol.* **42**, 1984–1989.

Scheinost A. C., Kirsch R., Banerjee D., Fernandez-Martinez A., Zaenker H., Funke H., and Charlet L. (2008) X-ray absorption and photoelectron spectroscopy investigation of selenite reduction by FeII-bearing minerals. *J. Contam. Hydrol.* **102**, 228-245.

ROBL-CRG	**Experiment title:** Identification of thioarsenate XAS spectra in liquid and solid samples	**Experiment number:** 20-01-680
Beamline: BM 20	**Date of experiment:** From: 27/07/2008 to: 30/07/2008	**Date of report:** 23/12/2008
Shifts: 9	**Local contact(s):** Dr. Andreas Scheinost	*Received at ROBL:*

Names and affiliations of applicants (* indicates experimentalists):

E. Suess[1], G. Bernhard[2], WA. Gezahegne[1], BJ. Merkel[1], B. Planer-Friedrich[3], AC. Scheinost*[2,4]

[1]Institute for Geology, TU Bergakademie Freiberg, 09599 Freiberg, Germany

[2]Institute for Radiochemistry, Research Center Dresden, 01314 Dresden, Germany

[3]Environmental Geochemistry, University of Bayreuth, 95447 Bayreuth, Germany

[4]ESRF-ROBL/CRG, 38043 Grenoble Cedex, France

Report:

Background. In natural systems As and S often occur together and thus inter-elemental reactions and complex formations play a major role for mobility and toxicity of arsenic. There are controversies whether the As-S species occurring under reduced conditions are thioarsenites[1-4] or thioarsenates[4-7]. The recent study focused on obtaining X-ray Absorption Spectroscopy (XAS) data for thioarsenate standards already identified as such by XRD[5], indispensable for all further studies.

Experimental. The solid thioarsenate salts (mono-, di-, and tetrathioarsenate; pellets with 8.9 mg total As in 300 mg Boronitrite), and liquid and flash-frozen thioarsenate solutions (10 mM, pH ≈ 12) were subject to XAS experiments at the Rossendorf Beamline (BM20) in Grenoble, France. XAS spectra were collected at the As K-edge (11867 eV) at room temperature (liquids) and at 15 K (He-Cryostat; solids and flash-frozen samples) in absorption (Oxford ionization chamber) and fluorescence mode (Canberra 13-element Ge-Detector). The spectra were averaged, dead-time corrected, background subtracted and normalized using *SixPack*[8]. EXAFS shell fitting was performed using FEFF 7.02 and WinXAS 3.1[9].

Results. The As-O and As-S coordination numbers (Tab. 1) confirmed the structure as the expected mono- (AsO_3S^{3-}), di- ($AsO_2S_2^{3-}$), and tetrathioarsenates (AsS_4^{3-}). The As-O bond distances of 1.69 to 1.70 Å are comparable with those stated for arsenates (e.g. scrondiotite 1.60 Å[10]), and are easily distinguishable from those for arsenite at 1.78 Å. The As-S distances with 2.13 to 2.18 Å were clearly shorter than those published for arsenite-sulfide minerals with 2.24 to 2.34 Å[10]. As expected, no As-O bonding was determined in tetrathioarsenate, which is fully coordinated with S. As the extent of sulfide-groups increases, the position of the absorption edge shifts systematically and linearly towards lower energies compared to that of arsenate. The structural data for the individual solid and liquid samples, measured at room temperature or at 15 K, did not show obvious differences, suggesting that the aqueous complexes have similar structures as the XRD-identified solids and are stable in solution.

Table 1: As-K edge energies and EXAFS fit results of thioarsenate standards

Thioarsenate samples	**E_0 [eV]**	**O coordination**			**S coordination**			**ΔE_0 [eV]**	**χ^2_{res} %**
		CN	**R[Å]**	**σ^2[Å^2]**	**CN**	**R[Å]**	**σ^2 [Å^2]**		
Mono- (liquid, 15K)	11871.0	2.9	1.70	0.0007	0.9	2.17	0.0001	6.0	23.9
Mono- (liquid, RT)	11871.0	2.8	1.70	0.0025	0.7	2.13	0.0013	4.8	23.4
Mono- (solid)	11871.0	2.6	1.70	0.0016	0.7	2.14	0.0014	6.2	20.2
Di- (liquid, 15K)	11870.0	2.0	1.70	0.0015	1.7	2.15	0.0007	6.4	22.3
Di- (solid)	11870.0	1.6	1.70	0.0007	1.9	2.17	0.0022	8.2	17.7
Tetra- (liquid, 15K)	11869.5				4.5	2.18	0.0029	9.8	25.3
Tetra- (liquid, RT)	11869.0				4.1	2.18	0.0030	8.8	15.0
Tetrathioarsenate (solid)	11869.5				3.9	2.17	0.0025	7.8	16.9
CN: coordination number, error ± 25 %, R: Radial distance, error ±0.01 Å, σ^2: Debye-Waller factor, error ±0.0005 Å^2									

References.

(1) Wood, S.et al. *Geochem. Trans.* **2002**, *3*, 31.
(2) Wilkin, R. T.et al. *Geochem. Trans.* **2003**, *4*, 1.
(3) Beak, D. G.et al. *Environ. Sci. Technol.* **2008**, *42*, 1643.
(4) Helz, G. R.et al. *Geochim. Cosmochim. Acta* **2008**, 72, 4457.
(5) Wallschlager, D.et al. *Anal. Chem.* **2007**, *79*, 3873.
(6) Stauder, S.et al. *Environ. Sci. Technol.* **2005**, *39*, 5933.
(7) Planer-Friedrich, B.et al. *Environ. Sci. Technol.* **2007**, *41*, 5245.
(8) Webb, S. M. *Phys. Scr.* **2005**, *T115*, 1011.
(9) Ressler, T. *J. Synchrot. Radiat.* **1998**, *5*, 118.
(10) Foster, A. L. *In:* Welch, A. H. & Stollenwerk, K. G., Eds.; Kluwer Academic Publishers: Boston, 2003; 27.

ESRF	**Experiment title: "EXAFS spectro-electrochemical study of U(III), U(IV), U(V) and U(VI) chloro complexes in ionic liquids"**	**Experiment number**: CH-2297
Beamline: BM20	**Date of experiment**: from: 10/03/07 to: 13/03/07	**Date of report**:
Shifts: 9	**Local contact(s)**: Christoph Hennig	*Received at ESRF:*

Names and affiliations of applicants (* indicates experimentalists):

Marie-Olga Sornein*, Claire Le Naour*, Mickaël Mendes, Céline Cannes,

CNRS/IN2P3/Univ. Paris sud, Institut de Physique Nucléaire, 91406 Orsay cedex, France

Christoph Hennig*

ESRF-ROBL – Forschungszentrum Dresden-Rossendorf, 38000 Grenoble, France

Jean-Claude Berthet,
CEA, DSM, IRAMIS, SCM, CNRS URA 331, 91191 Gif-sur-Yvette, France

Report:

The measurements were performed using a double crystal Si(111) monochromator in equidistant *k*-steps of 0.05 Å^{-1} across the EXAFS region. Higher harmonics were rejected by two platinum-coated mirrors. The measurements were carried out at ambient temperature in transmission mode using argon-filled ionization chambers. For the energy calibration the first inflection point of an yttrium metal foil at 17038 eV was used. The uranium L_{III} threshold energy, $E_{k=0}$, was arbitrarily defined at 17185 eV. EXAFS data extraction and data fit were performed with the program EXAFSPAK [1]. Theoretical phase and amplitude functions were calculated with FEFF 8.2 [2]. The amplitude reduction factor, S_0^2, was defined as 0.9. The multiple scattering paths in the uranyl unit were included in the curve fit by constraining its Debye-Waller factor and its effective path-length to twice the values of the corresponding U–O_{ax} single-scattering path. The overall goodness of the fits, *F*, is given by χ^2 weighted by the magnitude of data.

EXAFS measurements were carried out on a solution of $[UCl_6]^{2-}$ (0.02M) in [Bmim][Tf_2N] before and after quantitative oxidation. The electrolysis was performed in a classical electrochemical cell at controlled potential with a carbon working electrode and the two compartments were separated with a frit. The results obtained for the sample before electrolysis were in good agreement with the ones already reported [3]. The results obtained after electrolysis were compared with a sample containing the uranyl tetrachloro complex. Indeed, the UV-visible spectroscopic analysis has shown that the $[U^{IV}Cl_6]^{2-}$ compound is converted into $[U^{VI}O_2Cl_4]^{2-}$ by oxidizing electrolysis. The EXAFS measurements confirm that the electrolysis was successful and that the uranium(IV) hexachloro complex was transformed almost quantitatively into the uranyl(VI) tetrachloro complex.

EXAFS measurements were also performed on solutions of $UO_2(OTf)_2$ (0.02 M) in presence of 4 equivalents of [Bmim]Br and [$MeBu_3$N]Br in [Bmim][Tf_2N] and [$MeBu_3$N][Tf_2N] respectively. The UV-visible spectroscopic analysis has shown that the predominant chemical form in these sample is the uranyl tetrabromo complex ($[U^{VI}O_2Br_4]^{2-}$). Theoretical phase and amplitude functions were calculated using the crystal structure of $[NH_4]_2[UO_2Br_4]\cdot 2H_2O$ [4]. Bromide ions are the main coordinating ligands, but beside the solvent, the residual water contained in the ionic liquid may also act as a ligand. Therefore, the possibility of a participation of oxygen from water in the coordination of U(VI) bromo-complex has to be considered. The k^3 weighted U L_{III}-edge EXAFS spectra obtained for the 0.02 M $[UO_2Br_4]^{2-}$ solutions in [Bmim][Tf_2N] and [$MeBu_3$N][Tf_2N] at room temperature are shown in Figure 1. In both ionic liquids, the first peak of the Fourier transform in the k range of 4.2–16.2 Å^{-1} (Fig. 1), corresponds with the two axial oxygen atoms with a U–O distance of 1.77 Å. The second shell indicates bromine atoms in a U–Br distance of 2.82 Å in [Bmim][Tf_2N] and 2.83 Å in [$MeBu_3$N][Tf_2N] (Table 1). These distances are in a good agreement with a fourfold Br coordination, although the determined equatorial coordination numbers are slightly higher than 4. An inclusion of solvent or water molecules did not improve the fit procedure. Therefore, we can conclude that the $[UO_2Br_4]^{2-}$ coordination polyhedron is maintained in [Bmim][Tf_2N] and [$MeBu_3$N][Tf_2N] without any other ligand in the coordination shell. From these results, the ionic liquid cation seems to have no influence on the coordination sphere of the tetrabromo uranyl complex and on the U–Br and U–O distances.

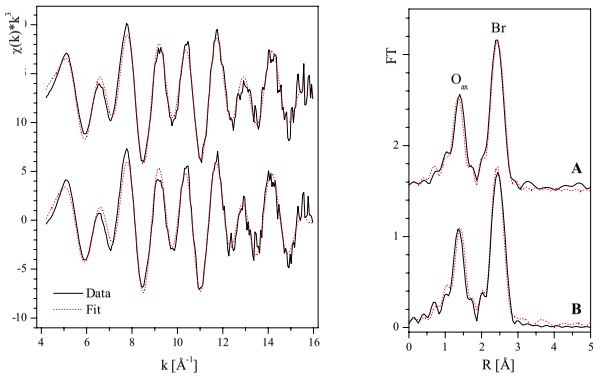

Figure 1. U L_{III}-edge k^3-weighted EXAFS data (left) and the corresponding Fourier transforms (right) of a 0.02M $[UO_2Br_4]^{2-}$ solution in [Bmim][Tf_2N] (A) and [$MeBu_3$N][Tf_2N] (B) at 25°C, with raw data (solid line) and fit results (dotted line).

Sample	Scattering path	*R* [Å]	*N*	σ^2 [Å^2]	$\Delta E_{k=0}$	*F*
$[UO_2Br_4]^{2-}$ in	U–O_{ax}	1.766(2)	2.0(1)	0.0015(3)	-2.6	0.24
[Bmim][Tf_2N]	U–Br	2.821(2)	4.4(2)	0.0051(2)		
$[UO_2Br_4]^{2-}$ in	U–O_{ax}	1.768(2)	1.9(1)	0.0013(3)	-1.8	0.24
[$MeBu_3$N][Tf_2N]	U–Br	2.827(2)	4.2(2)	0.0047(2)		

Table 1 : EXAFS fit parameters of $[UO_2Br_4]^{2-}$ (0.02M) in [Bmim][Tf_2N] and [$MeBu_3$N][Tf_2N]
Standard deviations are given in bracket. The threshold energy, $E_{k=0}$, was arbitrarily defined at 17185 eV and varied as a global fit parameter resulting in the energy shift $\Delta E_{k=0}$.

Results were submitted and accepted for publication in Polyhedron. These researches are supported by the Actinet program, an European network for actinide sciences.

References

[1] G. N. George, I. J. Pickering, EXAFSPAK, a suite of computer programs for analysis of X-ray absorption spectra; Stansford Synchrotron Radiation Laboratory, Stanford, 2000.

[2] A. L. Ankudinov, B. Ravel, J. J. Rehr, S. D. Conradson, Phys. Rev. B 58 (1998) 7565-7576.

[3] S. I. Nikitenko, C. Hennig, M. S. Grigoriev, C. Le Naour, C. Cannes, D. Trubert, E. Bossé, C. Berthon, P. Moisy, Polyhedron 26 (2007) 3136-3142.

[4] G. Van den Bossche, M. R. Spirlet, J. Rebizant, J. Goffart, Acta Cryst. C 43 (1987) 383-384.

ESRF

Experiment title: **Se(IV) / Fe(II) on imogolites: sorption and redox processes**	**Experiment number**: CH2300
Beamline: BM20	**Date of experiment**: from: 3/2/07 to: 6/2/07; from: 12/2/07 to: 12/2/07 — **Date of report**: 20/2/07
Shifts: 9	**Local contact(s)**: Andreas Scheinost — *Received at ESRF:*

Names and affiliations of applicants (* indicates experimentalists):

*** Alejandro Fernández-Martínez, * Gabriel J. Cuello**

Institut Laue-Langevin, 6 rue Jules Horowitz, 38042 Grenoble, France

*** Laurent Charlet**

Equipe de Géochimie de l'Environnement, LGIT-UJF, BP 53, 38041 Grenoble, France

*** Gabriela Román-Ross**

Universidad de Girona, Dpt. de Química, Campus de Montilivi 17071 Girona, España

*** Fabrizio Bardelli**

BM8-GILDA, European Synchrotron Radiation Facility, BP 220, 38043 Grenoble, France

Report:

The main objectives of this proposal were (1) to study the structure of complexes of Se and Fe sorbed on Imogolite and (2) to elucidate, by XANES analysis, what kind of redox reactions (if any) are taking place on the system Fe^{2+}/SeO_3^{2-}/Imogolite.

The first objective has an interest in parallel to the study of the Fe/Se/Imogolite system itself: the structure and charge distribution of Imogolite, a nanotubular clay material, is not well known. Some authors claim the existence of a permanent charge of different sign on the inner (-) and outer (+) surfaces. The nature (in the absence of isomorphic substitutions in the structure of the clay) of this permanent charge is under study.

The study of a serie of Se/Imogolite and Fe/Imogolite samples at different pH values may help us to understand this charge distribution. We have measured 3 different samples of Se/Imogolite at pH 4, 7 and 9. EXAFS data at Se K-edge show a low frequency from a first shell of O atoms, covalently bonded into the structure of Selenite (SeO_3^{2-}). Fourier transform of Se EXAFS oscillations show the presence of a second shell. The high frequency signal is more appreciable at low pH (pH 4). This could be indicating a tendency towards inner-sphere complexation; further measurements at more pH values could help us to complete this investigation. The analysis of XANES data shows as well a difference between XANES signal of sample at pH 9 and pH 4. Se sorbed on Montmorillonite and in Na_2SeO_3 solid have been shown for comparison. Further reference data of SeO_3^{2-} in solution will be measured in next experimental rounds.

The outer surface of Imogolite is a curved Gibbsite sheet, while the inner surface has SiOH groups. Data of Se sorbed on silica are presented in Figure 1, showing a first shell and apparently the existence of an outer sphere complexation. Reference samples of Se sorbed on Gibbsite are going to be measured in next experimental rounds for comparison with present data.

In the case of Fe one Fe/Imogolite sample has been measured in fluorescence mode, showing a noisy spectrum from which a XANES analysis can be done. The Fe^{2+} ion is expected to diffuse into the nanotubes' internal pores which may be preventing a good detection of the fluorescence signal. Further samples are going to be measured at different pH in order to clarify the complexation structures formed on the Imogolite surface. A reference sample of $FeCl_2$(l) has been measured. More reference samples of Fe^{2+}/Silica are going to be measured.

Once the structure of this complexes is precisely determined, the study of 5 samples with different times of reaction SeO_3^{2-} vs. Fe^{2+}/Imogolite will be measured. The combined EXFAS/XANES analysis of these data will give light into the nature of redox reactions. We expect to complete this work in a future experiment at BM20.

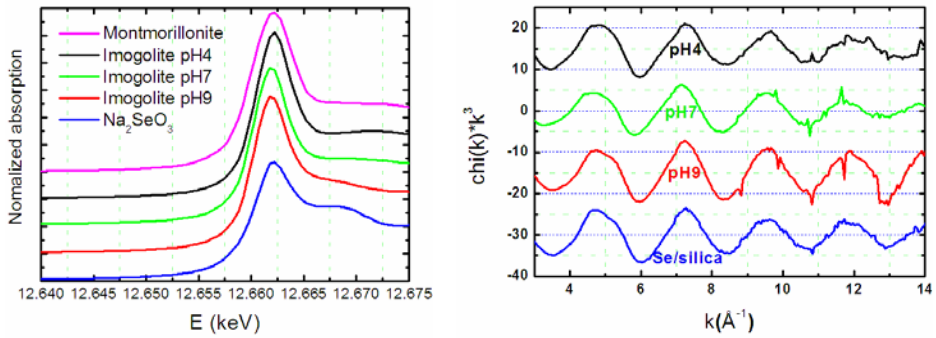

Figure 1. XANES and EXAFS spectra of SeO32- sorbed on Imogolite and on different reference materials.

The experimental apparatus at BM20 is perfectly suitable for this experiment. It allows a very fast exchange of the sample into the closed-cycle He-cryostat, keeping a cold atmosphere of 15 K.

ROBL-CRG	**Experiment title:** Free and silica-gel-bound tetraazamacrocycles as complexing agents of actinide cations: investigation of the solid-state coordination scheme.	**Experiment number**: CH-2423
Beamline: BM 20	**Date of experiment**: from: 23/11/2007 to: 26/11/2007	**Date of report**: February 18, 2009
Shifts: 12	**Local contact(s)**: Dr. Andreas SCHEINOST (scheinost@esrf.fr)	*Received at ROBL:* February 19, 2009

Names and affiliations of applicants (* indicates experimentalists):

*Dr. Michel MEYER
Institut de Chimie Moléculaire de l'Université de Bourgogne
(ICMUB - UMR 5260 du CNRS)
9, avenue A. Savary
21078 DIJON Cedex

*Dr. Andreas SCHEINOST
Rossendorf Beamline at ESRF (ROBL - BM 20)

Report:

The development of separation processes aimed at the selective uptake of radiotoxic metal ions from dilute wastewaters and industrial process streams is of paramount importance for preventing environmental contamination, but still remains a challenging scientific task. From that point of view, solid-liquid extraction using chelating agents covalently grafted on hydrophilic supports is appealing, mainly because the affinity and selectivity of the scavenging material towards the targeted species can be fine-tuned by molecular design. Hybrid organic-inorganic materials consisting of *N*-functionalized tetraazamacrocycles bearing either three acetate ($n = 0$) or propionate ($n = 1$) dangling arms, which are covalently grafted on the surface of mesoporous silica-gel beads (Figure 1), proved to be efficient extracting agents for various actinides (U, Pu, Am) contained at sub-ng/L concentration levels in real aqueous effluents.[1]

In order to probe the coordination scheme of metal cations at the surface of the modified silica gels, and thus gain further insight into the extraction mechanism at the molecular level, we have recorded the low temperature (20 K) XAFS spectra at the L_{III} edge of both hybrid materials loaded with uranium(VI) and plutonium(IV). In addition, uranyl nitrate adsorbed on amorphous Kieselgel 60, used as solid support for these materials, was also studied for comparison purposes as well as a series of solid compounds that precipitated out upon reacting the four model ligands H_3TEPr3A, H_3TEPr3P, H_4TETA, and H_4TETP (Figure 1) with uranium(VI) and plutonium(IV) nitrate in acidic media. To the best of our knowledge, this study represents the first structural investigation of plutonium(IV) complexes formed with polyazamacrocyclic ligands.

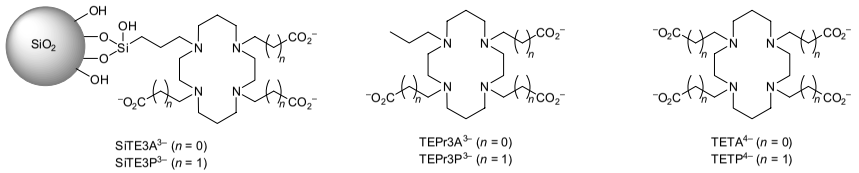

Figure 1. *Structural formula and nomenclature of the modified silica gels and model ligands considered in this work.*

Analysis of the EXAFS spectra at the U L_{III} edge pertaining to both hybrid gel samples provided evidence of two well-separated oxygen coordination shells in the equatorial plane at 2.3 and 2.5 Å, suggesting the formation of uranyl surface complexes. Taking into account multiple scattering contributions, the spectral morphology could be best reproduced by a binding model that involves a pentacoordinate uranium center interacting with oxygen atoms belonging both to the silica support and the organic ligand. Similarly to bare Kieselgel (Figure 2a), each uranyl ion is bound to a surface silanolate group in a bidentate fashion, thus forming an inner sphere complex. In the presence of macrocyclic chelators, carboxylate groups provide two oxygen atoms belonging either to a pair of monodentate or, more probably, to a single bidentate $-CO_2^-$ binding unit (Figure 2b). Preliminary results were disclosed at the *Actinide XAS 2008* meeting hold in Saint-Aubin (France) in July 2008, while an brief account of the work has been accepted for publication in the proceedings of this conference.[2]

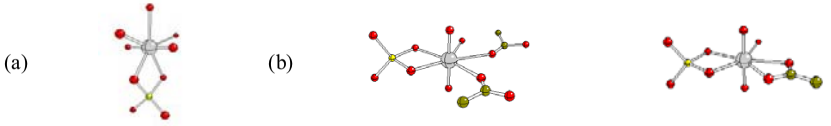

Figure 2. *Suggested binding schemes of UO_2^{2+} at the surface of (a) Kieselgel 60 and (b) the modified silica gels SiTE3A and SiTE3P.*

As far as the Pu L_{III} edge spectra are concerned, analysis of the XANES region enabled to safely conclude that plutonium did not undergo significant reduction and thus remained in the +IV oxidation state during the preparation of all six samples. The EXAFS spectra recorded for the isolated complexes involving the free macrocycles are almost superimposable and show great similarities with those pertaining to both silica gels. The first peak appearing in the 1–2.1 Å region was assigned to the backscattering signal from 8 to 9 oxygen atoms comprising the first coordination sphere around the absorbing plutonium(IV) centers. Together with a relatively intense peak in the FT near 3.8 Å, which was assigned to 3 or 4 Pu–Pu contributions, these features point to the presence in all samples of small plutonium clusters whose structures are reminiscent of PuO_2. However, the 2–2.8 Å range exhibits subtle differences that enabled to discriminate free from immobilized complexes. The corresponding spectral morphology was explained either by Pu–C back scattering paths involving two mono- (3.46 Å) and two bidentate (2.88 Å) carboxylate groups for the complexes, or by Pu–C (3.88 and 3.45 Å) and Pu–Si (3.11 Å) interactions in the case of the silica-based materials.

1 F. Barbette, F. Rascalou, H. Chollet, J. L. Babouhot, F. Denat, R. Guilard, *Anal. Chim. Acta* **2004**, *502*, 179-187. H. Chollet, J. L. Babouhot, F. Barbette, R. Guilard, WO 01 15806, **2001**.

2 L. Giachini, S. Faure, M. Meyer, L. V. Nguyen, B. Batifol, H. Chollet, R. Guilard, A. C. Scheinost, C. Hennig, *Proceedings of the 5th Workshop on Speciation, Techniques, and Facilities for Radioactive Materials at Synchrotron Light Sources (Actinide XAS 2008)*, Saint-Aubin, France, in press.

100

ESRF

Experiment title: Free and silica-gel-bound tetraazamacrocycles as complexing agents of actinide cations: investigation of the solid-state coordination scheme.	**Experiment number:** CH-2423
Beamline: BM 20	**Date of experiment:** from: 18/04/2007 to: 20/04/2007
Shifts: 6	**Local contact(s):** Dr. Andreas SCHEINOST (e-mail: scheinost@esrf.fr)
	Date of report: 15/12/2007
	Received at ESRF:

Names and affiliations of applicants (* indicates experimentalists):

Dr. Michel MEYER
Institut de Chimie Moléculaire de l'Université de Bourgogne
(ICMUB - UMR 5260 du CNRS)
9, avenue A. Savary
21078 DIJON Cedex

Dr. Andreas SCHEINOST

Rossedorf Beamline at ESRF (ROBL - BM 20)

Report:

The development of separation techniques, which selectively extract metal ions from dilute wastewaters and industrial process streams, is a challenging scientific problem. A series of functionalized tetraazamacrocyclic ligands covalently bound on the surface of silica-gel beads have been developed by the Institut de Chimie Moléculaire de l'Université de Bourgogne (ICMUB, UMR 5260, Dijon-France) for the selective extraction of actinides.[1] In collaboration with the Commissariat à l'Energie Atomique (CEA Center of Valduc), one of these materials has been prepared on a semi-industrial scale and used in the final decontamination step of real effluents for removing the residual α-emitters (U, Pu, Am) contained at the sub-ng/L level.[2] The next goal is to unravel the coordination scheme of the radiotoxic metal ions embedded in this material in order to shed light on the structural aspects of the extraction process.

To this aim we have performed L3-edge X–ray Absorption Spectroscopy (XAS) measurements at BM20 of the Eu^{3+} ions bound to two materials used as sequestrants of lanthanide ions (see Fig. 1). Eu^{3+} is taken as a structural model of the highly emitting Am^{3+} cation since the maximum allowed amount of ^{241}Am does not exceed 1.5 mg. For comparison purposes XAS spectra have been collected also for the same ion bound to a number of isolated metal complexes formed with the corresponding macrocycles, well known for their affinity towards transition and non-transition metallic cations (see Fig. 2).[3,4] A number of control measurements have also been performed on $EuCl_3$, $EuOH_3$, $EuNO_3$ and Eu^{3+} sorbed on silica gel samples.

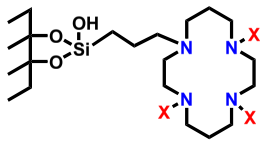

Fig. 1. The two investigated silica gel bound ligands Si2323Ac ($X = CH_2CO_2^-$) and Si2323Pr ($X = CH_2CH_2CO_2^-$).

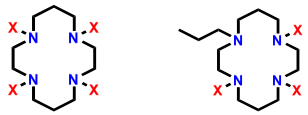

Fig. 2. ligands used to form the reference europium complexes.
Left: TETA ($X = CH_2CO_2^-$) / TETPr ($X = CH_2CH_2CO_2^-$).
Right: TE3A ($X = CH_2CO_2^-$) / TE3Pr ($X = CH_2CH_2CO_2^-$).

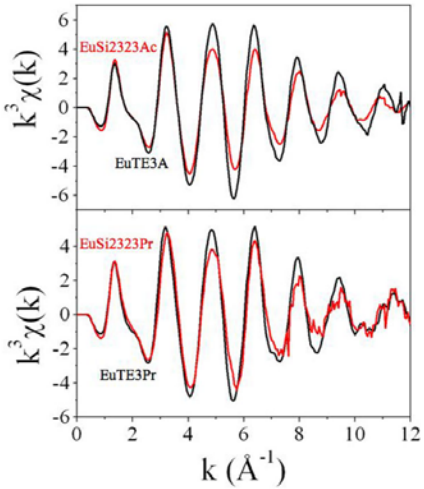

Fig. 3. Collected EXAFS functions for the materials shown in Fig. 1 (red lines) and for the two reference complexes EuTE3A and EuTE3Pr (see Fig. 2).

Data of very good quality have been collected for the reference compounds as well as for the investigated materials. As an example we report in Fig. 3 raw data collected for the investigated materials EuSi2323Ac and EuSi2323Pr (red line) compared to those collected for the two reference models EuTE3A and EuTE3Pr (black line).

The EXAFS functions of the two materials exhibit quite different spectral features as compared to those collected for the corresponding reference models, suggesting a different coordination scheme. Preliminary first shell analysis indicates an average coordination number of 8 O(/N) atoms for the investigated materials and an average distance of 2.42 Å with a Debye Waller factor of about 0.01 $Å^2$. The high value found for the disorder parameter (we recall at this respect that all the measurements have been performed at 20 K) suggests the presence of structural disorder of the first neighbors. A detailed data analysis, using both multiple-scattering and difference analysis approach, is still in progress. This analysis is expected to clarify the stereochemical arrangement of the neighboring atoms in the vicinity of Eu^{3+} for the isolated complexes versus that formed on the silica gel surface.

[1] H. Chollet, J. L. Babouhot, F. Barbette, R. Guilard, PCT application WO 01 15806, **2001**.
[2] F. Barbette, F. Rascalou, H. Chollet, J. L. Babouhot, F. Denat, R. Guilard, *Anal. Chim. Acta* **2004**, *502*, 179-187.
[3] R. M. Izatt, K. Pawlak, J. S. Bradshaw, R. L. Bruening, *Chem. Rev.* **1995**, *95*, 2529-2586.
[4] M. Meyer, V. Dahaoui-Gindrey, C. Lecomte, R. Guilard, *Coord. Chem. Rev.* **1998**, *178-180*, 1313-1405.

ROBL-CRG	**Experiment title:** EXAFS study of the uranyl speciation in a new task specific ionic liquid	**Experiment number:** CH-2424
Beamline: BM 20	**Date of experiment:** from: 07.07.2007 to: 10.07.2007	**Date of report:** 22.03.2009
Shifts: 9	**Local contact(s):** Dr. Christoph Hennig	*Received at ROBL:*

Names and affiliations of applicants (* indicates experimentalists):

Dr. Rik Van Deun
Dr. Peter Nockemann
Drs. Diederik Huys

K.U.Leuven
Chemistry Department
Molecular Design and Synthesis Division
Coordination Chemistry Group
Celestijnenlaan 200F
3001 Heverlee
Belgium

Report:

The speciation of uranyl complexes in ionic liquids has received a great deal of attention, due to the possible use of ionic liquids as extraction agents in the processing of nuclear waste. The fundamental understanding of the coordination chemistry of the uranyl ion in this new and peculiar class of solvents is necessary for the further development of new extraction processes.

In earlier experiments, we investigated the formation of tetrachloro and trinitrate complexes of uranyl in acetonitrile and in the ionic liquid 1-butyl-3-methylimidazolium bis(trifluoromethylsulfonyl)imide [1-3]. The goal of this project was double: (a) investigate the coordination of cyanate ligands towards the uranyl ion in cyanate containing ionic liquids (figure 1); (b) study the X-ray absorption spectrum of a crystalline tetrameric chloro complex of uranyl.

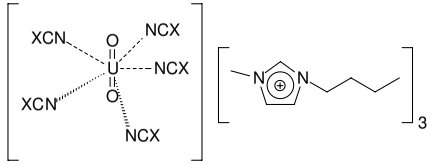

X = O, S, Se

Figure 1: Presumed chemical structure of the ionic liquid $[C_4mim]_3[UO_2(NCX)_5]$

As can be seen in Figure 1 and also from crystal structures available in literature, up to five 'cyanate' ligands can coordinate to the uranyl ion. 'Cyanate' is used here as a general term to indicate the NCO^- ligand (isocyanate), NCS^- (isothiocyanate) and $NCSe^-$ (isoselenocyanate). The interpretation of the EXAFS spectra of the 'cyanate' series is still in progress. Due to synthetic difficulties, it might be necessary to repeat some of the measurements with freshly prepared samples in a next experiment.

As a second part of this project, a tetrameric chloro complex of the uranyl ion, which had been isolated from an acetonitrile solution with a $[Cl^-]/[UO_2^{2+}]$ ratio of ~2, was subjected to an EXAFS experiment. The EXAFS spectrum and corresponding Fourier Transform are shown in Figure 2 (left) (black curve is experimental signal, red curve is fitted signal).

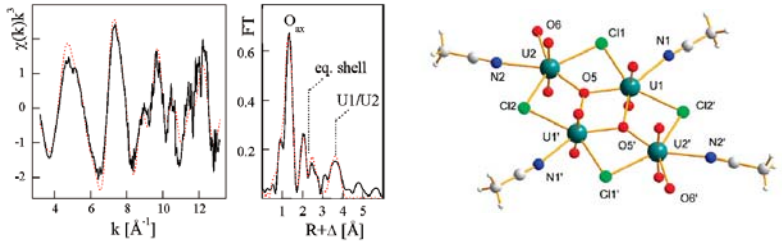

Figure 1: (left) EXAFS spectrum and Fourier Transform of tetrameric chloro uranyl complex; (right) crystal structure of tetrameric chloro uranyl complex

This EXAFS spectrum significantly differs from the that of the solution from which the crystals had been isolated, indicating that the tetrameric complex is different from the uranyl chloro species in solution. Most likely, the tetramer has a poor solubility and precipitates from the solution as soon as it is formed. Although the EXAFS spectrum is rather noisy (due to the fact that it had to be taken in fluorescence mode from crystals smaller than 0.4 mm), it clearly indicates the U-U interactions in the range R + Δ = 3.6 to 3.9 Å, thereby confirming the crystal structure which had been solved from similar crystals (Figure 2 (right)). The results of this study (the speciation of uranyl chloro complexes as the chloride-to-uranyl ratio in acetonitrile solution gradually increases from 0:1 to 4:1) have been published in *Inorganic Chemistry* [4].

References

[1] Structure of $[UO_2Cl_4]^{2-}$ in acetonitrile
K. Servaes, C. Hennig, R. Van Deun, C. Görller-Walrand, *Inorg. Chem.*, **2005**, *44*, 7705-7707.

[2] Speciation of uranyl nitrato complexes in acetonitrile and in the ionic liquid 1-butyl-3-methylimidazolium bis(trifluoromethylsulfonyl)imide
K. Servaes, C. Hennig, I. Billard, C. Gaillard, K. Binnemans, C. Görller-Walrand, R. Van Deun, *Eur J. Inorg. Chem.*, **2007**, 5120-5126.

[3] Speciation of uranyl complexes in ionic liquids by optical spectroscopy
P. Nockemann, K. Servaes, R. Van Deun, K. Van Hecke, L. Van Meervelt, K. Binnemans, C. Görller-Walrand, *Inorg. Chem.*, **2007**, *46*, 11335-11344.

[4] Species distribution and coordination of uranyl chloro complexes in acetonitrile
C. Hennig, K. Servaes, P. Nockemann, K. Van Hecke, L. Van Meervelt, J. Wouters, L. Fluyt, C. Görller-Walrand, R. Van Deun, *Inorg. Chem.*, **2008**, *47*, 2987-2993.

ESRF	**Experiment title:** **Uptake of neptunium and plutonium by topologically constraint peptides**	**Experiment number:** CH-2539
Beamline: BM20	**Date of experiment:** from: 23/01/2008 to: 28/01/2008	**Date of report:** 21/02/2008
Shifts: 15	**Local contact(s):** C. Hennig	*Received at ESRF:*

Names and affiliations of applicants (* indicates experimentalists):

***C. Den Auwer, *A. Jeanson, Ph. Moisy, *S. Petit, *S. Dahou**

CEA Marcoule DEN/DRCP/SCPS, 30207 Bagnols sur Cèze

S. Coantic

Université Montpellier 1, IBMM, LAPP, Montpellier

In the field of human toxicology, internal contamination with actinides can induce both radiological and chemical toxicity. Although there is a tremendous volume of data available on the interaction of plutonium with living organisms as plants, nearly all the studies are limited to macroscopic or physiological measurements with no specific information at the molecular level. In order to mimic the metal binding site of potential actinide carriers in the human body (metalloproteins, enzymes etc…) amino-acids known to bear high affinity donor groups such as carboxylates have been selected [1]. Such amino acids have been used as molecular bricks in order to design specific peptides of small molecular weight. We have combined here a screening approach of the possible peptide candidates with a structural investigation of one model peptide-cation complex. With such small peptides, one should however keep in mind that the cooperative effects originating from the macromolecule tertiary structure as in metalloproteins are not taken into account. For instance the tertiary structure of metalloproteins dramatically modifies the chelation properties of each functional group of the metal binding site.

The "split mix" method has been used to produce a library of over 1000 supported pentapeptides for which Fe(III) has been selected as a screening "test cation". Iron has been selected because colorimetric tests are easily available (for instance with phenantroline) and Fe(III) can be considered as a biological surrogate of Pu(IV). Among the sequences present in the library, those able to complex Fe(III) with the largest affinity have been detected by the colorimetric test and identified by mass spectrometry. Not surprisingly, most of the sequences that do complex Fe(III) contain several aspartic units because carboxylate groups have a high affinity for hard acid cations. On the other hand, one of the targeted peptide, AcAsp-Asp-Pro-Asp-AspNH_2 (also noted DDPDD, shown in Figure 1) has been selected as a model and synthesized in weighted amounts for aqueous complexation studies. Characterization of the peptide-metal complex by UV-Vis spectroscopy has suggested that 1:1 complexes are formed in the case of Fe(III), Th(IV), Np(IV) and Pu(IV). Complexation is carried out in aqueous/HEPES solution at pH around 4.

In our previous report (20-01-659) we have presented our first EXAFS data with Th, Np, Pu suggesting that all three cations yield similar complexes. The typical shortening of the coordination sphere from Th to Pu is observed in the present data. In the first coordination sphere, at least two contributions are present. Complementary NMR data have suggested that the oxygen atoms of the amide functions play a major role in the complexation. The EXAFS spectrum of the well characterized $Np(NTA)_2^{2-}$ complex (NTA = nitrilotriacetic acid) is presented in Figure 2. NTA is a small aminocarboxylate acid with three available carboxylic groups. With this ligand, the actinide cation (from Th to Pu) is surrounded by the 6 carboxylate oxygens plus the 2 amine nitrogens [2]. In that sense, NTA and DDPDD (D = asp, P = pro) bear very similar functional groups although the topology is radically different. Figure 2 suggests that the peptide ligand dramatically modifies the actinide environment. Since our last report, we have prepared a series of slightly modified peptides in order to better understand the role of the side chain functional groups in the structure of the actinide coordination sphere. In order to identify the binding mode of the peptide (bridging, terminal….) we have varied the positioned of the aspartic acid (with lateral carboxylate groups) or the length of the peptide : pentapeptide with 4 aspartic acids (DDPDD) or two aspartic acids (ADPDA) (A = ala); decapeptide identical to two times the pentapeptide (DDPDDDDPDD). The use of larger peptides is expected to produce chains or helices around the actinide cations. Figure 2 compares the neptunium L_{III} edge of this series of Np(IV)-peptide complexes. At this point, similar spectra have been obtained as shown in Figure 2.

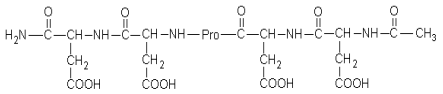

Fig. 1 : Formula of the DDPDD pentapeptide

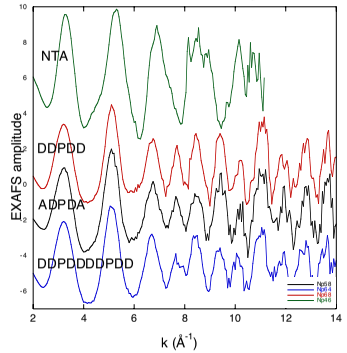

Fig. 2 : EXAFS spectra at the neptunium L_{III} edge of the following complexes (from top to bottom) : $[Np^{(IV)}(NTA)_2]^{2-}$, $Np^{(IV)}$:DDPDD, $Np^{(IV)}$:ADPDA, $Np^{(IV)}$:DDPDDDDPDD.

Fitting in the EXAFS data shows that the actinide coordination sphere is split in two distances, one short corresponding to hydroxo bridges as in actinide colloids [3] and one long corresponding to either carboxylate and/or water coordination [4]. Remarkably, a strong additional metal contribution indicates the presence of actinide neighbors. Overall, the NTA complex has been adjusted with *6* O at 2.33 Å (σ^2 = 0.0066 Å^2) (the two additional N are invisible with the EXAFS probe) and the DDPDD complex with 2-3 O at 2.21 Å (σ^2 = 0.0063 Å^2), 6-7 O at 2.41 Å (σ^2 = 0.0071 Å^2) (6+3 fixed to *9*) and 1-2 Np at 3.81 Å (σ^2 = 0.0041 Å^2). Very similar results have also been obtained with Th(IV) and Pu(IV) (EXAFS spectra not shown). The model proposed to date is an actinide chain with hydroxo bridges and bridging or terminal peptides. The similarity between all the peptide complexes, whatever the position of the D chain supports the NMR results suggesting that only the amide groups of the principal chain play a role in the complexation. On should add that in the same conditions without any peptide, the neptunium cations precipitates and forms colloids. This result confirms the essential role of the peptide in the complexation process.

These results suggest that unlike the NTA case, oligomeric species are formed with peptide ligands. However surprisingly enough, the sequence or length of the peptide does not seem to have any effect on the structure of the complex. The corresponding cyclic peptides are being synthesized. Cyclic decapeptides are topologically constraint and this should induce a major modification of the actinide coordination sphere by disabling the hydroxo bridging chain.

[1] A. Jeanson, C. Den Auwer, P. Moisy, C. Vidaud, OECD-NEA Proceedings on Speciation, Techniques and Facilities for Radioactive Materials at Synchrotron Light Sources, Karlsruhe, NEA n° 6288 (2007), 235-247.
[2] L. Bonin, A. Jeanson, D. Guillaumont, M. Grigoriev, S. Coantic, C. Den Auwer, J-C. Berthet, P. Thuéry and P. Moisy, to be submitted.
[3] J. Rothe, C. Walter, M. Denecke T. Fanghänel, Inorg. Chem. (2004), 43, 4708.
[4] L. F. Rao, Z. C. Zhang, P. L. Zanonato, P. Di Bernardo, A. Bismondo, S. B. Clark, Daton Trans. (2004), 2867.

ROBL-CRG	**Experiment title:** Hydration, Hydrolysis and Sorption of Sm^{3+} and Eu^{3+} in the Interlayer Space of the Clay Mineral	**Experiment number:** CH 2544
Beamline: BM 20	**Date of experiment:** from: 20.02.2008 to: 23.02.2008	**Date of report:** 14.11.2008
Shifts: 9	**Local contact(s):** Dr. Andreas SCHEINOST	*Received at ROBL:*
Names and affiliations of applicants (* indicates experimentalists): **Dr. Oleg SOBOLEV* (LGIT, CNRS&UJF)** Prof Laurent CHARLET **(LGIT, CNRS&UJF)** Dr. Gabriel CUELLO (ILL) Dr. Andreas SCHEINOST (ESRF)		

The clay minerals consist of negatively charged alumino-silicate layers held together by cations to give a stacked (crystalline) structure. Under humid conditions the interlayer cations and the internal clay surfaces hydrate. Clay materials have been selected as the most suitable buffer material for high level radioactive waste repositories in order to retard the migration of radionuclides in case the waste containers corrode. For our investigation we have chosen Eu^{3+} and Sm^{3+} cations because of their chemical similarity to Pu^{3+} and Am^{3+}. In our previous neutron diffraction experiment [1,2] we studied the structural parameters of the coordination of Sm^{3+}, adsorbed in the interlayer space of the montmorillonite. It was found that the number of hydrogen atoms (5.5 ± 2.0) in the first coordination shell of Sm^{3+} is equal or even slightly smaller than those of oxygen atoms (7.5 ± 1.0). It was supposed that the Sm^{3+} ion binds to the clay surface via oxygen siloxane atoms, and it is probably partially hydrolyzed.

The aims of this experiment

1) To determine the number of oxygen atoms nearest to Eu and Sm and to distinguish between the oxygen atoms belonging to the montmorillonite layers and the oxygen atoms of water molecules.

2) To determine the oxidation state of Eu in Fe(II) doped montmorillonite. Fe(II) contained in natural montmorillonite can affect the sorption ability of the redox sensitive radionuclides in the interlayer space through the redox reaction $Mn^{+} \rightarrow Mn^{(n-1)+}$, $Fe(II) \rightarrow Fe(III)$.

The measured samples

- Eu –Fe(II) doped montmorillonite
- Sm aqueous solution (0.05M)
- Sm-montmorillonite samples with different concentration of Sm

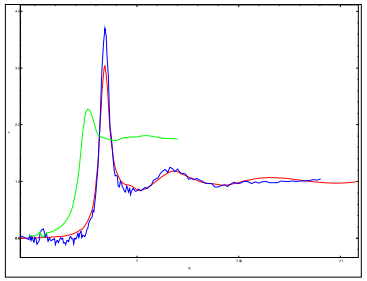

Fig. 1 Eu LIII-edge XANES of Eu – Fe(II) doped montmorillonite (blue) in comparison to $EuCl_3$ (red, E=6982.2 eV) and $EuCl_2$ (E=6972.6 eV, green).

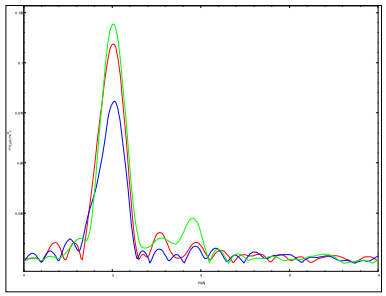

Fig. 2 Sm LIII-edge EXAFS. Sm-1 (high concentration, red), Sm-2 (low cocentration blue), Sm^{3+} aqua 0.05 M in nitric acid (green)

Results

- An experiment with Eu –Fe(II) doped montmorillonite (Fig. 1) did not show reduction of Eu^{3+}. Threfore there is no electronic transfer between the structural iron and the interlayer Eu^{3+}.

  Analysis of the experiments with Sm aqueous solutions and Sm-montmorillonite samples is still in progress. However, preliminary results do not reveal any indications of the contacts of the Sm^{3+} cations with the clay surface. Thus we can suppose that the Sm^{3+} cation is sorbed as an outer sphere complex with water molecules.

References

[1] ILL Experimental Report No: 6-02-365
[2] O. Sobolev, L. Charlet, G. J. Cuello, A. Gehin, J. Brendle, N. Geoffroy, J. Phys.: *Cond. Matt.* 2008, 20 104207

ESRF	**Experiment title:** EXAFS study of neptunium(V) uptake by kaolinite	**Experiment number:** EC-144
Beamline: BM20	**Date of experiment:** from: 03.03.2007 to: 06.03.2007	**Date of report:** 28.02.2008
Shifts: 9	**Local contact(s):** Dr. A. Roßberg	*Received at ESRF:*

Names and affiliations of applicants (* indicates experimentalists):

S. Amayri*, M. Breckheimer*, J. Drebert*, T. Reich*

Institute of Nuclear Chemistry, Johannes Gutenberg-Universität Mainz, 55099 Mainz, Germany

Report:

In June 2005, Np L_{II}-edge EXAFS spectra for Np(V) sorbed onto kaolinite were measured for the first time for samples prepared at different pH values in the absence and presence of CO_2 (see Experimental Report ME-1090). The EXAFS spectra of the samples prepared in air revealed that $[NpO_2(CO_3)_2]^{3-}$ species are present at the kaolinite surface. EXAFS spectra of samples prepared under CO_2-free conditions were different and showed two oxygen coordination shells at 1.87 and 2.47±0.02 Å, similar to the Np(V) aquo ion. Unfortunately, the beam intensity for experiment ME-1090 was strongly reduced due to a mirror alignment problem that could not be fixed during the beam time. Although the data quality was sufficient to observe significant differences in the Np near-neighbor surrounding under the influence of HCO_3^-/CO_2^{2-}, two important questions could not be answered due to lacking signal statistics: 1) Does Np form inner-sphere or outer-sphere sorption complexes with kaolinite? The ionic-strength dependencies shown in Fig. 1 indicate formation of inner-sphere complexes in the CO_2-free system and of outer-sphere complexes under ambient CO_2. 2) Are polynuclear Np carbonato species sorbed at the clay surface? Although the total Np concentration of 8 µM was below the solubility limit of any relevant Np(V) solid, some EXAFS spectra prepared in the presence of HCO_3^-/CO_2^{2-} could be modeled including a weak Np-Np interaction at 4.9 Å.

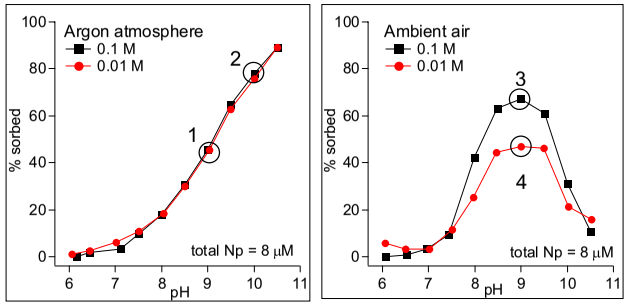

Figure 1: Sorption of Np(V) onto kaolinite as a function of pH and ionic strength. The total Np concentration was 8 µM. The ionic strength was 0.1 and 0.01 M $NaClO_4$, respectively. Experiments were performed under Ar atmosphere (left) and ambient CO_2 partial pressure of $10^{-3.5}$ atm (right).

To complete this sorption study, the Np L_{III}-edge EXAFS spectra of the samples indicated in Fig. 1 were measured. Samples 1-4 were prepared as wet paste and measured at room temperature. Duplicates of samples 1 and 3 were prepared as dry powder and measured at 13 K (indicated as 1' and 3' in Tabs. 1 and 2). Tables 1 and 2 summarize the results of the preliminary EXAFS analysis. It should be noted that all EXAFS spectra could be collected with excellent signal-to-noise ratios.

Table 1: EXAFS structural parameters for Np(V) sorbed onto kaolinite under Ar atmosphere.

Sample	2 × O_{ax}		4 × O_{eq}		1 × Al/Si		2 × Al/Si	
	R(Å)	σ^2(Å^2)	R(Å)	σ^2(Å^2)	R(Å)	σ^2(Å^2)	R(Å)	σ^2(Å^2)
1	1.84	0.0044	2.50	0.0158	3.19	0.0034	3.84	0.0047
2	1.84	0.0040	2.49	0.0148	3.19	0.0079	3.84	0.0059
1'	1.85	0.0062	2.45	0.0135	3.16	0.0087	3.83	0.0107

Table 2: EXAFS structural parameters for Np(V) sorbed onto kaolinite in ambient air.

Sample	2 × O_{ax}		6 × O_{eq}		2 × C		2 × O_{dis}	
	R(Å)	σ^2(Å^2)	R(Å)	σ^2(Å^2)	R(Å)	σ^2(Å^2)	R(Å)	σ^2(Å^2)
3	1.83	0.0039	2.56	0.0144	2.99	0.003*	4.32	0.0133
4	1.84	0.0040	2.55	0.0156	2.98	0.003*	4.35	0.0125
3'	1.83	0.0037	2.57	0.0113	2.98	0.003*	4.36	0.0139

*) fixed during the fit

In addition to the confirmation of the main results of our previous EXAFS experiment, the following observations were derived from the new measurements due to the improved signal statistics: i) The EXAFS spectra of the samples preapred under exclusion of CO_2 showed two Np-Al/Si coordination shells at 3.2 and 3.8 Å in addition to the axial and equatorial oxygen coordination shells at 1.8 and 2.5 Å, respectively. The detection of Np-Al/Si interactions in these samples confirmes that inner-sphere sorption complexes of Np(V) with the aluminol/silanol groups of kaolinite are formed under CO_2-free conditions. This agrees with the observation obtained by the batch experiments, i.e., the Np uptake is independent from ionc strengh (see Fig. 1 left). ii) The fomation of Np(V) carbonato complexes at the kaolinite surface under ambient air conditions could be comfirmed both at 0.01 and 0.1 M $NaClO_4$ electrolyte concentrations. The preliminary EXAFS analysis of samples 3 and 4 showed that the reduced error of the theoretical fit to the data decreases when a Np-Al/Si coordination shell at 3.8 Å is included in the fit. More detailed EXAFS analysis, including the modelling of a reference spectrum of $NaNpO_2CO_{3(s)}$, is in progress to verifiy the presence of Np-Al/Si interaction in the spectra of samples 3 and 4. If confirmed, it would indicate that ternary Np carbonato complexes are formed at the kaolinite surface at pH 9 under ambient air conditions.

The precipitation of Np phases can be ruled out in case of the samples prepared under Ar atmosphere. The Fourier transforms (FT) of samples 1 and 2 do not show any intenstity above 4 Å. However, the FTs of samples 3 and 4 do show a pronounced structure that is centered around 5 Å. Several strucutral models are under consideration to describe this spectral feature. Therefore, the formation of a surface precipitate cannot be ruled out.

Acknowledgement

This work was supported by the German Bundesministerium für Wirtschaft und Technologie (Project 02 E 9653). We acknowledge the ESRF for provision of synchrotron beam time and thank H. Funnke, C. Hennig, A. Roßberg, and A. Scheinost from Forschungszentrum Dresden-Rossendorf for assistance in using beamline BM20.

ROBL-CRG	**Experiment title:** **Uranium solid-phase speciation in presence of pyrite (FeS_2) at slightly alkaline conditions**	**Experiment number**: EC-205
Beamline: BM 20	**Date of experiment**: from: 01-02-2008 to: 05-02-2008	**Date of report**: 31-03-2009
Shifts: 12	**Local contact(s)**: Andreas SCHEINOST	*Received at ROBL:*
Names and affiliations of applicants (* indicates experimentalists): Christophe BRUGGEMAN* Norbert MAES Sven AERTS* Philippe RAEYMAEKERS* SCK•CEN, Boeretang 200, B-2400 Mol (Belgium)		

Report:

Several authors have noted a partial reduction of U(VI) (mostly to $UO_{2+x(s)}$) by pyrite in lightly acidic (pH 3-6) conditions and at relatively high initial U concentrations (> 10^{-4} mol·l^{-1}) (Wersin *et al.*, 1994; Aubriet *et al.*, 2006; Eglizaud *et al.*, 2006; Scott *et al.*, 2007). In the present study, the uptake of U(VI) by pyrite was investigated under slightly alkaline conditions (pH 8-9) at variable U concentrations (10^{-8} – 10^{-4} mol·l^{-1}) and in the presence of 0.014 M $NaHCO_3$. As an additional parameter, also the presence of dissolved organic carbon (DOC) was researched. The uranium solid phase speciation in batch systems with high initial U concentration was analysed using X-ray Absorption Near-Edge Structure (XANES) and Extended X-ray Absorption Fine Structure (EXAFS) spectroscopy.

A total of six samples were analysed, which comprised the presence and absence of DOC, different equilibration times (10 and 120 days), and different FeS_2 solid-to-liquid ratio. Uranium was added initially as $UO_2(NO_3)_2$. Table 1 gives an overview of these samples, together with some experimental details concerning solution analysis after equilibration. Apart from the six experimental standards, a number of U standards (e.g., 0.1 mol·l^{-1} solutions of $UO_2(CO_3)_2^{2-}$, $UO_2(CO_3)_3^{4-}$, $UO_2(NO_3)_2$ and UO_2(OAc), and $U_3O_{8(s)}$, $UO_{2(am)}$, $UO_{2(s)}$, U^{VI} adsorbed onto FeOOH solid phases in absence and presence of DOC) were equally analysed.

In the figures presented below, the XANES and k³-weighted EXAFS spectra (top figures), and their Fourier transform (FT) and the FT's imaginary part (bottom figures) are shown. XANES spectra were interpreted using Principal Component Analysis and Linear Combination Fitting. A combination of two standards, $UO_{2(s)}$ and U(VI) adsorbed onto FeOOH, was sufficient to adequately reconstruct the spectra of all six samples. The EXAFS spectra were equally interpreted and fitted using a combination of the crystal structure of uraninite and uranyl surface complex, similar to the analysis of U speciation in sediments performed by Kelly *et al.* (2008). This resulted in good fits for all samples.

From the results it appears that at alkaline pH, and at the investigated bicarbonate concentration, U(VI) uptake by FeS_2 is almost quantitative, and a partial redox transformation to $UO_{2(s)}$ occurs. The presence of dissolved organic carbon was the major factor hindering this reduction. Although the nominal amounts of U(IV)/U(VI) from analysis of the XANES and EXAFS spectra do not agree completely, the same trends were clearly demonstrated.

Table 1: Overview experimental samples measured by XAFS

Sample	**FeS_2**	**U(VI)*ini*** (M)	**U_{liq}*fin*** (M)	**U_{solid}*fin*** (mol/kg)	**Equilibration time**	**DOC**
S1	19.2 g/L	1.5×10^{-4}	2.3×10^{-6}	7.9×10^{-3}	120 days	0 mg/L
S2	19.3 g/L	1.5×10^{-4}	1.7×10^{-6}	7.6×10^{-3}	120 days	58 mg/L
S3	21.0 g/L	1.7×10^{-4}	3.2×10^{-6}	7.8×10^{-3}	10 days	0 mg/L
S4	21.1 g/L	1.7×10^{-4}	1.9×10^{-5}	7.0×10^{-3}	10 days	38 mg/L
S5	4.1 g/L	1.7×10^{-4}	9.4×10^{-5}	1.8×10^{-2}	10 days	0 mg/L
S6	4.1 g/L	1.7×10^{-4}	2.6×10^{-5}	3.4×10^{-2}	10 days	63 mg/L

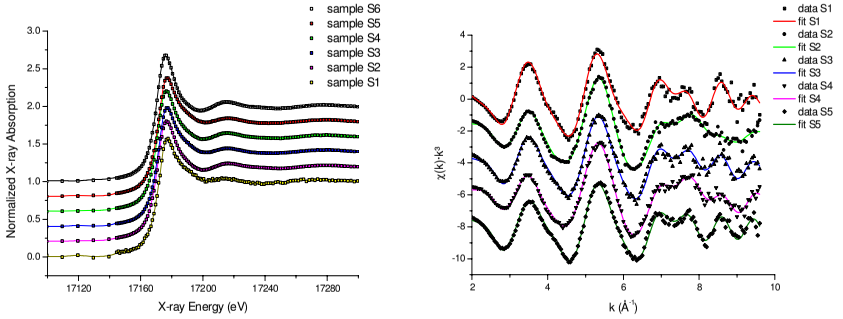

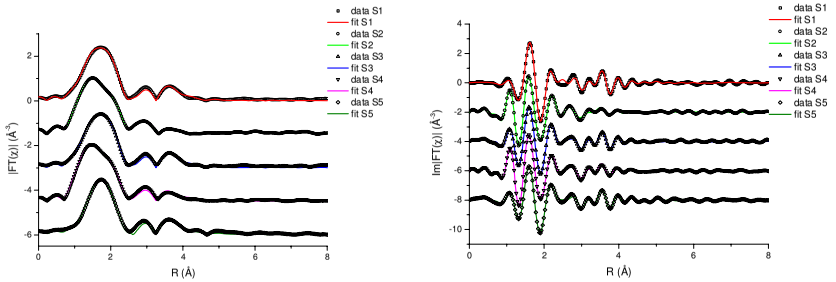

Figure: Normalised XANES (upper left), EXAFS X(k)·k³ (upper right), magnitude of the Fourier Transform (FT) (lower left), and imaginary part of the FT (lower right) of U-FeS_2 samples S1 to S6 (EXAFS spectra of sample S6 not included due to poor data quality). Open symbols represent experimental data, full lines are best fits.

References

Aubriet, H., Humbert, B., Perdicakis, M. "Interaction of U(VI) with pyrite, galena and their mixtures: a theoretical and multitechnique approach" *Radiochim. Acta* **2006**, *94*, 657-663

Eglizaud, N., Miserque, F., Simoni, E., Schlegel, M., Descostes, M. "Uranium(VI) interaction with pyrite (FeS_2): chemical and spectroscopic studies" *Radiochim. Acta* **2006**, *94,* 651-656

Kelly, S.D., Kemner, K.M., Carley, J., Criddle, C., Jardine, P.M., Marsh, T.L., Phillips, D., Watson, D., Wu, W.-M. "Speciation of uranium in sediments before and after in situ biostimulation" *Environ. Sci. Technol.* **2008**, *42*, 1558-1564

Scott, T.B., Riba Tort, O., Allen, G.C. "Aqueous uptake of uranium onto pyrite surfaces; reactivity of fresh versus weathered material" *Geochim. Cosmochim. Acta* **2007***, 71*, 5044-5053

Wersin, P., Hochella, M.F., Persson, P., Redden, G., Leckie, J.O., Harris, D.W. "Interaction between aqueous uranium (VI) and sulfide minerals: spectroscopic evidence for sorption and reduction" *Geochim. Cosmochim. Acta*, **1994**, *58*, 2829-2843

ROBL-CRG	**Experiment title:** Adsorption of U(VI)onto FeS and its subsequent reduction	**Experiment number**: EC279
Beamline: BM 20	**Date of experiment**: from: 25 / 06/ 2008 to: 30 /06 /2008	**Date of report**: 3 February 2009
Shifts: 15	**Local contact(s)**: Dr. Andre Rossberg	*Received at ROBL:*
Names and affiliations of applicants (* indicates experimentalists): Dr. Thilo Behrends * Vasso Alexandratos * Dr. Andreas Scheinost *		

Report:

The goal of experiment EC279 was to evaluate the possiblity and kinetics of U(VI) reduction by a) FeS or b) by sulphide in the presence of other mineral phases, and to characterize the reaction product. For this purpose samples from three different types of experiments were analyzed 1) U(VI) added to freshly precipitated FeS suspension at pH 8.0, 2) S(-II) added to aluminum oxide suspension containing adsorbed U(VI), 3) S(-II) added to lepidocrocite suspension containing adsorbed U(VI).

Technical aspects

At the beginning of the experiment we experienced some short storage ring failures, but afterwards it has been possible to make optimal use of the allocated beamtime. The support by the beamline staff was excellent, and collaborating with the staff members during the experiment was very fruitful and inspiring. The very userfriendly software and set-up of the beamline as well as the general performance of the beamline is outstanding. The only drawback was that the new monochromator crystal created glitches in the spectra (see figure, the arrows indicate minor glitches observed in addition to the major glitch at around 17.43 keV). Nevertheless, we consider the outcome of the experiment as very successful and the results enabled us to answer major questions related to the research objectives. In total EXAFS spectra of 17 frozen wet paste samples were collected in fluorsecence mode at about 30K.

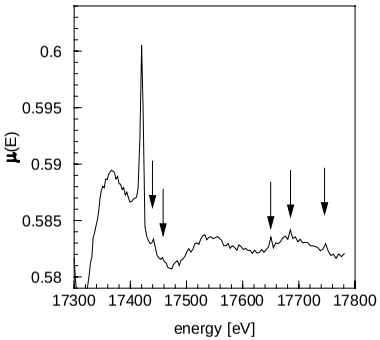

Scientific results

Performing iterative transformation factor analysis of the XANES spectra from all samples with the program ITFA (ROSSBERG et al., 2003) revealed that two components are sufficient to reproduce the features of the XANES spectra. The two components can be conceived as representing the XANES spectra of U(VI) and U(IV), respectively. Based on this approach, the relative fraction of reduced U was derived from the ITFA analysis. Practically no reduction of U(VI) occurred within a period of 4 days in experiments with Al oxides to which S(-II) solution was added, irrespective of pH (6 or 8), or S(-II) addition (1 or 5 mM). Uranium became reduced when added to iron oxide suspension, which have been reacted with S(-II) solution prior to U(VI) addition. Up to 65 % of initially added U(VI) was reduced within 2 days. However, the rate of U(VI) reduction varied considerably in the different experiments depending on the age of the suspension and the occurrence of Fe(II) and S(-II) in solution. When added to freshly precipitated FeS, U(VI) was completely reduced within 1h. However, over time reoxidation occurred and after two weeks incubation only about 10% of initial U was still in its reduced form.

At least four components are required to reproduce the EXAFS chi (k^3) spectra, indicating that U(VI) coordination is not identical in all the samples and that also different U(IV) species might occur. One component can be assigned to the group of samples from Al oxide experiments, whereas the EXAFS spectra are very similar in this group. Hence, addition of S(-II) seems not to have an effect on the coordination of U(VI) adsorbed onto Al oxides, and, secondly, U(VI) speciation on Al-oxides differs from U(VI) speciation in suspensions containing iron oxides or iron sulfides. Interestingly, the results of the ITFA analysis suggest, that U(VI) coordination at the surface of precipitated FeS is different compared to that of U(VI) adsorbed to the surface of the transformation product of Fe oxide reduction by S(-II), which, in turn, both differ from U(VI) coordination at iron oxide surfaces. EXAFS fitting is still ongoing and will hopefully provide more information about the difference of U(VI) binding at the surface of the different iron containing phases.

Literature

Rossberg A., Reich T., and Bernhard G. (2003) Complexation of uranium(VI) with protocatechuic acid-application of iterative transformation factor analysis to EXAFS spectroscopy. *Analytical and Bioanalytical Chemistry* **376**, 631-638.

ESRF

Experiment title:	Experiment number:
EXAFS/XANES investigation of plutonium and americium pyrochlores considered as targets for transmutation	HS-3178

Beamline:	Date of experiment:	Date of report:
BM20	from: 07/02/07 to: 10/02/07	02/2008
Shifts:	**Local contact(s):**	*Received at ESRF:*
9	Dr. Andreas SCHEINOST	

Names and affiliations of applicants (* indicates experimentalists):

P.M. Martin, *R. Belin, *P. Valenza, *A. Pieragnoli

CEA-Cadarache (DEN/DEC) F-13108 Saint Paul lez Durance.

Report:

Management of long-lived nuclear wastes is, after safety, the main issue of nuclear industry, both in terms of scientific challenge as well as public acceptance. Among the different options that have been envisioned and explored for minor actinides over the past thirty years, two alternatives currently remain: long term disposal in a safe repository or nuclear wastes "burning" in a so-called transmutation process. Materials selected for such applications have to meet the following criteria: high incorporation amount of actinides, good structural and chemical stability, low thermal dilatation and resistance to radiation.

Among the various ceramics envisaged, zirconia based pyrochlore oxides of composition $An_2Zr_2O_7$ (An=actinide) appear to be a very good candidate. Results obtained with lanthanide pyrochlores submitted to ion-beam irradiation show that Zr based pyrochlores, unlike Ti based, remain crystalline with a transition from pyrochlore structure to a defect fluorite structure [1]. The ordered pyrochlore belongs to the Fd-3m space group and is a superstructure of the ideal defect fluorite structure (Fm-3m) with exactly twice the lattice constant. In the pyrochlore structure, Am and Zr cations have first coordination shells clearly different: 8 (2+6) oxygen atoms and 6 oxygen atoms respectively. Whereas second coordination shell (cation-cation) is the same for both cations (6xAm+6xZr at the same distance). The structural phase transition from pyrochlore to defective fluorite involves the randomization of the oxygen atoms into the anionic and vacant positions of the pyrochlore structure. In the ideal fluorine defect structure, the Am and Zr cations share the same position and thus have the same local environment: a first coordination shell consisting of 7 oxygen atoms at the same distance and the same second coordination shell observed in the pyrochlore structure.

However, this strong radiation tolerance still has to be confirmed on alpha emitter materials (e.g. americium). In that prospect, $^{241}Am_2Zr_2O_7$ sample was synthesized [2] and its evolution under the effect of alpha self-irradiation as a function of time was followed by XRD. A transition from the pyrochlore phase to a defect-fluorite phase was observed after ~200 days as the superstructure peaks slowly vanish and completely disappear after about 200 days [3]. However, the fluorite structure is surprisingly resistant to self-irradiation induced amorphization as compared to other materials considered for transmutation or long-term storage [4]. In order to better understand the underlying phenomena involved in this phase transition as well as the significant resistance to amorphization of the defect fluorite phase, characterization of Am and Zr local environments by XAS have been undertaken.

Results

XANES and EXAFS spectra on 2 $Am_2Zr_2O_7$ samples have been collected at Zr K edge and Am L_{II} edges at a temperature of 15 K. The first sample (called "fresh") has been synthesized a few weeks before the experiment whereas the second sample (called "old") was a year old. X-ray diffraction measurements performed prior to XAS measurements attested for a pyrochlore structure (Fd-3m a=10.667Å) for the "fresh" sample and for a defect-fluorite (Fm-3m a=5.323Å) for the "old" one. The Fourier transforms at both edges are compared in Figures 1 and 2.

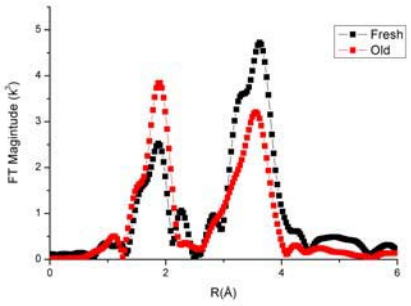

Figure 1: Fourier transforms at americium L_{II} edge.

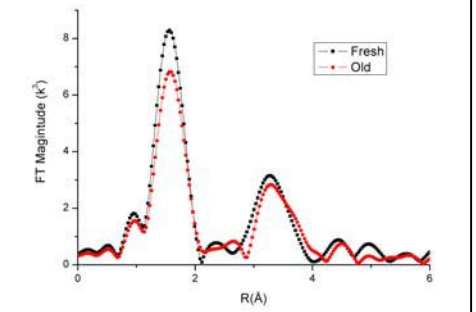

Figure 2: Fourier transforms at zirconium K edge.

In the case of americium, a clear modification of radial distribution around Am ions can be observed. For the fresh sample, the fit gives the expected pyrochlore local environment with: 2.8±0.5 O at 2.31±0.02 Å, 4.8±0.5 O at 2.53±0.02 Å, 6±0.5 Am at 3.76±0.02 Å and 6±0.5 Zr at 3.74±0.02 Å. For the one year old sample, the fit confirms the fluorite structure with a first coordination shell consisting of only one shell of 6.6±0.5 O at 2.35±0.02 Å (peak at ~1.9 Å in Figure 1). The cation-cation shells included in the second (peak at ~3.8 Å in Figure 1) are clearly distorted with 5.2±0.5 Am at 3.75±0.02 Å and 6.3±0.5 Zr at 3.65±0.02 Å. The Am-Am distance is coherent with the fluorite structure but the Am-Zr distance is shorter than expected. Such observations seem to indicate that Zr local environment does not follow the evolution observed around Am ions.

Results obtained at Zr K edge validate that hypothesis as the Zr-O polyhedra, with only coordination shell of 6.6±0.5 O at 2.14±0.02 Å (peak at ~1.8 Å in Figure 2) for both samples, appear to be stable in regard to alpha self-irradiation. Moreover, the cation-cation coordination sphere (peak at ~3.3 Å in Figure 2) follows the same evolution observed for Am with a distortion due to Zr-Zr and Zr-Am distances clearly different.

Unlike picture given by XRD measurement, Am and Zr cations local environments after self-alpha irradiation are clearly non equivalent. Modifications appear to be mainly localized around Am cations whereas the ZrO_7 polyhedra seem to be very robust against irradiation. Same conclusions have been obtained on $Gd_2(Ti,Zr)_2O_7$ pyrochlore samples submitted to ion irradiation [5]. Thus, the structural phase transition from the pyrochlore structure to the fluorite defect structure appears to be rather a disruption of the long-range order probed by XRD due to cation disorder and interpolyhedral (ZrO_7 and AmO_7) rotations along edges and corners leading to the change in Am environment and the disorder in second coordination shells [6]. To definitively conclude on the mechanism induced by self-alpha irradiation, XAS measurements on two years aged sample is proposed.

References

[1] K.E. Sickafus *et al*, Nature Materials 6(2007)217.
[2] R.C. Belin *et al*, J. Alloys Compounds 448(2008)321.
[3] R.C. Belin *et al*, Actinides 2005 Conference - Recent Advances in Actinide Science 4-8 July 2005 Manchester (UK) University of Manchester RSC Publishing, p. 352
[4] K. Trachenko, J. Phys.: Cond. Matt. 16(2004)1491.
[5] N.J. Hess *et al*, J. Phys. Chem. B 106(2002)4663.
[6] P.M. Martin *et al*, submitted to Journal of nuclear materials (2008).

ESRF	**Experiment title:** XAS study of uranium and plutoniumlocal environment in $(U,Pu)O_2$ solid solution: influence of the Pu/(U+Pu) ratio and of the synthesis method	**Experiment number:** MA-233
Beamline: BM20	**Date of experiment:** from: 8 February to: 12 February	**Date of report:** 08/2007
Shifts: 12	**Local contact(s):** Dr. Andre ROSSBERG	*Received at ESRF:*

Names and affiliations of applicants (* indicates experimentalists):

***P. MARTIN[a], G. LETURCQ[b], B. ARAB-CHAPELET[b], S. GRANDJEAN[b], H. PALANCHER[a], *A.C. ROBISSON[b], C. VALOT[a]**

[(a)] CEA-Cadarache (DEN/DEC) F-13108 Saint Paul lez Durance.

[(b)] CEA-Valrho (DEN/DRCP) F-30207 Bagnols-sur-Cèze.

Report:

New synthesis methods were recently optimized in the CEA Atalante facility at Marcoule in order to obtain $(U,Pu)O_2$ solid solutions with a minimal content of synthesis impurities and a O/M ratio equal to 2.0. The impurities, mainly residual carbon, were probably responsible for the formerly detected disorder in the local environment of both actinides. The first method based on the oxalic co-precipitation of U(IV) and Pu(III) followed by the thermal conversion of the co-precipitate into oxide, produces solid solutions whose cell parameters deduced from X-Ray diffraction experiments obey the Vegard's law. The second one based on the internal gelation of a U(VI)-Pu(IV) solution (or a U(IV)+Pu(III) one) followed by a thermal treatment at around 1000°C, produces mixed oxide whose structure was more difficult to establish due to possible various oxidation states for plutonium in the oxide or obtainment of non-ideal solid solution.

The objective of this new experiment is to study the local uranium and plutonium environment of mixed U-Pu oxide depending on the molecular precursor i.e. either a crystallized mixed oxalate (oxalic co-precipitation) or a mixed hydrated oxide (internal gelation). Thus, the local environment around each cation will tell us if ideal solid solution is obtained or not with the two preparation methods.

Results

Five samples were prepared using both previously described methods:

- $(U,Pu)O_2$ with Pu/(U+Pu) equal to 15 at. % (internal gelation of U(IV) and Pu(III))
- $(U,Pu)O_2$ with Pu/(U+Pu) equal to 28 at. % (oxalic co-conversion)
- $(U,Pu)O_2$ with Pu/(U+Pu) equal to 45 at. % (oxalic co-conversion)
- $(U,Pu)O_2$ with Pu/(U+Pu) equal to 55 at. % (oxalic co-conversion)
- $(U,Pu)O_2$ with Pu/(U+Pu) equal to 50 at. % (internal gelation of U(VI) and Pu(IV))

Measurements were performed at 15K using an helium cryostat and for each sample U L_3 edge (Fig. 1 and 2) and Pu L_2 edge (Fig. 3 and 4) XANES and EXAFS spectra were collected.

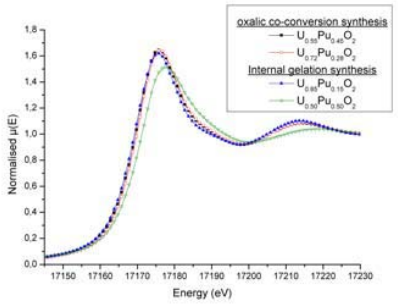

Fig 1: Uranium L_3 edge XANES spectra.

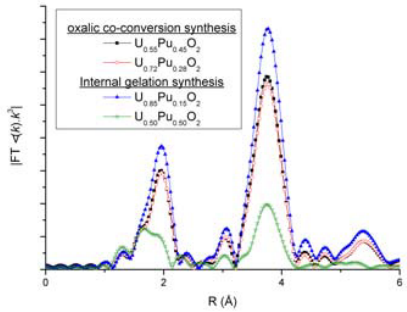

Fig 2: Fourier transforms U L_3 edge ($2.4<k(Å^{-1})<14.4$).

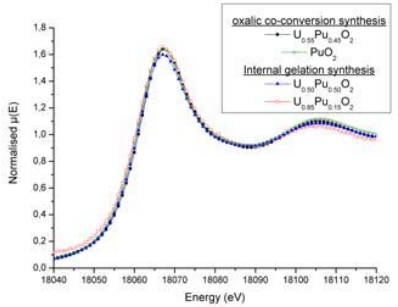

Fig 3: Plutonium L_3 edge XANES spectra.

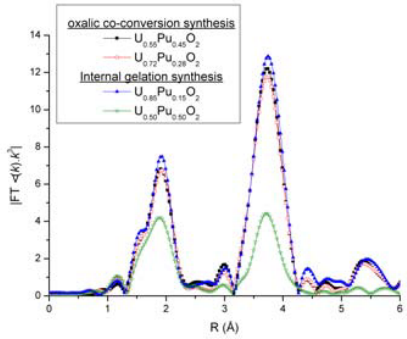

Fig 4: Fourier transforms Pu L_2 edge($2.4<k(Å^{-1})<14.0$)

Concerning all the samples synthesised by oxalic co-conversion and the $U_{0.85}Pu_{0.15}O_2$ sample obtained by inter gelation of a U(IV)-Pu(III) solution, the same conclusions are obtained:

- XANES interpretation shows that uranium and plutonium ions oxidation degree is +IV.
- EXAFS fits demonstrate that both uranium and plutonium local environments are the same and corresponds to the face centred cubic structure expected. Moreover a shortening of bond lengths is observed as the plutonium content increases.

These new XAS characterization clearly demonstrated the formation of an ideal $(U,Pu)O_2$ solid solution with oxalic co-conversion synthesis method. Same conclusion can be made for the sample based on the internal gelation of a U(IV)-Pu(III) solution ($U_{0.85}Pu_{0.15}O_2$).

This is not the case for the sample obtained by internal gelation of a U(VI)-Pu(IV) solution ($U_{0.5}Pu_{0.5}O_2$). Compared to the other samples, a shift of the white line and a shoulder at +20 eV can be observed on the uranium XANES spectrum collected on this sample. Those features clearly indicate that a significant part of uranium is oxidized to U^{+VI}. Moreover, Fourier transforms confirms this observation as two U-O distances are evidenced in the first coordination shell: the first and short U-O distance is attributed uranyl-type bond and the second corresponds to U-O distance expected for a fluorite type solid-solution. Concerning the plutonium environment, the same behaviour observed in our previous study [1] is obtained: Pu^{+IV} ions in a disordered $(U,Pu)O_2$ solid solution. The sample obtained by internal gelation seems thus to be of mixing of two phases: a U^{+VI} phase without a long range order and a disordered $(U,Pu)O_2$ solid solution. Clearly, the thermal treatment of the last sample was not efficient to reduce all U(VI) into U(IV).

[1] P. Martin et al, J. Alloys & Compounds 444-445(2007)410-414.

3.2. Experimental Reports Materials Research

ROBL-CRG	**Experiment title:** *XRD and GISAXS investigations on ion beam induced Si surface ripples*	**Experiment number:** 20-02-645
Beamline: BM20	**Date of experiment:** from: 21 February 2007 to: 28 February 2007	**Date of report:** 15.10.2008
Shifts: 21	**Local contact(s):** Dr. Carsten BAEHTZ	*Received at ESRF:*

Names and affiliations of applicants (* indicates experimentalists):

Adrian Keller*, Stefan Facsko and Jörg Grenzer*

Forschungszentrum Dresden-Rossendorf,
Institute of Ion Beam Physics and Materials Research
01314 Dresden, Germany

Report:

Nanopatterned templates are a popular tool for creating novel nanostructures and controlling the properties of thin films. Recently, nanoscale ripple patterns which form self-organized during low energy ion sputtering have been used as templates for the deposition of metallic thin films. It was shown, that these patterns can induce magnetic and optical anisotropies in the deposited films. A crucial parameter for the further application of these substrates, e.g. in CVD or MBE growth, is the thermal stability of the patterns. Therefore, the annealing behavior of ion induced ripple patterns on Si(100) has been studied *in-situ* by GISAXS.

The samples were fabricated by sputtering of Si(100) at room temperature with Ar^+ ions with energies between 300 and 800 eV. Due to the high fluxes used for the sputtering, the Si(100) surface gets amorphized by the ion impact and an amorphous top layer of few nanometer thickness is formed. After removal from the vacuum chamber, the amorphous Si surface develops a native oxide of ~ 1 nm thickness. Different so prepared ripple samples with periodicities ranging from ~ 20 to ~ 50 have been annealed in high vacuum for several hours at temperatures up to 800°C. During annealing, consecutive GISAXS profiles have been obtained by using a position sensitive detector.
Figure 1 depicts GISAXS profiles of one sample at different times during annealing at 750°C. The position and the intensity of the observed side peaks correspond to the periodicity (~ 30 nm) and the amplitude (~ 1 nm) of the ripple pattern, respectively. As can be seen clearly from Fig. 1, even after annealing for several hours, neither the periodicity nor the amplitude of the pattern has changed. This observation could also be confirmed by atomic force microscopy as shown in figure 2..

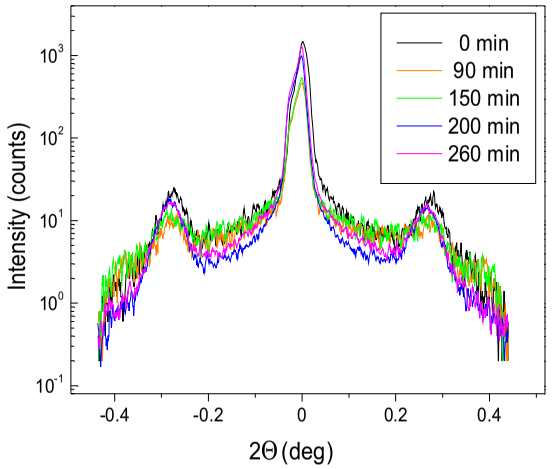

Fig. 1 GISAXS profiles taken at different times during annealing at 750°C.

These results are in contrast to previous observations on crystalline, oxide free ripple patterns where the ripple amplitude was found to decay within less than one hour of annealing at 667°C (cf. Erlebacher et al., Phys. Rev. Lett. **84**, 5800 (2000)). This discrepancy can be attributed to the lower thermal diffusivity of the amorphized and oxidized Si surface. Therefore, its enhanced thermal stability makes this type of rippled substrates promising templates for growth processes that require elevated temperatures but no crystalline substrates.

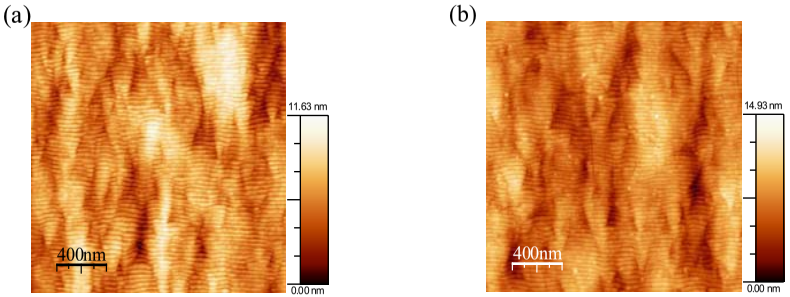

Fig. 2 AFM images of the sample of Fig. 1 before (a) and after (b) annealing for 4.5h at 750°C.

ROBL-CRG	**Experiment title:**	**Experiment number**: 2002647
Beamline: BM 20	**Date of experiment**: from: 20.06.2007 to: 26.06.2007	**Date of report**:
Shifts: 18	**Local contact(s)**: Carsten Bähtz	*Received at ROBL:*
Names and affiliations of applicants (* indicates experimentalists): Sven Philip Krüger Institut für Röntgenphysik, Universität Göttingen Tim Salditt Institut für Röntgenphysik, Universität Göttingen		

Report:

Nanometer sized x-ray beams with controlled coherence properties are needed for high resolution x-ray imaging and holography. X-ray waveguides are in principle be capable to deliver beams with cross sections down to below 10nm, values currently not achieved by other focussing optics. In practice, however, waveguide optics and applications are limited by the small transmission T of mono-modal waveguides.

To optimize the transmission and to minimize absorption losses, we have implemented a novel waveguide design based on a two-component cladding. The transmission T is strongly enhanced by using an appropriate *Mo* interlayer between the *Ge* cladding and a mono-modal guiding core made from amorphous carbon *C*. Thereby the absorption of the evanescent tails of the fundamental mode is significantly reduced, while a second (outer) cladding with a high absorption coefficient is used to efficiently block the radiative modes. The index profile of the two-component waveguide is shown in fig. 1, simulated for the experimental photon energy E=19.5 keV. For the experiment, a layer sequence *Ge*/*Mo*[d_i =30 nm]/*C* [d]/*Mo* [d_i =30 nm]/*Ge* was deposited on 3mm thick *Ge* single crystal substrates (Incoatec GmbH, Germany). Out of a series of different guiding layer thicknesses d, we present data measured of the waveguide with the smallest value d=18 nm. From the wafer a piece of l=2.4 mm was cut by a stainless steel filament wetted with an emulsion of 9 µm *SiC* crystallites.

The experiment was performed at the BM20 bending magnet beamline using a 19.5 keV beam defined by a double *Si*(111) monochromator, placed in the middle between two conjugate *Pt* mirrors for higher harmonic rejection. The beam size at the horizontally placed sample was 0.02 mm (vertical) x 2 mm (horizontal), as controlled by motorized entrance slits. Thus, the wavefront entrance front side was placed in the essentially unfocussed monochromatic beam of 1-2 x 10^8 photons/sec, depending on the ring current. After careful alignment of the waveguide translation z and the waveguide rotation α_i, the transmission was determined to T=0.081, which is 83% of the ideal (theoretical) transmission (T=0.098), calculated from the FD simulations. To characterize the divergence of the exiting beam and to unambigiously evidence waveguiding, the farfield intensity distribution was measured (fig. 1) at different angles of incidence α_i. In these scans, the center (maximum) of the farfield distribution is always found to be α_f=0, i.e. the farfield pattern maximum is constant with respect to the waveguide coordinate system.

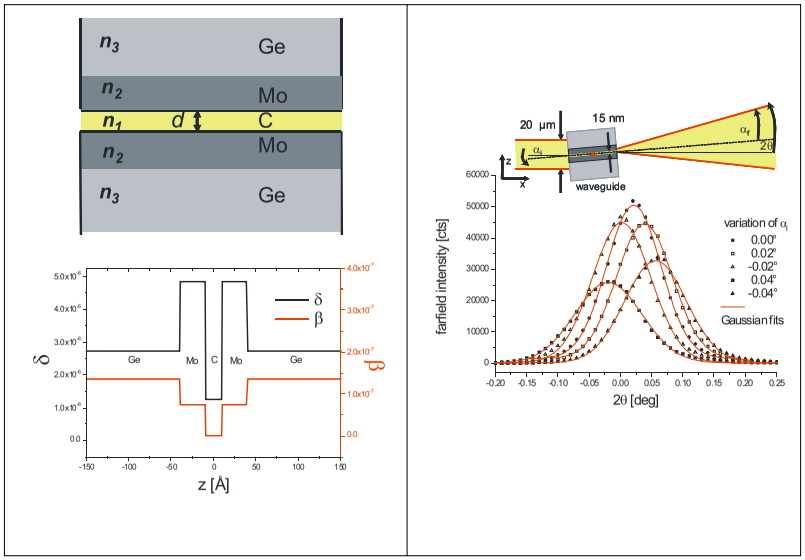

Figure 1(left) schematic and index profiles n=1-δ(z)+iβ(z) for the two-component waveguide, calculated for a photon energy E=19.5 keV. (right) The farfield intensity distribution as a function of exit angle 2θ together with a Gaussian fit (solid lines) for different incidence angles α_i.

The experimental results show that high transmission values can be obtained even for small beam diameters below 20 nm and for long waveguide length needed for efficient blocking of the over-exposed beams in the multi keV photon energy range. Simulations show that this can be extended to waveguides below 10 nm.

ROBL-CRG	**Experiment title:** SR-µ-XRD stress measurements of ultra low-k dual damascene inlaid copper inter-connect structures at temperatures between RT and 500°C	**Experiment number**: 20-02-648
Beamline: BM 20	**Date of experiment**: from: 19-SEP-07 to: 25-SEP-07	**Date of report**:
Shifts: 18	**Local contact(s)**: Dr. Carsten Baehtz	*Received at ROBL:*

Names and affiliations of applicants (*,[1] indicate experimentalists):

Hartmut Prinz*, Jochen Rinderknecht*, Inka Zienert*

*AMD Saxony LLC & Co. KG, Dresden, Germany

Carsten Baehtz

Forschungszentrum Rossendorf (FZR), Dresden and ROBL-CRG, Grenoble, France

Report:

Following the previous projects, the stress state of copper interconnect structures at temperatures between 25 and 350 °C has been examined. The samples contained the newest generation of metal stacks with ultra low-k material as dielectric. For all experiments in the past the high angle (311) reflection was used as the accuracy of XRD stress measurement directly depends on the diffraction angle. It showed up that on the newest samples the intesity of this reflection was not high enough to enable a correct data evaluation and the (111) reflection had to been chossen. The final data evaluation showed that the measurement of the (111) is not suitable for further measurements as the error of the stress data rises above the temperature dependant signal in some cases. As a consequence only a rough characterization of the stress temperature relation was possible.
The low intesity is a consequence of continous down scaling of interconnect structures. For XRD measurements the decreasing structure height leads to a much lower diffracting volume. Unfortunately the height reduction is strictly necessary to keep the structures within a manufacturable aspect ratio.
The only possible solution is the enlargement of the structure array. The new litho masks are already available and will be used in sample production for the next experiments.
Even though the data quality only enables a rough comparison, some interesting, new aspects and possible risks of the new materials could be derived from the last experiments.

The room temperature stress state is very similar to low-k interconnect structures. With rising temperature the tensile stress decreases faster in the ultra low-k dielectric, although the exact slope cannot be determined. The zero stress temperature is lower. At temperatures above 200-300°C, the stress starts to level in the compressive region.
For low-k and conventional dielectrics the stress leveling at high temperatures is connected with the start of copper yielding. In the case of the ultra low-k samples the temperature and the stress is in fact too low for copper yielding, so it is supposed, that other mechanisms for stress relieve like plastic deformation of the dielectric are important.
For device testing, there are several possible consequences.
For stress testing (temperature cycles) the higher slope of the stress means higher mechanical load per cycle. Plastic deformation of the dielectric even more encourages the formation of dielectric voids and interface delamination. Voids and delamination cracks can form copper diffusion paths and may lead to electrical shortage failures.
For electromigration (EM) testing, the stress leveling observed at test temperatures means that the maximum back stress, which is an important counterforce to electromigration, is much lower. EM may be less retarded and in the worst case copper extrusions and voids could be formed much more easily.

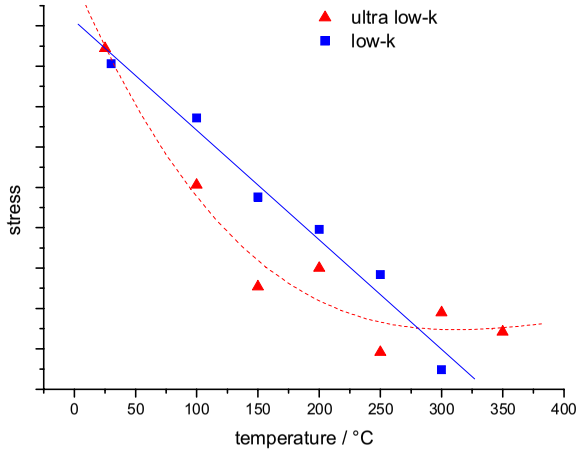

[1] Geisler, H., Prinz, H., Zienert, I. Rinderknecht, J., Kiene, M., and Zschech, E. Temperature-Dependent Stress Measurements at Inlaid Copper Interconnect Lines, Eigth International Workshop on Stress-Induced Phenomena in Metallization, AIP conference Proceedings **Vol. 817** (2006), p.277-287

[2] Prinz, H., Zienert, I., Rinderknecht, J., Geisler, H., Kiene, M., and Zschech, E. Effect of capping layer on temperature-stress relation in copper/low-k dual inlaid interconnect structures, Materials Research Society, AMC Conference Proceedings **Vol. 21** (2005), ISBN: 1-55899-865-9

ROBL-CRG	**Experiment title:** Structural investigation of Fe implanted TiO_2	**Experiment number:** **20_02_650**
Beamline: BM 20	**Date of experiment:** from: 06.05.2007 to: 08.05.2007	**Date of report:** 17.12.2007
Shifts: 9	**Local contact(s):** Dr. Carsten Baehtz (baehtz@esrf.fr)	*Received at ROBL:*
Names and affiliations of applicants (* indicates experimentalists): S. Zhou*, K. Potzger, C. Baehtz* Forschungszentrum Rossendorf, Institute of Ion Beam Physics and Materials Research, P.O.B. 510119, 01314 Dresden, Germany		

Report:

TiO_2 is a kind of wide-band gap semiconductor. The bandgap is 3.0 eV for rutile TiO_2 (3.2 eV for anatase). Transition metal doped rutile and anatase TiO_2 have been reported to be ferromagnetic above room temperature by various groups [1]. However, it was also found that the measured ferromagnetic properties can originate from nanoscale precipitates, or defects inside TiO_2. Recently several review articles have addressed the complexity of transition metal doped oxides concerning the origin of ferromagnetism [2, 3]. In order to unambiguously clarify the origin of the observed ferromagnetism, a highly sensitive structural analysis, i.e. synchrotron radiation x-ray diffraction (SR-XRD), and an elemental selective magnetization measurement, i.e. x-ray magnetic circular dichroism (XMCD), is required. By XMCD, Co and Fe_3O_4 precipitates are found to be responsible for the ferromagnetism in $CoTiO_2$ [4] and Fe:TiO_2 [5], respectively. In the current paper, a correlation between structure and ferromagnetism in transition metal implanted TiO_2 is presented. SR-XRD was used to detect the phase separation, superconducting quantum interference device (SQUID, Quantum Design MPMS) magnetometry has been used to determine the temperature dependent magnetization and the hysteresis curves. We assign the observed ferromagnetism to Fe nanocrystals (NCs). The post-annealing procedure resulted in the out diffusion of Fe and a phase transformation of the precipitates. These Fe NCs are highly textured.

Results

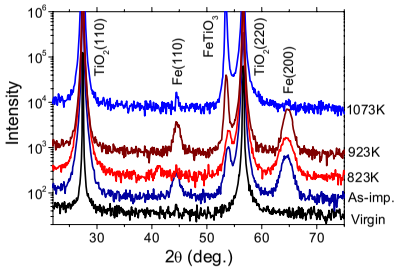

Fig. 1 SR-XRD symmetric 2θ-θ scans reveal two secondary phases: α-Fe and $FeTiO_3$ (annealing temperatures are indicated). After annealing at 1073 K, $FeTiO_3$ is the predominant precipitate.

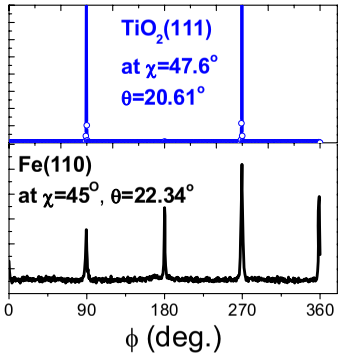

Fig. 2 SR-XRD φ-scans of Fe(110) and TiO2(111) for the 923 K annealed sample. Fe(110) and TiO_2(111) peaks are in the same azimuthal position, revealing the in-plane orientation relationship of Fe[010]//TiO_2 [1$\underline{1}$0].

References

[1] R. Janisch, et al., J. Phys.-Condens. Matter 17, R657 (2005).

[2] S. A. Chambers, Surf. Sci. Rep. 61, 345 (2006).

[3] T. Dietl, J. Phys.-Condens. Matter 19, 165204 (2007).

[4] J. Y. Kim, et al., Phys. Rev. Lett. 90, 017401 (2003).

[5] Y. J. Kim, et al., Appl. Phys. Lett. 84, 3531 (2004).

ROBL-CRG	**Experiment title:** **Real-time evolution of ZnO:Al thin film structure and electrical properties during annealing**	**Experiment number:** **20_02_651**
Beamline: BM 20	**Date of experiment:** from: 11.07.2007 to: 17.07.2007	**Date of report:** 07.01.2008
Shifts: 18	**Local contact(s):** Dr. Carsten BAEHTZ	*Received at ROBL:* *00.01.2008*

Names and affiliations of applicants (* indicates experimentalists):

A. Rogozin*, N. Shevchenko*, M. Vinnichenko

Forschungszentrum Dresden Rossendorf (FZD), Institute of Ion Beam Physics and Materials Research, D-01326 Dresden, Germany

C. Baehtz*

FZD and ROBL-CRG, Grenoble, France

Report

Application of transparent conductive oxides in advanced photovoltaic cells and flat-panel displays requires thin films with high transmittance (>90%) and low resistivity (~10^{-4} Ohm·cm). Reorganization and improvement of the film structure should be key factors for enhancement of the electron mobility [1], however it requires additional investigation. The aim of the experiment is relation of the ZnO:Al film structure (texture, grain size etc.) with the film electrical resistivity. For this propose the changes of structure and electrical resistivity of ZnO films with different initial crystalline quality and Al content were studied during annealing in vacuum using *in-situ* techniques.

Undoped ZnO films were deposited by medium frequency pulsed reactive magnetron sputtering at the base pressure of 3.4×10^{-7} mbar using a mixture of Ar and O_2 (partial pressure of 7.4×10^{-3} mbar and 1.4×10^{-3} mbar, correspondingly). The substrates were 10 mm x 10 mm x 0.3 mm pieces of Si(100) single crystals covered by 200 nm of thermally grown SiO_2 layer. The ZnO films were implanted with aluminium ions at ion energy of 110 keV and fluences of 1×10^{16} and 5×10^{16} Al^+ ions/cm^2.

The implanted samples were characterized by *in-situ* synchrotron XRD analysis (photon energy of 8.045 keV) and simultaneous four-point probe measurements during non-isothermal (T-ramp: 13 K/min) and isothermal (temperature range of 450–800°C) annealing.

The x-ray diffraction patterns of as-implanted ZnO films demonstrate only a (002) ZnO peak with FWHM in the range of 0.3 – 0.55° depending on the deposition temperature as well as implantation fluence. Figures 1 demonstrates the intensity and FWHM of ZnO (002) peak as a function of annealing temperature. The XRD patterns show no structural changes below the temperature of 450 °C. A further increase of annealing temperature leads to growth of the (002) peak intensity and decrease of FWHM. However, the recrystallization rate of the low-fluence implanted films (1×10^{16} Al^+/cm^2) is essentially higher than that of the samples implanted at 5×10^{16} Al^+/cm^2. The low-fluence implanted ZnO films become structurally identical after annealing at maximum temperature of 880 °C and there is no difference between the films deposited at 250 and 550 °C. The four-point probe measurements (not shown here) demonstrate significant decrease of the film resistivity with increasing temperature at the very early stage of non-isothermal annealing (100 - 300 °C) before an outset of recrystallization. Further increase of temperature leads to the crystallinity improvement at relatively weak resistivity changes.

The evaluation of the XRD and four-point probe data and calculation of the kinetic parameters of recrystallization as well as the activation energy are in progress.

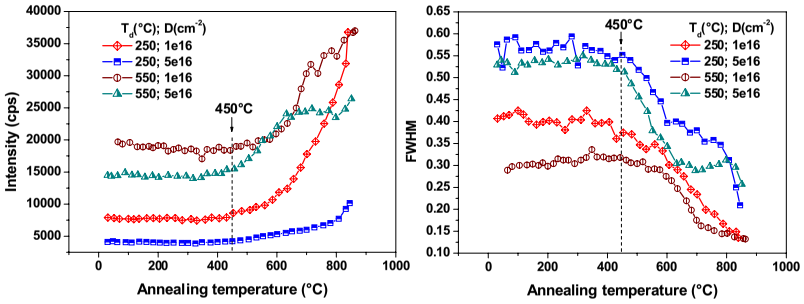

Fig. 1: *The temperature dependence of the XRD intensity and FWHM of the ZnO (002) peak of Al^+-implanted samples during non-isotermal annealing (T-rate: 13 K/min) .*

References

1. Birkholz M. et al, Phys. Rev. B 68, 205414 (2003)

ROBL-CRG	**Experiment title:** X-ray investigations for determining the aspect ratio in CdSe nanorods	**Experiment number:** 20-02-652
Beamline: BM 20	**Date of experiment:** from:14/11/2007 to:20/11/2007	**Date of report:**
Shifts:	**Local contact(s):** Carsten Baehtz	*Received at ROBL:*
Names and affiliations of applicants (* indicates experimentalists): Özgül Kurtulus – University of Siegen Andreas Biermanns – University of Siegen		

Report:

Semiconductor based 1D nanostructures are the subject of many scientific and technological developments as a result of their ability to provide multiple functionalities within a single structure. The preparation of nanorods and nanowires (NW) with modulated compositions and new methods has led to further developments. Catalyst assisted solution-liquid-solid synthesis is a new method where Bi nanocrystal catalysts are used to grow CdSe NW from solution. Inspection by TEM have revealed that the length of these NWs can be large as few microns. Therefore this kind of preparation technique is very challenging for application of 1D conductivity.

The aim of this experiment is to investigate prepared CdSe NWs by means of x-ray diffraction. In particular we are interested in the inspection of the NW structure along the c-axis of an individual NW as a function of NW diameter and temperature and seeing if there is any texture disturbing the homogeneity. In particular, it is important to investigate the structure close to the Bi seed to answer the question of whether Bi creates a eutectic with one of the components or not and what the composition is. In the TEM picture (Figure 1), the Bi particles are seen attached to the NW ends with diameters larger than the NWs'.

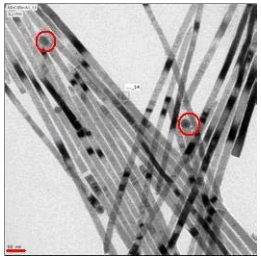

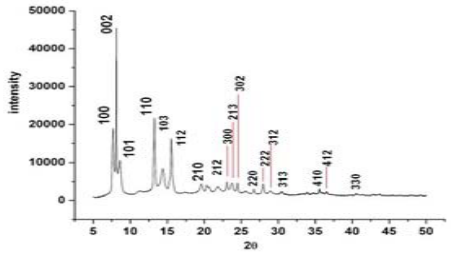

Figure1. TEM pictures of CdSe NWs. Figure2. Powder diffraction curve of a NW fraction.

Previous investigations was performed at DELTA, then new measurements have been done at ROBL synchrotron with a larger energy and the ability of turning the sample around its axis. It is observed that there is no preference in direction. Figure 2 shows a powder diffraction curve of a NW fraction taken at ROBL with a point detector and energy of 25keV. The peak positions can be interpreted by crystal structure of wurtzite. It is clearly seen that the 002 peak is sharper than 100 and other directions oblique with respect to the wurzite c-axis which is in accordance with previous works [1, 2]. The crystalline sample extensions are determined along and perpendicular to the c-axis using Scherer equation. It is always found an aspect ratio of 3…10, only. This is in contradiction with TEM measurements (Figure 1), showing a length of the rods in the order of 1µ and a width of 5 nm. Presently our finding is interpreted by the appearance of stacking faults which separate uniformly stacked AB, AB layers from each other. Our experiments with NWs prepared at different conditions to determine the parameters affecting the structure of NWs are going on. The results obtained will be helpful for the development of CdSe NWs imbedded in liquid crystals.

We would like to thank all the ROBL beamline staff for their great help during the measurements.

References

1. L.Ouyang, et al., J. Am. Chem. Soc., **129**, 133 (2007)

S.D. Bunge, et al., Journal of Materials Chemistry, **13**, 1705 (2003)

ROBL-CRG	**Experiment title:** Micro focusing with capillary optics and/or KB Mirror systems at ROBL	**Experiment number:** **20_02_653**
Beamline: BM 20	**Date of experiment:** from: 10.10.2007 to: 17.10.2007	**Date of report:** 5.11.2007
Shifts: 21	**Local contact(s):** Dr. Carsten Baehtz (baehtz@esrf.fr)	*Received at ROBL:*

Names and affiliations of applicants (* indicates experimentalists):
C. Baehtz*
Forschungszentrum Rossendorf, Institute of Ion Beam Physics and Materials Research, P.O.B. 510119, 01314 Dresden, Germany

Report:

Microfocussing is one of the great challenge for future investigations using Xray techniques. Therefore a monocapillary was tested for diffraction experiments on BM20. A new motorized and in the control software integrated alignment stage was also tested. The beam entrance of this capillary is 4.25 mm whereby the centred beamstop is around 2.6 mm, so only approx. 1.65 mm^2 beam area was accepted by this device. To test the performance reciprocal space maps (RSM) of (400) were also recorded.

Results

The device works at 8 kev with a gain of 445 and at 17 kev the gain decreases down to 110. At higher energies this device is not applicable. The smalles spot size was approx. 30*50 µm at 8 keV.

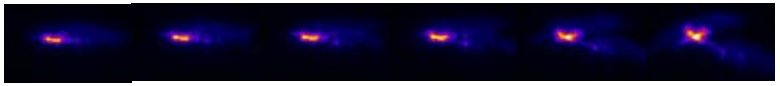

Fig1: Focus at 8 keV by different bending (30, 20, 17, 14.5, 12 respectively 9,5km) of mirror 2, recorded with an Photonics FDII.

The focus spot was recorded using a CCD camera with 12 µm pixel size. Additionally the focus size was mapped by the use of an 10 µm pin hole and a scintillation counter. In both cases side maximas were observed. To demonstrate the loss of resolution in an diffraction experiment, the RMS of Si (004) with and without capillary was recorded (Fig.3).

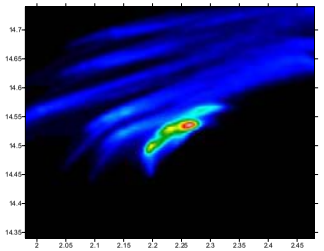

Fig 2: Focus mapped by the use of a pin hole, scaling in mm, intensity in logarithm scale.

Results

The intensity gain especially at 8keV is satisfactory, the energie range is competetive with other systems. Due to the fact, that incoming beam is divided into two parts by the central beam stop of the capillary and then reflected, leads to two itself at the focus crossing separate beams. Therefore the use of this device should only be recomanded in vertical scattering geometrie, where this effect can be neglected.

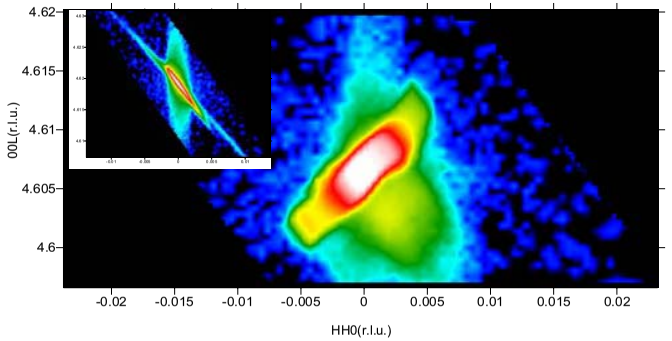

Fig.3: RSM of Si (004) reflection at 8keV, measured with capillary and without (inlay).

ROBL-CRG	**Experiment title:** Structural investigation of Fe implanted MgO	**Experiment number:** **20_02_654**
Beamline: BM 20	**Date of experiment:** from: 24.08.2007 to: 30.08.2007	**Date of report:** 17.12.2007
Shifts: 18	**Local contact(s):** Dr. Carsten Baehtz (baehtz@esrf.fr)	*Received at ROBL:*

Names and affiliations of applicants (* indicates experimentalists):

A. Shalimov*, S. Zhou*, K. Potzger, C. Baehtz*

Forschungszentrum Rossendorf, Institute of Ion Beam Physics and Materials Research, P.O.B. 510119, 01314 Dresden, Germany

Report:

Embedded ferromagnetic nanoparticles are currently under intense research due to their application capability in ultrahigh density data storage, magneto-optics, and magneto-transport, as well as in basic research as model systems for time-resolved experiments for fast magnetization switching or electron holography.[1] Investigations on Fe nanoparticles inside MgO single crystals, synthesized by means of high temperature ion implantation, are performed.

In recent study of the Fe implanted MgO crystals, superparamagnetic temperatuire dependences and hysteretic magnetization isoterms were observed using superconducting quantum interference device (SQUID, Quantum Design MPMS). It was found that the magnetic moment of MgO:Fe structures is stronly depend on the dose of implanted ions and applied temperature. This magnetic behavior of MgO:Fe is associated with self-organized iron nanoparticles, which can be presented by two structural phases, namely, α- and γ-Fe. In order to determine the iron phase responsible for observed magnetization and the size distribution of Fe nanoparticles, a highly sensitive structural analysis, i.e. synchrotron radiation x-ray diffraction (SR-XRD), is required.

Results

The measurements of SR-XRD point out to the strong correlation between the implanted dose of Fe and structural properties of MgO:Fe. The samples with low dose of implanted Fe do not show a presence of iron phases. It can be a consecution of a very small dimension of the nanoparticles and eventually could be analized using a diffuse scattering of x-ray diffraction pattern. The MgO crystals implanted with doses $(0.6\text{-}1)\times10^{17}$ cm^{-2} possess embedded γ-Fe nanoparticles. The α-Fe nanoparticles appear in the sample with the highest dose of implanted ions, especially intensively after thermal annealing. We belive that creation of α-Fe nanoparticles in the sample with the highest dose of implanted ions take place as a result of internal strain decreasing due to increased dimension of γ-Fe nanoparticles. Strong crystallographic correlation between α-, γ-Fe nanoparticles and MgO matrix was observed. The theoretical modeling of the magnetization properties, using the obtained structural characteristics of the studied systems, is in preparation.

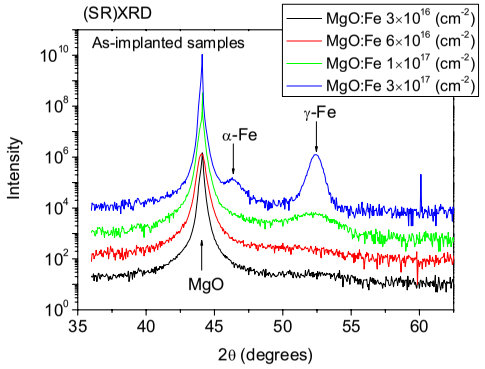

Fig. 1. SR-XRD 2θ/ω scans of MgO:Fe crystals with different dose of implanted Fe ions (doses of implantation are indicated).

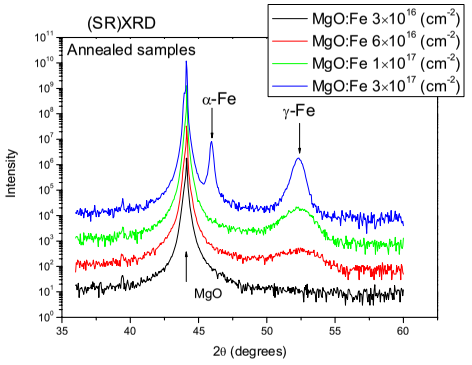

Fig. 2. SR-XRD 2θ/ω scans of annealed at 1023K MgO:Fe crystals with different dose of implanted Fe ions (doses of implantation are indicated).

References

[1] K. Potzger et al., J. Appl. Phys., 99, 08 N 701 (2006).

ROBL-CRG	**Experiment title:** Investigation of carbon encapsulated transition metal nanoparticles bythe means of GISAXS	**Experiment number**: 20-02-656
Beamline: BM 20	**Date of experiment**: from: 22/03/2008 to: 26/03/2008	**Date of report**:
Shifts: 12	**Local contact(s)**: Dr. Nicole Martha JEUTTER	*Received at ROBL:*

Names and affiliations of applicants (* indicates experimentalists):

*Gintautas Abrasonis, Forschungszentrum Dresden-Rossendorf, Germany

* György János KOVACS, Forschungszentrum Dresden-Rossendorf, Germany

*Markus Berndt, Forschungszentrum Dresden-Rossendorf, Germany

*Andrius Martinavicius, Forschungszentrum Dresden-Rossendorf, Germany

Report:

The above experiments concern the investigation by the means of GISAXS of the metallic inclusion morphology in the carbon-transition metal (TM=V, Co, Ni, Cu) nanocomposite thin films grown by ion beam co-sputtering in the temperature range of RT-500° C. The obtained results allow establishing the following tendencies which are summarized in Table 1.

System	Growth regime
C:V	granular uncorrelated at low T →granular correlated at high T
C:Co	granular uncorrelated at low T →columnar at high T
C:Ni	granular uncorrelated at low T →columnar at high T
C:Cu	granular correlated at low T →columnar at high T

It can be seen that for Co and Ni nanocomposites, there is a transition from a granular towards a columnar morphology. For C:Cu system, the growth at lower growth temperatures is granular but proceeds in a correlated manner, i.e. the renucleation occurs at relatively well determined distances and angles in relation to the substrate surface. At ~400° C, there is a transition towards a columnar growth. For C:V nanocomposites, the growth proceeds in a un-correlated manner at low growth temperatures which undergoes a transition at higher temperatures towards correlated granular growth.

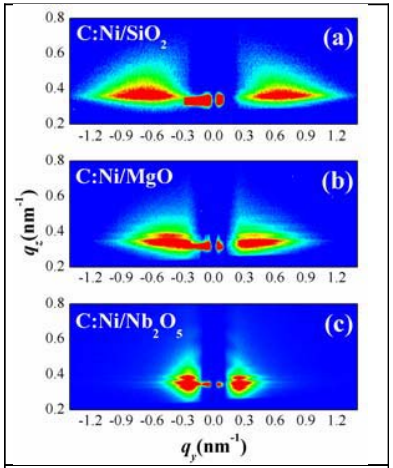

Fig. 1. GISAXS patterns of the C:Ni (~15 at. %) films grown on the SiO_2 (a), MgO (b), Nb_2O_5 (c) substrates.

The substrate type influence on the nanoparticle morphology was investigated for C:Ni(~15 at.%) films grown at 400° C. At this temperature, the columnar growth takes place which is confirmed by the GISAXS results presented in Fig. 1. In addition, it is observed that the substrate type plays a crucial role on the nanocolumn diameter and interparticle distance. The results strongly suggest that the metallic islands formed at the initial stages of the film growth act as trap centers for the subsequently deposited metal adatoms. The results on the substrate type influence have been submitted to Journal of Physical Chemistry.

Despite the possibility to establish the tendencies of the nanoparticle growth, the measurement geometry needs to be re-optimized to cover the whole morphology range, as for the actual experiments very often the positions of the GISAXS spot maxima were either behind the beam stopper or out of the detector range. In addition, the intensity to noise ratio for C:V was rather poor which should be attributed to low density contrast of VC nanoparticles in relation to the carbon matrix.

ROBL-CRG	**Experiment title:** Thermal behaviour of Fe and Ni thin film onto Si	**Experiment number:** **20_02_657**
Beamline: BM 20	**Date of experiment:** from: 12.12.2007 to 14.12.2007	**Date of report:** 5.11.2007
Shifts: 6	**Local contact(s):** Dr. Carsten Baehtz (baehtz@esrf.fr)	*Received at ROBL:*

Names and affiliations of applicants (* indicates experimentalists):

C. Baehtz*

Forschungszentrum Rossendorf, Institute of Ion Beam Physics and Materials Research, P.O.B. 510119, 01314 Dresden, Germany

Report:

In the center of interest in this investigation is to evaluate the possibility of *in-situ* investigation of the dewetting process of thin Fe film. Therefore different film thicknesses 5 and 10 nm onto different substrates with SiO_2 or Al_2O_3 buffer layers were studied. The use energy was 12keV, as sample environment the ROBL standard furnace was in use.

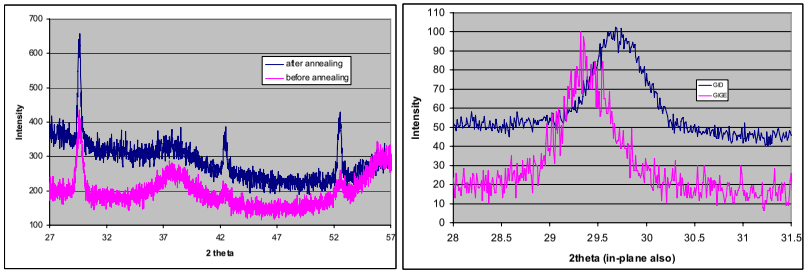

Fig. 1: Diffration pattern out-of-plane (left) and in-plane (right) of 10 nm Fe onto SiO_2.

Results

10 nm Fe onto SiO_2 as well as Al_2O_3 can be observed in grazing incident diffraction (GID) with α_i=0.5° up to 60°2theta without problems even before annealing and advanced crystallization. Of course after dewetting the corresponding reflection are sharper and much more pronounced as before as shown in Fig.1 left side. In contrast to this, only the Fe reflection around 29.5°2theta can be observed by grazing incident grazing exit

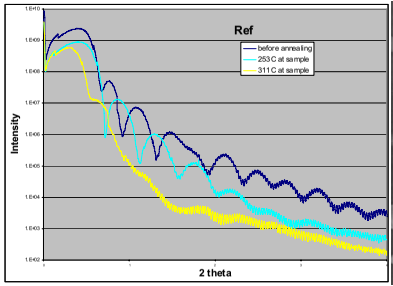

Fig.2: XRR-plot of 10 nm Fe onto SiO_2.

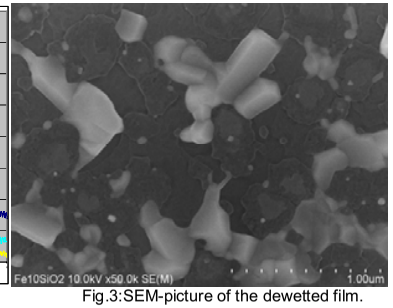

Fig.3:SEM-picture of the dewetted film.

diffraction (GIGE), other reflections suffer from shading effect of the furnace sample holder and the dramatic drop in the polarization factor which also determinates the signal intensity. But the signal-to-noise ratio is much better. The XRR-measurement show first a slight change in the oszillation and between 253 and 311°C clearly the dewetting of the film, which is proven by SEM-image in Fig. 3. 10 nm Fe onto Al_2O_3 shows the same behavior but dewettes at slightly higher temperatures. Before annealing is no crystalline Fe detectable in 5 nm Fe onto SiO_2 only afterward. The film splitting itself was clearly visible by XRR.

Outlook

On basis of this investigation further experiments concerning the film dewetting under different atmospheres like hydrogen, oxygen or vacuum ar planned, as well as in-situ growth experiments of carbon-nano tubes with the dewetted film in acetylene/hydrogen atmosphere. Due to the use of explosive gases these experiments are extremely sophisticated and need therefore the prove of feasibility before. These experiments will be carried out on in 2008.

ESRF	**Experiment title:** In-situ growth of Ge and Si NC´s out of a Ge, SiOx/SiO2 multilayer structure	**Experiment number:** SI20-02-658
Beamline: BM20	**Date of experiment:** from: 12.02.2008 to: 19.02.2008	**Date of report:** 06.11.2008
Shifts: 18	**Local contact(s):** Dr. Baehtz	*Received at ESRF:*

Names and affiliations of applicants (* indicates experimentalists):

Dr. Nicole Jeuttter

Dr. Carsten Baehtz

Report:

Metal or semiconductor nanocrystals (NCs) are of fundamental interest for new generations of light emitters or high-efficiency solar cells [1]. Within this experiment, Ge NCs have been fabricated by decomposition of GeO_x ($1< x <2$) within a (GeO_x-SiO_2) superlattice (SL) structure which enables a precise control of the size and the position of the NCs. The SL (2.5 nm GeO_x / 3.9 nm SiO_2)^{19x} was grown by reactive DC magnetron sputtering from elemental Si, Ge targets onto a SiO_2 / Si substrate. The deposition was performed at 250°C with 0.5 Pa working pressure in an Ar/O_2 mixture using the ROBL dual-magnetron sputter chamber [2], whereby the *in-situ* characterization using X-ray diffraction methods of thin film systems during growth and and subsequent annealing is possible. Varying the oxygen partial pressure, the deposition temperature and the DC power, the GeO_x stoichiometry and the thickness ratio of the GeO_x-SiO_2 sub-layers can be tailored in a well-defined manner.

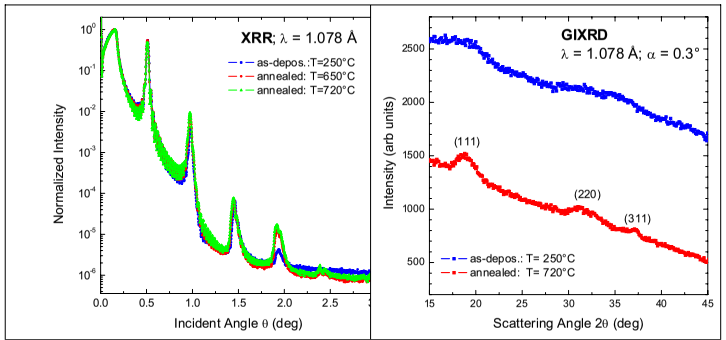

Fig. 1: X-ray reflectivity after deposition and subsequent annealing steps

Fig. 2: XRD pattern of the Ge NCs after deposition and 700°C annealing

Fig. 1 shows X-ray reflectivity (XRR) collected after deposition and during annealing. The intensity of the higher-order superstructure peaks increases during annealing indicating an enhancement of thickness uniformity (periodicity) and smoothing of the SL interfaces. Interface roughness (< 0.5 nm) have been derived from the simulation of the XRR curves. The formation of Ge nanocrystals by phase separation $GeO_x \rightarrow Ge + GeO_2$ has been observed by grazing-incidence diffraction (Fig. 2).Although in the diffraction pattern a near-order hump is already present in the as-deposited state, a pronounced Ge(111) signal appears after 650°C annealing which did further increase after annealing at 720°C. From Scherrer's equation the crystal size was determined to 2.5 nm which corresponds perfectly to the thickness of the GeO_x film. The NCs formation was proved *ex-situ* by transmission electron microscopy (TEM).

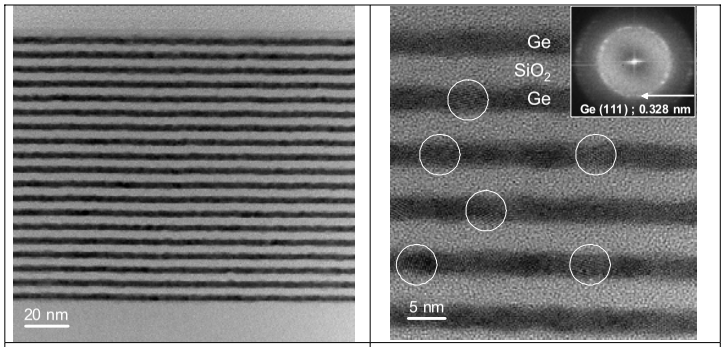

Figure 3a: TEM-image of the GeO_x-SiO_2 SL after 720°C post-annealing.

Figure 3b: HR-TEM-image with the Ge NCs (marked with white circles), the inset shows the corresponding FFT image.

Fig. 3a shows a cross-sectional image of the superlattice after 720°C annealing, confirming the smooth interfaces and negligible interdiffusion of the SL. Applying high-resolution TEM, Ge NCs were detected by imaging of Ge(111) lattice planes (Fig. 3b) or the corresponding spots at the FFT image (Fig. 3b, inset). For this sample, more a nanocrystalline Ge film have been realized which can be changed towards separated Ge nanoclusters by increasing the oxygen content in the GeO_x sub-layers during deposition.

References:

[1] S. Foss, T.G. Finstad, A. Dana, A. Aydinli, Thin Solid Films **515**, (2007), 6381-6384

[2] W. Matz, N. Schell, W. Neumann, J. Bøttiger, J. Chevallier, Review of Scientific Instruments **72**, (2001), 3344-3348

ROBL-CRG	**Experiment title:** SR-µ-XRD stress measurements of ultra low-k vs. low-k dual damascene inlaid copper interconect structures with different line widths at temperatures between RT and 500°C	**Experiment number**: 2002660
Beamline: BM 20	**Date of experiment**: from: 11.06.08 to: 16.06.08	**Date of report**: 25.11.08
Shifts:	**Local contact(s)**: Dr. Carsten Bähtz	*Received at ROBL:*

Names and affiliations of applicants (* indicates experimentalists):

Hartmut Prinz*, Jochen Rinderknecht*, Inka Zienert*,

*AMD Saxony LLC & Co. KG, Dresden, Germany

C. Bähtz

Forschungszentrum Rossendorf (FZR), Dresden and ROBL-CRG, Grenoble, France

Report:

The experiment was focused on the influence of interlayer dielectric material (ILD) on the temperature dependence of the stress in copper interconnect structures. The continuous increase of transistor density on microelectronic devices requires a proportional shrinking of the on-chip interconnect structures. Modern copper interconnect structures have line widths of less than 200 nm and are build on more than 9 different levels. The complex structure and the small dimensions result in very strict requirements for the mechanical stability of the system.
Metal structures that are exposed to mechanical stress may show deformation if the stress increases above a certain level. Under normal production and operation conditions this level is globally not exceeded, however on a local level stress gradients may build up and copper migration phenomena can be observed. This migration can lead to void formation and in the case of thin lines to a complete interrupt and device failure.

Large arrays of parallel copper interconnect lines with different linewiths were measured at the copper (111) reflection in the side-inclination mode. This mode, where the diffraction geometry is keeped constant and the sample is tilted in Chi and Phi, enables the calculation of the full 3D-stress state. The measurement of higher angle reflections would yield better stress resolution and lower error bars, but diffraction intensity was not sufficient to utilize this setup.
The small structure sizes, especially the small structure height, lead to very low diffraction volumes, so that the highest possible beam intensity has to be focused on the sample. One sample with a slight overpolish, were the structure height was reduced below 100nm, was nearly unmeasurable in the current experimental setup. As heights below this range will become common in the predictable future it was decided that a mayor upgrade of beam optics and and detector sensitivity is needed for project continuation.

Figure 1 shows a sample with a special ILD material. The stress temperature curve shows a completely different behaviour compared to normal low-k or ultra-low-k materials (Figure 2). The last process step for all samples is the addition of a capping layer at higher temperatures. The different coefficients of thermal expansions (CTE) lead to a tensile stress in the copper structures at room temperature after the cooling down. When the samples are heated up again, normally the stress decreases more or less linearly, whereas the rate of decrease depends on all the different materials CTEs and the geometry. The stress than reaches a zero level at a given temperature, that is not necessaryly the same as the capping layer deposition temperature. This due to irreversible processes like copper grain growth or chemical interlayer reactions that can take place. Further temperature increase leads to compressive stress, that reaches a constant level when copper yielding (plastic deformation) or ILD deformation begins.
The sample with the special ILD material shows a small increase of tensile stress in the first heating step, this may be due to the sample preparation. The sample cutout enables adsorbtion of water and other species from air which is prevented in the normal production process. The desorption changes the ILD volume and induces additional stress in the copper structures. Further heating decreases the stress, but with a much lower rate compared to the other samples. An explanation for this issue is even more speculative as further desorbtion, unusual thermal or thermo-elastic properties are possible.
With higher temperatures the stress decreases very fast and turns compressive. A stress plateau trough beginning yielding is not observed and maybe covered by different processes.
The examined ILD material shows much more complicated behaviour than expected and further analysis is going on for better understanding.

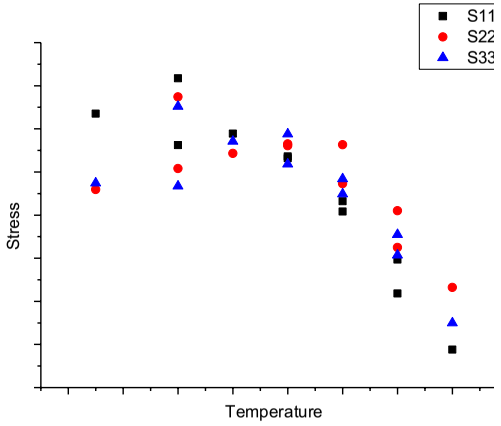

Figure 1: Stress-Temperature curve of a sample with special ILD material

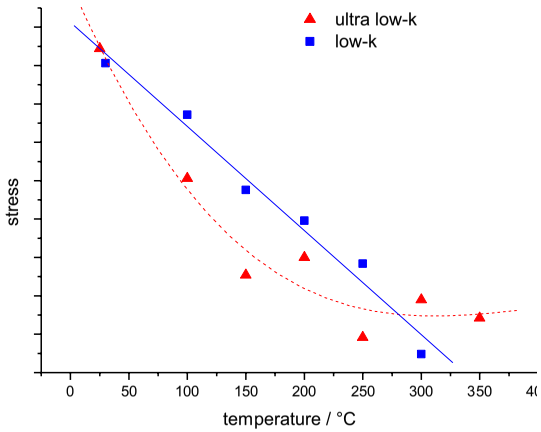

Figure 2: Stress-Temperature curve of samples with "common" low-k, ultra low-k ILD Material (taken for comparision from last report)

ROBL-CRG	**Experiment title:** ***In-situ study of oscillations during epitaxial and non-epitaxial thin film growth studied by specular and diffuse x-ray scattering***	**Experiment number:** **20_02_661**
Beamline: BM 20	**Date of experiment:** from: 11.03.2008 to: 18.03.2008	**Date of report:** 13.03.2009
Shifts: 18	**Local contact(s):** Carsten Baehtz	*Received at ROBL:* *13.03.09*

Names and affiliations of applicants (* indicates experimentalists):

M. Beckers*, F. Eriksson*, Linköping University, Sweden
C. Baehtz, Forschungszentrum Rossendorf, Germany & ROBL-CRG, France

Report

AIM:

In situ x-ray growth oscillations during epitaxial depositions are mostly characterized by specular x-ray reflectivity at the so-called anti-Bragg position. They are treated as roughness oscillations between nucleation and coalescence of individual monolayers. The amplitude decay caused by roughening is fitted in the kinematical approximation using a step model for the coverages of each monolayer proposed by Cohen [1]. In another approach, measurements during non-epitaxial depositions are carried out close to the critical angle of the deposited material. Correspondingly, the growth oscillations are treated as interference effects (time-resolved Kiessig fringes). Here, the amplitude decay caused by roughening is fitted by employing dynamic scattering using the Parratt formalism together with Nevot-Croce and Debye-Waller roughness models. One way to distinguish between roughness oscillations and thickness interference effects is the simultaneous measurement of specular and diffuse scattering, since for roughness oscillations the specular and diffuse scattering intensity should be exactly out of phase. This has been carried only for a few experiments [2], but up to now is missing a systematic approach. The **aim** of this experiment is to close this gap by a **systematic study of specular and diffuse growth oscillations for a set of film-substrate combinations with epitaxial and non-epitaxial growth**.

EXPERIMENTAL:

A set of 12 samples of different film-substrate combinations was deposited by magnetron sputtering from a Ti target, employing heteroepitaxy with high adatom mobility onto smooth substrates (Ti on to Al_2O_3(0001) and TiN onto MgO(001)), heteroepitaxy with high mobility onto rough substrates (Ti onto MgO(111)), heteroepitaxy with low mobility onto smooth and rough substrates (TiN onto Al_2O_3(0001) and MgO(111)) and polycrystalline film growth (Ti and TiN onto amorphous SiO_2). All films were deposited at a substrate temperature of 300°C. Ti was deposited at a target power of 40 W with an Ar flux of 3.4 sccm and a working pressure of 0.55 Pa, leading to a deposition rate of ~0.53 Å/s. TiN was deposited at a power of 70 W with Ar/N_2 fluxes of 2.16/0.66 sccm and a working pressure of 0.35 Pa, leading to a deposition rate of ~0.76 Å/s.
Each deposited film was characterized *in situ* by specular reflectivity (XRR) for thickness and roughness determination and large angle x-ray diffraction (XRD) to determine phase formation and off-plane lattice parameters, using monochromatized x-rays of λ=1.053 Å.
During each deposition both, the time-resolved specular reflectivity at ($\theta/2\theta$=1.75°/3.5°) and diffuse scattering at the Yoneda peak position in grazing exit configuration ($\theta/2\theta$=1.75°/1.95°) was measured, to distinguish between intensity oscillations due to oscillating roughness and thickness interferences.

RESULTS

The figure shows *in situ* data obtained for specular reflectivity (labelled Detector 1) and diffuse scattering (labelled Cyberstar) during the deposition of eight Ti and TiN films onto various subsrates.

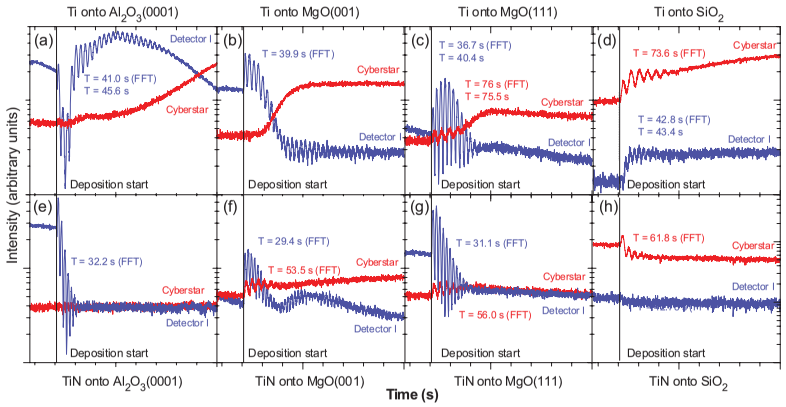

The melting point of Ti is 1668 °C, hence the homologous temperature during deposition was 0.18, yielding sufficient adatom mobility, especially on the Ti (0001) basal plane. A Ti deposition onto Al_2O_3(0001) (a) leads to an intially strained heteroepitxial layer with decrease in the specular reflectivity, but no increase in the diffuse signal, before after breakdown of the interfacial layer the specular growth oscillations decay due to slow surface roughening in accordance with slow increase of the diffuse signal. A deposition onto a relatively smooth MgO(001) substrate (b) without epitaxial matching yields a rough, non-textured polycrystalline Ti film, hence also a faster decay of the specular reflectivity right after deposition start and correspondingly to a steep increase of the diffuse signal with fast saturation before deposition stop. For epitaxial deposition of Ti onto a rough MgO(111) (c), the initial substrate roughness induces a fast decay of the specular growth oscillations with a concurrent oscillating increase of the diffuse signal, before signal saturation of both for later growth states. The ratio between the diffuse and specular oscillation periods is close to two, with a phase coherence (specular: max-max-max, diffuse: max-min-max) between them. The same doubling of the oscilation period is observed for a non-epitaxial – however still (0001)-oriented fiber-textured – deposition of Ti onto a rough amorphous SiO_2 substrate (c), although with less pronounced specular interference fringes due to interfacial reactions between the Ti and the SiO_2, as proven by *ex situ* compositional analyses.
The dissociation temperature of TiN is 2950 °C, hence the homologous temperature during deposition was reduced to 0.11. Furthermore, the surface binding energy of TiN is highly anisotropic with (111) being the high-energy surface. Correspondingly, the oscillations and overall intensity of the specular signal for epitaxial TiN(111) deposition onto smooth Al_2O_3(0001) (e) and rough MgO(111) (g) vanish quickly after deposition start. For epitaxial deposition of the low energy-surface TiN(001) onto MgO(001), the specular oscillations are disnernible for a longer period of time. Here, and for the MgO(001) case, also oscillations of the diffuse signal can be observed, with the same doubling of the period as for Ti deposition. A depositon onto rough SiO_2 yields polycristalline TiN, hence no visible oscillations in the specular signal, but oscillations in the diffuse signal which exhibit a comparable oscillation period as for depositions onto MgO(111) and MgO(001).

REFERENCES

[1] P. I. Cohen., *et al.*, Surface Science. **216**, 222 (1989).
[2] A. C. Mayer, *et al.*, Organic Electronics. **5**, 257 (2004).

ROBL-CRG	**Experiment title:** **MgO crystals implanted with Fe and Pt ions**	**Experiment number**: 20-02-662
Beamline: BM 20	**Date of experiment**: from: 21.06.2008 to: 24.06.2008	**Date of report**: 13.11.2008
Shifts: 9	**Local contact(s)**: Dr. Nicole Martha JEUTTER	*Received at ROBL:*

A. Shalimov*, G. Talut*

Forschungszentrum Dresden-Rossendorf e. V.
Institute of Ion-Beam Physics and Materials Research
01324 Dresden, Germany

Report:

In order to investigate possibility of formation of strongly ferromagnetic Fe-Pt secondary phase in MgO crystals, Fe and Pt ions (with equal fluences of 4.6×10^{15} cm^{-2}) were implanted to MgO matrix at energies of 173 and 500 keV respectively. The Fe implantation was performed at room temperature (RT) and at high temperature (HT) of 800 ^{o}C. Selected samples were annealed during 2 hours at 800^{o}C in vacuum with residual gases pressure less then 2×10^{-6} mbar. The structural characterization was performed using monochromatic synchrotron x-ray radiation with a wavelength λ=1.239864 Å. Longitudinal and transverse scans were used to analyse the coherent and diffuse x-ray scattering.

Diffraction peaks from secondary phases were not detected for the as-implanted, as well as, for annealed samples. However, there is clear evidence, that after implantation, a region enriched with Fe-Pt creates strongly strained layer near the specimen surface (FIG. 1a). The strain, ε, reaches value of 6.77×10^{-3}. After annealing, strains in near-surface area disappear. Enhanced diffuse x-ray scattering of annealed samples (FIG. 1b), points out to a presence of embedded substrusture in the annealed samples. According to our computations, embedded particles create strong deformations in a range of 35 nm from the particle core. Estimated concentration of nanoparticles is 1.5×10^{11} per sample ($10\times10\times0.5$ mm^3).

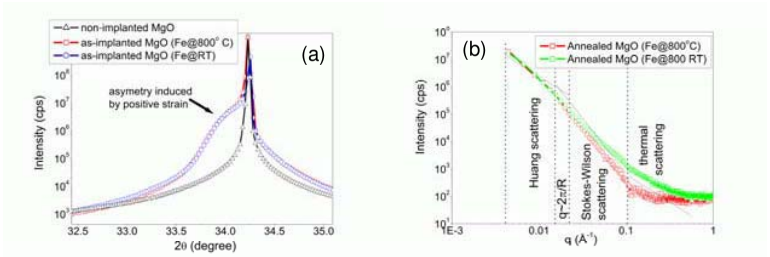

Fig. 1. a) 2θ- ω scans of MgO and MgO implanted with Fe and Pt; b) Diffuse scattering of annealed MgO crystals implanted with Fe and Pt.

Influence of annealing at 800^{o}C under high hydrostatic pressure (HP) of 10 kbar on secondary phase formation was studied for the set of MgO crystals implanted with Fe ions (fluences: MgO:Fe#1 -3×10^{16} cm^{-2}, MgO:Fe#2 -6×10^{16} cm^{-2}, MgO:Fe#3 -1×10^{17} cm^{-2}, MgO:Fe#4 -3×10^{17} cm^{-2}, E=100 keV, at target temperature of 800 ^{o}C).

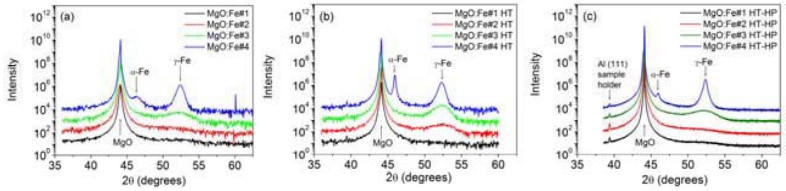

Fig. 2. 2θ/ω scans of MgO:Fe: a) as-implanted, b) after HT and c) after HT-HP annealing.

HT-HP annealing leads to formation of smaller ferromagnetic α-Fe particles and bigger paramagnetic γ-Fe particles with respect to as-implanted or HT annealed samples (dimensions were calculated from 2θ/ω scans shown in FIG.2).

ROBL-CRG	**Experiment title:** Spinodal decomposition and formation and structural properties of transition metal clusters	**Experiment number**: 20-02/663
Beamline: BM 20	**Date of experiment**: from: 03.05.2008 to:05.05.2008	**Date of report**: 22.10.2008
Shifts: 8	**Local contact(s)**: Dr. Nicole Martha JEUTTER	*Received at ROBL:*

G. Talut*, D.Bürger*, A. Shalimov* and J. Grenzer*

Forschungszentrum Dresden-Rossendorf e. V.
Institute of Ion-Beam Physics and Materials Research
01324 Dresden, Germany

Report:

One of the challenges in the engineering of ferromagnetic diluted magnetic semiconductors is the determination of their microstructure. We have investigated wurtzite gallium nitride (GaN) layers on sapphire implanted with 200 keV Fe ions and fluences of $8\cdot10^{16}$ cm^{-2} and $1.6\cdot10^{17}$ cm^{-2} at room temperature. The samples were subsequently annealed by using the flash lamp method for 3 ms, 20 ms and 2×20 ms in Ar-flow. In order to investigate a possible spinodal decomposition as well as the formation and structural properties of transition metal clusters or other secondary phases structural investigations were carried out with a 10 keV monochrome x-ray radiation in the ω-2θ geometry.

In as implanted samples no secondary phases like bcc-F or iron nitrides were detected using x-ray diffraction techniques (Fig. 1). However, a clear ferromagnetic response was found by SQUID magnetometry in these samples. This behavior is a clear indication of a spinodal decomposition.

In the sample implanted with $8\cdot10^{16}$ cm^{-2} a broad peak at about 35.2° was detected after 3 ms flash lamp annealing. This peak could be attributed to nanometer sized clusters of ε-$Fe_{2.4}N$(221-reflection). This peak disappears for longer annealing times. For 20 ms annealing a peak at 34.7° appeared. This one has to be assigned to ε-Fe_3N(200) because the sample has turned to be strong ferromagnetic. Longer annealing times (2x20 ms) lead to an additional peak at about 33.9°. This cannot be assigned to a certain phase and could be related to some nonstochiometric iron nitride.

For a higher Fe fluence ($1.6\cdot10^{17}$ cm^{-2}), i.e. higher Fe concentration, already a 3 ms annealing lead to an elevation at about 34.7°, that is ε-Fe_3N. It grows to a broad peak after annealing for 20 ms. An intensive broad peak at about 35.5° was detected upon annealing for 2x20 ms and was related to bcc-Fe what was supported by Mössbauer spectroscopy.

Therefore, the following process during annealing can be suggested. During the implantation Fe is randomly distributed in the GaN lattice. For high fluences (≥ $8\cdot10^{16}$ cm^{-2}) spinodal decomposition may occur. Short annealing times cause short diffusion lengths. Furthermore they enable the formation of metastable iron nitrides. The increase of annealing times results in a higher Fe content in the forming iron nitrides. Finally, for large Fe fluences and/or highest annealing times (>40ms) metallic bcc-Fe clusters are formed that have an epitaxial relationship with the GaN matrix. Further annealing would result in the growth of that bcc-Fe as it is known from the literature [1].

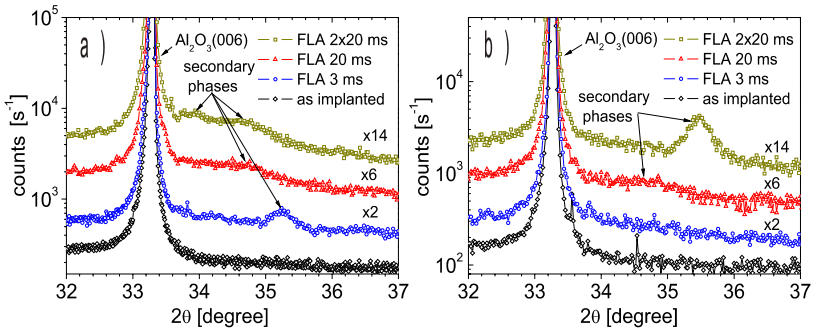

Fig. 1: Coplanar ω-2θ scans of samples implanted with a) $8\cdot10^{16}$ cm^{-2} and b) $1.6\cdot10^{17}$ cm^{-2} Fe and subsequently flash lamp annealed. Scans are shifted along the ordinate.

[1] *G. Talut, H. Reuther, A. Mücklich, F. Eichhorn, and K. Potzger, Appl. Phys. Lett.,* ***89****, 161909 (2006).*

Postal address: FZD, Postfach 510119, D-01314 Dresden; Germany
Telephone: +49 (351) 260 3122; Fax: (0351) 260 3438.
ROBL-CRG at the ESRF, B.P. 220, F-38043 Grenoble Cedex, France
Telephone: +33 (476) 88 24 62; Fax: +33 (476) 88 2505

Postal address: FZD, Postfach 510119, D-01314 Dresden; Germany
Telephone: +49 (351) 260 3122; Fax: (0351) 260 3438.
ROBL-CRG at the ESRF, B.P. 220, F-38043 Grenoble Cedex, France
Telephone: +33 (476) 88 24 62; Fax: +33 (476) 88 2505

ROBL-CRG	**Experiment title:** In-situ structural investigations of the $L1_0$ ordering in FePt layers during magnetron sputtering	**Experiment number:** 20-02-665
Beamline: BM 20	**Date of experiment:** from: 30.04.2008 to: 01.05.2008	**Date of report:** 28.01.2009
Shifts: 9	**Local contact(s):** Dr. Nicole Jeutter	*Received at ROBL:*

Names and affiliations of applicants (* indicates experimentalists):
V. Cantelli*, J. Grenzer*, J. von Borany* FZR, FWIS
N. Jeutter* FZR, FWIS, ROBL-CRG

REPORT

FePt is widely investigated because of its peculiar high magneto anisotropy density $K_U = 3.7 - 6.2 \times 10^{19}$ eV/cm^3 [1] that allows to strongly reduce the volume of a single switching magnetic domain still satisfying the thermal stored data stability condition $K_U V/k_B T = 50 - 70$ [1]. To ensure an acceptable noise reduction, FePt domains have to be magnetically decoupled, for example, by a diamagnetic matrix like Ag having a lower surface energy ($\sim 7.11 \times 10^{14}$ eV / cm^2 [2]) than FePt ($\sim 1.31 \times 10^{15}$ eV / cm^2 [3]) and therefore to not segregate into the FePt particles. RT deposited FePt layers exhibit a metastable soft - ferromagnetic A1 fcc phase. Subsequent annealing at temperatures above 500°C gives the tetragonal distortion to the strong ferromagnetic $L1_0$ phase [4].

In previous studies [5], we reported of low transition temperatures (T ~ 350°C) achieved using the ROBL dual magnetron deposition chamber [6]. In this study, we investigated FePt nanostructures evolution during deposition at 400°C as function of the Ag thickness (sample *A*: 7.3 nm thick $Fe_{54}Pt_{46}$ layer separated by 0.2 nm Ag and sample *B*: 7.5 nm thick $Fe_{57}Pt_{43}$ layer separated by 6.0 nm Ag) by in-situ grazing incident small-angle X-ray scattering (GISAXS) at an energy of E = 10 keV. To detect the formation of the $L1_0$ FePt phase, a scintillation detector (BEDE) was positioned to analyse the (110) FePt superstructure peak at 2θ = 26°.

Figure 1 shows the GISAXS patterns of sample *A* recorded during deposition at $\alpha_i = 0.35°$, close to the Ag critical angle for total external reflection. During film growth,

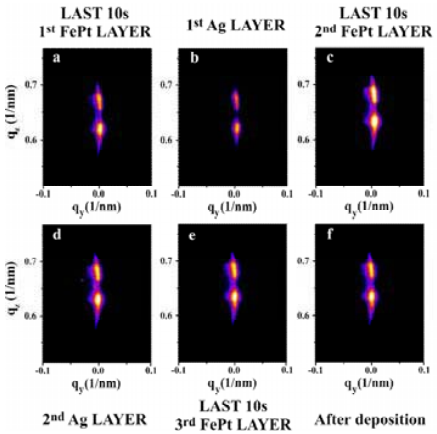

Figure 1: GISAXS evolution patterns collected for 10s during deposition at an incident angle $\alpha_i = 0.35°$ for sample *A* (intensity in logarithmic scale); figure (f) is collected just after deposition at 400°C.

there is no significant change in the GISAXS patterns: specular and transmitted signals broadening points out only a roughness increasing. Ag amount is too low to separate FePt islands.

The FePt phase evolution, detected by the point detector, is reported in figure 2 as function of the deposition time. The $L1_0$ phase formation began around 300 s. Therefore, we obtained the $L1_0$ phase at 400°C with a minimum FePt thickness of about 12 nm.

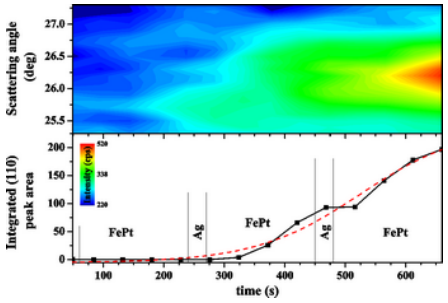

Figure 2: GIXRD ($\alpha i = 0.5°$) results on the (110) FePt peak during deposition of sample *A*. Lower graph: peak integrated area vs. deposition time (experimental data: black line with dots corresponding to the middle of each scan; simulation: red dashed line. Upper graph: (110) peak evolution vs. time.

In figure 3, the GISAXS evolution is shown for sample *B*: during growth figure 3a to figure 3e and after cooling down at RT, figure 3f. 6 nm of Ag directly on the a-SiO_2 at 400°C forms islands [7]. The subsequent FePt layer is, therefore, replicating the low frequency roughness created by Ag enhancing the GISAXS signal (figure 3c). Ag is forcing FePt agglomeration into clusters. From the GISAXS patterns collected at the end of deposition (fig. 3e, 3f) FePt clusters have side facets tilted by almost 25° from sample surface normal and characteristic length size that shrinks at RT (fig. 3f) to 150 nm from 180 nm at the end of the first FePt deposition (fig. 3c).

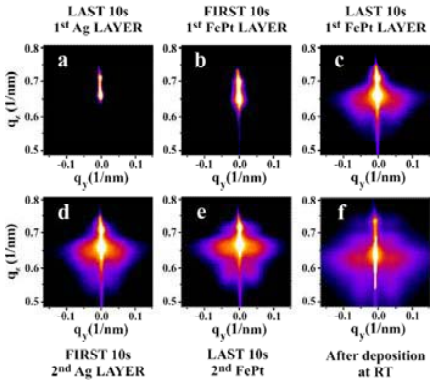

Figure 3: GISAXS evolution patterns collected for 10s during deposition at an incident angle $\alpha_i = 0.35°$ for sample *B* (intensity in logarithmic scale): (a) is the profile at the end of the first Ag layer deposition, (b) is the beginning of the FePt deposition concluded in (c), (d) is the last Ag deposition and (e) the last FePt layer at 400°C; (f) is taken at RT directly after deposition.

The simultaneous detection of cluster growth and evolution by GISAXS and phase transition in XRD geometry was successful applied to investigate, in-situ, the deposition of the FePt/Ag system on amorphous SiO_2 at a deposition temperature of 400°C. Using a certain amount Ag it is possible to trigger islands growth of the hard ferromagnetic $L1_0$-FePt phase.

References:

[1] D. Weller, A. Moser, *IEEE Trans. Magn.* 1999, *35*, 4423
[2] Y.M. Chiang, *et al.* in *Physics Ceramics*, WILEY, **New York 1997**, 357
[3] J. -S. Kim, Y. M. Koo, B. J. Lee, *J. Appl. Phys.* **2006**, *99*, 053906
[4] Yun-Chung Wu *et at.*, *Appl. Phys. Lett.* 2007, *91*, 072502
[5] V. Cantelli, J. von Borany, A. Mucklich, SQ. Zhou, J. Grenzer, *Nucl. Instr. Meth. B* **2007**, *257*, 406
[6] W. Matz, N. Schell, W. Neumann, J. Bøttiger, J. Chevallier, *Rev. Sci. Instrum.* **2001**, *72*, 3344
[7] T. Oates, A. Muecklich, *Nanotechnology* **2005**, *16*, 2606

ROBL-CRG	**Experiment title:** In-situ XRD/XRR of thin film catalysis during carbon nanotube growth	**Experiment number:** **20_02_666**
Beamline: BM 20	**Date of experiment:** from: 18.6.2008-20.6.2008	**Date of report:** 5.11.2007
Shifts: 12	**Local contact(s):** Dr. Carsten Baehtz (baehtz@esrf.fr)	*Received at ROBL:*

Names and affiliations of applicants (* indicates experimentalists):

C. Baehtz*, T. Wirth[1)]*

Forschungszentrum Rossendorf, Institute of Ion Beam Physics and Materials Research, P.O.B. 510119, 01314 Dresden, Germany
1) Centre for Advanced Photonics and Electronics, University of Cambridge, 9 JJ Thompson Avenue, Cambridge CB3 0FA, UK

Results

Metal nano-particles act as catalist in the carbon nano tube CNT growth process [1,2]. We focused on catalyst formation by the dewetting of polycrystalline Ni-films with different thickeness on SiO_2 support during annealing under a reducing hydrogen atmosphere at 0.7 mbar. For the subsequent CNT growth at 550°C acetylene (55% H_2 and 45% H_2C_2 at 1.4 mbar) was added as carbon source. The synthesis process was observed by X-ray diffraction (XRD) for determination of the crystalline phases and X-ray reflectivity (XRR) to monitor the thin film parameter [3]. At 200°C the XRR signal in Fig 1 left displays a slightly increasing film thickness due to the reduction of an amorphous surface oxide layer of approx. 0.7 nm. Also the surface smoothens significantly proven by the more pronounced oscillations in XRR. Between 200-250°C the signal vanishes, the film has completely dewetted. At this temperature the bragg reflection of Ni is visible at first time, the increasing intensity in XRD by decreasing FWHM clearly show the ongoing nickel crystallization at higher temperatures. By this process the size of the emerging crystallites is around 9 nm. Upon acetylene exposure at 550°C XRD indicates the formation of CNT (graphite diffraction reflection at 18°2theta, not shown) and Ni_3C accounting on the Ni phase. As-grown CNT in figure 2 show an acceptable distribution in its diameter at a low yield. The dewetting temperature strongly depends on the metal film thickness. With increasing layer thickness the interface interactions with the buffer layer are less pronounced and the dewetting temperature increases. The CNT yield, thickness and morphology correlate with the metal particle size and therefore with the pristine layer thickness. Further experiments were planed to elucidate the growth mechanism of CNTs and the role of Ni_3C in it. Also open is the question if Ni_3C and not Ni act as catalyst in this growth process.

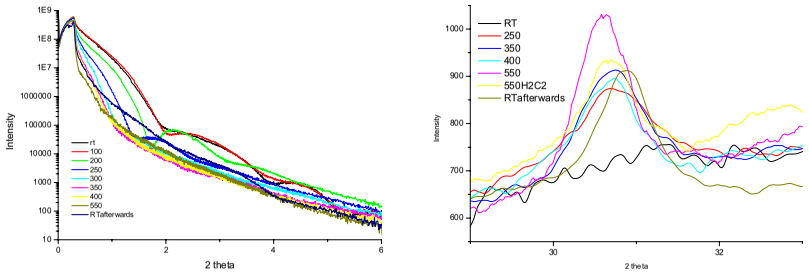

Fig.1: 2 nm Ni onto 200nm SiO_2 buffer layer on Silicon. Left: XRR data display first the reduction of the surface oxide layer and accompanying film smoothening and secondly the film dewetting. The high frequent oscillations visible in the data are due to a 200nm SiO_2 buffer layer of the system under investigation. Rigth: XRD data of the Ni (111) reflection show Ni-crystal growth during heating by crystallization.

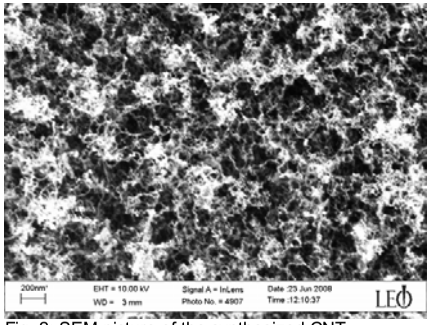

Fig. 2: SEM picture of the synthesized CNT.

References

[1] Surface Diffusion: The low activation energy path for nanotube growth, Hofmann S., Csányi G., Ferrari A. C., Payne M. C., Robertson J., Phys. Rev. Lett. 95, 036101 (2005).
[2] In-situ observations of catalyst dynamics during surface bond carbon nanotube nucleation, Hofmann S., Sharma R., Ducati C., Du G., Mattevi C., Cepek C., Cantoro M., Pisana S., Parvez A., Ferrari A. C., Dunin-Borkowski R., Lizzit S., Petaccia L., Goldoni A., Robertson J., Nano Lett. 7, 602 (2007).
[3] In situ study of the dewetting behavior of Ni-films on oxidized Si(001) by GISAXS
R. Felici, N.M. Jeutter, V.Mussi, F. Buatier deMongeot, C. Boragno, U. Valbusa, A. Toma, Y. Wei Zhang, C. Rau, I.K. Robinson, Surf. Sci. 601, 4526 (2007).

ROBL-CRG	**Experiment title:** In-situ XRD/XRR of thin film catalysis during carbon nanotube growth	**Experiment number:** 20_02_671
Beamline: BM 20	**Date of experiment:** from: 21.10.2008-28.10.2008	**Date of report:** 6.5.2009
Shifts: 18	**Local contact(s):** Dr. Carsten Baehtz (baehtz@esrf.fr)	*Received at ROBL:* **6.5.2009**

Names and affiliations of applicants (* indicates experimentalists):
C. Baehtz*, T. Wirth[1)]*, C.S. Esconjauregui[1)]*

Forschungszentrum Rossendorf, Institute of Ion Beam Physics and Materials Research, P.O.B. 510119, 01314 Dresden, Germany
1) Centre for Advanced Photonics and Electronics, University of Cambridge, 9 JJ Thompson Avenue, Cambridge CB3 0FA, UK

Results

Metal nano particles like Fe or Ni can act as catalyst in the carbon nano tube (CNT) growth process [1,2]. These metals were first deposited as thin film onto Si-wafer with SiO_2 or Al_2O_3 buffer layers and then heated up under inert or reducing atmosphere.

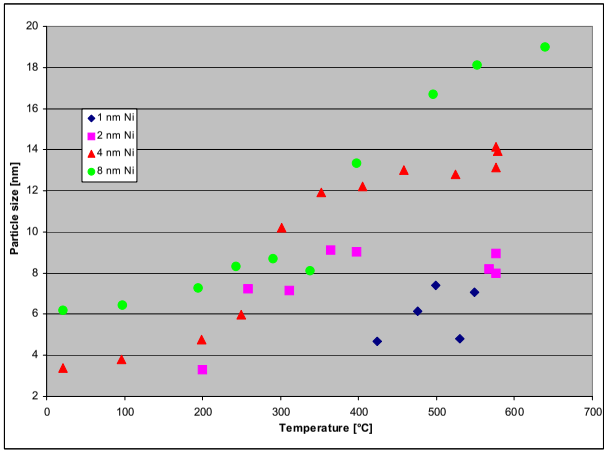

Fig.1: Temperature dependence of the Ni nano-crystallite sizes during heating and the subsequent dewetting. process.

Hereby the film dewets and the nano particles are formed. The crystal sizes of the resulting nano-particle depend on the thickness of the initial film. A crude approximation shows that the particles became three times bigger than in the film.

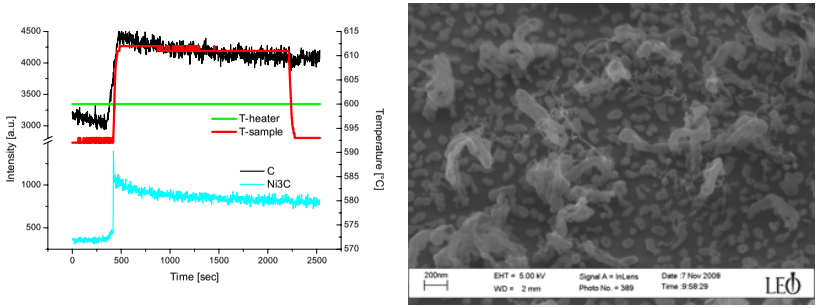

Fig. 2: Time resolved measurement of the Ni_3C and C signal and the corresponding SEM picture (right).

During the growth experiment using 2 or 4 nm thick Ni film system a second phase Ni_3C is observed. This raises the question if this could be the catalytic active material. Time resolved XRD in Figure 2 monitoring the Ni_3C and graphite signal shows the Ni_3C formation directly after the H_2C_2 injection, which act as carbon source. With a slight delay the C signal also increases. Both signal are stable after approx. 10 min. The increased sample temperature during the H_2C_2 feed indicates an exothermic reaction. Based on the corresponding SEM picture the C-signal can be attributed to the low yield CNT but also on surface coking carbon. Further experiments to elucidate this aspect were planed in future.

References

[1] Surface Diffusion: The low activation energy path for nanotube growth, Hofmann S., Csányi G., Ferrari A. C., Payne M. C., Robertson J., Phys. Rev. Lett. 95, 036101 (2005).
[2] In-situ observations of catalyst dynamics during surface bond carbon nanotube nucleation, Hofmann S., Sharma R., Ducati C., Du G., Mattevi C., Cepek C., Cantoro M., Pisana S., Parvez A., Ferrari A. C., Dunin-Borkowski R., Lizzit S., Petaccia L., Goldoni A., Robertson J., Nano Lett. 7, 602 (2007).

ESRF

ESRF	**Experiment title:** Structure stability of short period GaAs/AlGaAs and AlInAs/InGaAs superlattices	**Experiment number:** HS-3291
Beamline: BM20	**Date of experiment:** from: 18-07-2007 to: 21-07-2007	**Date of report:** 21-12-2007
Shifts: 9	**Local contact(s): Dr Carsten BAEHTZ**	*Received at ESRF:*

Names and affiliations of applicants (* indicates experimentalists):

Jarosław Gaca, Marek Wojcik, Krystyna Mazur
Institute of Electronic Materials Technology, Warsaw, Poland

Report:

The aim of the project was to investigate the chemical composition profile of the AlAs/GaAs superlattices to be used as distributed Bragg reflectors for vertical cavity surface emitting lasers (VCSELs), and heterostructures making up quantum cascade lasers (QCLs).

1: Distributed Bragg Reflectors.

High quality Bragg mirrors for VCSEL applications should be characterized by high reflectivity and low series resistance of the stack in order to protect the whole structure from the thermal heating. It was reported [1] that by using graded interfaces the DBR series resistance can be significantly reduced compared to abrupt interfaces. In our project two different techniques were employed to modify interfaces between successive layers of the AlAs/GaAs based Bragg mirror: one consists in growing intermediate layer with varying chemical composition between AlAs and GaAs layers, another one consists in applying high energy ion irradiation and thermal annealing to introduce grading in the interfaces. In order to determine the chemical composition profile for structures with modified interfaces high resolution x-ray diffraction analysis was employed and rocking curve for each sample has been measured. In the case of a rocking curve the low-order satellites close to the Bragg peaks give the overall shape of the composition through the period, whereas the higher-order satellites give information about the finer details, for example the interface shape [2]. Due to this fact the investigation of the chemical composition profile by means of x-ray diffraction calls for collecting data in wide angular range and this makes that we are dealing with very low intensities, in this case the synchrotron radiation proves to be invaluable. In the course of the experiment a series of superlattices with modified interfaces by means of both mentioned above methods have been investigated. In Fig.1 there are experimental and calculated rocking curves presented for superlattice with intermediate $Al_{0.5}Ga_{0.5}As$ layer, in Fig.2 & 3 rocking curves for superlattices where ion intermixing technique and thermal annealing has been employed to modify interfaces.

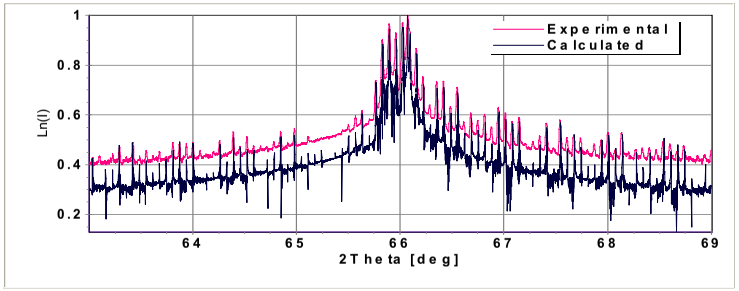

Fig.1 (004) experimental and symulated rocking curves for 23- period (52.9nm GaAs, 20nm $Al_{0.5}Ga_{0.5}As$, 63nm AlAs i 20nm $Al_{0.5}Ga_{0.5}As$) superlattice.

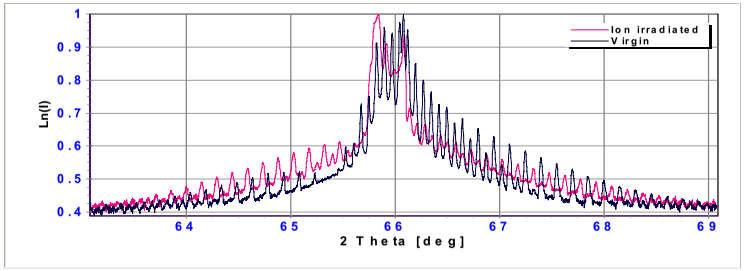

Fig.2 (004) experimental rocking curves for virgin and ion irradiated DBRs.

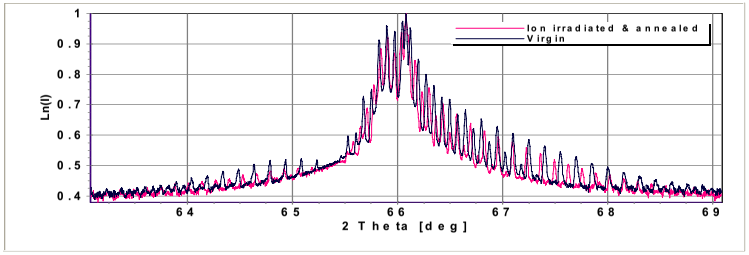

Fig.3 (004) experimental rocking curves for virgin and ion irradiated & annealed DBRs.

2. Quantum cascade lasers.

Another type of heterostructures which have been investigated in the course of the project were the ones designed for application as a quantum cascade laser. The full structure of such a laser consists of a few hundred ultra thin layers with varied chemical composition making up a superlattice where each period is a superlattice in itself. To find out the chemical composition profile for such a structure it is necessary to perform rocking curve measurement in even wider angular range than that used for DBR investigation. We could also expect very weak intensities of higher order satellite reflections. Synchrotron radiation is sufficiently strong to allow registration of these remote satellite reflections. In the course of the experiment we have investigated samples containing: active region, injector, active region + injector, 30x(active region + injector) and the full structure of quantum cascade laser. As an example, in fig.4,5 there are presented QCL structure and its TEM image, experimental and simulated rocking curves for full QCL structure.

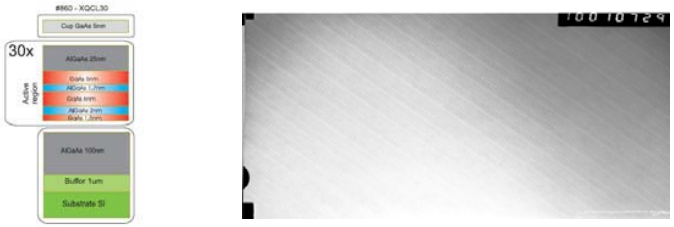

a) b)

Fig. 4 a) Structure of quantum cascade laser b) TEM image for heterostructure presented in a)

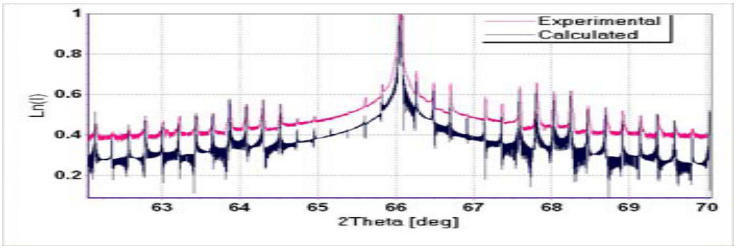

Fig. 5 Experimental and calculated rocking curves for heterostructure presented in fig. 4.

3.Results

The results of the HRXRD analysis of the AlAs/GaAs superlattices designed for DBRs, combined with the measurement of the optical reflectance and Rutheford backscattering allowed to answer the question how thickness variation and composition grading at the heterointefaces affect the DBR reflectivity [3,4]. We also hope to find the relationship between structure quality of the DBR and its reflectivity, especially in cases when the reflectivity is greater then 98%. HRXRD analysis of the heterostructures designed for quantum cascade lasers combined with numerical simulations allowed to determine their chemical composition profile in the growth direction and in this way to answer many questions concerning growth conditions, crystal quality, periodicity, structure of the interfaces and lattice coherence [5]. As a result it enabled to achieve an excellent quality of interfaces in the QCL structures and long term growth rate stability, necessary for obtaining strict periodicity of the structures and to draw a conclusion about the influence of the laser structure variation on the laser emission.

References

1. J. Fastenau, and G. Robinson, *Appl. Phys. Lett.* **74**(25), pp.3758-3760, 1999.
2.] P.F.Fewster J.Appl.Cryst. 21, (1988) 524-529
3. J.Gaca, M.Wójcik, A.Jasik, J.Muszalski, K.Pierściński, A.Turos, A.M. Abdul-Kader “, 15th International Conference on Crystal Growth, August 12-17, 2007, Salt Lake City, Utah
4. J.Gaca, M.Wójcik, A.Jasik, J.Muszalski, K.Pierściński, A.Turos, A.M. Abdul-Kader, Opto-Electronics Review, to be published
5. K. Kosiel, M. Bugajski, J. Muszalski, J. Kubacka-Traczyk, J. Ratajczak, A. Łaszcz, P. Romanowski, R. Mogiliński, J. Gaca, M. Wójcik, International Conference on Semiconductor Materials and Optics 18-21 October 2007, Warszaw, Poland

ROBL-CRG	**Experiment title:** ***In-situ x-ray scattering during formation of MAX phase (V,Cr)2AlN thin films by reactive co-sputtring and solid-state reaction***	**Experiment number:** **HS 3443**
Beamline: BM 20	**Date of experiment:** from: 07.11.2007 to: 13.11.2007	**Date of report:** 13.03.2009
Shifts: 18	**Local contact(s):** Carsten Baehtz	*Received at ROBL:* *13.03.09*

Names and affiliations of applicants (* indicates experimentalists):

M. Beckers*, F. Eriksson*, Linköping University, Sweden
C. Baehtz, Forschungszentrum Rossendorf, Germany & ROBL-CRG, France

Report

AIM:

The family of ternary nitrides and carbides grouped under the name **$M_{n+1}AX_n$ phases** – with M being a transition metal, A an A group element and X nitrogen or carbon – exhibit a unique combination of metallic and ceramic properties including good electrical conductivity, high temperature stability and machinability [1]. Due to these properties, $M_{n+1}AX_n$ phase bulk material as well as thin films have been extensively studied during the past years. Various carbide thin film $M_{n+1}AX_n$ phases have been deposited by DC magnetron sputtering. For the nitrides, only Ti_2AlN has been synthesized as thin film, either deposited **by reactive DC magnetron sputtering from compound or elemental Ti and Al elemental targets** [2] or by **self-organized topotaxial solid-state reaction between AlN(0001)/Ti(0001) stacks** [3]. During this experiment, the aim is a transfer from the Ti-Al-N system to the Cr-Al-N and V-Al-N systems, hence the **synthesis of Cr_2AlN and V_2AlN** either by reactive sputtering or by solid-strate-reaction between stacks of (Cr,V)N/Al or AlN/(Cr,V).

EXPERIMENTAL:

A total of **12 samples** was deposited onto $Al_2O_3(0001)$ substrates by reactive and non-reactive magnetron sputtering from Cr, V and Al targets at temperatures between 200 and 700°C. The deposition parameters for the V, Cr and Al metal layers were target powers of 40 W, 20 W and 20 W, respectively, with an Ar flow of 3.4 sccm at a working pressure of 0.5 Pa, leading to V, Cr and Al deposition rates of 0.34, 0.53 and 0.42 Å/s, respectively. The deposition parameters for the VN, CrN and AlN layers were target powers of 60 W, 70 W and 27 W, respectively with an Ar/N_2 flow ratio of 2.16/0.66 sccm and a working pressure of 0.35 Pa, leading to VN, CrN and AlN deposition rates of 0.8, 1.2 and 0.21 Å/s, respectively. Each sequential deposition step was characterized by specular x-ray reflectivity (XRR) for thickness and roughness and symmetric x-ray diffraction (XRD) for phase determination and off-plane lattice parameters. During each deposition, the time-resolved specular reflectivity was measured at a fixed incident angle of 1°, to monitor each layer's growth mode. Subsequent to deposition, some layers were annealed up to 750 °C substrate temperature to **check for possible $(Cr,V)_2AlN$ formation**. The x-rays were monochromatized to a wavelength of λ=1.053 Å.

RESULTS

Fig. 1 shows the *in situ* data obtained for two series of AlN/Cr and CrN/Al stacks that were deposited onto $Al_2O_3(0001)$ at 200°C substrate temperature and subsequently annealed to 750 °C.
The XRD data in Fig. 1(b) for a sequential deposition of ~20 nm AlN and ~10 nm Cr reveal heteroepitaxial growth of AlN(0001) and Cr(110) with low Cr peak intensity due to high mosaicity induced by the high 7% lattice mismatch. Accordingly, both peak signals do not increase significantly during subsequent depositions.

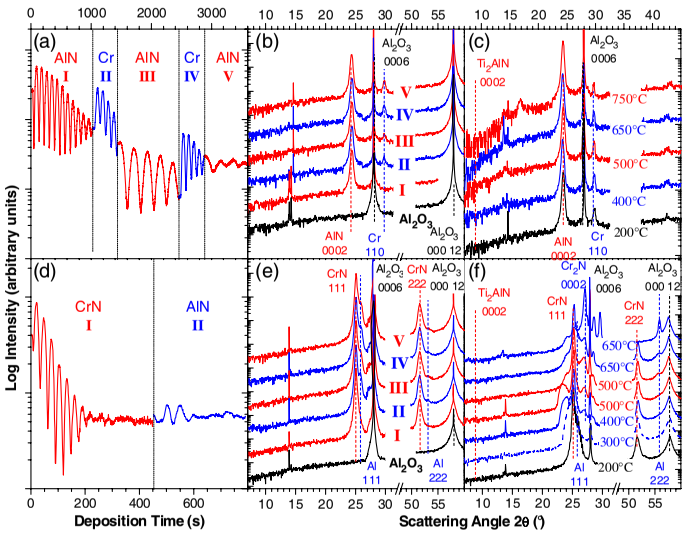

Fig. 1: *In situ* results of AlN/Cr and CrN/Al stacks: (a,d) time-resolved XRR during each deposition step (b,e) sequential XRD during deposition at 200°C, (d,f) XRD data during annealing

The lattice mismatch is also reflected in the time-resolved XRR data, where the growth oscillation amplitude decays with each deposition. During annealing, shown in Fig. 1(c), the system remains stable up to 750 °C, with sharp interfaces as detected by XRR and *ex situ* Rutherford backscattering spectroscopy (RBS). This is in contrast to AlN-Ti, where at 400 °C AlN decomposition is induced, with subsequent Ti_2AlN formation at 500 °C. This can be explained by the higher affinity of Ti towards N in comparision to Cr. Based on this low affinity of Cr towards N, also CrN/Al stacks were investigated. The XRD data in Fig. 1(e) for a sequential deposition of ~30 nm CrN and ~15 nm Al reveal cube-on-cube heteroepitaxial growth of CrN(111) and Al(111). The absence of the Al 222 peak points towards rather low crystalline quality, which can also be extracted from the time-resolved XRR data in Fig. 1(d). Growth on the high energy CrN(111) surface leads to quick roughening due to the low adatom mobility at the given substrate temperature. The roughening persists for Al growth, despite the higher mobility on the Al(111) surface. During annealing [Fig. 1(f)], already a temperature of 400 °C is sufficient to induce CrN decomposition and layer-by-layer topotaxial $Cr_2N(0001)$ formation, as is discernible by the appearing and shifting Laue fringes around the CrN(111) peak for a holding time at 400 °C and higher annealing temperatures. An annealing temperature of 650 °C is sufficient for an almost complete transformation of the intial CrN, as can be deduced from the lack of the CrN 222 peak and the appearance of the metallic Cr 110 signal. Obviously the initial CrN/Al stack loses a substantial amount of N into the vacuum, which was confirmed by *ex situ* RBS. These also revealed a substiantial loss of Al in comparison to the as-deposited state. In conclusion, neither annealing of CrN/Al and AlN/Cr stacks nor a direct deposition of 2CrAlN at higher temperatures (data not shown) yield Cr_2AlN formation. The same applies to VN/Al and AlN/V stacks, as well as to 2VAlN depositions (data not shown). Based on the the conducted experiments **we conclude that – in contrast to the Ti-Al-N system – no stable M_2AX phase exists in the ternary Cr-Al-N and V-Al-N systems.**

REFERENCES

[1]: M. W. Barsoum: Progr. Sol. State Chem. **28**, 201 (2000).
[2]: M. Beckers, *et al.:* Appl. Phys. Lett. **89**, 074101 (2006).
[3]: C. Höglund,. M. Beckers, *et al.:* Appl. Phys. Lett. **90**, 174106 (2007).

ESRF	**Experiment title:** *Ion bombardment of Ni-Ti thin films*	**Experiment number:** MA-232
Beamline: BM 20	**Date of experiment:** from: 14.02.2007 to: 19.02.2007	**Date of report:** 26.11.2007
Shifts: 18	**Local contact(s):** Dr. J. von Borany	*Received at ESRF:* *13.12.2007*

Names and affiliations of applicants (* indicates experimentalists):

F.M. Braz Fernandes*, Rui J. C. Silva*: CENIMAT-Centro de Investigação de Materiais, Campus da FCT/UNL, 2829-516 Monte de Caparica, PORTUGAL
Rui M.S. Martins*, J. von Borany*: FZD, P.O. Box 510119, 01314 Dresden, GERMANY
N. Schell*: GKSS, Max-Planck-Str. 1, 21502 Geesthacht, GERMANY

REPORT:

A negative substrate bias voltage causes a higher energetic ion bombardment of the growing film, resulting in an enhanced surface-atom mobility, but, at sufficiently high voltage, leads to defect formation. The configuration of the unbalanced magnetrons permits the plasma to extend to the region of the substrate (increasing the efficiency of the ionisation) and, thus, a greater number of ions are directed toward the growing film. When positive bias voltage is applied to the substrate, the energy of bombarding ions decreases. Conversely, when negative bias is applied, ion bombardment energy increases. Therefore, we concluded that the control of the ion bombardment energy would be one of the key factors in determining the microstructure and properties of the Ni-Ti Shape Memory Alloy (SMA) films. During this beamtime complementary tests have also been performed to complete a series of methodical investigations on Si(111), and NiTiHf on HfN/SiO_2/Si(100).

EXPERIMENTAL

The sputtering experiments were carried out in a D.C. magnetron sputtering chamber that has been described elsewhere [1]. Two unbalanced magnetrons, equipped with a 25.4 mm Ni-Ti target (51 at% Ni – 49 at% Ti) and a 25.4 mm Ti (or Hf) target (purity 99.99%), respectively, were positioned at a distance of 100 mm from the substrate. The base pressure at the deposition temperature of ≈ 470°C was 2×10^{-5} Pa and the working pressure during deposition was 0.42 Pa. For the deposition of the TiN (HfN) buffer layers, the Ti (Hf) target was run at a constant power of 80 W with an Ar/N_2 gas flow of 2/0.5 sccm and for the Ni-Ti (NiTiHf) films the Ni-Ti and Ti (Hf) magnetrons were driven at a power of 40 and 24 W (60 and 8 W), respectively. The processing conditions of the samples studied are presented in Tab. 1. Scans were run in Bragg-Brentano geometry, using 0.675 Å radiation, to reveal the type of preferential orientation during the deposition and annealing processes and to determine off-plane lattice parameters.

Sample	*Substrate*	*Buffer layer*	*Substrate bias (V)*		*Deposition (min.)*		*Annealing (min.)*	
			TiN (HfN) deposition	*Ni-Ti deposition*	*Buffer layer*	*Ni-Ti (NiTiHf)*	*Buffer layer*	*Ni-Ti (NiTiHf)*
S56	SiO_2^*/Si(100)	–	–	0	–	120 (at ≈520°C)	–	52 (at ≈520°C)
S57	SiO_2^*/Si(100)	TiN	-30	+20	41	131	31	60
S58	SiO_2^*/Si(100)	–	–	0	–	119 (at ≈520°C)	–	78 (at ≈520°C)
S59	SiO_2^*/Si(100)	TiN	-30	+20	41	124	33	55
S60	Si(111)	–	–	0	–	122	–	61
S61	SiO_2^*/Si(100)	HfN	-30	0	41	122	40	61

**1400 Å amorphous SiO_2 capping layer*

Tab. 1: Deposition parameters for the various samples investigated.

RESULTS AND DISCUSSION

The effect of a substrate bias voltage on the growth of near equiatomic Ni-Ti thin films on a TiN buffer layer of approximately 215 nm (topmost layer formed mainly by <111> oriented grains) has been investigated in previous beamtimes [ME-1255]. The anomalous behaviour of the electrical resistivity (ER) response in Ni-Ti films is attributed to lattice distortion and twinning, which are dominant mechanisms in self-accommodation R-phase transformation. The study of the temperature dependence of the ER has shown that the degree of ion bombardment alters the phase transformation behaviour of the films. The Ni-Ti film deposited without applying a substrate bias voltage exhibits higher phase transformation temperatures. We attributed this phenomenon to the presence of higher residual compressive stress in the film. The increase of the resistivity during R-phase formation for the Ni-Ti sample deposited with a substrate bias voltage of -90 V is not as high as for the other samples probably due to structural defects created by the higher energy of the bombarding ions during film growth. SEM observations have revealed that an increase of the substrate bias voltage from -45 V to -90 V led to the appearance of surface steps on the crystals. Previously, a continuous decrease of a_o during the deposition of the Ni-Ti film without applying bias voltage (suggesting a reduction of compressive stresses with increasing thickness) has been observed [2]. Here, we have studied the effect of a positive substrate bias voltage (+20V) showing an overall decrease and practically constant value of a_o during the deposition (Fig. 1).

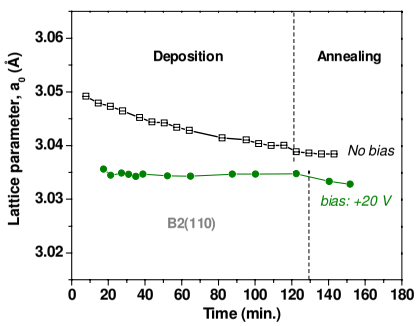

Fig. 1: Lattice parameter a_o, recorded as a function of time after start of Ni-Ti film growth on a TiN layer (≈ 215 nm). Results obtained for a Ni-Ti film deposited without applying substrate bias voltage and results obtained for a film deposited with +20 V are represented.

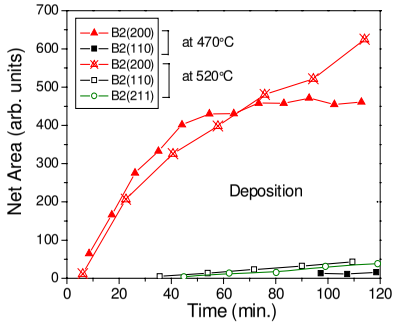

Fig. 2: Integrated intensity of the Bragg-Brentano B2 diffraction peaks recorded as a function of time for Ni-Ti films deposited on naturally oxidized Si(100), without applying substrate bias voltage, deposited at 470 and at 520°C.

As shown in Ref. [3] (results obtained during beamtime ME-936), for a Ni-Ti film deposited on thermally oxidized Si(100) at ≈ 470°C without applying a substrate bias voltage, after ≈ 540 nm film thickness, there is a stabilization of the intensity of the B2(200) peak due to a gradual change of the crystallographic direction of the growing columnar crystals. This orientation favoured the diffraction of the (310) peak of the B2 phase. In order to explore this phenomenon, a near equiatomic Ni-Ti film was deposited on thermally oxidized Si(100) without applying a substrate bias voltage but this time at a deposition temperature of ≈ 520°C. Figure 2 shows the variation of the integrated intensity of the Bragg-Brentano B2 diffraction peaks as a function of time (for both deposition temperatures). With an increase of the deposition temperature, the intensity of the B2(200) increases along the deposition process. The variation of the value of a_o as obtained from the positions of the Bragg-Brentano B2(200) peak does not exhibit such a continuous decrease during the deposition (Fig. 3). There is a convergence to a common value of a_o [values calculated using the diffraction peaks B2(200), B2(211) and B2(110)].

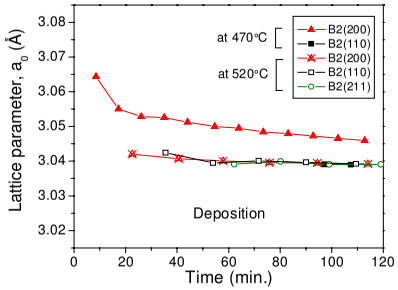

Fig. 3: Lattice parameter as obtained from the positions of Bragg-Brentano B2 diffraction peaks as a function of time for the films of *Fig. 2*.

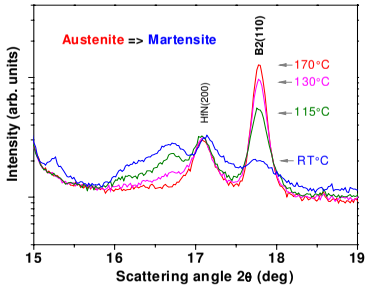

Fig. 4: XRD evaluation of phase transformation during cooling for the NiTiHf sample.

For the NiTiHf film, a preferential growth of <110> oriented grains of the B2 phase from the beginning of the deposition could be obtained using a HfN buffer layer. The higher transformation temperatures of the NiTiHf SMA, when compared to what was previously observed for Ni-Ti films, have been confirmed by XRD (Fig. 4). The deposition of Ni-Ti on Si(111) has given a preferential diffusion of Ni along <111> with $NiSi_2$ formation which was confirmed by an interface analysis by X-TEM that is presented in Ref. [4].

CONCLUSIONS

- When no substrate bias is applied, the ions bombarding the film surface during growth of the Ni-Ti film on a TiN buffer layer lead to residual compressive stress raising the transformation temperatures of the film (detected *ex-situ* by the temperature dependence of the electrical resistivity). The control of the energy of the bombarding ions is thus a tool for the manipulation of the transformation temperatures.
- The gradual change of the preferential crystallographic direction along which the columnar crystals grow (Ni-Ti films) during the deposition on SiO_2/Si(100), after an initial stacking of the B2 phase onto (h00) planes, is attributed to the combined effects of low surface mobility and shadowing (due to tilting of the magnetrons). At lower temperatures the crystallographic direction (100) shifts towards the direction of incident flux.
- The magnetron-sputtering chamber installed at ROBL proves to be a very efficient instrument to deposit, and follow *in situ* the evolution of the structure of NiTiHf films.

References

[1] N. Schell, J. von Borany, J. Hauser, *AIP conference proceedings* **879** (2007) 1813.
[2] R.M.S. Martins, N. Schell, R.J.C. Silva, L. Pereira, K.K. Mahesh, F.M. B. Fernandes, *Sens. Actuators B* **126** (2007) 332.
[3] R.M.S. Martins, N. Schell, M. Beckers, K.K. Mahesh, R.J.C. Silva, F.M. B. Fernandes, *Appl. Phys. A* **84** (2006) 285.
[4] R.M.S. Martins, A. Mücklich, N. Schell, R.J.C. Silva, K.K. Mahesh, F.M. B. Fernandes, *Microsc. Microanal.* (submitted).

ROBL-CRG	**Experiment title:** In situ study of nanostructured NiTi shape memory alloys during annealing after severe plastic deformation	**Experiment number:** MA-419
Beamline: BM 20	**Date of experiment:** from: 07.02.2008 to: 12.02.2008	**Date of report:** 22.11.2008
Shifts: 15	**Local contact(s):** **Carsten Baehtz**	*Received at ROBL:*

Names and affiliations of applicants (* indicates experimentalists):

F.M. Braz Fernandes*, Rui J. C. Silva*, K. K. Mahesh: CENIMAT-Centro de Investigação de Materiais, Campus da FCT/UNL, 2829-516 Monte de Caparica, PORTUGAL

J. von Borany*, Nicole Jeuter*: FZD, P.O. Box 510119, 01314 Dresden, GERMANY

Report:

This campaign has suffered from a significant instability of the beam supplied (~40% beam time loss due to low intensity and no refilling during 6 shifts due to booster failure). As a consequence, only a small part of the scheduled experiments have been performed: the annealing at 200 and 300ºC for 2 Ni-Ti alloys: a Ni-rich (alloy "N") and a Ti-rich (alloy "H") that have been subject to severe plastic deformation by cold-rolling to 40% thickness reduction.

It was intended to complement these studies with the following information (not possible during MA-419):

- the effect of deformation heterogeneity (in depth) by analysing the surface of a sample extracted from mid-thickness of the rolled material;
- the effect of annealing temperature of 350ºC (only 200 and 300 have been studied previously)

EXPERIMENTAL

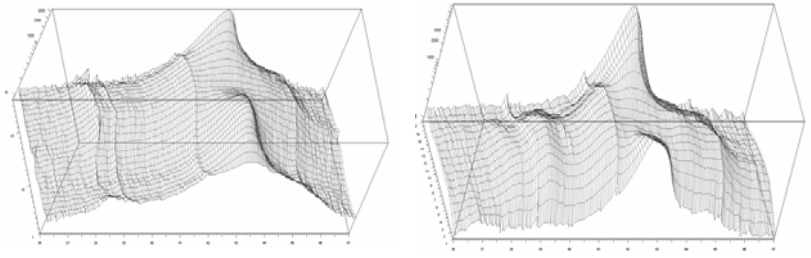

(a) (b)

Fig.1: In situ XRD of Ti-rich NiTi alloy initially cold-rolled (up to 38% thickness reduction):
(a) structural evolution during annealing up to 200ºC, cooling to -100ºC, heating to +80ºC;
(b) structural evolution during annealing up to 300ºC, cooling to -115ºC, heating to +80ºC.

The results obtained with Ti-rich alloy (H) are shown in Fig. 1. It may be noticed that:

- during the first heating cycle – annealing up to 200ºC, Fig. 1 (a); annealing up to 300ºC, Fig. 1 (b) – the transformation temperature (As) from martensite (B19') to austenite (B2) is shifted above 200ºC (compared with the As close to 100ºC of this alloy); this transformation seems to take place without intermediate phase (R-phase) formation;
- during the thermal cycle between room temperature and – 100ºC (Fig. 1 –b) for the determination of the transformation characteristics of the annealed material, the transformation from B2 to B19' (cooling) and B19´to B2 (heating) is taking place in one single step, without the formation of the R-phase.

The results obtained with Ni-rich alloy (N) are shown in Fig. 2. It may be noticed that:

- the as deformed material (at room temperature) contains stress induced martensite;
- during the first heating cycle, the transformation temperature (As) from martensite (B19') to austenite (B2) is shifted above 250ºC, so that after annealing at 200ºC still some martensite remains; only after annealing at 300ºC the martensite diffraction peaks fully disappear;
- during the thermal cycle between room temperature and – 100ºC (Fig. 1 –b) for the determination of the transformation characteristics of the annealed material, the transformation from B2 to B19' (cooling) and B19´to B2 (heating) seems to take place in one single step, without the formation of the R-phase.

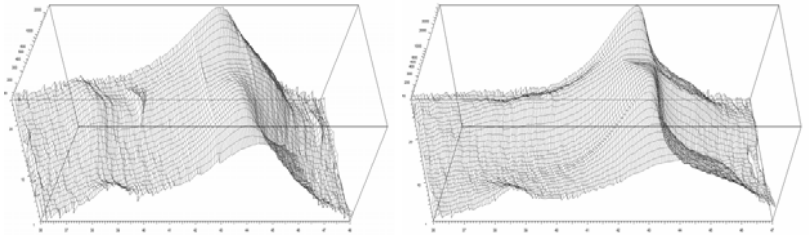

(a) (b)

Fig. 2: In situ XRD of Ni-rich NiTi alloy initially cold-rolled (up to 38% thickness reduction):
(a) structural evolution during annealing up to 200ºC, cooling to -115ºC, heating to +100ºC;
(b) structural evolution during annealing up to 300ºC, cooling to -118ºC, heating to +100ºC.

Estimation of the crystallite size using Scherrer formula gives 150 nm and 90 nm for the austenite at 300ºC, respectively for the Ti-rich and the Ni-rich alloy.

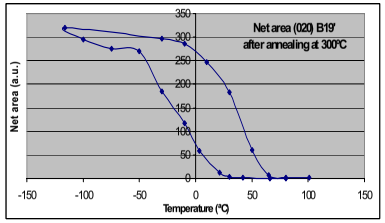

Fig. 3 – Transformation characteristics of cold-rolled H alloy (Ti-rich) after annealing at 300ºC.

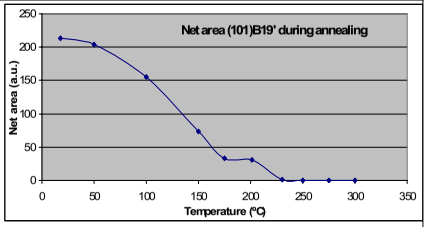

Fig. 4 – Stability of martensite during annealing of cold-rolled N alloy (Ni-rich).

ESRF

ESRF	**Experiment title:** XRD study of nano glass ceramic powders	**Experiment number:** MA 644
Beamline: BM20	**Date of experiment:** from: 05/09/2008 to: 09/09/2008	**Date of report:** 03/12/2008
Shifts: 15	**Local contact(s):** Dr. N.M. Jeutter	*Received at ESRF:*

Names and affiliations of applicants (* indicates experimentalists):

Dr. Christian Eisenschmidt* Martin-Luther-University Halle-Wittenberg, Hoher Weg 8, D-06120 Halle (Saale), Germany

Dr. Michael Hanke* Martin-Luther-University Halle-Wittenberg, Hoher Weg 8, D-06120 Halle (Saale), Germany

Dr. Bastian Henke* University of Paderborn, Warburger Straße 100, 33098 Paderborn

Report:

X-ray diffraction is a powerful tool to investigate the structure and size of nanoparticles which are created in glass ceramics upon thermal annealing. The focus of our work was on fluorozirconate (FZ) glasses which are additionally doped with chlorine to enable the growth of $BaCl_2$ nanocrystals in the glasses. The nominal composition of 5 mol% EuF_2-doped fluorochlorozirconate (FCZ) glasses is $48ZrF_4$-$10BaF_2$-$10BaCl_2$-20NaCl-$3.5LaF_3$-$3AlF_3$-$0.5InF_3$-$5EuF_2$ (values in mole percent). The samples were subsequently

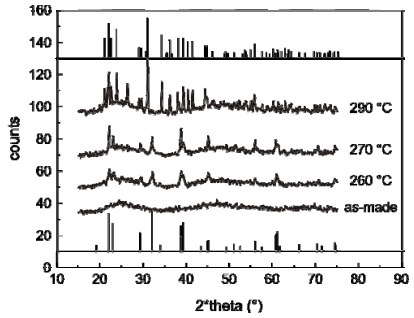

Figure 1: XRD data of 5 mol% EuF_2 doped glass ceramics: as made and annealed at 260, 270, and 290 °C. The curves are vertically displaced for clarity; the line pattern of hexagonal phase $BaCl_2$ (PDF #45-1313) and orthorhombic phase $BaCl_2$ (PDF #24-0094) are shown for comparison.

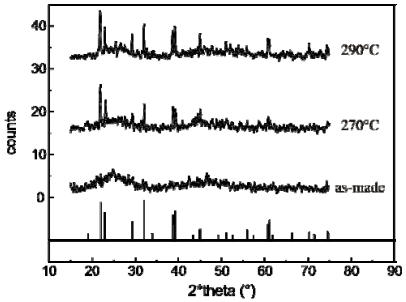

Figure 2: XRD data of 2 mol% $EuCl_2$ doped glass ceramics: as made and annealed at 270 and 290 °C. The curves are vertically displaced for clarity; the line pattern of hexagonal phase $BaCl_2$ (PDF #45-1313) is shown for comparison.

brought to temperatures above the glass transition temperature of approximately 210 °C and held there for 20 minutes. This thermal treatment was performed in an inert nitrogen atmosphere and in ambient atmosphere. The visible appearance of the as-made glass is almost clear, but after thermal processing there is evidence of crystallization in all of the glasses, i.e. the glasses become milky white. However, samples tempered in ambient atmosphere became milky white at lower annealing temperatures compared to the samples annealed in a nitrogen atmosphere. The corresponding XRD spectra after annealing in nitrogen are shown in Figure 1.

In the as-made glass no evidence of crystallization can be found, i.e. only the broad reflections due to the glassy background can be seen. For the samples annealed at 260 and 270 °C the XRD data comprise sharp peaks that we identify as arising from hexagonal $BaCl_2$ (space group P-62m (189), a = 0.8066 nm, c = 0.4623 nm). In the spectrum of the sample annealed at 290 °C several sharp peaks appear; these are associated with orthorhombic $BaCl_2$ (space group Pnam (62), a = 0.7865 nm, b = 0.9421 nm, c = 0.4731 nm). However, there are additional peaks from unknown phases. The XRD pattern for the main unknown phase can be fitted to a structure of hexagonal symmetry with lattice parameters a = 0.390 nm, c = 0.407 nm and a P6/mmm (191) space group. These peaks are marked with asterisks in Figure 1. We have been unable to determine the composition of this phase.

The same experiments were performed for samples annealed under ambient conditions. Despite the fact that these samples change their visible appearance at lower temperatures the XRD data are similar to those obtained for the samples annealed in nitrogen (within experimental error).

Furthermore, another series of Eu-doped FCZ glass ceramics was prepared. The nominal composition was $51ZrF_4$-$20BaCl_2$-20NaF-$3.5LaF_3$-$3AlF_3$-$0.5InF_3$-$2EuCl_2$ (values in mole percent). The corresponding XRD data are shown in Figure 2. Again in the as-made glass no evidence for crystallization was found. For the samples annealed at 270 and 290 °C several reflections can be found; these can be attributed to hexagonal phase $BaCl_2$. No reflections from orthorhombic phase $BaCl_2$ can be found which is in contrast to the first sample set.

ESRF	**Experiment title:** Lattice parameter determination of structured Zn:$LiNbO_3$ thin films epitaxially grown on $LiNbO_3$ substrates	**Experiment number:** SI-1518
Beamline: BM 20	**Date of experiment:** from: 08/12/2007 to: 11/12/2007	**Date of report:** 19/03/2009
Shifts: 9	**Local contact(s):** Dr. Carsten Baehtz	*Received at ESRF:* 19/03/2009

Names and affiliations of applicants (* indicates experimentalists):

Dr. J. Kräußlich *[1)] Dr. C. Dubs [2)]
PhD U. Zastrau *[1)] Prof. A. Tünnermann [2)]

Friedrich-Schiller-University of Jena
[1)] Institute for Optics and Quantum Electronics
[2)] Institute of Applied Physics
Max-Wien-Platz 1
07743 Jena
Germany

Report:

Due to its outstanding optical and electro-optical properties, $LiNbO_3$ is a suitable material to optical waveguide devices (such as modulators and switches) and to second-harmonic generation devices for integrated optical applications (see for example [1, 2, 3, 4]). Optical waveguides demand a well-defined modification of the local refractive index. For this purpose, Zn-doped $LiNbO_3$ thin films with a thickness up to 4 µm were grown on standard x-cut $LiNbO_3$ single crystal substrates by means of the liquid phase epitaxy (LPE) method [5, 6]. Zinc-substituted stoichiometric Zn:$LiNbO_3$ shows an increased refraction index and also an enhanced damage threshold. However, a lattice mismatch of the epitaxial films to the substrate is the consequence of the Zn-substitution. It was assumed and also with the recently taken measurements experimentally verified [7, 8] that this lattice mismatch causes an additional inherent strain in the grown films with influence on the required refraction index.

The aim of the current experiment was to characterize epitaxially grown Zn:$LiNbO_3$ thin films which were subsequently laterally structured (Fig. 1) in view to the generation of optical wave guide strips. These strips were microfabricated by reactive ion etching (RIE) using an inductively coupled plasma (ICP) source [9], recently described ba Ren et a. [10].

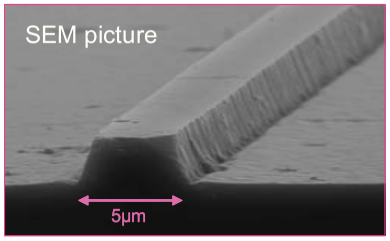

Fig. 1: Zn:$LiNbO_3$ rib waveguide, produced by ICP-RIE etching technique [9]

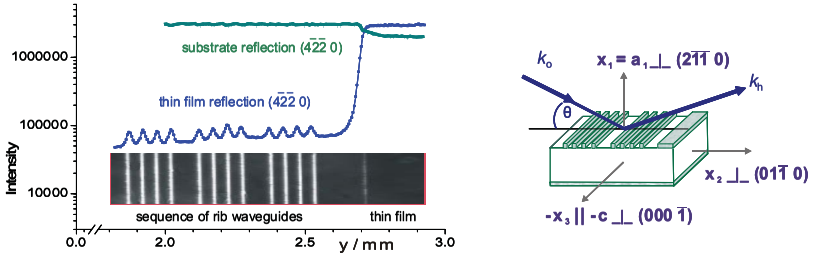

Fig. 2: Lateral y-scan taken with the symmetric 4-2-2 0 thin film and substrate reflection, respectively. A photographic real dimension detail of the sample is shown in the insert. On the left side a sequences of rib waveguides are visible whereas on the right side still the homogeneous thin film is presented .

Using high-resolution x-ray diffraction measurements (HRXRD) with symmetric reflections thin film lattice parameters perpendicular to the sample surface can be won, in reference to the x-cut LiNbO3 substrate with a relative accuracy of $(\Delta d/d)_\perp < 10^{-5}$ (Fig. 2, 3).

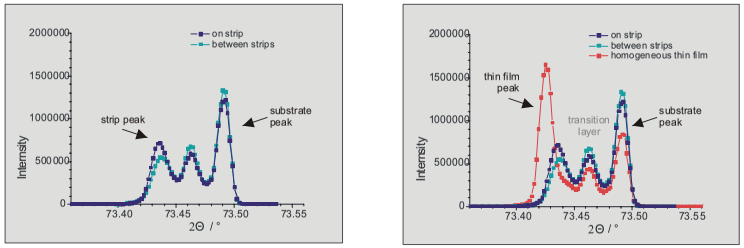

Fig. 3: θ/2θ scan taken up with the symmetric (4-2-2 0)-reflection on and between the ribs, respectively (on the left side), and of the homogeneous thin film to the comparison (on the right side).

For homogeneous Zn:$LiNbO_3$ thin films with a Zn doping of 5.3 mol-% we get a relative lattice parameter increase of $7.8 \cdot 10^{-4}$ perpendicular to the sample surface. Such thin films show an experimentally determined change of refractive index of $\Delta n = 5 \cdot 10^{-3}$ [11].

In plane lattice parameters of the epitaxially grown Zn:$LiNbO_3$ thin films in respect to the substrate can be won from **r**eciprocal **s**pace **m**aps (**rsm**) recorded with asymmetric reflections [8]. In this case one obtains a precision of $(\Delta d/d)_\parallel < 10^{-4}$ (Fig. 4). It is seen, that the in Zn:$LiNbO_3$ thin films grow pseudomorphously on the x-cut $LiNbO_3$ substrate, characterized by the fact that $\Delta d\parallel = 0$ but $\Delta d\perp \neq 0$ (Fig. 4 top right). Hence, the homogeneous Zn:$LiNbO_3$ thin films are laterally stressed. However after structuring, the waveguide strips appear laterally relaxed related to the homogenous thin film, how is to be seen in the rsm recorded in ´on-a-strip-position´ (Fig. 4 top left). In this case the lateral and normal change of lattice parameter related to the homogenous thin film are the same.

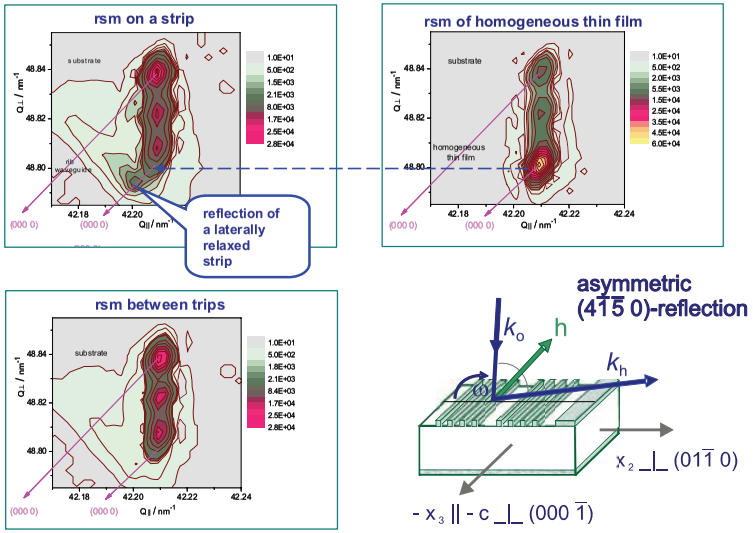

Fig. 4: Reciprocal space maps recorded with the asymmetric (4-1-5 0)-reflection on (top left) and between (down left) the strips, respectively, and of the homogeneous thin film to the comparison (top right).

Using the lattice parameters obtained from these rsm, it is now possible to calculate the inherent normal and lateral stress components [8] of the epitaxially grown homogeneous Zn:$LiNbO_3$ thin films and of the waveguide strips prepared from it.

We thank all members of the ROBL beamline team, especially Dr. C. Bähtz, for the helpful support at the time of realization this experiment.

References

[1] E. J. Murphy: Integrated optical circuits and components: Design and application, Marcel Dekker, New York, (**1999**) 1048
[2] M. Asobe, O. Tadanaga, H. Miyazawa, Y. Nishida, H. Suzuki: NTT Technical Review 1 (**2003**) 59-
[3] J. Kondo, K. Aoki, A. Kondo, T. Ejiri, Y. Iwata, A. Hamajima, T. Mori, Y. Mizuno, M. Imaeda, Y. Kozuka, O. Mitomi, M. Minakata: IEEE Photon. Technol. Lett. 17 (**2005**) 2077-2079
[4] J.-P. Ruske, A. Tuennermann: Photonik International **2007**, 122-125
[5] C. Dubs, A. Lorenz, J.-P. Ruske, J. Fuchs and A.Tünnermann: Zeitschrift für Kristallographie, Supplement Issue 22 (**2005**) 52
[6] T. Kawaguchi, K. Mizuuchi, T. Yoshino, M. Imaeda, K. Yamamoto, T. Fukuda: J Crystal Growth 203 (**1999**) 173
[7] J. Kraeusslich, O. Wehrhan, U. Zastrau: Report to the ESRF experiment SI-1346 at BM20 (**2006**)
[8] J. Kraeusslich, C. Dubs, A. Lorenz, A. Tünnermann: physica status solidi (a) **204**, 2585 – 2590 (**2006**)
[9] H. Hartung, unpublished results]
[10] Z. Ren, P.J. Heard, J.M. Marshall, P.A. Thomas, S. Yu:Etching characteristics of LiNbO in reactive ion etching and inductively coupled plasma, Journal of Applied Physics **103,** 34109 (**2008**},
[11] C. Dubs, J.-P. Ruske, J. Kraeusslich, A. Tuennermann: Submitted to Optical Materials **2008**

ESRF	**Experiment title:** Interdiffusion studies in $Si_{1-x}Ge_x$ alloys with high Ge content by x-ray diffraction	**Experiment number:** SI-1617
Beamline: BM 20	**Date of experiment:** from: 30.8.2007 to: 5.9.2007	**Date of report:** 21.12.2007
Shifts: 18	**Local contact(s):** Carsten BAEHTZ (baehtz@esrf.fr)	*Received at ESRF:*

Names and affiliations of applicants (* indicates experimentalists):

M. Meduna*, O. Caha*, P. Mikulik, *Department of Condensed Matter Physics, Masaryk University, Brno, Czech Republic*

G. Bauer, M. Keplinger*, E. Wintersberger, *Institute of Semiconductor Physics, J.Kepler University, Linz, Austria*

D. Grützmacher, *Institute for Bio-and Nanosystems, Forschungszentrum Jülich, Jülich, Germany*

Report:

The mechanism of interdiffusion and diffusion processes in SiGe alloys including self and impurity diffusion and interdiffusion coefficients are known with very low precision and only for low Ge content SiGe alloys. The situation is complicated mainly by the non-linearity of the diffusion process. The diffusion coefficient strongly depends on Ge content and also on strain. Since the diffusion coefficient can be written in the shape of Arrhenius equation, the problem reduces to the determination of activation energy and diffusion prefactor for certain Ge content and strain. In our recent experiments, we have reported the study of interdiffusion in $Si_{0.5}Ge_{0.5}$ and $Si_{0.75}Ge_{0.25}$ alloys but the data for the range from 50% to 100% of Ge were still missing in the literature. In this experiment, we have performed the in situ x-ray diffraction (XRD) measurements on SiGe multiple quantum wells (MQW) with average Ge content 70% and 90%. These studies will extend the knowledge about interdiffusion in Ge rich SiGe alloys and are very important for diffusion modeling of complicated SiGe electronic structures.

Two types of samples were investigated; 70% Ge samples contained MBE-grown (300°C) MQW's with 30 periods of $Si_{0.45}Ge_{0.55}$ (160Å)/Ge (80Å) bilayers grown on a $Si_{0.30}Ge_{0.70}$ constant composition relaxed pseudo-substrate and 90% Ge samples contained $Si_{0.15}Ge_{0.85}$ (160Å)/Ge (80Å) bilayers grown on $Si_{0.10}Ge_{0.90}$ pseudo-substrate. The superlattices were strain symmetrized in order to avoid the formation of misfit dislocations in the MQWs. We have performed a series of XRD measurement for the samples annealed *in-situ* at different temperatures in the range from 620°C up to 720°C. We have obtained the evolution of Ge content during annealing and found a temperature limit, at which the inter-diffusion started to affect these structures.

X-ray reflectivity and diffraction reciprocal space maps (RSM) have been obtained at room temperature and during annealing for different annealing periods, using a wavelength λ=1.5405 Å. We have used a small furnace with a Be dome available at BM20, in order to perform the *in-situ* annealing study. A position sensitive detector was used, to record the scattering signal intensity.

An example of XRD RSM around (224) diffraction point recorded at room temperature before annealing is shown in Fig. 1(a). XRD RSM of 90% Ge sample after annealing at temperature 710°C for 1.5 hour is shown in Fig. 1(b). In Figs. 1(c-d), the evolution of Bragg peaks during annealing of 70% sample at 710°C and 90% sample at 650°C are presented showing the difference in ***inter-diffusion velocity*** in these samples. It is evident that the interdiffusion process is much stronger in samples with the higher Ge content. The simulations of diffraction signal along Q_z cuts are plotted together with the measured ones also in Figs. 1(c-d) for both investigated structures. Results of these fits confirm the high quality of the samples and the fact the MQWs stay pseudomorphic during the annealing.

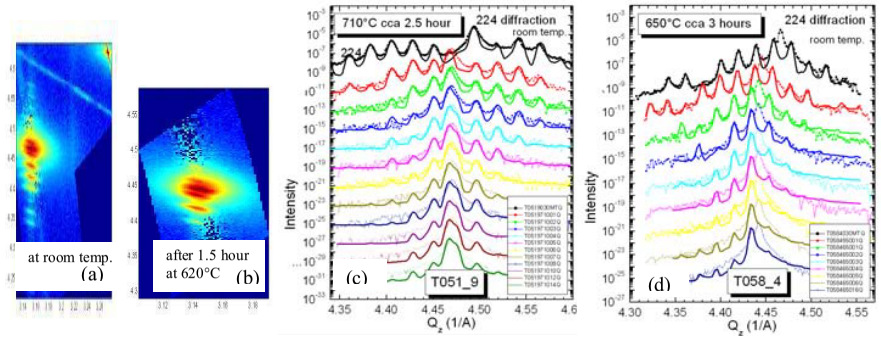

Fig. 1: XRD reciprocal space map around 224 diffraction of MQW sample with Ge content 90% (a) at room temperature and (b) after 1.5 hour of annealing at 620°C. (c)-(d) evolution of the diffraction pattern cuts in direction paralel to Q_z across the pseudosubstrate peak for 70% Ge (sample T051_9) and 90% Ge (sample T058_4) of Ge content. These figures show that the interdiffusion is definetely stronger in samples with higher Ge content.

From the simulations of XRD scans we have obtained the decay of maximum contrast of Ge content Δρ in the MQW. From the slope of exponential decay of Δρ, we have determined the diffusion coefficients for all 6 various temperatures measured in the range 630°C - 720°C by 70% Ge samples and for 4 various temperatures measured in the range 620°C - 650°C by 90% Ge samples. The typical time of one measurement cycle was in the range from 5 to 25 min, nevertheless for slower diffusion processes only selection of measured maps was involved into analysis.

The series of obtained diffusion coefficients at different temperatures has allowed estimating the activation energy E_A and the diffusion pre-exponential factor D_0 for $Si_{0.3}Ge_{0.70}$ and $Si_{0.1}Ge_{0.90}$. Since the MQW was annealed up to a detection limit of diffraction satellites, we can assume that the structure was almost interdiffused at the last stage of annealing and only the Ge content of the pseudosubstrate (± 5%) was present inside the structure. The obtained values of activation energy E_A and the diffusion pre-exponential factor D_0 are shown in the Figs. 2(a-b) together with the results obtained in our previous experiments.

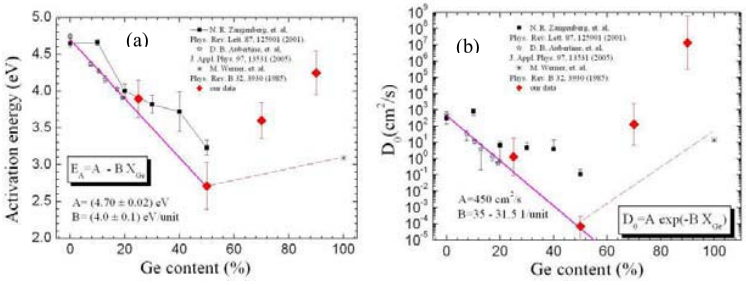

Fig. 2: (a) Activation energy E_A and (b) diffusion prefactor D_0 versus Ge content X_{Ge}. A comparison is made between values obtained in our experiments for X_{Ge}=25%, 50%, 70% and 90% (red diamond point) and recently published data determined for different Ge concentrations. The full line represents the extrapolation of data from Aubertine et al.. The dashed line represents just a guide for the eye from our data at 50% to data published for pure Ge. The data obtained in this experiment correspond to the points at 70% and 90% of Ge content.

ROBL-CRG	**Experiment title:** In-situ Evolution of Phase Composition and Internal Growth Stresses in Nanostructured Oxide Layers grown on Iron Aluminides	**Experiment number:** SI-1711
Beamline: BM 20	**Date of experiment:** from: 18 March 2008 to: 26 March 2008	**Date of report:** 24 November 2008
Shifts: 24	**Local contact(s):** Dr. Nicole Martha Jeutter	*Received at ROBL:*

Names and affiliations of applicants (* indicates experimentalists):

Dr.-Ing. Haroldo Pinto*, Max-Planck-Institut für Eisenforschung, Düsseldorf Germany
Dipl.-Ing. Pedro Paiva Brito*, Max-Planck-Institut für Eisenforschung, Düsseldorf Germany
Prof. Dr. Anke Pyzalla, Helmholtz-Zentrum Berlin für Materialien und Energie, Berlin, Germany

Report:

Iron aluminides are important materials for high temperature applications because of their ability to form an adherent α-Al_2O_3 scale on the metal surface Critical to oxidation resistance of these alloys are growth stresses that develop within the scale during oxidation. Nevertheless, the origin of such stresses is not yet completely understood for many metal-oxide systems /Veal 2006/.

The main objective of this project was to study the evolution of the growth stresses in oxide scales formed at low temperature (700°C). In this case a multi-layered oxide scale is formed, composed of α-Al_2O_3 and α-Fe_2O_3, with an overall thickness of 80 to 100nm (figure 1).

In order to assess the influence of substrate microstructure and chemical composition on the oxide scale development, both single crystals and polycrystals of two Fe-Al alloys (ferritic Fe-15at.%Al and intermetallic Fe-26at.%Al) were used in the studies. The stresses in the growing

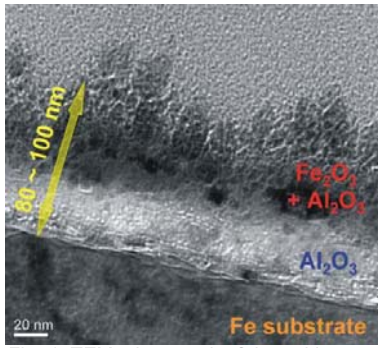

Fig. 1: TEM micrograph of the oxide scale grown on an Fe-15at.%Al substrate after 5h oxidation at 700°C.

in the scales were determined in-situ by applying the $\sin^2\Psi$ method with a grazing incidence angle of 0,3° /Ma 2002/.

The evolution of growth stresses in the oxide layer formed on an Fe-15at.%Al single crystal is shown in figure 2. The stresses exhibit a transient behavior, in which initially elevated values gradually relax as oxidation progresses. In the initial stages of oxidation growth stress development was found to be governed by the epitaxy between the two main oxide phases present in the scale, due to reduced layer thickness /Panicaud 2006/. Because they share the same crystal strucutre α-Al_2O_3 and α-Fe_2O_3 exhibit parallel epitaxy relationships in the basal planes /Wang 2002/. Preliminary texture analyses have also indicated that the (104) planes of α-Al_2O_3 and α-Fe_2O_3 are also parallel to each other (figure 3). This is reflected in the development of the growth stresses, where the positive strain on the (104) plane of α-Fe_2O_3 is balanced by compressive strains on the (104) plane of α-Al_2O_3.

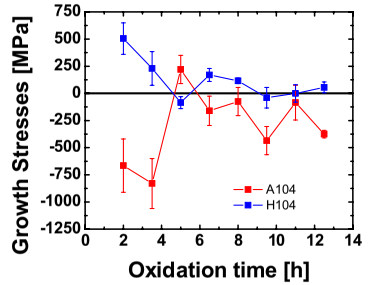

Fig. 2: Evolution of growth stresses in the oxide layer grown on an Fe-15at.%Al (100) single-crystal at 700°C.

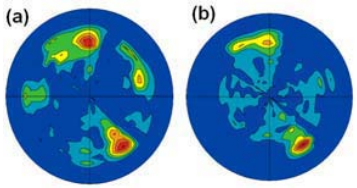

Fig. 3: Experimental pole figures of (a) α-Al_2O_3 (104) and α-Fe_2O_3 (104).

References:

1. B.W. Veal et al, Nat. Mater. 5 (2006) 349.
2. C.-H. Ma et al, Thin Solid Films 418 (2002) 73.
3. B. Panicaud et al, Appl. Surf. Sci. 252 (2006) 5700.
4. C.-M. Wang et al, Thin Solid Films 414 (2002) 31.